



UNIVERSITÀ
DEGLI STUDI
FIRENZE

DOCTORAL PROGRAMME IN INDUSTRIAL
ENGINEERING
DOTTORATO DI RICERCA IN INGEGNERIA
INDUSTRIALE

XXXI

**Architecture, design and implementation
of CAM software for Wire and Arc
Additive Manufacturing**

ING/IND-16

Doctoral Candidate

Ing. Giuseppe Venturini

Supervisor

Prof. Gianni Campatelli

Dean of Doctoral Programme

Prof. Maurizio De Lucia

External referees

Prof. Masakazu Soshi
Prof. Giuseppe Ingarao

Years 2015/2018

© Università degli Studi di Firenze – School of Engineering
Via di Santa Marta, 3, 50139 Firenze, Italy

Tutti i diritti riservati. Nessuna parte del testo può essere riprodotta o trasmessa in qualsiasi forma o con qualsiasi mezzo, elettronico o meccanico, incluso le fotocopie, la trasmissione fac simile, la registrazione, il riadattamento o l'uso di qualsiasi sistema di immagazzinamento e recupero di informazioni, senza il permesso scritto dell'editore.

All rights reserved. No part of the publication may be reproduced in any form by print, photoprint, microfilm, electronic or any other means without written permission from the publisher.

Summary

Wire and Arc Additive Manufacturing (WAAM) technology is a promising Direct Energy Deposition (DED) process for metallic components that is achieving wide diffusion in the research and industrial sectors. It exploits a traditional Metal Inert/Active Gas (MIG/MAG) welding machine to deposit material via an electric arc established between a thin metal wire and a metal substrate. The deposition rate of this technology is very high, making it attractive to produce large aerospace components such as stiffened panels, especially when considering that WAAM only need a local shielding gas and not a completely sealed building chamber. Moreover, being a DED technology, WAAM can be used even in a five-axis machine to produce parts without the needing for supports since, in that kind of machine, the part can be oriented under the torch making every new layer rest exactly on the top of the previous one.

However, this technology still presents some issues that are limiting its diffusion and application to real industrial applications. Among the main issues there are the lack of automatic CAM software for the toolpath programming for complex parts, high residual stresses and distortions due to the high energy input of the process. Moreover, defects often occur during the deposition process and these are usually casual and hardly predictable. These are often the limits of the WAAM technology that must be overcome to allow a wide diffusion of this technology that would bring high cost and material savings in the industry, especially when producing large metallic components.

In this sense, the main goal of this thesis is the design and development of a CAM software for Direct Energy Deposition (DED) Additive Manufacturing (AM) technologies, especially dedicated to Wire and Arc Additive Manufacturing (WAAM). The developed software aims at determining the deposition toolpath starting from an input geometry of the part to be produced. The whole thesis is addressed to thin walled components, since these are the most economically convenient to be produced using WAAM. Both three-axis and five-axis toolpath calculation modules have been developed. Regarding the three-axis module, it is an automatic software tool especially addressed to the toolpath calculation for stiffened panels, tubulars and impellers and it is based on a feature-based approach. For this last reason, a strategy for each different feature has been developed and experimentally tested. The five-axis toolpath calculation module is composed of several sub-modules, each one dedicated to a

specific geometrical shape such as impellers, freeform ducts and twisted blades. Since the virtual simulation of the calculated toolpath is mandatory in the case of five axis operations, a simulation module has been implemented. Such module can simulate the deposition of the material and the movements of the machine components. The toolpath calculation algorithms laying behind the CAM modules are almost automatic and request to the user the setting of a few inputs such a geometrical element (like a curve or a point) and the dimensions of the weld bead.

Since WAAM technology is prone to casual defect occurring during the deposition phase, a monitoring system based on a 3D scanning device is presented. It can extract the width and height of the deposited bead during the manufacturing process. The future goal is to integrate this system and its output in the numerical control of the machine, thus obtaining a reliable tool capable of correcting the occurred defects with a closed loop approach.

The experimental activity has been carried out using a 3-axis WAAM machine that was already available in the Manufacturing Technologies Research Laboratory of the University of Firenze and on a 5-axis machine designed and built during the research activity. Such 5-axis machine has been obtained through the retrofitting of a three-axis traditional milling machine for which a roto-tilting table has been designed and assembled. The roto-tilting-table, made of laser-cut sheet metal parts, shows an innovative design particularly suitable to WAAM technologies.

Finally, since the toolpath obtained by the two developed CAM modules could be an important tool to calculate the manufacturing cost of components manufactured using WAAM, a toolpath-based cost model has been implemented. This can be directly integrated with the 3-axis CAM framework and aims at calculating the total manufacturing cost for the component including both the deposition and post-finishing operations.

Table of contents

Summary	7
Table of contents	11
List of figures	15
List of tables	27
Acronyms List	29
1. The WAAM technology and the need for a synergic framework	31
1.1. The Wire and Arc Additive Manufacturing Technology.....	31
1.2. The WAAM process: characteristics and related issues	36
1.3. Three and five-axis deposition for WAAM	45
1.4. The 5-axis WAAM process as a result of a synergy.....	48
2. A toolpath-based cost model for WAAM	51
2.1. Review of the state of the art: available cost models for WAAM.....	54
2.2. The cost model used for CNC milling roughing and finishing	57
2.2.1. Material cost	58
2.2.2. Machining costs.....	60
2.2.3. Setup Costs	66
2.2.4. Non-productive time cost.....	67
2.2.5. Calculation of the total manufacturing cost and time	68
2.3. A cost model for WAAM.....	69
2.3.1. Deposition efficiency parameters: experimental determination.....	71
2.3.2. Material cost	75
2.3.3. Manufacturing cost	80

2.3.4. Setup cost	82
2.3.5. Non-productive cost.....	83
2.3.6. Overall production cost.....	85
2.4. Comparison with CNC milling and sensitivity analysis	86
3. 3-axis feature-based CAM software for WAAM	91
3.1. Proposed toolpath generation framework: general description	92
3.2. Proposed toolpath generation framework: description of the input	94
3.3. Proposed toolpath generation framework: the feature recognition module	96
3.4. Proposed toolpath generation framework: a deposition strategy for each feature .	106
3.4.1. Deposition strategies for direct crossings	106
3.4.2. T-crossings: deposition strategies with specific deposition directions	110
3.4.3. T-crossings: deposition strategies without specific deposition senses	120
3.4.4. Deposition strategy for free end walls	121
3.4.5. Deposition strategies for tubulars	121
3.4.6. Deposition strategies for open impellers.....	124
3.5. Proposed toolpath generation framework: implementation and testing	128
3.6. A proposal for an integrated three axis CAM framework for WAAM	131
4. Design and construction of a 5-axis machine for WAAM operations	133
4.1. The choice of the best configuration for the WAAM machine	140
4.2. The mechanical design.....	143
4.2.1. Design and installation of the support and transmission system for motors	145
4.2.2. Design and construction of the roto-tilting table	153
4.2.3. The welding unit and the design and construction of the torch support	170
4.3. The implementation of the numerical control	172
4.4. Machine testing	178
5. A vertical 5-axis CAM software for WAAM.....	181
5.1. Toolpath calculation module for open impellers.....	187
5.2. Toolpath calculation module for twisted hollow blades	194
5.3. Toolpath calculation modules for freeform ducts	199
5.4. A machine simulation module for five axis operations	211
6. A monitoring system for WAAM deposition operations	215
6.1. The need for a process monitoring system for WAAM operations.....	215

6.2. Process monitoring systems for AM: state of the art and proposed approach	217
6.3. Introduction to the developed system: input, output and general architecture.....	222
6.4. Preliminary design of the system.....	224
6.5. Welding spectrum analysis, optical filter and projected pattern selection.....	227
6.6. Configuration of the cameras	233
6.7. The pattern projector.....	244
6.8. The structure of the software.....	248
6.9. Testing of the monitoring system and setting of the software parameters.....	255
6.9.1. Artificial tests	255
6.9.2. Tests in a real welding scenario	258
7. Conclusions and final remarks	267
Bibliography	271

List of figures

Figure 1 Classification of AM technologies for metallic components (from [1])	31
Figure 2 WAAM equipment; (1) Computer and Control Cabinet, (2) Positioning structure, (3) Welding unit (welding power source, wire feeder and shielding gas bottle), (4) Final Part.....	32
Figure 3 Geometric parameters of a bead cross section (W = width, P = penetration, H = height)	32
Figure 4 (a) Robotic welding facility and (b) cartesian welding facility.....	33
Figure 5 Schematic representation of (a) GMAW, (b) GTAW and (c) PAW processes	33
Figure 6 Exploded view of a GTAW torch.....	34
Figure 7 Weld bead deposited with shielding gas (above), and without shielding gas (below)	34
Figure 8 Three types of feeding directions according to the given deposition direction (from [2])	35
Figure 9 A typical GMAW welding facility	36
Figure 10 The parameters influencing the quality of the WAAM process (from [6])	37
Figure 11 Effects of the process parameters on the appearance of the welding bead	37
Figure 12 Relationship between wire feed speed and welding current for GMAW	38
Figure 13 Reciprocal position between torch and substrate	38
Figure 14 Example of relationship between CTWD and welding current for GMAW	39
Figure 15 The effect of the shielding gas	39
Figure 16 The large robotic WAAM facility implemented by Cranfield University (from [9])	40
Figure 17 A wing rib	40
Figure 18 Cost vs removed/added material for WAAM and machining operations.....	41
Figure 19 A CAD model (left) and its bounding box (right).....	42
Figure 20 A schematic cross section of a single bead wall or “thin wall” (left) and a multiple bead wall (right)	42
Figure 21 A wall manufactured using WAAM and its cross section (in green the final wall after machining, in red the zones to be machined away).....	42
Figure 22 Parameters of a wall to consider for hybrid WAAM operations (from [12])	43
Figure 23 The typical appearance of a deposited bead.....	43
Figure 24 (a) Part deformation during the building procedure due to heat accumulation (the blue dotted line is the expected shape, the black line the real one), (b) Collapse of a thin section of the part during the building procedure due to excessive heat input	43
Figure 25 Effect of interpass temperature on the surface quality of a straight wall. (Left) optimal interpass temperature, (right) interpass temperature too low (from [17]).....	44

Figure 26 Effect of the interpass temperature on the cross section of a wall. Interpass temperature increasing from left to right (from [16]).....	44
Figure 27 Different deposition patterns affect in a different way the final distortion and residual stresses of the part (from [18]).....	45
Figure 28 The WAAM machine available at MTRL	45
Figure 29 3-axis WAAM deposition	46
Figure 30 5-axis WAAM deposition	46
Figure 31 Relative position between a workpiece and a tool	47
Figure 32 CAM software scheme	47
Figure 33 An example of conformal channels for a mold (left) (from [26]) and of lightweight lattice structure (right) (from [27]). Both these parts must be manufactured using powder bed techniques	51
Figure 34 Close view of an aluminum stiffened panel (left) and of an open pump impeller (right).....	52
Figure 35 Repairing cycle for a worn turbine blade (from [28])	52
Figure 36 Software framework for the presented cost models. Only the main inputs are shown	54
Figure 37 WAAM feature classification framework used in [29]	55
Figure 38 Final shape of the component (left) and shape of the component right after the deposition process (right).....	56
Figure 39 Final shape of the component (left) and the midsurface (right) that is the input both for the cost model and for the toolpath generation module	56
Figure 40 The determination of the bounding box for the input CAD model	59
Figure 41 The bounding box after the XY scaling operation	59
Figure 42 Visual explanation of the cutting parameters for an endmill	61
Figure 43 Intersection between the input midsurface and a plane (left) to obtain the base curve (right).....	62
Figure 44 The input midsurface is composed by several surface entities	64
Figure 45 Surface nomenclature. Blue = top surface, Purple = bottom surface, Green = side surface.....	64
Figure 46 Steps for the calculation of the convex hull curve of the base curve extracted from the input CAD model.....	65
Figure 47 The surface delimited by the convex-hull curve of the base curve of the input CAD model	65
Figure 48 WAAM process workflow (from [40]).....	70
Figure 49 The sides of a deposited wall are never perfectly straight	72
Figure 50 The input CAD model and the resultant deposition toolpath for a single straight wall	72
Figure 51 WAAM wall.....	73
Figure 52 The four equally spaced measurements taken on the wall.....	73
Figure 53 Graphical method to obtain the length of the extra toolpath to be added for the free end walls	74
Figure 54 One of the manufactured walls divided in five parts to measure the surface waviness	74
Figure 55 Graphical determination of the effective wall width and deposition efficiency	75
Figure 56 Unmachined substrate (left), part deposited upon the substrate (center), final machined part and substrate (right).....	76

Figure 57 Unmachined substrate (left), machined substrate (center), part deposited upon the previously machined substrate (right)	76
Figure 58 Procedure to determine the total volume of material to be removed from the substrate through roughing operations	77
Figure 59 Calculation of the total area of the selected surfaces (red color) in the Grasshopper auxiliary module	77
Figure 60 Speed profile for the motors of the five-axis machine	80
Figure 61 The test case used for the cost model	86
Figure 62 Cost comparison between WAAM and CNC milling	86
Figure 63 Effect of scale	87
Figure 64 Direct Crossing with no internal fillets (a) and with internal fillets (b)	92
Figure 65 The complete CAD model (left) and the midsurface-only CAD model (right) for a stiffened panel	93
Figure 66 The three modules composing proposed CAM software.....	93
Figure 67 Base curve (left) and midsurface-only CAD model obtained extruding the base curve (right)	94
Figure 68 The several surfaces composing the input CAD model.....	95
Figure 69 Definitions of Effective Wall Width and Total Wall Width. Adapted from [3]. ...	95
Figure 70 Input midsurface-only CAD model (a) and the several surfaces composing it (b and c)	97
Figure 71 In the CAD skeleton representation, each crossing feature is represented with a point located in the intersection of the surfaces composing the feature itself	97
Figure 72: Flowchart explaining the procedure to obtain the “End-Points Strategy Array” and “Intersection Strategy Array”	98
Figure 73 The small red spheres highlight a continuous junction between two adjacent walls	100
Figure 74 Defects at the ends of a WAAM-manufactured wall	100
Figure 75 Result of the feature recognition procedure: every different feature is highlighted using a different colour.	102
Figure 76 A connected shape (A) and an isolated tubular (B).....	102
Figure 77 Flowchart of the algorithm developed to detect isolated tubulars.....	104
Figure 78 Example of isolated tubular (left, green) and not isolated tubular (right, blue) ...	105
Figure 79 Deposition strategies for Direct Crossings (a) and (c) from [55] (b) and (d) from [54].....	106
Figure 80 The deposition strategy for Direct Crossings developed by the Authors. Original curves resulting from slicing operation (left) and toolpath for the direct crossing after processing (right).....	107
Figure 81 The procedure to calculate the toolpath for the direct crossing implemented in the proposed CAM software	107
Figure 82: Minimum value of the influence (a) and cutting (b) circle radii	108
Figure 83 Some results of the sample direct crossings manufactured to show the importance of the values of the influence and cutting radii	109
Figure 84 Taxonomy for T-Crossing. (a) back surface, (b) internal corner	110
Figure 85 A T-crossing with sharp internal corners cannot be accessed from the top with an end mill (left), while a T-crossing with fillets or extra material in the internal corners can be easily post-machined using a simple end mill (right)	111
Figure 86 The six developed deposition strategies	112

Figure 87 Graphical determination of the radius of the fillet for the toolpath of the S3. S3_I1, S3_I2 strategies	113
Figure 88 A T-Crossing feature seen from the top. The points were the measurements have been taken during the building procedure are shown.	113
Figure 89 The big deposition failure (pointed by the red arrow) in one of the specimens manufactured using the S3 deposition strategy.....	115
Figure 90 A back surface of a T-Crossing with high flatness.....	115
Figure 91 The back surface of a T-Crossing with a small depression in the central zone due to the used deposition strategy	116
Figure 92 The difference between the height of the C point and the average height of the zones of the T-Crossing far from the central one.	116
Figure 93 Slope of the best fit line for the data of Figure 92.....	117
Figure 94 Average value of the D parameter.....	117
Figure 95 The acquisition of the back surface of one of the manufactured specimens in the CMM machine	117
Figure 96 The scanning scheme used to acquire the back surface of the T-Crossings using the CMM machine	118
Figure 97 The eight acquired profiles for a specimen manufactured using the S3_I2 strategy	118
Figure 98 The surface constructed using the points acquired with the CMM machine and the best fit plane for a specimen manufactured using strategy S4.....	119
Figure 99 A T-Crossing built using the S3_I2 strategy.....	120
Figure 100 The new deposition strategy proposed by the Authors for T-Crossings. The original curves from the “First Layer Curve List” (left) and the toolpath optimized for the T Crossing (right)	120
Figure 101 The importance of toolpath extensions for free end walls for a straight wall (a) toolpath with no extensions, (b) toolpath with extensions, (c) expected result (red) and effective result (red) in the no-extensions case, (d) expected result (red) and effective result (blue) in the case of a toolpath with extensions.....	121
Figure 102 Deposition strategies for tubulars	122
Figure 103 Overlapping angle concept for Aligned Deposition Strategy	123
Figure 104 Difference between the mean height and six measurements taken along the cylinder circumference to compare the different deposition strategies	123
Figure 105 Top surfaces for three different tubulars manufactured with the three presented deposition strategies	123
Figure 106 Open impeller printable using a 3-axis machine	124
Figure 107 Final CAD (left) and midsurface (right) of an open impeller	124
Figure 108 Taxonomy of the input midsurface of the open impeller.....	125
Figure 109 A possible printing sequence for the blades of the impeller	125
Figure 110 Input geometry (left) and union bounding box of the blades (right)	125
Figure 111 The curves resulting from the intersection procedure	126
Figure 112 Intersection curves (left), end points of the intersection curves (center) and generation of the rapid movements (right)	127
Figure 113 Input midsurface (left) and final toolpath (right) for an open impeller	128
Figure 114 The workflow of the proposed CAM software	128
Figure 115 The result of the proposed feature recognition routine on different geometries	129
Figure 116 The midsurface-only input CAD file (a); the result of the feature recognition module (b); the manufactured part before the finish machining operations (c); the arc	

ignitions and stops on a generic N layer (d); the arc ignitions and stops on a generic N+1 layer (e)	130
Figure 117 Scheme for the proposed three-axis CAM framework for WAAM	131
Figure 118 The 3 axis WAAM based machine from Mutoh	133
Figure 119 The WAAM based machine from Addilan (from [58]).....	134
Figure 120 The Variaxis J-600AM WAAM machine from Mazak (left). An additive operation and a milling operation performed on the machine (right)	134
Figure 121 Configuration of spindle and welding torch for the Variaxis J600 AM	135
Figure 122 The machine by Karunakaran et al. (from [61]).....	136
Figure 123 The machine obtained by Cranfield university through the retrofit of a former friction stir welding machine (from [8]).....	136
Figure 124 the retrofit head developed by 3D Hybrid (from [62])	137
Figure 125 A WAAM robotic welding facility.....	137
Figure 126 Robotic welding facility with robot arm and roto-tilting table	138
Figure 127 The 3D demonstrator by Stratasys and Siemens (from [64]).....	138
Figure 128 Deposition of inclined walls using a robot. Deposition pattern (left) and various resulting walls (right). From [24].	139
Figure 129 Influence of the welding parameters on the deposition of a horizontal wall (left) and the deposition of a horizontal wall using a robot (right). From [24].	139
Figure 130 The three possible table-table configurations for a 5-axis machine: (a) XYZAC, (b) XYZBC, (c) XYZBC with B axis at 45 degrees.	140
Figure 131 Preliminary design of a machine (left) and of a rotary table (right) for WAAM operations	141
Figure 132 The BF20 Vario 3-axis manual milling machine used as basis for the 5-axis machine retrofit project.....	142
Figure 133 Configuration of the reference system in the BF20 Vario machine	143
Figure 134 Views of the 3D CAD model	144
Figure 135 Front, side and top view of the 3D CAD model of the BF20 Vario machine....	144
Figure 136 An exploded view from the manual of the BF20 Vario milling machine	145
Figure 137 General configuration of the motor and screw (green element) for a linear axis of the machine. The yellow element in the picture is the toothed belt	145
Figure 138 Control scheme for stepper motors (left) and servo motors (right)	146
Figure 139 The dimensions of the motor selected for the linear axes	147
Figure 140 Generic Pull-in and Pull-out curves for a stepper motor	148
Figure 141 The HY-DIV268N-5A driver used to control the motors of the linear axes	148
Figure 142 Overview of the application implemented in Grasshopper to calculate the data for the belt transmission	149
Figure 143 The configuration of the X-axis screw before (left) and after (right) the removal of the hand wheel and the installation of the pulley	150
Figure 144 Configuration of the motor for the X-Axis	150
Figure 145 Configuration of the motor for the Y-Axis	151
Figure 146 Configuration of the motor for the Z-Axis.....	151
Figure 147 The metal frame built to lift the machine to create room for the motor of the Y axis	152
Figure 148 The configuration of the tensioning system for the Z axis. On the left the system is in the non-tensioned configuration, while on the right the right belt has the right tension	152
Figure 149 The system to stretch the belt for the X-axis.....	153

Figure 150 The system to stretch the belt for the Y axis	153
Figure 151 The workspace of the BF20 Vario still in the 3-axis configuration	154
Figure 152 Mounting an AC table on the machine (left) would result in possible collision between the column of the Z axis and the table itself (right).....	154
Figure 153 BC table configuration.....	155
Figure 154 Side view of the BF20 Vario machine. The encumbrance of the BC table is inside the X axis carriage	156
Figure 155 Working space of the roto-tilting table	156
Figure 156 Maximum deflection in the horizontal position (left) and in the $B = 90^\circ$ position (right).....	157
Figure 157 Cutting forces for a 5-axis roughing (left) and finishing (right) operation. (from [69]).....	157
Figure 158 Joints for sheet metal parts. (left) finger joint, (center) slot and tab joint, (right) half lap joint (adapted from [70]).....	158
Figure 159 Configuration of the motors for the C and b axis	158
Figure 160 Technical data of the bearings of the B and C axes (from [70])	159
Figure 161 Cutaway of a commercial direct drive rotary table for machine tools (from [71])	159
Figure 162 Close view of the bolts holding the frame of the roto-tilting table	160
Figure 163 The finite element model	161
Figure 164 The evolution of the reinforcements for the frame of the table	161
Figure 165 The evolution of the reinforcements for the tilting table	161
Figure 166 The configuration for the frame (left) and for the tilting table (right) that achieved the best performance in terms of total deflection	162
Figure 167 Contour plot resulting from the static analysis of the roto-tilting table in the $B = 0^\circ$ configuration	162
Figure 168 Contour plot resulting from the static analysis of the roto-tilting table in the $B = 90^\circ$ configuration	163
Figure 169 Contour plot resulting from the free-size analysis	164
Figure 170 The roto-tilting table (only the midsurface is shown) after the modifications carried out looking at the results of the free-size analysis	164
Figure 171 The complete 3D model of the roto-tilting table	165
Figure 172 Milling of one of the bearing supports	165
Figure 173 The bearing supports of the B and C drives. The bearings are shown inserted in the supports.....	166
Figure 174 Milling of the C axis table (left) and final result (center and right)	166
Figure 175 The B table assembled before the welding operations	167
Figure 176 The complete roto-tilting table after the welding operations mounted on the machine for testing purposes.....	167
Figure 177 The table and the frame of the roto-tilting table.....	168
Figure 178 All the components of the roto-tilting table	168
Figure 179 The roto-tilting table mounted on the machine	169
Figure 180 The solution adopted to connect the ground cable of the welding unit to the rotary table	169
Figure 181 Exploded view of the system to attach the substrate to the rotary table.....	170
Figure 182 The disposition of the cooling fans for the belt of the C axis	170
Figure 183 The Prestomig 200 MP by SAF-FRO.....	171
Figure 184 The WMT2 manual torch.....	171

Figure 185 The LCD screen of the welding unit with an explanation of the adjustable parameters	171
Figure 186 The support for the torch.....	172
Figure 187 Layout of the numerical control (only one driver and one motor are shown) ...	174
Figure 188 The custom graphic user interface of the Mach3 software	174
Figure 189 Mach3 motor setting window.....	175
Figure 190 The USB breakout board used for the project.....	175
Figure 191 Image showing the input and output ports of the DDSM6V5.0 board.....	175
Figure 192 The driver used for the numerical control and the wiring diagram to connect it to the breakout board.....	176
Figure 193 The photoresistor assembly mounted on the machine (left) and the photoresistor circuit and its housing (right)	177
Figure 194 The electrical cabinet of the numerical control.....	177
Figure 195 A measurement taken on the machine	178
Figure 196 A picture taken during the determination of the steps/degree ratio for the C axis	179
Figure 197 The five-axis WAAM machine during a deposition test	179
Figure 198 Two pictures of the 5-axis WAAM machine	180
Figure 199 An example of indexed five-axis operation	181
Figure 200 Slicing approach (left) and surface isocurve extraction (right).....	182
Figure 201 The elbow pipe (left) and the machine used to produce it (right) (from [57]) ...	182
Figure 202 An example of application of the algorithm by Xiangping to a curved tube. From left to right: input mesh, normal and tangent vectors, segmented mesh, output slices (from [74]).....	183
Figure 203 Global coordinate and Frenet frame for skeleton (from [75]).....	183
Figure 204 Defeaturing of an STL geometry: (b) original STL geometry, (c) detected holes, (d) simplified model without holes (from [76])	184
Figure 205 Input STL model (left) and resulting deposition toolpath (right) (from [76]) ...	184
Figure 206 Non-planar slicing procedure for an open impeller (left) and WAAM manufactured impeller (right) (from [25]).....	184
Figure 207 Original milling toolpath (left) and the additive toolpath obtained reversing the milling toolpath (right) (from [77])	185
Figure 208 The steps to generate the toolpath for a complicate part (source: Siemens).....	185
Figure 209 The production of a WAAMpeller (a marine propeller) (from [80])	186
Figure 210 An image of the additive toolpath simulation module integrated in the ESPRIT CAM software (from [81]).....	186
Figure 211 The three geometrical shapes the developed modules of the presented five-axis CAM software are addressed to. From left to right: twisted blade, open impeller and freeform duct.....	187
Figure 212 CAD model of the final part (left) and the midsurface CAD model that is the input for the presented CAM software (right)	187
Figure 213 Open impeller (left) and impeller taxonomy (right).....	188
Figure 214 Machining of an open impeller from stock.....	188
Figure 215 Impeller manufactured using WAAM technology (left) and its post finishing operation (right) (source: Gefertec).....	188
Figure 216 A cost-effective way to produce an impeller is to obtain the hub (orange part in the picture) using traditional subtractive technologies, and to add the blades (green) using a direct energy deposition additive manufacturing technology	189

Figure 217 Hybrid building procedure for a shrouded impeller (from [82]).....	189
Figure 218 Time savings achieved using the hybrid production approach for a closed impeller (from [82])	190
Figure 219 The input geometry of the impeller hub is intersected with a series of parallel and equally spaced planes	190
Figure 220 The result of the intersection procedure is a series of curves	191
Figure 221 The green curves are the result of the offset procedure	191
Figure 222 The planes orthogonal to the base curve of the blade (left) and the curves resulting from the intersection between such planes and the blade (right)	192
Figure 223 The generated points compose the deposition toolpath for one of the blades of the impeller	193
Figure 224 The curve obtained at step (5) before (left) and after the extension (right).....	193
Figure 225 The points obtained on the extended curves (left) and the points valid for the deposition toolpath (green points in the right picture)	193
Figure 226 The final points composing the deposition toolpath (red crosses) and the torch axes (green vectors).....	194
Figure 227 A twisted blade	194
Figure 228 Machining of a blisk (from [83]).....	195
Figure 229 Blisk hybrid manufacturing (source: DMG Mori)	195
Figure 230 The two ways to obtain a turbine rotor: hub and blades assembly (left) and blisk (right) (from [83]).....	195
Figure 231 The root-shaped substrate (left) and the final component (right). The blade (orange part) is manufactured using WAAM	196
Figure 232 The input midsurface (left) and its bounding box (right)	196
Figure 233 The slicing procedure (left) and its result (right).....	197
Figure 234 The points composing the deposition toolpath.....	197
Figure 235 Original array (left) and re-assembled array (right)	198
Figure 236 Definition of reference frame for every toolpath point	198
Figure 237 Definition of cross angle Ω and torch axis.....	199
Figure 238 The points composing the deposition toolpath for a twisted blade (red crosses) and their torch axes (green vectors)	199
Figure 239 An example of freeform duct	200
Figure 240 (a) Layer by layer toolpath, (b) Helical toolpath.....	200
Figure 241 Elbow pipe with internal stiffeners.....	200
Figure 242 A freeform duct produced in a five-axis machine by Beam (from [84]).....	201
Figure 243 The midsurface of an elbow pipe composed by two halves	201
Figure 244 Taxonomy of the edges in a BRep	202
Figure 245 An elbow pipe before and after the edge recognition procedure. The red edges are the naked ones, while the blue the interior ones	202
Figure 246 The base curve of a freeform duct is the curve that lays on the building platform	202
Figure 247 Centroid c of an area A	203
Figure 248 Close view of the base curve of the duct with the plane laying on it	203
Figure 249 If the point is inside the BRep (left) the process goes on, otherwise (right) the process is stopped.....	204
Figure 250 The re-orientation of the first-attempt slice	204
Figure 251 Final toolpath for an elbow pipe (left) and definition of the elements composing the layers (right)	205

Figure 252 input geometry (left) and calculated toolpath (right) for a freeform duct with variable diameter	206
Figure 253 Input geometry (left) and resulting deposition toolpath (right) for a freeform duct with constant diameter	206
Figure 254 Elbow pipe with internal stiffeners	206
Figure 255 Intersection taxonomy for an elbow pipe with internal stiffeners. (a) Intersection curves, (b) Internal curves, (c) External Boundary	207
Figure 256 Conceptual application of the 3-axis feature recognition module to a slice from an elbow pipe with internal stiffeners	207
Figure 257 Helical deposition toolpath for a cylinder	208
Figure 258 The input midsurface (left) and (right) highlight of the naked edges (red) and interior edges (blue).....	208
Figure 259 The base curve highlighted in red (left) and the equally spaced points generated on the base curve (right, yellow dots)	209
Figure 260 The longitudinal isocurves	209
Figure 261 Input geometry (left) and resulting helical deposition toolpath (right) for an elbow pipe	211
Figure 262 Input geometry (left) and resulting helical deposition toolpath (right) for a freeform duct with variable diameter (the layer height is exaggerated for the sake of clarity).	211
Figure 263 The conceptual idea of the keyframe animation	212
Figure 264 Original (left) and simplified (right) CAD model of the five-axis machine presented in this thesis.....	212
Figure 265 Composition of the roto-translation matrix for the components of the simplified model	213
Figure 266 Simulation of the deposition of a hollow twisted blade.....	214
Figure 267 Visual explanation of WAAM defects. (a) Porosity, (b) Lack of material, (c) Humping	215
Figure 268 WAAM defect caused by local lack of deposited material and its propagation	216
Figure 269 WAAM defect caused by local excess of deposited material and its propagation	216
Figure 270 Desired shape of a sharp corner (left, top and side view) and real obtained shape (right, top and side view)	217
Figure 271 The monitoring system developed by Xiong (from [90])	219
Figure 272 Schematic of the monitoring system from Doumanidis [92]	220
Figure 273 Schematic of the acquisition system from Saeed [93].....	220
Figure 274 The surface fitting the shape of the molten pool reconstructed by the software (from [93])	221
Figure 275 Main geometrical parameters of a weld bead.....	222
Figure 276 Scheme of the proposed acquisition/monitoring system	223
Figure 277 An image of a typical speckle pattern (from [98])	225
Figure 278 The problem of a mono vision system: the pattern must follow the weld bead (left), otherwise no useful data can be triangulated (right)	226
Figure 279 A couple of welding glass filters	226
Figure 280 Visible wavelengths	227
Figure 281 Emission spectrum for steel welded using MAG at a welding current of 180 A (from [100]).....	228
Figure 282 Correlation between welding current and total emission (from [100])	228

Figure 283 An example of spectrum for a 532 nm OD 6 laser-line bandpass filter, 2.0 nm bandwidth (from [101])	229
Figure 284 Electrical scheme of the full range RGB led apparatus used in the tests	230
Figure 285 A wooden box that can be used for the tests of the welding glasses	230
Figure 286 The experimental setup used to test the welding filtering glasses	231
Figure 287 ROI considered for the investigation of the transmittance property of the welding glass	231
Figure 288 Chart for the Dan Bruton's approximation to obtain the wavelength from the RGB value of each pixel.....	232
Figure 289 Spectrum of the DIN5 welding glass filter	232
Figure 290 Originating a laser speckle pattern using a scattering medium (from [102]).....	233
Figure 291 A green light laser diode (left) and its cross section (right).....	233
Figure 292 Scheme of a stereovision 3D scanning system.....	234
Figure 293 Parameters of a 3D stereovision scanning system.....	234
Figure 294 Schematic representation of the pixel size of a camera sensor	235
Figure 295 Visual explanation of the focal length of a camera lens	236
Figure 296 Top view and side view of the filters for the lenses	237
Figure 297 Top view of the support for the cameras with the cameras mounted on	238
Figure 298 Front view of the camera assembly	239
Figure 299 Side view of the camera assembly.....	239
Figure 300 Bottom view of the camera assembly.....	240
Figure 301 Back view of the camera assembly.....	241
Figure 302 A standard connection element used to create the support for the cameras	241
Figure 303 Fixturing of the camera lens.....	242
Figure 304 The two cameras mounted on the support and placed in front of the prism for the calibration procedure	243
Figure 305 One of the results of the calibration procedure	244
Figure 306 The PET sheet used to manufacture the lens for the speckle before (left) and after it has been impressed with a P600 sheet of sandpaper (right)	245
Figure 307 Bottom (left) and top view (right) of the plastic speckle lens attached on the C-Mount flange	245
Figure 308 The speckle pattern obtained with the selected laser diode and the manufactured plastic lens.....	246
Figure 309 Front view (left) and side view (right) of the pattern projector assembly	247
Figure 310 The pattern projector disassembled	247
Figure 311 A close view of the laser diode inside the case of the pattern projector.....	248
Figure 312 Blobs in a speckle pattern	249
Figure 313 The Matlab form showing some of the properties that can be extracted from the blobs of the speckle pattern in the acquired image	250
Figure 314 Acquired speckle pattern before (left) and after (right) binarization (from [108])	250
Figure 315 Feature extraction algorithm flowchart.....	251
Figure 316 Features matching for a single cluster algorithm flowchart.....	252
Figure 317 Parameters extraction algorithm flowchart	253
Figure 318 Point cloud resulting from the acquisition of a planar surface.....	255
Figure 319 Sample image acquired by one of the two cameras. The green speckle pattern is visible. The blue marks are the points used by the software for the triangulation....	256

Figure 320 Point cloud resultant from the acquisition of the inclined surface with the pattern projector on and the optical filters mounted on the lenses of the cameras	256
Figure 321 Inclined surface (left) and two-levels step (right) acquisition scheme	257
Figure 322 Acquisition test in near-to-real conditions. A led simulates the light emitted from the welding arc	257
Figure 323 The monitoring system installed in the Roland Modela MDX40 machine	258
Figure 324 One of the specimens produced for the testing of the monitoring system.....	259
Figure 325 Two image acquired during one of the real welding tests. The image on the left is from the left camera, the one on the right is from the right one	260
Figure 326 The images of Figure 325 after the filtering procedure has been carried out	260
Figure 327 One of the acquired images (left) and the reconstructed point cloud (right) for the deposition of a linear bead. The blue marks on the real image are the triangulated points	260
Figure 328 One of the acquired images (left) and the reconstructed point cloud (right) for the deposition of a curved bead	260
Figure 329 Current and voltage values for different MIG welding technique (adapted from [113])	261
Figure 330 Different acquisition densities for the different zones of a weld bead	262
Figure 331 The point cloud for a linear bead and the best fitted gaussian curve. The system detected a width of 5.645 mm and a height of 3.063 for the weld bead.....	263
Figure 332 A possible configuration in which the monitoring system is mounted on a welding robot.....	263
Figure 333 Failure of the parameter extractor software	264
Figure 334 After the segmentation of the point cloud, the software can correctly extract the geometrical parameters of the weld bead	264

List of tables

Table 1 Buy To Fly Ratio for some aerospace components (data and figures taken from [10])	41
Table 2 Cost drivers for CNC milling	57
Table 3 Tool life Taylor index for HSS and Carbide tools	66
Table 4 Machine setup time and tool setup time for a machining center	66
Table 5 Cost drivers for WAAM	71
Table 6 Measurements taken on the wall	73
Table 7 Effective Wall Width and deposition efficiency for the used welding parameters set	75
Table 8 Main WAAM Manufacturing parameters for the case study	87
Table 9 Main process parameters for CNC machining from solid	88
Table 10 Classification and schematic view of T-Crossing and Direct Crossing features	92
Table 11 The Intersection Taxonomy developed by the authors on which the Feature Recognition procedure is based	99
Table 12 Odd Direct-Crossing and Odd T-Crossing topology	101
Table 13 Topology of isolated tubulars	103
Table 14 Process parameters used for the experiments	109
Table 15 The welding parameters used to test the deposition strategies for the T-Crossings	114
Table 16 Back surface error for the proposed deposition strategies	119
Table 17 The number of start/stop phases for each deposition strategy	119
Table 18 Input and outputs of the toolpath generation modules and of the linker module	132
Table 19 The characteristics of the WAAM machines by Gefertec (from [60])	135
Table 20 Comparison between the possible configuration for a WAAM facility capable of five-axis operations	142
Table 21 Technical data of the BF20 Vario 3-axis manual milling machine	143
Table 22 Torque target for each linear axis	146
Table 23 Technical data for the stepper motor of the linear axes	147
Table 24 Belt and pulley configuration for the linear axis	149
Table 25 Belt drive configuration for the B and C axes	159
Table 26 Axes nomenclature and description	173
Table 27 Axes dependencies in the five-axis machine	212
Table 28 Classification of WAAM defects	215
Table 29 In-situ measurement modules for AM technologies (from [91])	218
Table 30 Software and hardware comparison between mono and stereo active 3D scanning systems	224

Table 31 Characteristics of the used CMOS USB camera	236
Table 32 Characteristics of the used zoom lenses	237
Table 33 Expected characteristics of the monitoring system	238
Table 34 The parameters for the triangulation and the weld bad parameters extractor	262
Table 35 Comparison between the width and height of the deposited beads obtained using a manual caliper and the values extracted with the presented monitoring system	265

Acronyms List

AM	Additive Manufacturing
BRep	Boundary Representation
BTF	Buy To Fly (Ratio)
CAD	Computer Aided Drawing
CAM	Computer Aided Manufacturing
CL File	Cutter Location File
CMT	Cold Metal Transfer
DED	Direct Energy Deposition
EBAM	Electron Beam Additive Manufacturing
EBM	Electron Beam Melting
FDM	Fused Deposition Modeling
GMAW	Gas Metal Arc Welding
GTAW	Gas Tungsten Arc Welding
LED	Light Emitting Diode
LPD	Laser Powder Deposition
LWD	Laser Wire Deposition
MAG	Metal Active Gas
MIG	Metal Inert Gas
MQL	Minimum Quantity Lubrication
MRR	Material Removal Rate
NTWD	Nozzle To Work Distance
PAW	Plasma Arc Welding
PBF	Powder Bed Fusion
RANSAC	RANdom SAmples Consensus
ROI	Region Of Interest
SGR	Surface Generation Rate
SVD	Single Value Decomposition
TTL	Transistor-Transistor Logic
WAAM	Wire Arc Additive Manufacturing

1. The WAAM technology and the need for a synergic framework

1.1. The Wire and Arc Additive Manufacturing Technology

The Wire and Arc Additive Manufacturing technology is an arc-based process. It uses an electric arc as heat source to melt a metallic feedstock wire to create components stacking one layer over the other. Therefore, WAAM technology can be classified as a Direct Energy Deposition Additive Manufacturing technology (Figure 1).

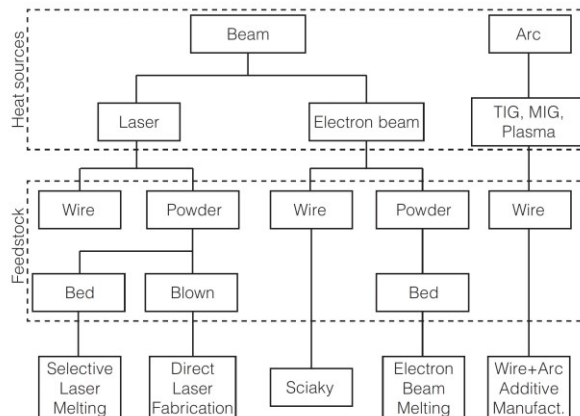


Figure 1 Classification of AM technologies for metallic components (from [1])

A WAAM facility is composed by a welding unit, a torch and a positioning system (Cartesian or anthropomorphic) controlled by a numerical control (Figure 2).

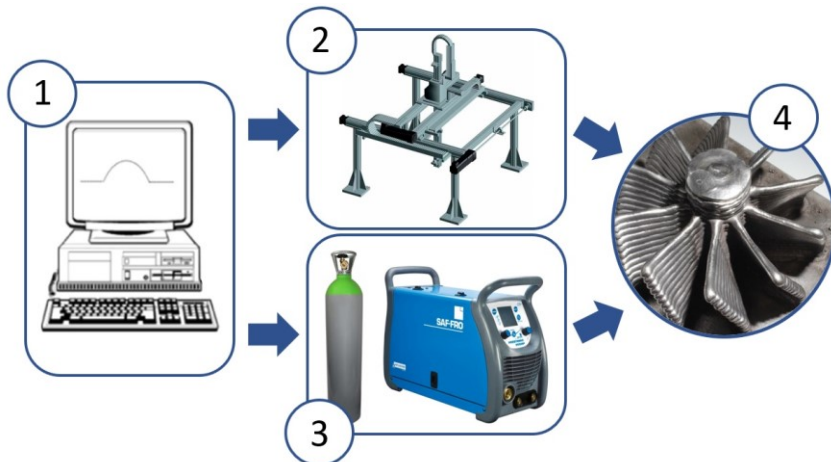


Figure 2 WAAM equipment; (1) Computer and Control Cabinet, (2) Positioning structure, (3) Welding unit (welding power source, wire feeder and shielding gas bottle), (4) Final Part

The welding machine provides the power to overcome the breakdown potential of the gas medium, thus igniting an electric arc between the substrate (or, in general, the workpiece) and an electrode located in the torch. The electric arc is used to melt a metal wire that is the feedstock material. If the torch moves and the wire is continuously brought in the proximity of the welding arc, a bead can be deposited characterized by a width and a height (Figure 3).

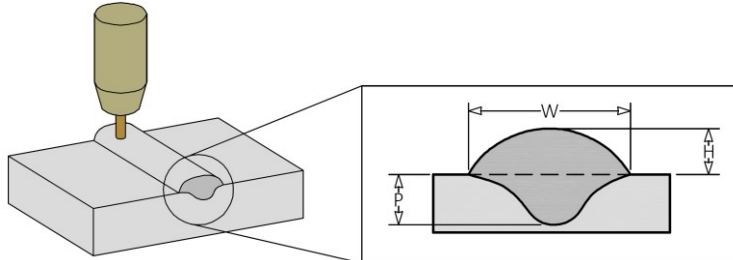


Figure 3 Geometric parameters of a bead cross section (W = width, P = penetration, H = height)

To move the torch both anthropomorphic or Cartesian CNC apparatus can be used (Figure 4). Both cited positioning systems have advantages and disadvantages that will be widely discussed in the next sections of the thesis.



Figure 4 (a) Robotic welding facility and (b) cartesian welding facility

Regarding the power source and the used arc-based technologies many roads can be taken. Indeed, many traditional arc welding technologies are available in the market that can be used to create a WAAM machine. The most commonly adopted in literature and industry applications are GMAW (Gas Metal Arc Welding), GTAW (Gas Tungsten Arc Welding) and PAW (Plasma Arc Welding) (Figure 5).

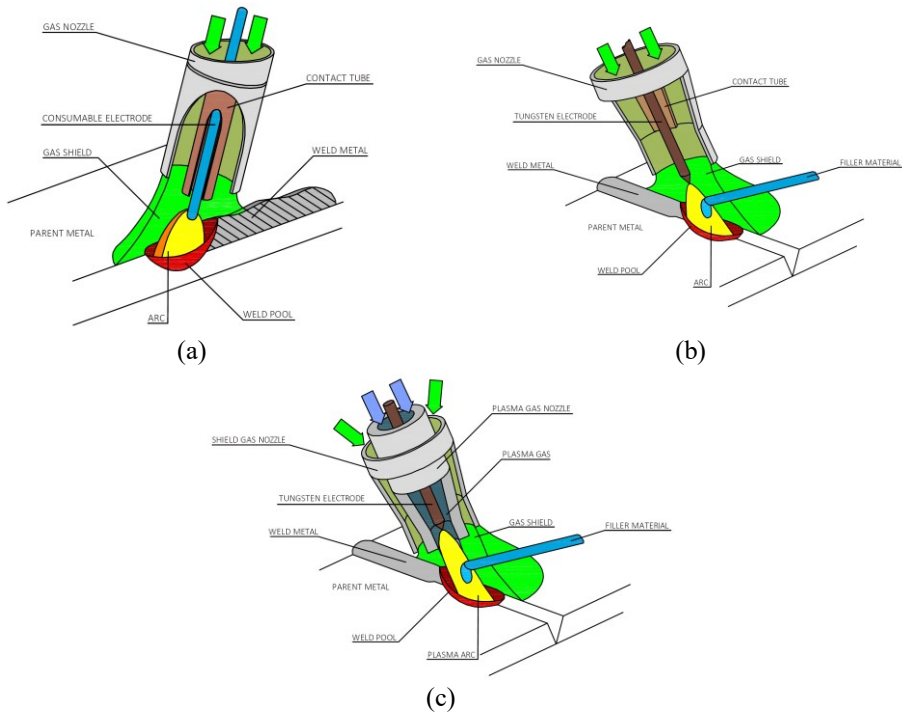


Figure 5 Schematic representation of (a) GMAW, (b) GTAW and (c) PAW processes

In the GMAW technology the electrode is the filler material itself that is fed coaxially to the torch by an automatic wire feeding system. The power flows from the welding power source to the wire/electrode thanks to the presence of a contact tube, also visible in Figure 6.

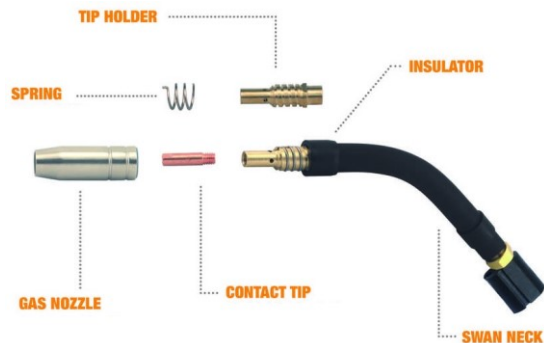


Figure 6 Exploded view of a GTAW torch

For contrary, in GTAW the arc is generated between a non-consumable tungsten electrode that is coaxial to the torch and the workpiece. A filler wire is then supplied using a wire feeding system with a certain inclination respect to the axis of the torch and of the electrode. In both GMAW and GTAW processes, an inert shielding gas is supplied to the torch nozzle to protect the molten pool from oxidation (Figure 7). The composition of the shielding gas depends on the kind of deposited material.

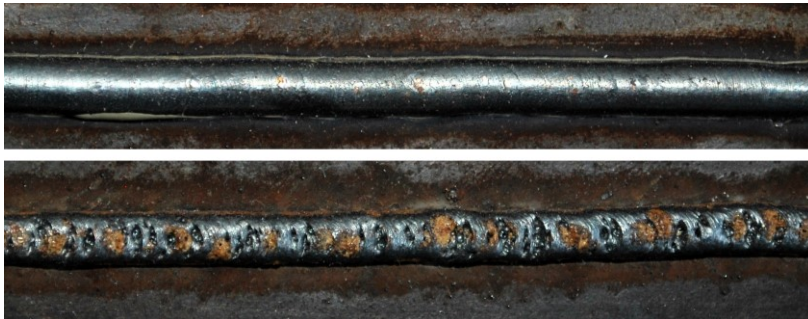


Figure 7 Weld bead deposited with shielding gas (above), and without shielding gas (below)

Finally, PAW hardware comprises a torch made of two coaxial nozzles; the outer one supplies an inert shielding gas, while the inner one supplies a second inert gas flow that is used for the plasma generation. Inside the plasma nozzle a coaxial tungsten electrode is located. Such electrode is the cathode of the circuit, while the workpiece or the inner nozzle itself is the anode. The gas flowing through the inner nozzle is ionized by the voltage drop between the anode and the cathode, thus creating a plasma stream that can be focused on the surface of a substrate generating a molten pool. A wire feeding system like the one of the GTAW process takes care of supplying a filler wire to the molten pool.

The use of a coaxial wire feeding system, like in GMAW, is a big advantage, especially in the case of complex multi-axis deposition operations. This because an off-axis feeding of the filler wire affects the shape and appearance of the deposited bead [2]. In practice,

depending on the orientation between the relative movement between the torch and the workpiece and the wire feeding direction, the appearance of the deposited bead will change as already studied also for other deposition processes such LWD (Laser Wire Deposition) [2] (Figure 8).

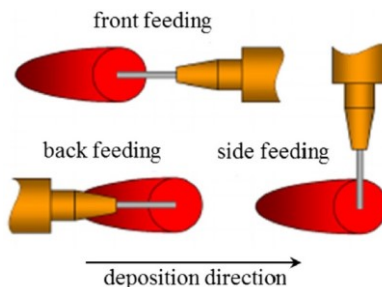


Figure 8 Three types of feeding directions according to the given deposition direction (from [2])

However, despite the disadvantage of the off-axis feeding of the filler wire, PAW and GTAW shows some advantages respect to GMAW technologies. The main one is the high stability of the arc [3]. This leads to a more stable transfer of the filler metal resulting in less spatter and a much more even bead. Moreover, GTAW and PAW are very suitable to deposit high-grade aerospace material such as Ti-6Al-4V [4].

For what concerns the electric arc efficiency, GMAW process achieves the best performance showing an electric efficiency ranging from 75% to 95%, while for GTAW arc efficiency ranges from 20% to 80% [5].

The analysis of the state of the art regarding the arc-based technologies revealed that GTAW and PAW are very suitable for specific materials that require a very high process stability, while GMAW can be considered a general-purpose process able to deposit all kinds of materials. Moreover, it shows big advantages for what concerns the process planning because of the coaxial feeding of the feedstock material. For all these reasons, the GMAW-based WAAM process has been selected for the research activity presented in this thesis. A typical GMAW welding facility, like the one used in the activities of the thesis, is reported in Figure 9.

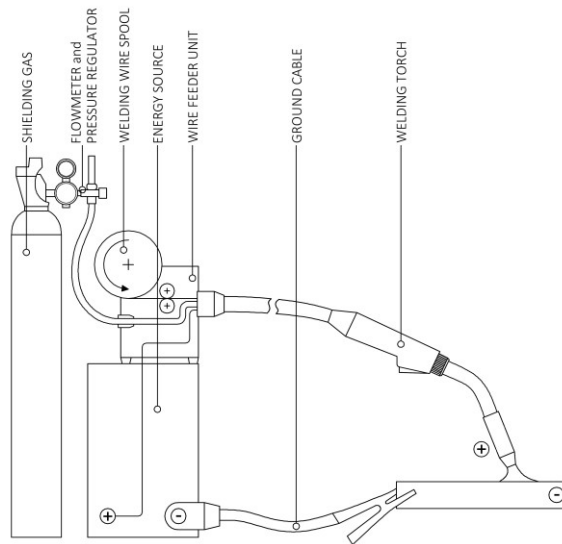


Figure 9 A typical GMAW welding facility

1.2. The WAAM process: characteristics and related issues

Referring to GMAW-based WAAM and looking at Figure 10, it can be stated that WAAM technology is a very complicated process involving lots of different parameters that can have influence both in the micro and macro scale of the phenomenon. In this thesis, only the macro effects of the process parameters will be considered. The main process parameters that influences the appearance and quality of the parts are:

- Welding voltage;
- Wire feed speed;
- Nozzle to work distance (NTWD);
- Deposition Feed.

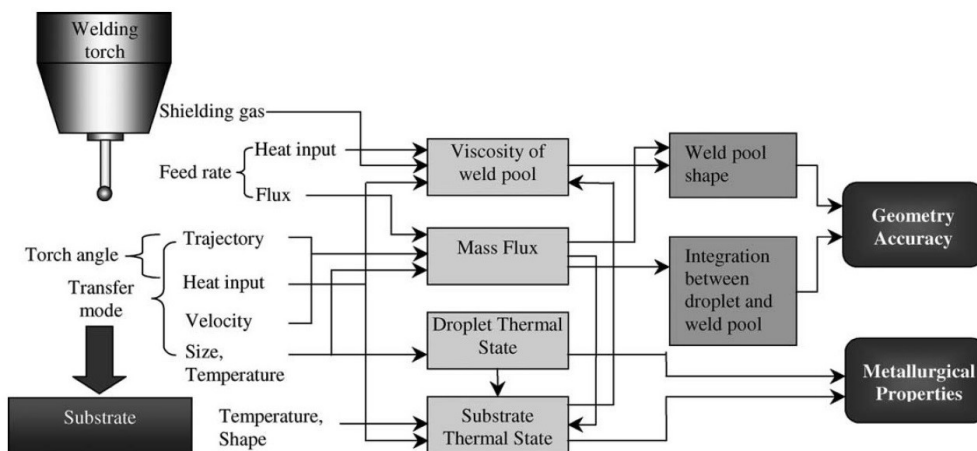


Figure 10 The parameters influencing the quality of the WAAM process (from [6])

The cited parameters greatly affect the quality of the weld bead as Figure 11 shows.

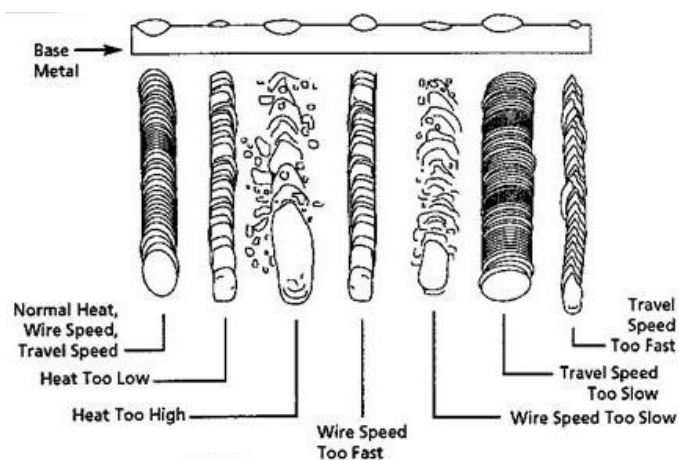


Figure 11 Effects of the process parameters on the appearance of the welding bead

The wire feed speed is directly related to the welding current (Figure 12), while increasing the welding voltage, the bead gets wider.

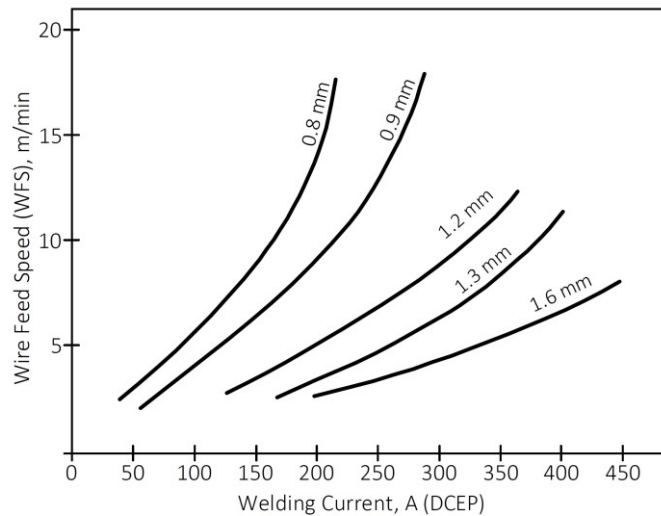


Figure 12 Relationship between wire feed speed and welding current for GMAW

To better understand the concept of Nozzle to Work Distance or Contact Tip to Work Distance it is possible to refer to Figure 13.

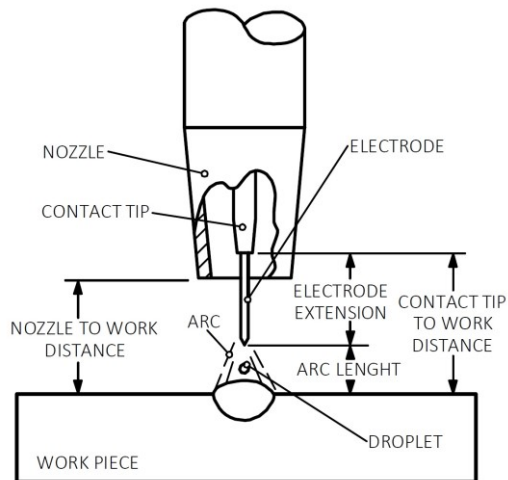


Figure 13 Reciprocal position between torch and substrate

Also the nozzle to work distance has an influence. Indeed, it affects the welding current, as shown by Figure 14.

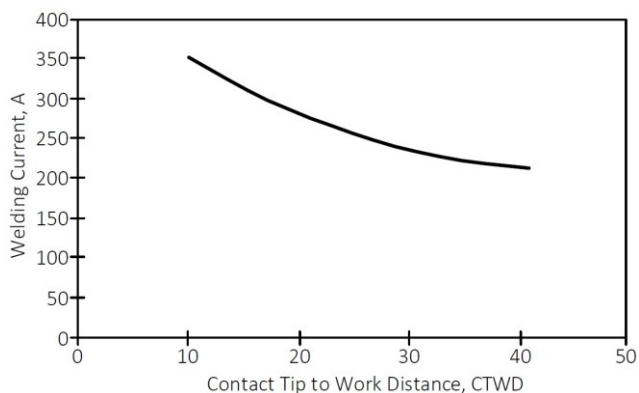


Figure 14 Example of relationship between CTWD and welding current for GMAW

Finally, the shielding gas can influence the shape and the cross section of the bead too. Moreover, it can affect the penetration of the weld bead into the substrate or the previous layer (Figure 15). Penetration and dilution of the deposited weld bead are critical aspect to consider when building a component using WAAM, since a good compromise between high mechanical strength (given by a high dilution and penetration) and dilution must be achieved [7].

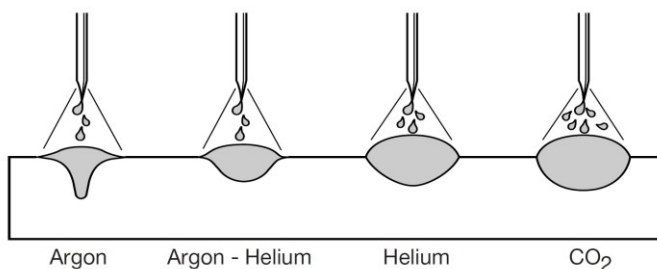


Figure 15 The effect of the shielding gas

The WAAM technology is particularly suited to the production of large components because of its high deposition rate that can assume values as high as 10 kg/h [8]. Moreover, the need for a local gas shield (even if for materials like titanium a completely controlled atmosphere in the building chamber is needed [8]), allows for the development of very large facilities such the one proposed by Cranfield University [9] (Figure 16).



Figure 16 The large robotic WAAM facility implemented by Cranfield University (from [9])

Therefore, WAAM is very suitable to produce medium to large components with a low to medium complexity. Nowadays, the interest in developing WAAM mainly comes from the aerospace sector where both difficult-to-cut or expensive materials such as titanium or high-grade aluminum are widely used and large parts such as stiffened panels or wing ribs are produced (Figure 17).

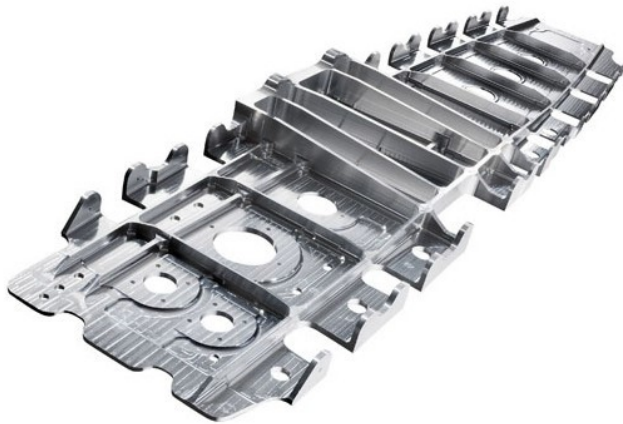

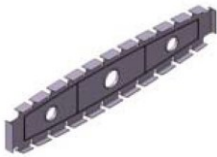



Figure 17 A wing rib

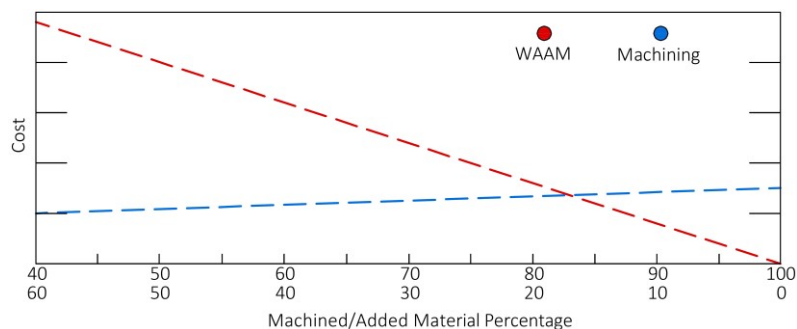
Now, components like the one showed in Figure 17 are obtained machining solid blocks of materials, thus achieving very high BTF (Buy to Fly) ratios like those reported in Table 1.

Table 1 Buy To Fly Ratio for some aerospace components (data and figures taken from [10])

Component	Initial Weight of Billet [kg]	Final Weight of the Part [kg]	Buy to Fly Ratio
Stiffened Panel 	63.95	9.64	6.63
Rib Component 	76.6	2.9	26.4
Flap Track 	81.8	16.2	5.05

Therefore, partially replacing the traditional technologies with the WAAM process, thus obtaining a hybrid manufacturing approach could result in huge material and cost savings. Moreover, using the WAAM technology no problems related to the supply chain of the stocks will occur, since a generic welding wire can be used to produce components with different shape and dimensions.

From an early implementation of the cost model for WAAM and machining proposed in [11] and carried out during the preliminary phases of the literature research carried out for the presented activity the chart reported in Figure 18 can be obtained.

**Figure 18 Cost vs removed/added material for WAAM and machining operations**

The chart of Figure 18 compares WAAM and pure-milling operations and let us understand that considering the bounding box of a given component (Figure 19) to be manufactured, it is convenient to use the WAAM technology if the component itself has a volume that is 18% of the volume of the bounding box, otherwise it is convenient to use a pure

subtractive approach (using a stock with the external dimensions of the aforementioned bounding box).

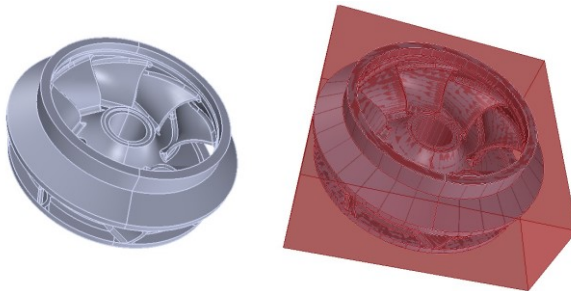


Figure 19 A CAD model (left) and its bounding box (right)

Moreover, the chart of Figure 18 helps us understanding that WAAM is very suitable for the manufacture of thin walled components. In general, a component is defined as “thin-walled” if the thickness of the walls is very small respect to the overall dimensions of the component. However, this thesis considers a wall “thin” when it can be manufactured using a collection of stacked single beads, for a given welding apparatus. Figure 20 clarifies the distinction between single and multiple passes strategies.

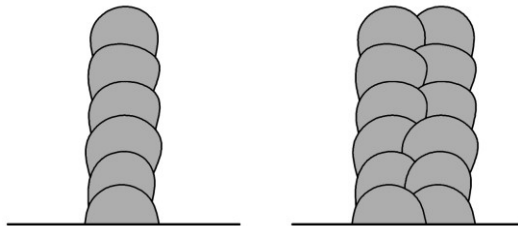


Figure 20 A schematic cross section of a single bead wall or “thin wall” (left) and a multiple bead wall (right)

As already shown by Figure 20, the walls manufactured by WAAM have an accentuated waviness (Figure 21).



Figure 21 A wall manufactured using WAAM and its cross section (in green the final wall after machining, in red the zones to be machined away)

Therefore, it is mandatory to perform a finish milling operation on the deposited component to match the required surface quality. For what concerns the process planning, it is important to know the relationship between the used welding parameters and the dimensions

of the bead, especially width and height. Moreover, it is important to assess the relationship between the process parameters and the total amount of material that will must be removed using milling operations (Figure 22).

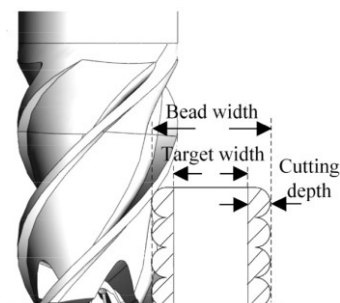


Figure 22 Parameters of a wall to consider for hybrid WAAM operations (from [12])

In literature many works are available that investigate in the relationship between the welding parameters and the shape of a single bead or a wall. For example, Ding et al. [13] showed an experimental activity to understand which the best mathematical curve was to describe the cross section of a bead, while Li et al. [12] proposed a framework to optimize and speed up the production of stiffened panels using WAAM and milling operations. Another important aspect to consider when performing the process planning for a WAAM operation, is the geometrical shape of the ending and starting zones of a bead. In fact, the appearance and geometrical conformation of these zones is almost opposite: the starting zone shows an excess of material, while the ending zone features a depression as showed in Figure 23.



Figure 23 The typical appearance of a deposited bead

Xiong et al. [14] showed how to deal with the problems related to the different shape of the starting and ending zones of a weld bead.

A relevant characteristic of the WAAM process is the high heat-input. Indeed, especially for small components, there are two main problems related to the high heat transfer occurring during the building procedure and showed in Figure 24.

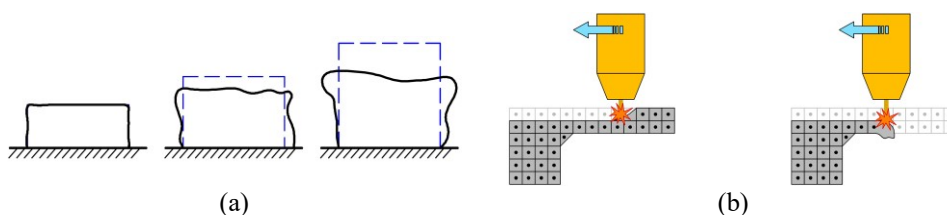


Figure 24 (a) Part deformation during the building procedure due to heat accumulation (the blue dotted line is the expected shape, the black line the real one), (b) Collapse of a thin section of the part during the building procedure due to excessive heat input

Referring to Figure 24 (a) the first big issue is the deformation of the part layer after layer because of an excessive rise of the average temperature of the whole part itself. The

problem showed in Figure 24 (b) occurs during the manufacturing of small and thin sections: the deposition of the new layer causes a total re-melting of the previous layer with a consequent collapse of the part. To avoid these issues an accurate thermal simulation of the deposition process must be carried out and the deposition toolpath must be optimized introducing idles with the objective of keeping the volume of the molten pool as constant as possible during the construction of the part, as well explained by Montecvecchi et al. [15]. The so-called interpass temperature, i.e. the temperature the previous layer reaches before depositing the next one, has a big effect on the surface quality and on the deposition efficiency. Both Almeida [16] and Geng [17] investigated in this aspect. They stated the interpass temperature has influence on the growth of the part (because it affects dilution) and on the surface quality and waviness of WAAM manufactured parts (Figure 25, Figure 26).

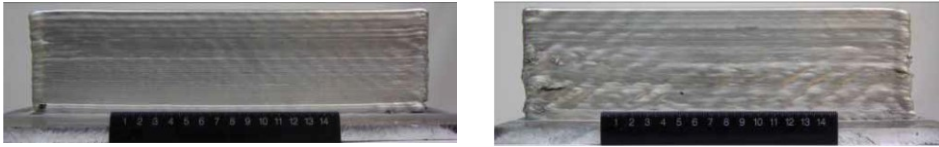


Figure 25 Effect of interpass temperature on the surface quality of a straight wall. (Left) optimal interpass temperature, (right) interpass temperature too low (from [17])



Figure 26 Effect of the interpass temperature on the cross section of a wall. Interpass temperature increasing from left to right (from [16])

The high heat input proper of the GMAW welding technologies causes the generation of residual stresses or distortion in the final component that can compromise the final manufacturing result. In this optic, even the configuration of the deposition pattern plays an important role in the distortion of the final part as showed by Figure 27.

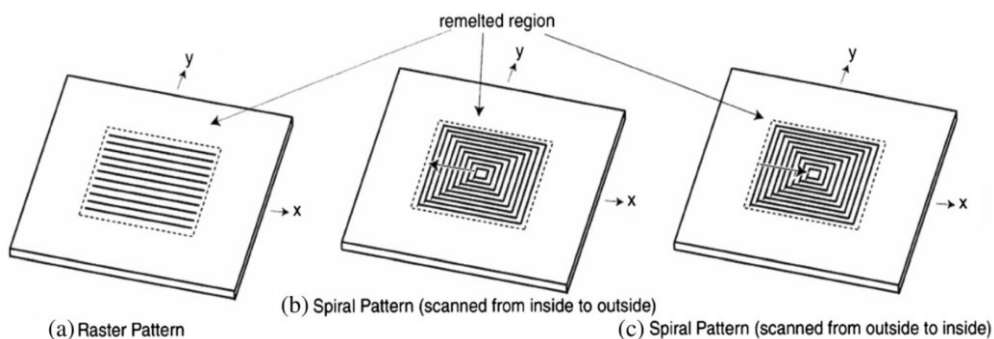
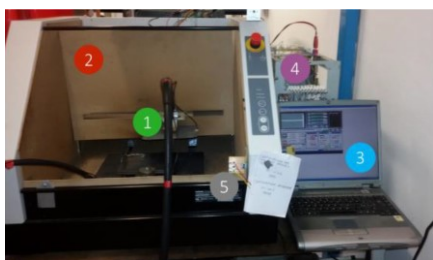


Figure 27 Different deposition patterns affect in a different way the final distortion and residual stresses of the part (from [18])

In the recent years, many companies that produce welding units, developed innovative GMAW variants that limits the heat input transferred into the workpiece. This is the case, for example, of the pulsed-GMAW process [19] that is the one implemented in the welding unit used for the 5-axis machine presented in this thesis. Another relevant example of GMAW variant with a very low heat input is the CMT (Cold Metal Transfer) developed by Fronius [20]. Such process combines a mechanical action on the welding wire and an accurate control of the voltage and current waveforms, to achieve a very low heat input. CMT process has been applied in many activities, such as the ones presented in [21] and [22].

1.3. Three and five-axis deposition for WAAM

Like many other DED AM technologies, WAAM is suitable both for 3 and five axis deposition operations. The first ones are carried out using a cartesian positioning device, or a robot, in which only three linear axes are available. Therefore, the torch axis always remains orthogonal to the building substrate during all the deposition procedure. Only three linear coordinates X, Y and Z are needed to describe the reciprocal position between the torch and the workpiece (Figure 29). Therefore, all the sections of the part which inclination overcomes the self-supporting one cannot be manufactured. At the manufacturing Technologies research Laboratory (MTRL) of the University of Firenze (where the presented PhD activity has been carried out) a three axis WAAM machine [23] obtained retrofitting a Roland Modela MDX 40 milling machine is available and has been used for all the three axis activities presented in this thesis. Such machine and its main features are reported in Figure 28.



- (1) Welding torch
- (2) Roland Modela MDX 40
- (3) PC-based CNC
- (4) Motor drivers
- (5) Arc light sensor

Figure 28 The WAAM machine available at MTRL



Figure 29 3-axis WAAM deposition

In the case of five-axis deposition, also the inclination between the torch axis and the workpiece can be varied during the deposition process. This allows the production of inclined walls without the needing of supports. This because the reciprocal orientation of the workpiece and torch is set point after point to allow the current layer to rest exactly over the previously deposited one (Figure 30) thus limiting or avoiding the needing for supports.

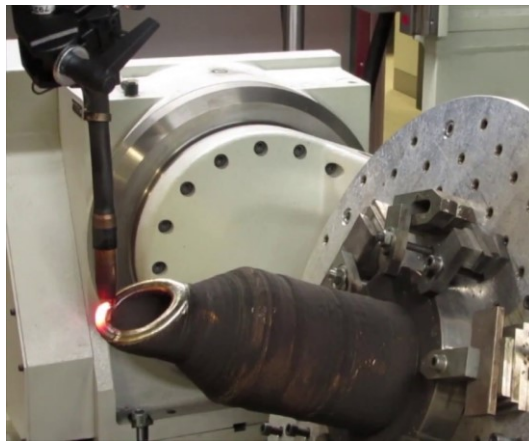


Figure 30 5-axis WAAM deposition

The relative inclination between the workpiece and the part can be achieved inclining the torch as reported in [24], or orienting the part using a roto-tilting table as shown in [25]. In the case of five-axis deposition the reciprocal orientation between the workpiece and the torch is defined, like for 5-axis milling operations, by three linear coordinates and a vector (Figure 31).

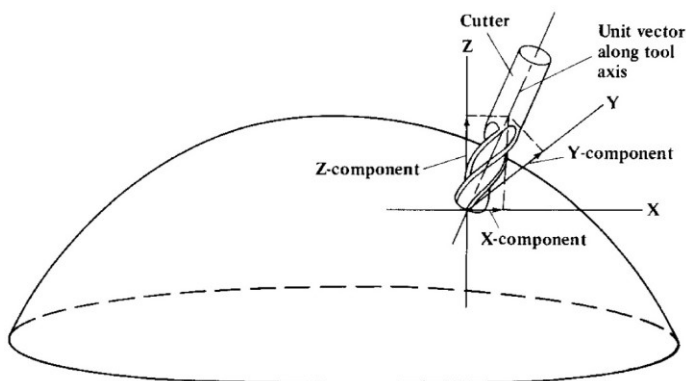


Figure 31 Relative position between a workpiece and a tool

The linear coordinates locate the torch tip, or in general, the programmed point of the torch, while the vector, usually called torch axis, specifies the inclination. Looking at a traditional structure for a five-axis machine, the reciprocal inclination between the part and the torch is obtained through the two possible rotations offered by the roto-tilting table.

Both in the case of the three and five-axis deposition, the toolpath can be calculated both manually or using a specific CAM software. Usually the manual approach is used to calculate the toolpath for small and very simple parts which cross section has no freeform curves. In the case of complex three-axis parts and especially for five-axis, the use of a CAM software is mandatory. The CAM software is able to calculate the deposition toolpath starting from the process parameters (given by the user) and the CAD geometry of the part. The general scheme for a toolpath calculation CAM software is reported in Figure 32.

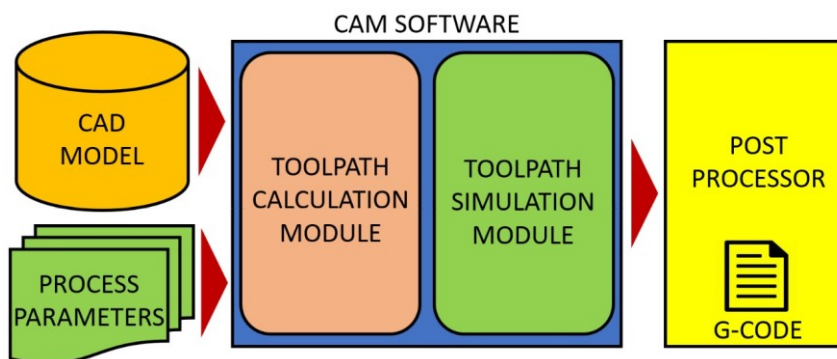


Figure 32 CAM software scheme

The starting point is the CAD model of the part. After it has been introduced in the CAM software environment, the toolpath calculation process can start. Usually the user must orient the part along the preferred building direction, input the process parameters and interact with the graphical interface of the CAM software (selecting surfaces, curves and so on) to obtain the final deposition toolpath. The CAM software writes all the points of the calculated toolpath in a so-called Cutter Location (CL) file (the name is mutated from the milling sector). It usually has a proprietary format and contains the points of the toolpath and the orientation of the axis of the torch expressed in the part reference system. After the toolpath has been

calculated, it is usually displayed in the screen in order to make the user able to visually check it. Especially in the case of five-axis operations, it is almost mandatory to perform a kinematic virtual simulation of the toolpath before testing it in a real machine. To do this a CAM software must have a simulation module that is able to read the CL file and simulate the deposition process showing the growing workpiece and the machine. During the simulation the user can see if there could be collisions between the part and parts of the machines. Moreover, the simulation of the CAM software usually stops when a collision occurs to warn the user. If collisions are detected, the toolpath must be recalculated trying to modify the section that causes the collision itself. In general, in a CAM software there are two different kinds of simulation. The first one shows only the workpiece and the tool/torch that moves around it; such simulation is in the workpiece coordinate system. The second kind of simulation shows also all the other parts of the machine and is the most useful since it can show not only the collisions between the tool/torch and the workpiece but also the collisions with other parts of the machine.

Finally, the CL File can be “translated” in the G-Code that will be the input for the numerical control of the machine. The G-Code contains all the points of the deposition toolpath and the respective inclinations of the torch (for five-axis operations); all the coordinates are expressed in the reference system of the machine. The G-Code is not integrated in the CAM software since, generally, each numerical control/machine combination must have its own post-processor able to generate a G-Code written in a language having the required flavor. Therefore, the post-processor is not a component of a CAM software and for this reason is outside the scope of this thesis.

1.4. The 5-axis WAAM process as a result of a synergy

From the previous chapter, it can be evinced that the WAAM process, especially in its five-axis version, is the result of a series of activities and pieces of hardware that work in synergy to obtain the best result. For example, it is impossible to develop and use a five-axis CAM processor without the possibility to test the calculated toolpath both virtually and using a real five-axis machine. On the other side it is impossible to use the five-axis machine without an adequate numerical control able to consider all the characteristics of the WAAM process. In addition, since the used GMAW process is prone to arc instabilities and to the occurrence of defects, it is mandatory to include in the machine a monitoring system able to detect such defects and stop the deposition process when a deposition failure occurs; this will allow to leave the WAAM machine unattended and will bring significant time and cost savings since even when the machine is unattended, the deposition process can be stopped (and the user can be warned) when a failure occur thus avoiding to waste welding wire and shielding gas. Moreover, since the companies are interested in the cost-effectiveness of the manufacturing processes they use, a cost model is very useful to understand whether it is convenient to start using the WAAM process or not. In addition, the cost model can also be used to compare several process planning strategies and to select or even optimize the best one. For all these reasons, the result of the WAAM process can be considered the result of a synergy of several tools.

The core of the present thesis is the development of toolpath generation algorithm for both 3 and 5 axis WAAM deposition operations. However, it has also been decided to develop a framework that could be as complete as possible, developing auxiliary tools such as a monitoring system for WAAM that can be used to validate and empower the choices carried out during the process planning. Moreover, in the future it will be possible to develop an

adaptive numerical control for WAAM machines able to read the output of the monitoring system and to perform corrective actions with a closed loop approach.

2. A toolpath-based cost model for WAAM

Nowadays companies are using additive manufacturing because it is an innovative manufacturing process enabling big advantages in the production of high-grade components both in terms of cost savings and performance improvement. Additive manufacturing technologies can produce very complicate parts such as molds with internal conformal cooling channels [26] or lattice structures (Figure 33) to obtain a lightweight part still matching the desired requirements in terms of stiffness and strength [27].



Figure 33 An example of conformal channels for a mold (left) (from [26]) and of lightweight lattice structure (right) (from [27]). Both these parts must be manufactured using powder bed techniques

Such parts cannot be created with traditional technologies such as milling or casting. The advantages brought by the manufacturing of parts with such characteristics are huge and the manufacturing cost become a secondary aspect since if a conformal cooling channel is needed or specific weight requirements are mandatory to create a winning application, the unique way to achieve the goal is using additive manufacturing. The cited elements (conformal cooling channels, lattice structures) can be manufactured only using powder bed techniques for metal components. In the case of direct energy deposition technologies such as WAAM, the situation is slightly different. In fact, it is almost impossible to manufacture very complicate shapes that cannot be created otherwise. WAAM, for example, can create near net shape components that must be post-milled to match the desired requirements in terms of surface quality. In this case, the additive manufacturing technology can replace the molding or casting process and the use of a cost model becomes very important to understand whether it is

convenient to manufacture the part using traditional or additive technologies. Indeed, in the case of components with a quite simple shape, such as stiffened panels, or open impellers (Figure 34), both additive and traditional technologies could be used and many companies will be attracted by additive manufacturing only if it is convenient from an economical point of view. So, these are interested in having a tool able to understand when it is convenient to manufacture a component using WAAM (and finish milling) or just pure milling operations.



Figure 34 Close view of an aluminum stiffened panel (left) and of an open pump impeller (right)

Another important application where a cost model to evaluate the convenience of additive manufacturing technologies becomes important or mandatory is the repairing or refurbishment of old or worn components [28]. In this case, in fact, a company likes to know if it is economically convenient to repair or refurbish a component using additive manufacturing or to manufacture a totally new component from scratch (Figure 35).

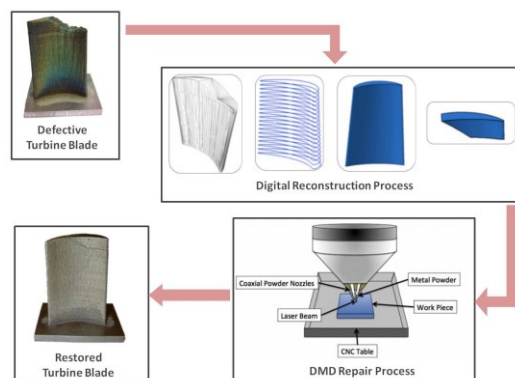


Figure 35 Repairing cycle for a worn turbine blade (from [28])

Therefore, a cost modelling tool is needed to evaluate the manufacturing or repairing cost. It is also important to have the cost model or even the experimental data for the traditional application used to manufacture/repair the same component to be able to make a comparison between different manufacturing strategies to choose the most convenient. In the

present thesis, a toolpath-based cost model is presented that can be easily integrated with the toolpath generation modules presented in section 3, since it uses almost the same input and output parameters. To give an idea of possible comparisons with a traditional manufacturing technique, a cost model for milling has been taken from literature and a sensitivity analysis for a test case has been carried out. Since nowadays WAAM is becoming very attractive for the manufacturing of high-grade aerospace components such as stiffened panels [12] that are traditionally manufactured through milling starting from a billet, the milling process has been considered as the best one to compare WAAM with. Moreover, a cost model for finishing operations must be implemented also in the cost model for WAAM itself, since a post-finishing operation is always needed to improve the fatigue properties of the part and to match the required surface quality.

The presented cost model takes advantage from the integration with the toolpath generation modules developed. Indeed, a cost model should require just a few inputs, since it is very useful in the early design stage when only an approximative shape of the component has been defined. This way, an early estimation and comparison can be carried out without spending too much time in calculating complex parameters or even manufacturing a test part. However, since the presented cost model is addressed to quite simple geometries such as stiffened panels or, in general, to geometries that can be manufactured using a three-axis machine, it is not difficult to obtain a CAD model of the part to be manufactured. Moreover, the CAD model is often already available, since the part which manufacturing cost must be evaluated is already being produced using traditional milling or casting technologies. The CAD model and a few manufacturing parameters are the inputs of the presented cost model and the toolpath generation module described in section 3 will automatically calculate the toolpath giving all the other inputs needed for the cost calculation. This way the user will obtain the final manufacturing cost of the part with a few clicks.

Both the cost models for milling and for WAAM have been implemented in a Microsoft Excel spreadsheet, also because Microsoft Excel is easily integrable with the Grasshopper Software. For this reason, an auxiliary module for the extraction of some important parameters such as the encumbrance dimensions of the part to be manufactured has been implemented using the graphic programming language of Grasshopper. This way, the input CAD model can be imported in Rhino/Grasshopper and all the necessary geometric data can be extracted thanks to the developed module and automatically inserted in the Excel spreadsheet. Then the required toolpath calculation module can be loaded in Grasshopper and all the data regarding the calculated deposition toolpath will be written in the same Excel file previously accessed by the auxiliary model for cost calculation. The scheme of the overall software framework is reported in Figure 36.

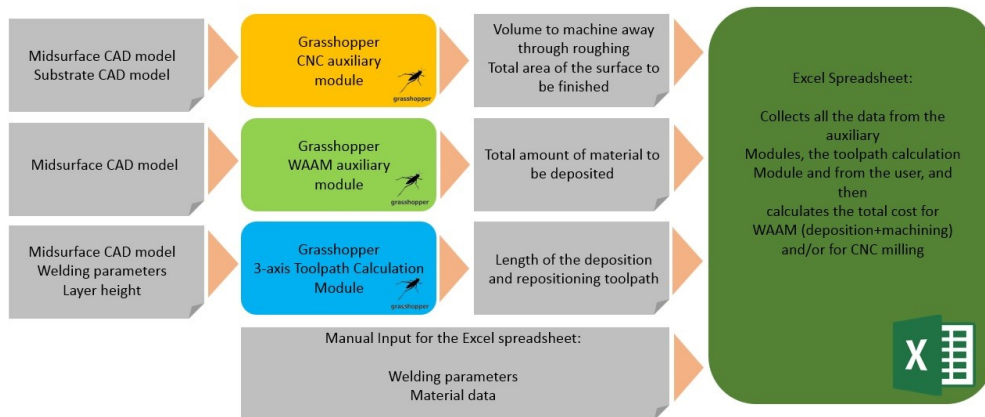


Figure 36 Software framework for the presented cost models. Only the main inputs are shown

The cost calculations are carried out by the Excel spreadsheet. It receives the inputs by the toolpath calculation module, the auxiliary modules for CNC milling and WAAM (that extract the data from the geometry of the part and of the substrate) and by the user who manually gives some input like welding travel speed or rapid speed. The result of the cost calculation is the total production cost both for milling and for WAAM production of the component. Therefore, it is also possible to carry out comparative analysis in order to understand whether it is convenient to produce a part by pure CNC milling or by WAAM.

2.1. Review of the state of the art: available cost models for WAAM

WAAM usage is getting wider in the last years and some cost models have already been developed and used by some research centers. In this paragraph these are reported and briefly described. Cranfield University is very active in WAAM research and in cost model definition. Indeed, most of the cost models found in literature have been developed by this institution. Going deeper in details, Guo [29] defined a cost model based on the features of the part to be manufactured; such cost model has been implemented in a software tool that automatically extracts the fundamental features from the CAD model of the part and calculates the associated manufacturing costs. This cost model has required a feature classification that is like the one developed in the present thesis for the presented three axis cam software; it is reported in Figure 37 for the sake of clarity.

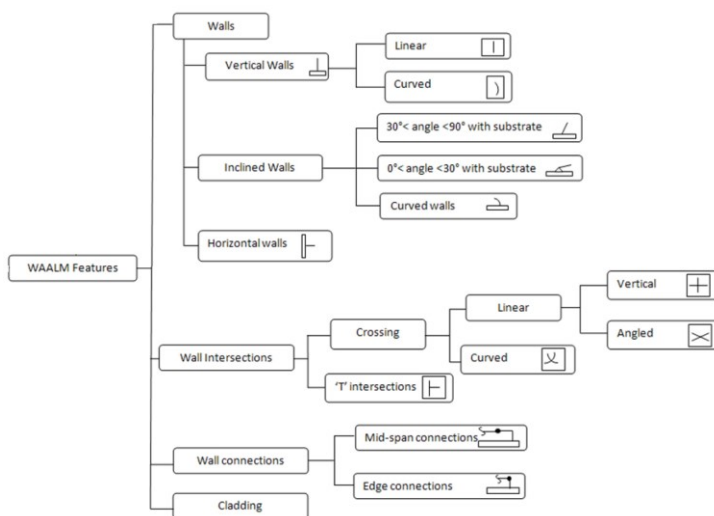


Figure 37 WAAM feature classification framework used in [29]

However, this cost model does not consider two important cost drivers in WAAM manufacturing. The first one is the cooling time spent between a layer and the next one that is often mandatory, especially if the part is small, to avoid issues due to thermal accumulation. The second one is the time spent during the repositioning movement of the torch, i.e. the movements that are necessary to move the torch from the end of the just deposited weld bead to the starting zone of the next one; these two points can also be very distant, especially if the part is big. This is not an unusual situation for WAAM, since it is an additive manufacturing technique suitable to produce parts big up to meters [8].

Zhai [11] developed another cost model to be used in the first stage of the design of the part. It is very straightforward and easy to use, since it requires only a few information to get the cost estimation. The author also defined a cost model for CNC milling to make comparisons between WAAM and CNC milling itself. This cost model takes into account also the time spent during the repositioning movements and the inter-layers dwells. However, this time is defined as a percentage of the total deposition time. This assumption may cause some problems since these quantities are strictly dependent on the deposition toolpath and can be very different, even for the same geometry, if different materials or deposition strategies are used.

Finally, Martina and Williams [1] implemented a cost model to calculate the cost of titanium parts manufactured using WAAM. The final aim is to compare the manufacturing cost for such parts using WAAM and traditional machining operations. This model includes also the cost related to the interpass rolling, a specific layer by layer post processing technique developed at Cranfield University [30]. For this model too, the time spent to reposition the torch is calculated as a percentage of the total deposition time, while cooling time and non-productive time are not taken into account at all.

Since all the cost models present in literature are not directly integrated with a toolpath calculation software, all of those uses only geometrical features to early estimate the manufacturing cost. This way the complexity of the part is usually not considered, except for the case of the model proposed by Guo. Anyway, since the toolpath is not taken as an input for the cost calculation, the geometry provided to the cost model must not be the final one,

since it is quite different from the geometry obtained after the WAAM operations. This because the part produced by WAAM must include some extra material on the walls and, for example, in the internal corners: this extra material will be removed during the finish milling operations (Figure 38)

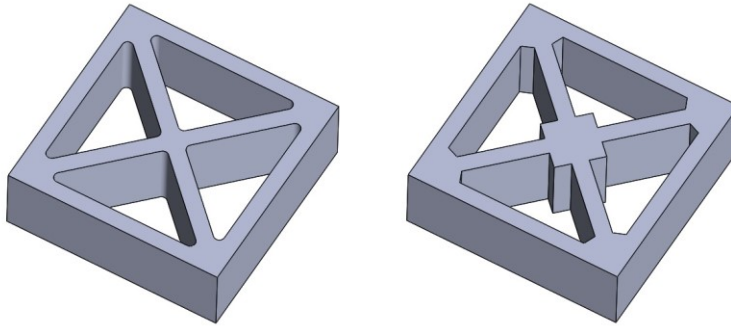


Figure 38 Final shape of the component (left) and shape of the component right after the deposition process (right)

For this reason, two CAD models must be created: the first one must have the extra material and is the shape obtained after the WAAM operations, while the second one is the final shape and it is used to calculate the cost related to the finish milling toolpath.

In the proposed cost model, a unique CAD model must be provided to the toolpath generation module and to the cost model. This CAD model contains only the midsurface of the part, since the interest is focused on thin walled components that are manufactured stacking only one single bead over the other (Figure 39).

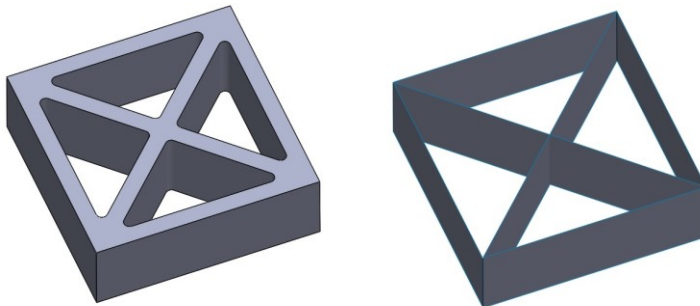


Figure 39 Final shape of the component (left) and the midsurface (right) that is the input both for the cost model and for the toolpath generation module

The toolpath generation module takes care of adding all the extra toolpath segments to add material in the zones where it is needed (refer to section 3). The total length of the toolpath and the length of the repositioning movements will be then the principal input for the cost model.

2.2. The cost model used for CNC milling roughing and finishing

Several cost models for CNC milling have been developed in the last years. Examples are reported in [31], [32] and [33]. In this thesis a cost model for CNC operations has been implemented in an Excel spreadsheet with the intention of comparing the WAAM technology with a pure CNC milling fabrication.

The costs related to the design stage of the part have not been considered, since these are out of the scope of the present thesis. Therefore, the main cost drivers related to a CNC milling operation are reported in Table 2.

Table 2 Cost drivers for CNC milling

Material Utilization	Billet Volume
	Cutting Fluid
Machining Time	Machine Utilization
	Energy Consumption
	Tool Replacement
Setup Time	Machine Utilization
	Direct Labor Force
Non-Productive Time	Machine Utilization
	Direct Labor Force

Looking at Table 2 it can be stated that the main cost drivers are the amount of material employed and the manufacturing hours required. On the one hand, the material used is the initial billet from which the final part will be obtained. In addition, the cutting fluid, which has the function of lubricate and cool down the tool and the part while being machined, has an important impact on the cost. On the other hand, regarding the costs incurred during the manufacturing time, these are due to the tool wear and the machine, energy and labor hourly rates. Particularly, the manufacturing time can be divided into the actual time in which the part is being machined, the setup time and the non-productive time.

The presented cost model for milling is addressed to thin walled components that can be manufactured using a three-axis milling machine. For what concerns the cost related to finishing, these are the same both for the case of pure CNC machining and for WAAM manufacturing. Since most of the industrial applications of WAAM are three-axis operations it is not reductive to address the cost model only to three-axis operations.

In the cost model no cost calculation of the whole lifecycle of the part is included. This because the final shape of the part is the same both manufacturing it using WAAM or milling and no advantages occur during the life of the components due to the exploitation of additive manufacturing technologies. An analysis of the costs or even of the energy consumption occurring during the lifecycle of the part becomes very interesting in the case of parts manufactured using additive technologies capable of increasing the performance of the part itself especially in terms of weight savings; anyway, this is the case of powder bed techniques and it is outside the scope of this thesis. Moreover, some simplifying assumptions have been made and are listed below:

- The chips obtained from the CNC operations are considered as waste, they are considered not to be sold and their potential selling cost is not subtracted from the total material cost;

- Although the energy consumption depends on the cutting forces and cutting speed that vary depending on the material being milled, an average machine power has been considered both for roughing and finishing operations;
- It is considered that optimum cutting conditions are used both in roughing and finishing operations;
- The finishing operations are considered to be executed with only one milling pass; no incremental milling passes are considered;
- The repositioning movements of the tool have not been considered, because it is assumed that the machining operation are executed using a high-speed milling machine;
- The thickness of the walls of the part to be milled is assumed to be constant; this because the whole thesis is addressed to thin walled components manufactured using WAAM and stacking just one single bead over the other. So, since this cost model is developed for comparison purposes, it is enough that it considers parts that can be easily manufactured through WAAM.

The following subsections contain the equation of the milling cost model; these are organized looking at the main cost drivers in milling that are material, machining, setup and non-productive time costs. At the end all these costs will be combined to obtain the total cost of the part. The cost models from Jung [31], Boothroyd and Reynolds [34] have been used as a reference; anyway, some modifications have been applied to tailor the resultant cost model for the specific application presented in this thesis.

2.2.1. Material cost

The two main cost drivers related to material cost are the cost of the billet from which the part is obtained, and the cost of the cutting fluid used during the milling operations.

For the parts considered in this activity such as stiffened panels or, in general, part that can be manufactured through three axis operations, the starting billet has usually the shape of a rectangular prism. In order to get the exact dimensions of such billet, it is necessary to know the dimensions of the so-called bounding box of the input CAD model, and this task is accomplished by the specifically developed Grasshopper auxiliary module for CNC. Some extra length will be added to such dimensions to consider the wall thicknesses and some allowance material. The bounding box can be obtained from the same CAD model supplied to the toolpath generation module and containing only the midsurface of the part. After the bounding box including all the geometry has been extracted (Figure 40), an XY scaling operation is applied to the bounding box itself to consider the thickness of the wall (that is assumed as an input parameter for the cost model) and a stock allowance.

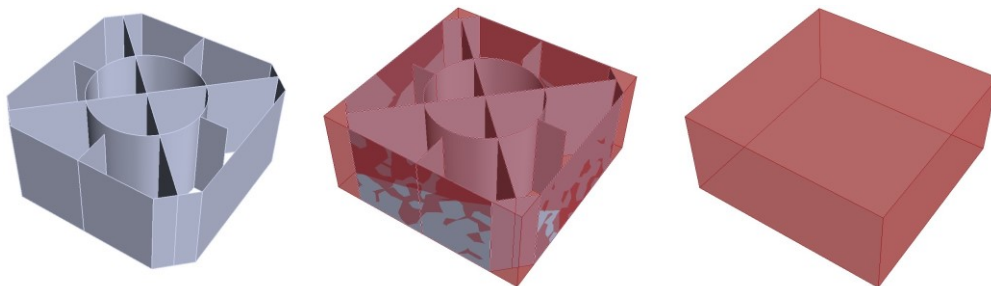


Figure 40 The determination of the bounding box for the input CAD model

The final bounding box is reported in Figure 41.

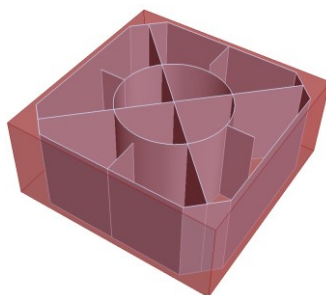


Figure 41 The bounding box after the XY scaling operation

Finally, the volume of the resulting bounding box, i.e. of the solid billet is extracted using a specific Grasshopper function. Known the volume of the billet and the kind of material, the cost of the billet itself C_b can be calculated using Equation 1:

$$C_b = V_b \cdot \rho \cdot c_b \quad \text{Equation 1}$$

Where:

C_b = total cost of the billet;
 V_b = total volume of the billet;
 ρ = density of the billet;
 c_b = unit price of the billet.

According to [35], the cost of the cutting fluid represents a high percentage of the total manufacturing cost. For this reason, it has been included in the present cost model, since even if nowadays the tendency is towards dry machining or MQL, lubricants and coolants are still widely used during milling operations, especially for difficult-to-cut materials. The costs related to the purchase, management and disposal can be assumed as the 17% of the total cost of a components [35]. So, the cutting fluid costs are calculated as follows (Equation 2):

$$C_{cf} = 0.17 \cdot C_{Mtotal} \quad \text{Equation 2}$$

Where:

C_{cf} = cost of the cutting fluid;

C_{Mtotal} = total cost of the machining process (not considering cutting fluid);

Therefore, the total material costs C_M can be obtained using Equation 3:

$$C_M = C_b + C_{cf} \quad \text{Equation 3}$$

2.2.2. Machining costs

The machining cost is related to the machining time that is defined as the time during which the tool touches the part being manufactured. Since when using a CNC machine, the operator intervention is unnecessary (since the machine can operate unattended [36]) it has been considered that no labor force is required during the machining operations, therefore no labor cost related to the machining time is considered. Besides, also the energy consumption cost has been integrated in the machining cost.

Moreover, since during the machining operations the tool becomes worn, it must often be replaced. According to [37], it is possible to include in the machining cost an allowance for the tool replacement without any relation with the specific kind of tool being used (and this is important to keep the model usable in the very early design stages). So, the tool replacement cost will be taken into account using the Taylor life index of the tool material.

Before determining the machining cost, it is necessary to calculate the machining time using Equation 4:

$$t_{\text{machining}} = t_{\text{roughing}} + t_{\text{finishing}} \quad \text{Equation 4}$$

Where:

$t_{\text{machining}}$ = total machining time;

t_{roughing} = total roughing time;

$t_{\text{finishing}}$ = total finishing time;

Since one of the assumptions of this cost model is that during finishing operations only one pass is necessary to remove all the extra material left by the roughing operations, it makes sense to consider that all the extra material is removed from the billet during the roughing operation and the allowance material left for finishing is neglected. This way, the machining time is linearly dependent on the total volume of material to be removed. To perform the roughing of the billet many different machining operations can be used, each of those having its own Material Removal Rate (MRR), that is the material removed per unit of time. Therefore, supposing that a number i of roughing operations is performed, the total roughing cost must be calculated following Equation 5:

$$t_{\text{roughing}} = \sum_i \frac{V_{r_i}}{MRR_i} \quad \text{Equation 5}$$

Where:

i = number of different roughing operations performed;
 V_{r_i} = volume removed by the i -th roughing operation;
 MRR_i = material removal rate proper of the i -th roughing operation.

It is important to notice that even the same kind of roughing operation changes its material removal rate value, if the cutting parameters or the tool are varied. Moreover, a specific MRR must be determined for each different case, since it depends on the used tool, the material and the cutting parameters.

Since most of the aerospace components like stiffened panels are machined using end mills and performing pocketing operations, this is the type of roughing operation that has been implemented in the cost model. However, if it is necessary to include another kind of roughing operation, it is enough to implement the material removal rate equation for that method in the Excel spreadsheet. The cost model will be still valid. Regarding pocket milling operations, using a flat end mill, the material removal rate can be calculated using Equation 6:

$$MRR_{mill} = a_p \cdot a_r \cdot f \quad \text{Equation 6}$$

Where:

a_p = axial depth of cut;

a_r = radial dept of cut;

f = feed rate.

The meaning of the above-mentioned parameters can be clearer looking at Figure 42 where a flat end mill engaging a workpiece is shown.

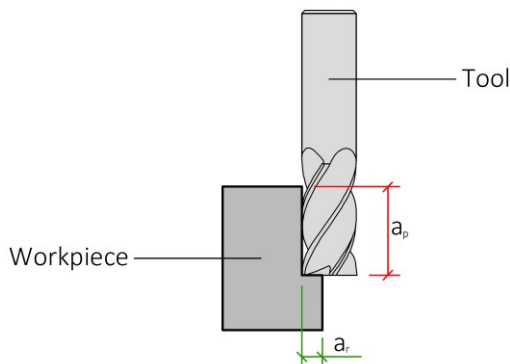


Figure 42 Visual explanation of the cutting parameters for an endmill

A supporting tool has been implemented in the auxiliary Grasshopper developed module to calculate the total volume of material to be removed in the case all the roughing operations are carried out through pocket milling. The workflow of this tool is as follows: firstly the volume of the bounding box that has been calculated previously is taken as input, then an intersection between the imported geometry and an horizontal plane is performed (for this purpose it is important to remember that this cost model is addressed to prismatic parts

that can be manufactured using just three-axis milling operations). The result of the intersection between the geometry and the plane is the base curve of the part itself (Figure 43).

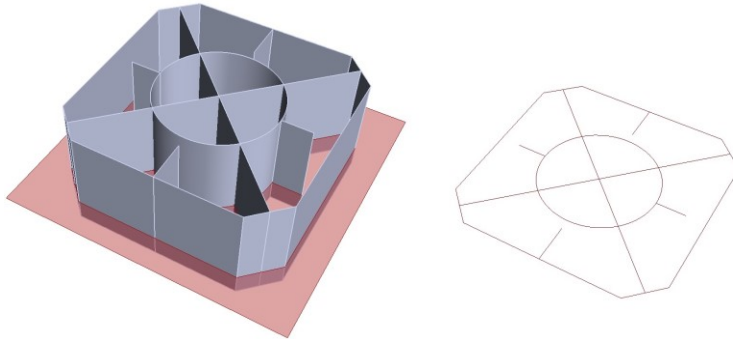


Figure 43 Intersection between the input midsurface and a plane (left) to obtain the base curve (right)

At this point, the total length of the base curve is calculated. Then the height of the bounding box is extracted. Given the wall thickness as input and remembering that it is constant for the whole part, the total volume of the part is calculated using Equation 7:

$$V_p = TL \cdot t \cdot h$$

Equation 7

Where:

V_p = total volume of the part;
 TL = total length of the base curve;
 t = thickness of the walls;
 h = height of the part.

Therefore, the total volume to be removed during the roughing operation will be calculated following Equation 8:

$$V_R = V_b - V_p$$

Equation 8

Where:

V_R = total volume to be removed;
 V_p = total volume of the part;
 V_b = total volume of the billet;

This volume is then written in the Excel spreadsheet and used to calculate the roughing time.

For what concerns the finish milling phase, it must be performed both in the case of WAAM manufacturing and in the case of pure CNC milling manufacturing, therefore it is examined in detail in this section, but it will be used also for the proposed cost model for

WAAM. One of the hypotheses of the presented cost model is that the finishing operation is carried out with a unique milling pass all over the surface of the part. Therefore, the finishing cost will be proportional to the total area to be machined and, in particular, to the amount of surface covered by the tool in the unit time; this latter quantity is called “Surface generation rate” (SGR) [38] and depends on many factors such as the material to be milled, the material of the tool, the cutting parameters and the tool geometry. Moreover, depending on whether the surface to be finished is a horizontal or vertical surface, the SGR will be calculated differently. Keeping all these aspects in mind, the finishing time can be calculated using the Equation 9:

$$t_f = \frac{S_{hor}}{SGR_{hor}} + \frac{S_{vert}}{SGR_{vert}} \quad \text{Equation 9}$$

Where:

S_{hor} = total area of the horizontal surfaces to be machined;

S_{vert} = total area of the vertical surfaces to be machined;

SGR_{top} = surface generation rate for a horizontal surface;

SGR_{ver} = surface generation rate for a vertical surface;

Supposing to use a vertical CNC machining centre, the finishing of the horizontal surfaces will be executed using the face of the end mill, while for the vertical surfaces the flank of the tool will be used. Adapting the calculation suggested by [31], the equations Equation 10 and Equation 11 show how to calculate SGR_{hor} and SGR_{ver} respectively.

$$SGR_{hor} = t \cdot F \quad \text{Equation 10}$$

$$SGR_{ver} = a_p \cdot f \quad \text{Equation 11}$$

Where:

t = thickness of the walls;

D = diameter of the end mill;

a_p = axial dept of cut;

f = feed rate.

To help finding the parameters needed to calculate the total finishing time t_f , a specific function has been implemented in the Grasshopper auxiliary module. This function, given the input CAD geometry, is able to calculate the total area of the surfaces of the part that must be finished. To do this the area of every surface composing the CAD model is calculated using a specific Grasshopper function. For this purpose, it is important to remember that, as depicted in Figure 44, the CAD model is composed by several surfaces. After selecting the surfaces in the Rhinoceros 5 CAD software, their area can be calculated using Grasshopper.

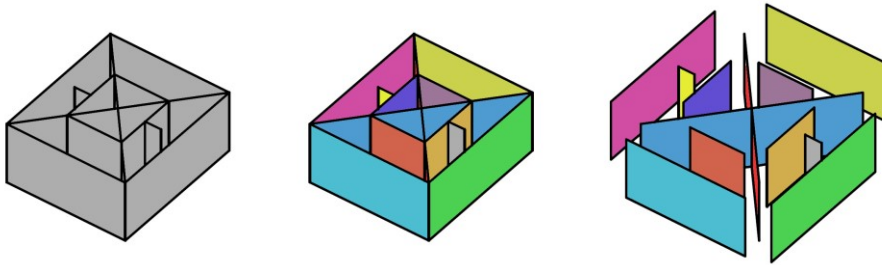


Figure 44 The input midsurface is composed by several surface entities

The result of such calculation is a list with all the areas of the single surfaces. All these values are added together and then the obtained value is doubled, since every surface is finished on both sides. This way the presence of the wall thickness is neglected; anyway, the thickness of the walls of a thin walled component is neglectable respect to the overall size of the part, and the approximation can be considered acceptable.

The total amount of horizontal surface to be machined is given by the sum of the area of top surface with the area of the bottom surface (Figure 45).

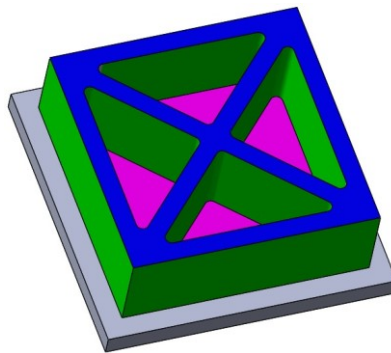


Figure 45 Surface nomenclature. Blue = top surface, Purple = bottom surface, Green = side surface

To calculate the total amount of horizontal surface (top and bottom) of the part, Grasshopper is used again. The base curve previously extracted from the CAD model is used as input and on every segment composing the curve, a high number of points is generated. All these points are included in an array that is the input for the function “Convex Hull” available in Grasshopper. This function calculates the curve that represents the smallest enveloping curves containing all the input points. Then, the area of the surface delimited by such enveloping closed curve is calculated; this area represents the total area of the horizontal surfaces to be machined. Figure 46 and Figure 47 show all the described steps.

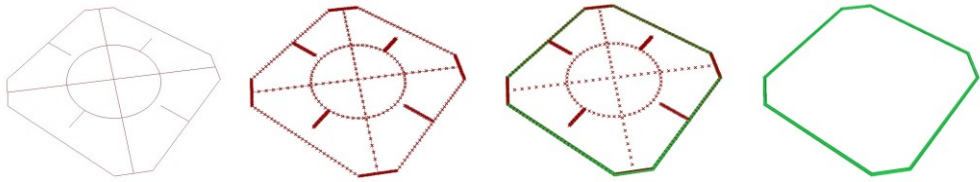


Figure 46 Steps for the calculation of the convex hull curve of the base curve extracted from the input CAD model

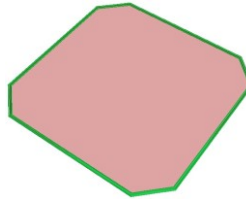


Figure 47 The surface delimited by the convex-hull curve of the base curve of the input CAD model

At this point the machine and energy hourly rates are needed. The energy hourly rate is calculated through Equation 12, considering an average value of power consumption:

$$her = P_m \cdot c_e \quad \text{Equation 13}$$

Where:

her = energy hourly rate;
 P_m = average power consumption;
 c_e = energy hourly price.

For what concerns the machine hourly rate, depreciation must be considered; therefore, the machine hourly rate is calculated as an amortized cost over the machine life time, as shown by Equation 14:

$$hmr = \frac{cme \cdot (1 + i)}{ay \cdot wy \cdot mu} \quad \text{Equation 14}$$

Where:

hmr = machine hourly rate for CNC milling;
 cme = total cost of the CNC facility;
 i = cost of money;
 ay = years of amortization for the CNC facility;
 wy = working hours per year;
 mu = utilization of the CNC facility;

In the end, the tool replacement cost is included in the machining cost, since it is directly related to that. Indeed, an optimal cutting speed is selected to find a minimum in the sum of

both the tooling and machining costs. The cost of the tools includes both the cost related to the machine idle times needed to replace the tool and the cost of a new tool. If the optimal cutting conditions are used, the machining cost can be expressed using Equation 15 ([37], [31]):

$$C_{mach} = \frac{t_{mach}}{(1-n)} \cdot (hmr + her) \quad \text{Equation 15}$$

Where:

t_{mach} = machining time;
 n = Taylor index for tool life;
 C_{mach} = machining cost.

Possible values for the Taylor index [37] are reported in Table 3:

Table 3 Tool life Taylor index for HSS and Carbide tools

Tool Material	High Speed Steel	Carbide
Taylor index	0.125	0.25

2.2.3. Setup Costs

Before starting the machining process, several setup operations must be carried out to set the CNC machine in a ready-to-cut condition. The operation that are generally required for a good setup are listed below:

- Gathering and positioning the jigs and fixtures;
- Clamping the stock;
- Placing the tools in the tool magazine of the machine;
- Setting the workpiece offset in the numerical control of the machine;
- Test the program “in air”.

Depending on the fixturing system and on the lot number, such operations can be carried out just one per lot or every time a new part is machined.

According to [31], the machine and tool setup times for a machining center are reported in Table 4. Since for small lots the part fixturing, and workpiece offset setting are carried out for each new part that is going to be machined, it has been assumed that these two operations take the 40% of the entire machine setup time reported in Table 4.

Table 4 Machine setup time and tool setup time for a machining center

Machine setup time	Tool setup time
2500	180

To calculate the setup cost for each component, Equation 16 can be used. It is important to notice that this equation refers to the manufacturing of small lots, since the fixturing and work offset setting are accounted for each single part.

$$mst = 0.3 \cdot t_{s,m} + \frac{0.7 \cdot t_{s,m} + n_t \cdot t_{s,t}}{B} \quad \text{Equation 16}$$

Where:

mst = machining setup time;
 $t_{s,m}$ = time to set up the machine;
 n_t = number of tools to be placed in the tool magazine;
 t_{st} = time to set up one single tool;
 B = size of the lot.

The main cost driver related to the setup time is the labor cost, since the power consumption during the idles of the machine is considered to be neglected. Therefore, the total setup cost can be calculated using Equation 17:

$$C_s^M = t_{s,m} \cdot (hmr + hlr) \quad \text{Equation 17}$$

Where:

C_s^M = total setup cost;
 hmr = machine hourly rate for CNC operations;
 hlr = labor hourly rate.

2.2.4. Non-productive time cost

The non-productive cost is related to the time needed to place the stock inside the machine, to unclamp the machined part and to remove it from the machine. Moreover, the time needed to clean the machine or refill the cutting fluid can be accounted in the non-productive time. The time spent by the tool to move from a zone of the part to another one without cutting is considered non-productive too.

For what concerns the time related to the handling of the stock, according to [34], it depends on the weight of the stock itself and can be calculated using Equation 18 that is valid until the total weight of the stock is below 27 kg:

$$t_{load} = 38 + 2.4 \cdot W \quad \text{Equation 18}$$

Where:

t_{load} = loading time;
 W = weight of the stock;

The non-productive time related to the non-cutting movements of the tool can be calculated using Equation 19:

$$t_{np} = n_o \cdot t_{npt} \quad \text{Equation 19}$$

Where:

t_{np} = tool non-cutting time;

n_o = number of operations;
 t_{npt} = non-cutting time for each tool.

Therefore, the total non-productive time can be calculated using Equation 20:

$$t_{np}^M = t_{np} + t_{load} \quad \text{Equation 20}$$

Where:

t_{np}^M = total non-productive time for machining.

While for the calculation of the total non-productive time cost, Equation 21 can be used:

$$C_{np}^M = t_{np}^M \cdot (hmr + her) \quad \text{Equation 21}$$

Where:

t_{np}^M = total non-productive time;
 hmr = machine hourly rate;
 $hler$ = labour hourly rate.

2.2.5. Calculation of the total manufacturing cost and time

Once all the calculations of the previous sections have been carried out, it is possible to calculate the total manufacturing cost and time. To obtain the total cost all the previously determined costs must be added, like in Equation 22:

$$C_{tot}^M = C_{mat}^M + C_{mach} + C_s^M + C_{np}^M \quad \text{Equation 22}$$

Where:

C_{tot}^M = total manufacturing cost;
 C_{mat}^M = material cost;
 C_{mach} = machining cost;
 C_s^M = setup cost;
 C_{np}^M = non-productive time cost.

However, since the cutting fluid cost depends on the total cost itself, considering Equation 2 and Equation 3 it is possible to rearrange Equation 22 obtaining Equation 23:

$$C_{tot}^M = \frac{C_b + C_{mach} + C_s^M + C_{np}^M}{0.84} \quad \text{Equation 23}$$

Regarding the total manufacturing time, it can be calculated using Equation 24:

$$t_{tot}^M = t_{mach} + t_s^M + t_{np}^M \quad \text{Equation 24}$$

Where:

t_{tot}^M = total manufacturing time;
 t_{mach} = machining time;
 t_s^M = setup time;
 t_{np}^M = non-productive time.

2.3. A cost model for WAAM

WAAM is a near-net-shape manufacturing technology, therefore the parts must be finish-milled in order to match the required surface quality. Only in rare cases a component produced by WAAM can be used in the as-printed condition [39]. For this reason, both additive and machining cost must be taken into account when calculating the manufacturing cost of a component produced by WAAM. For what concerns milling, the only operation that will be carried out on the part is the finishing one and the cost model for machining presented in the previous section can be used to calculate its cost. Regarding WAAM an approach to calculate the cost considering the deposition toolpath as input is presented and discussed. Generally speaking and referring to Figure 48, to produce a part using WAAM the following operations are executed:

- Design;
- Process planning
 During the process planning phase, the deposition parameters are chosen, and the deposition toolpath is generated using a CAM software or manually. If needed, a FEM simulation of the deposition process can be run, since it is important to evaluate the distortion of the part during the building procedure. In fact, if the part gets too much distorted while being manufactured the desired final shape is not matched. The FEM analysis gives also an indication regarding the thermal accumulation issues and its results can be used to optimize the deposition toolpath or to include some dwells for cooling during the deposition;
- Material procurement
 Since WAAM needs a substrate to build the part on, it is important to design and manufacture the substrate. In general, the best approach is to include the substrate in the final geometry of the part, but sometimes it is necessary to detach the part from it. Moreover, it is necessary to buy the welding wire with the required chemical composition and the best shielding gas suitable for the selected welding wire;
- Setting up the WAAM machine
 The welding wire and the gas bottle must be installed in the WAAM machine, the operator turns on the machine and setups all the adjustments on the numerical control and on the welding machine to match the requested welding parameters;
- Substrate clamping
 The substrate is placed in the machine and suitable jigs and fixtures are used to clamp it. Since in the toolpath calculation module presented in this thesis the work offset is

placed on the substrate, the operator must set the work offset in the numerical control of the machine in this phase;

- **Testing of the part program**
The calculated part program is executed “in air” (i.e. with the welding machine turned off) in order to check whether everything is ok; if not, the toolpath must be corrected using the CAM software;
- **Material deposition**
If everything is ok, the WAAM manufacturing cycle is launched;
- **Component cooling and inspection**
After the component has cooled down, it is inspected to be sure no excessive distortions have occurred during the material deposition;
- **Thermal treatment**
Sometimes a thermal treatment is needed to remove the internal stresses generated during the deposition process that could cause the distortion of the part during the finishing milling phase;
- **Finishing operations**
If the machine is hybrid, no repositioning of the part is needed, and the finishing operation is carried out on the same machine; otherwise, the part must be removed from the WAAM machine and placed in a milling machine. The workpiece offset (that will be in the same place both for additive and milling operations) must be set on the numerical control of the milling machine and the part must be clamped with suitable jigs and fixtures again. Finally, after an “air-cutting” test, the milling cycle is started;
- **Substrate removal**
If the substrate won’t be part of the final component it is removed through subtractive technologies, and the bottom part of the component is finish milled;
- **Part removal and inspection**
Finally, the part is removed from the milling machine and inspected.

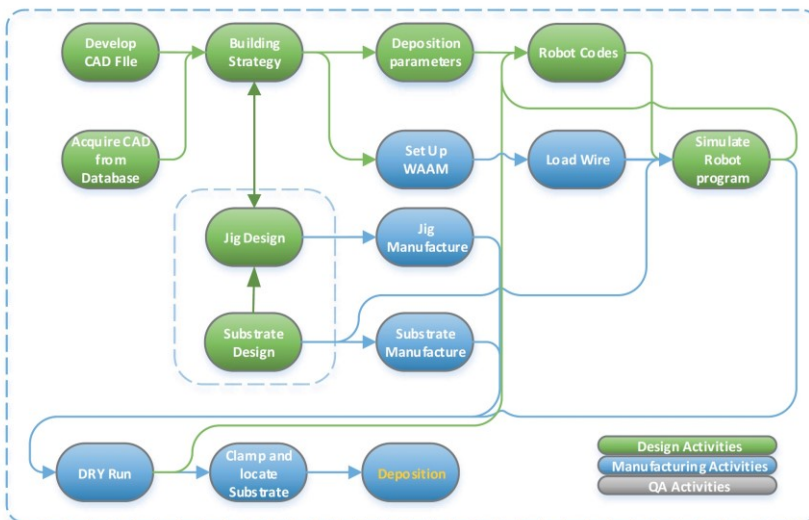


Figure 48 WAAM process workflow (from [40])

In the presented cost model for WAAM many machining operations have been considered. These are listed below:

- Manufacturing of the substrate;
- Finish milling of the top, lateral and bottom surface of the part
- Additional machining operation performed on the substrate after the deposition procedure;
- Machining of the bottom surface of the part after the removal of the substrate.

To calculate the cost of all these operations, the cost model for CNC milling operations presented in section 2.2 can be used.

The process planning, thermal treatment and inspection phases are not considered in the presented cost model, since the model is focused on the shaping processes. Besides, manufacture of parts performed in a hybrid machine in which milling and additive operations are executed alternatively during the part growth are not considered. Keeping in mind these details, the manufacturing cost drivers for WAAM are reported in Table 5.

Table 5 Cost drivers for WAAM

Material Utilization	Wire
	Substrate
	Shielding Gas
Manufacturing Time (Welding Time and Finishing Time)	Machine Utilization
	Energy Consumption
	Direct Labor Force (Tool Replacement)
Setup Time (WAAM Machine and Milling Machine)	Machine Utilization
	Direct Labor Force
Non-Productive Time (WAAM Machine and Milling Machine)	Machine Utilization
	Direct Labor Force

The proposed cost model is called “toolpath-based” since the toolpath is the main input for the cost calculation itself. All the data are organized in an Excel spreadsheet, while the toolpath is obtained by the toolpath calculation module described and presented in this thesis. The toolpath calculation module is able to calculate not only the actual deposition toolpath, but also the total length of the positioning movements, that are an important cost driver since they’re directly related to time.

The cost model is described in the following subsections. After the description of an experimental activity carried out to calculate the deposition efficiency parameters, like in section 2.2, in each subsection a main cost driver for the WAAM manufacturing is described.

2.3.1. Deposition efficiency parameters: experimental determination

As stated in section 3, when depositing a section of a part there are many parameters to be considered to obtain an optimal deposition and to understand which the final shape of the section will be. These parameters, recapped below, are related to the deposition efficiency but also have influence on the toolpath generation:

- Deposition efficiency related to waviness.
See Figure 69 and Equation 49 for definition and calculation of the deposition efficiency. It has no consequences on the toolpath generation, but different welding parameters can lead to different values of surface waviness and effective wall width (EWW). For this reason, a specific EWW is associated to a specific set of welding parameters. Given the desired wall thickness for the part to be manufactured, a welding parameter set will be chosen and will be the input both for the toolpath calculation module and for the cost model.
- Deposition efficiency related to uneven top surface
This is usually caused by casual defects or by a non-optimal interpass temperature (i.e. to a non-optimal choice of the inter-layer dwells). To be sure to have enough material to achieve the desired final shape one or more extra layers are added to the toolpath and this influences the deposition and finish-milling time and, consequently, the total manufacturing cost.
- Deposition efficiency related to uneven end wall sections (Figure 49);
To assure an allowance material on the free end walls, the toolpath is extended.

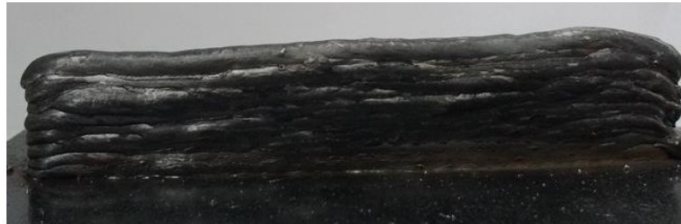


Figure 49 The sides of a deposited wall are never perfectly straight

All the amounts of the modifications carried out on the toolpath depend on the used welding technique, welding parameters and deposition parameters and must be determined experimentally. Moreover, these are inputs for the CAM software enabling it to calculate the right toolpath.

To determine such parameters, the first step is the individuation of a set of stable welding parameters that is intended to be used to manufacture the part. Then, several test walls are manufactured and analyzed as explained in the following lines.

A specific Grasshopper module has been developed to create the deposition toolpath starting from a rectangular input surface for a single straight wall with the deposition strategy reported in Figure 50.

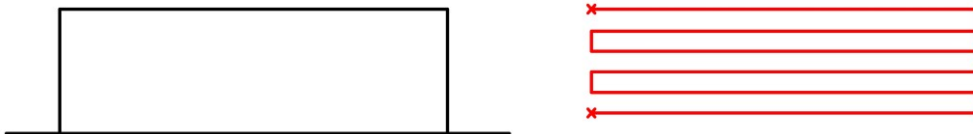


Figure 50 The input CAD model and the resultant deposition toolpath for a single straight wall

The calculated toolpath has neither additional layers nor extensions on the sides, since it is what is intended to be determined. Several walls have been manufactured using the same parameters and an example of manufactured wall is reported in Figure 51.



Figure 51 WAAM wall

First, to calculate the extra material to be added on the top of the wall, i.e. the number of extra layers to add to the toolpath, measurements of the height of the wall are performed using a Vernier Caliper and following the scheme reported in Figure 52.

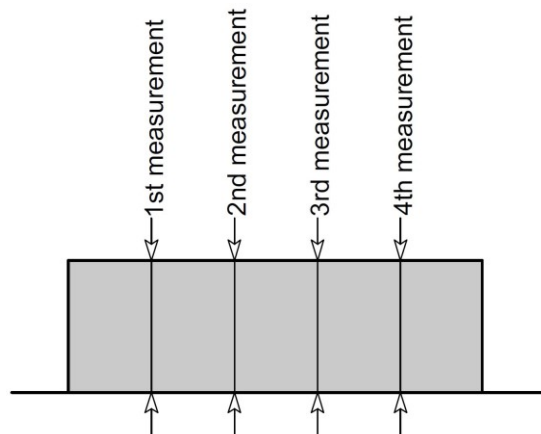


Figure 52 The four equally spaced measurements taken on the wall

The resultant mean values of the four measurements taken on the lot of walls manufactured using the same parameters are reported in Table 6.

Table 6 Measurements taken on the wall

Measurement	1st	2nd	3rd	4th
Height	26.0	24.9	24.7	24.9

From Table 6 it can be observed that the difference between the maximum and the minimum height is 1.3 mm, therefore that height of the wall should be removed to obtain an even top surface that means that an extra layer must be added to the toolpath. However, it is also necessary to remove the rounded part of the lowest point of the wall, since the top surface of the beads has a rounded shape. Therefore, considering that the layer height for the selected welding parameters is 1.5 mm, it is assumed that is necessary to add another extra layer to the toolpath. So, the total amount of extra layers to be added to the toolpath is two.

To determine the amount of the toolpath extension for a free end wall, the walls have been photographed keeping the camera parallel to the substrate and orthogonal to the surface of the walls. Later, the pictures have been imported in the AutoCAD 2016 software to be further processed. First these have been scaled knowing the length of the substrate. Later, the maximum inscribed rectangle has been drawn using the drawing tools of AutoCAD, and its length has been measured using the quoting tool (Figure 53).

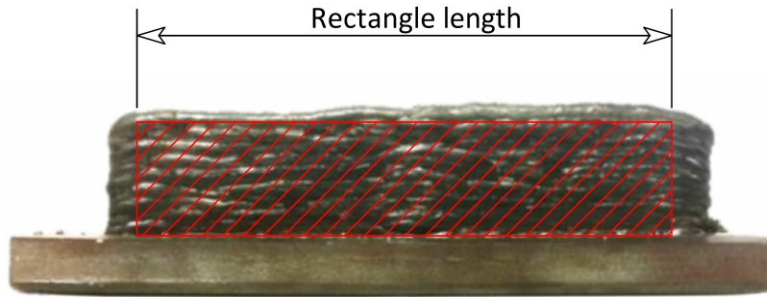


Figure 53 Graphical method to obtain the length of the extra toolpath to be added for the free end walls

The obtained value is subtracted to the total length of the wall and the result is divided by two. The result of the division is incremented by the 10 % to be sure to have enough extra material and represents the amount of extension of the toolpath for a free end wall.

Finally, the deposition efficiency related to the surface waviness is determined. The walls have been sectioned in four different points (Figure 54).



Figure 54 One of the manufactured walls divided in five parts to measure the surface waviness

Then, the surfaces of the five obtained specimens have been accurately polished using sandpaper applied on a planar and rigid surface. At this point, the surfaces of the specimens have been scanned using a traditional A4 size scanner at a resolution of 600 dpi.

The resultant images have been imported in the AutoCAD software where the contours of the cross sections have been reproduced manually using a spline. Then the resultant

area has been calculated (red area in Figure 55). Later, the widest inscribed rectangle has been drawn manually and its area has been measured too (green area in Figure 55).

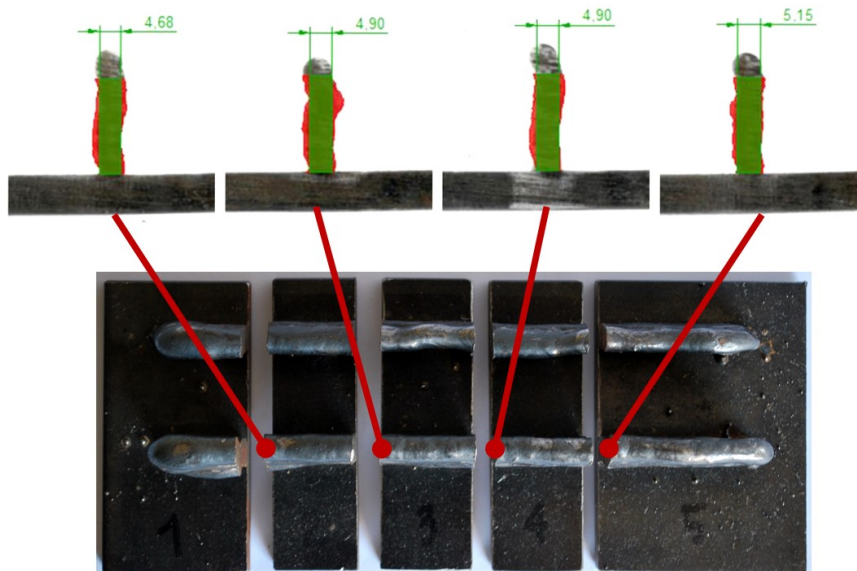


Figure 55 Graphical determination of the effective wall width and deposition efficiency

Finally, the deposition efficiency has been calculated using Equation 49 reported in section 3. Table 7 shows the average results of this operation.

Table 7 Effective Wall Width and deposition efficiency for the used welding parameters set

Section	Effective wall width (EWW) [mm]	Total Area [mm ²]	Effective Area [mm ²]	Deposition Efficiency
1	4,68	141,23	102,90	72,86
2	4,90	154,16	107,80	69,93
3	4,90	142,53	107,76	75,61
4	5,15	143,75	113,12	78,69

To be safe the minimum achieved wall width has been considered as the one obtainable with the used welding parameter set. The data determined through this experimental activity will be the input for the toolpath calculation module and, directly or indirectly, for the cost model.

2.3.2. Material cost

The material cost has three main cost drivers: the substrate cost, the welding wire cost and the shielding gas cost. For what concerns the cost of the material for the substrate, it can be calculated using Equation 25:

$$C_{sub} = V_{sub} \cdot \rho_{sub} \cdot c_{sub}$$

Equation 25

Where:

C_{sub} = total cost for the material of the substrate;
 c_{sub} = unitary price of the substrate material;
 ρ_{sub} = density of the substrate material;
 V_{sub} = volume of the substrate.

If needed, the substrate can be machined after or before the deposition operation as shown in Figure 56 and Figure 57.

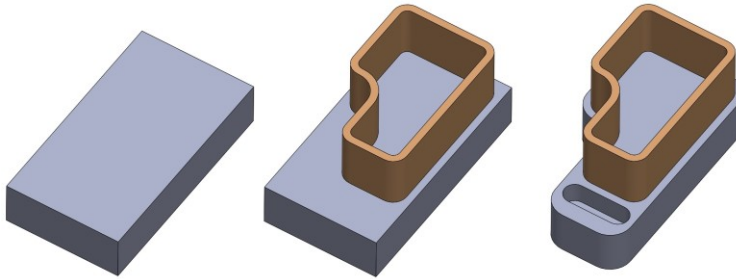


Figure 56 Unmachined substrate (left), part deposited upon the substrate (center), final machined part and substrate (right)

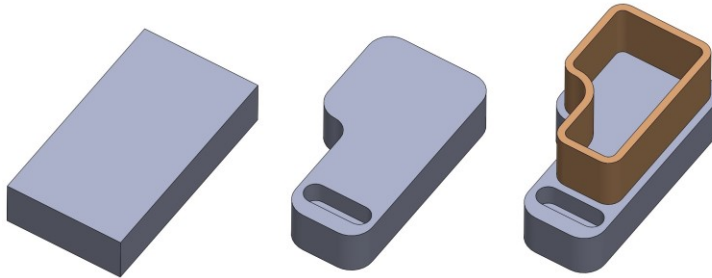


Figure 57 Unmachined substrate (left), machined substrate (center), part deposited upon the previously machined substrate (right)

To evaluate this additional cost related to the substrate, the cost model for CNC operations presented in section 2.2 can be used. To use that cost model, it is necessary to determine the total volume of material to be removed (related to the roughing costs) and the total area of the surfaces to be finished (related to the finishing costs). For this reason, a Grasshopper auxiliary module has been implemented. One of the functions implemented in the module takes as input the final 3D geometry of the substrate and calculate its bounding box and the volumes of the substrate and of the bounding box themselves. Finally, it makes the difference between the volume of the bounding box (i.e. the bar that will be used as stock to create the substrate) and the volume of the final shape of the substrate finding the total amount of volume that must be removed through machining (Figure 58).

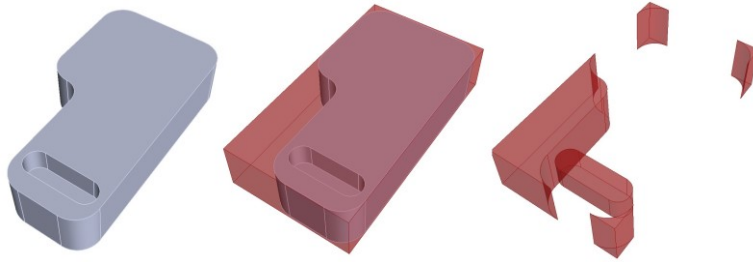


Figure 58 Procedure to determine the total volume of material to be removed from the substrate through roughing operations

Moreover, since to calculate the cost related to finish milling the total area of the surface to be milled is needed, another function of the auxiliary module allows to manually select the surfaces to be finished on the final CAD model of the substrate imported in Rhinoceros 5. The function also calculates the total amount of the area of the selected surfaces (Figure 59).

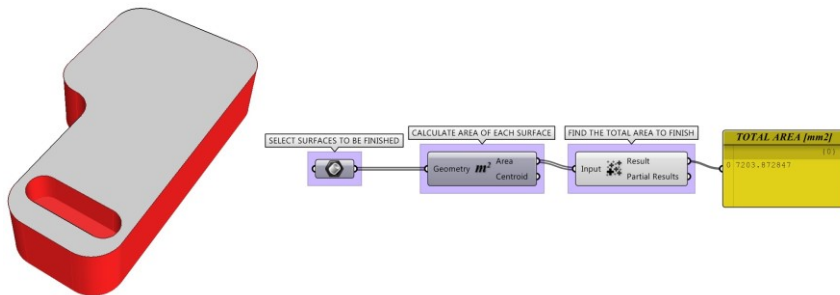


Figure 59 Calculation of the total area of the selected surfaces (red color) in the Grasshopper auxiliary module

For what concerns the total amount of deposited material, it is necessary to calculate first the total deposition time. For this purpose, the toolpath generation module can give to the cost calculation module the total toolpath length TL and the length of the repositioning movements RL . Moreover, the deposition feed rate FD and the rapid feed rate FR are inputs both for the toolpath calculation module and for the cost calculation module. Therefore, the total deposition time t_{dep} can be calculated using Equation 26:

$$t_{dep} = \frac{TL}{FD} \quad \text{Equation 26}$$

Then, using the process parameters, the build rate can be calculated using Equation 27:

$$B_{rate} = \frac{\pi \cdot D_{wire}^2 \cdot WFS \cdot \rho_{wire}}{4} \quad \text{Equation 27}$$

Where:

B_{rate} = build rate;
 D_{wire} = diameter of the welding wire;
 WFS = wire feed speed;
 ρ_{wire} = density of the welding wire.

Using Equation 26 and Equation 27, it is possible to calculate the total amount of deposited material M through Equation 28:

$$M = t_{dep} \cdot B_{rate} \quad \text{Equation 28}$$

Finally, the total cost due to the welding wire can be obtained using Equation 29:

$$C_{wire} = M \cdot c_{wire} \quad \text{Equation 29}$$

Where:

C_{wire} = total cost of the used welding wire;
 c_{wire} = unit cost of the welding wire.

During the material deposition, a shielding gas is used to protect the molten pool from the oxidation. The shielding gas flux is interrupted during the repositioning movements and the cooling idles. To calculate the cost of the shielding gas it is necessary to know the volumetric capacity of the used gas bottle. However, since the gas in the bottle is in a liquid state, a suitable conversion between the liquid state and gas state volumes of the gas must be determined. Assuming that the transformation between the liquid and the gas state is isothermal a relationship between the two volumes can be determined using the value of pressure inside the bottle and the atmospheric pressure. Therefore, as also suggested by [29], the total cost of the shielding gas can be calculated using Equation 30:

$$C_{gas} = \frac{\dot{V}_{gas} \cdot P_{atm}}{P_{gb}} \cdot \frac{c_{gb}}{V_{gb}} \cdot t_{dep} \quad \text{Equation 30}$$

Where:

C_{gas} = total cost of the shielding gas;
 \dot{V}_{gas} = gas flow rate;
 P_{atm} = atmospheric pressure;
 P_{gb} = pressure of the gas bottle [atm];
 c_{gas} = cost of a single gas bottle;
 t_{dep} = total deposition time;
 V_{gb} = volume of the gas bottle;

At this point the total building time must be determined. This time includes the deposition time, the cooling time and the repositioning time. Therefore, the cooling time and the deposition time must be determined. To have an accurate resultant cost, the exact prediction of the cooling time is crucial. To have a good prediction of the cooling time it is possible, for

small parts, to apply the method proposed in [15]. Otherwise, if no tools are available to predict the cooling time, this could be roughly assumed equal to the deposition time as suggested by [1], or an equation like Equation 31 taken from [40] can be used.

$$t_c = \frac{\left(\frac{Q}{(H_m - H_0) \cdot FD \cdot b} \right) \cdot 2}{4 \cdot a \cdot \left(\operatorname{erf}^{-1} \cdot \left(\frac{T - T_0}{T_m - T_0} \right) \right) \cdot 2} \quad \text{Equation 31}$$

Where:

t_c = time of cooling;
 Q = welding input power;
 $H_m - H_0$ = latent heat of fusion;
 a = thermal diffusivity;
 FD = deposition feed rate;
 erf^{-1} = error function;
 T_m = melting temperature;
 T_0 = environment temperature;

Regarding the repositioning time it can be calculated through the rapid feed rate and the total length of the repositioning movements calculated by the toolpath generation module (Equation 32).

$$t_{pos} = \frac{RL}{FR} \quad \text{Equation 32}$$

Where:

t_{pos} = total positioning time;
 RL = total length of the rapid/repositioning movements;
 FR = rapid feed rate.

Therefore, the total building time can be calculated using Equation 33:

$$t_{build} = t_{dep} + t_{cool} + t_{pos} \quad \text{Equation 33}$$

Where:

t_{build} = total build time;
 t_{dep} = total deposition time;
 t_{cool} = total cooling time;
 t_{pos} = total repositioning time.

Since the speed profile for each of the axis of the WAAM machines used for the activity presented in this thesis is the one reported in Figure 60, the maximum travel speed achievable by the machine is reached in a very short time.

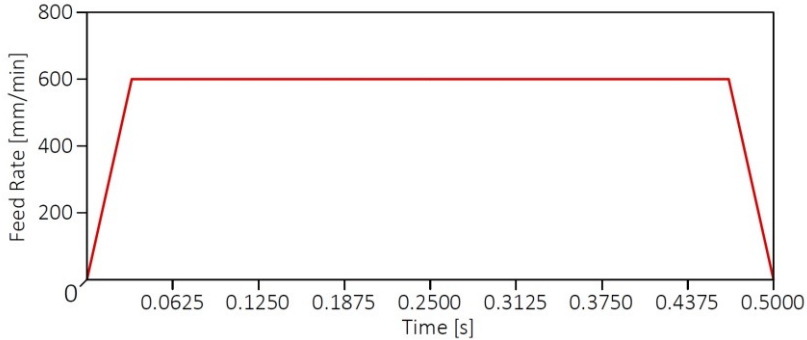


Figure 60 Speed profile for the motors of the five-axis machine

Therefore, the deviation between the programmed travel speed and the effective travel speed during the feed rate ramp-up is not considered.

2.3.3. Manufacturing cost

The manufacturing cost is directly related to the manufacturing time. The overall manufacturing time including both WAAM deposition and machining can be calculated using Equation 34:

$$t_{\text{manufacturing}} = t_{\text{build}} + t_{\text{mach}} \quad \text{Equation 34}$$

Where:

$t_{\text{manufacturing}}$ = total manufacturing time;

t_{build} = total building time;

t_{mach} = total machining time.

The cost to be accounted in this phase are due to the required labor force, the percentage of utilization of the machine and the energy consumption.

Regarding the labor force, it is accounted in different ways in literature. In [11] and [1] it is stated that one operator can attend only one machine, while in [29] it is assumed that one single operator can take care of three WAAM machines. The latter way has been chosen in this thesis to account the labor force. Therefore, if only one machine is used, the labor cost will be considered only for one third of the total manufacturing time.

To calculate the energy cost, both the energy consumption of the welding machine and of the motors of the WAAM CNC machine should be accounted. The energy consumption of the motors of the WAAM machine is neglected in the presented cost model, since it is very small respect to the energy of the welding machine which can be calculated using Equation 35:

$$r_e^{WAAM} = \left(\frac{I_W \cdot V_W}{e_w} \right) \cdot c_e \quad \text{Equation 35}$$

Where:

r_e^{WAAM} = energy hourly rate for the WAAM machine;
 I_W = average current value of the welding machine;
 V_W = average voltage value for the welding machine;
 e_w = electrical efficiency of the welding machine;
 c_e = energy unit price.

The average values of voltage and current depend on the welding parameters set on the control panel of the welding machine and can be read on the control panel itself during a test welding operation.

At this point the hourly rate of the WAAM machine must be calculated. The equipment needed to perform a WAAM operation is composed by the following items:

- CNC cartesian structure;
- Welding power source;
- Welding torch;
- Numerical control of the machine.

Moreover, the depreciation must be accounted. Therefore, the hourly rate for the WAAM machine can be calculated using Equation 36:

$$r_m^{WAAM} = \frac{E_{WAAM} \cdot (1+i)}{y_{WAAM} \cdot h_y \cdot U_{WAAM}} \quad \text{Equation 36}$$

Where:

r_m^{WAAM} = Hourly rate for the WAAM machine;
 E_{WAAM} = total cost of the WAAM facility;
 i = cost of money;
 y_{WAAM} = years of amortization of the WAAM machine;
 h_y = working hours per years;
 U_{WAAM} = WAAM machine utilization;

Finally, since the machine hourly rate, energy hourly rate and total building time have been determined, it is possible to calculate the total manufacturing cost for the deposition process using Equation 37:

$$C_{build} = t_{build} \cdot \left(r_m^{WAAM} + \frac{r_l}{3} + r_e^{WAAM} \right) \quad \text{Equation 37}$$

Where:

C_{build} = total WAAM manufacturing cost;

t_{build} = building time;
 r_m^{WAAM} = hourly rate of the WAAM machine;
 r_l = labor hourly rate;
 r_e^{WAAM} = energy hourly rate for the WAAM machine.

The cost due to the CNC milling is twofold. Firstly, the machining processes carried out on the substrate must be considered and secondly the finish milling operations performed on the deposited section must be accounted. For what concerns the milling operations on the substrate, they have already been examined and accounted in the substrate cost, determined in section 2.3.2. The finishing machining cost is directly related to the total amount of the area of the surfaces to be finished, as explained in section 2.2.2. Therefore, the equations presented in section 2.2.2 can be used to easily calculate the finish machining cost and time.

Therefore, the total manufacturing cost including both WAAM and machining operations is calculated through Equation 38:

$$C_{manuf}^{WAAM} = C_{build} + C_{finish} \quad \text{Equation 38}$$

Where:

C_{manuf}^{WAAM} = total WAAM manufacturing cost including (WAAM + machining);
 C_{build} = cost of WAAM additive operation;
 C_{finish} = cost of CNC finishing process.

2.3.4. Setup cost

To manufacture a component using the WAAM technology both additive and milling operations are needed. Since this cost model is not addressed to hybrid machines able to combine additive and subtractive operations in the same structure, two machines are needed to perform the deposition and post-finishing processes. Therefore, the setup cost for both the WAAM machine and the milling machine must be accounted. Regarding the WAAM process the setup operations that must be carried out are:

- Setting the welding parameter on the machine;
- Mounting the substrate in the machine;
- Setting the work offset in the numerical control;
- Test the part program.

The first and fourth operations of the list are carried out just once per lot, while the other once per part. However, since usually the substrate has a simple shape (like a plate in the three-axis machine and a disk in the five axis one), it is quite easy to provide a reference system for the substrate itself in the machine. Therefore, the setting of the work offset is carried out only when a substrate with different dimensions is loaded in the machine. The total setup time for the WAAM machine can be calculated using Equation 39:

$$t_s^{waam} = \frac{t_{setlot}^{waam}}{B} + t_{setpart}^{waam} \quad \text{Equation 39}$$

Where:

t_s^{waam} = total setup time for WAAM operations;
 $t_{set_{lot}}^{waam}$ = total setup time for operations to be carried out per lot;
 $t_{set_{part}}^{waam}$ = total setup time for operations to be carried out per part;
 B = lot size.

During the experimental activities carried out for the research presented in this thesis the setup times for both the three-axis and five-axis machines have been measured. Regarding the calculation of the testing time for the part program, the time calculated in Equation 33 can be used, while the time needed to set the parameters on the setting machine and set the reference system for the substrate can be neglected. Mounting the substrate in the machines used during the research activity presented in this thesis takes an average time of 5 minutes. Once the setup time has been calculated, the setup cost for the WAAM machine can be determined using Equation 40:

$$C_s^{build} = t_s^{waam} \cdot (r_m^{waam} + r_l) \quad \text{Equation 40}$$

Where:

C_s^{build} = total setup cost for WAAM;
 t_s^{waam} = total setup time for WAAM operations;
 r_m^{waam} = hourly rate of the WAAM machine;
 r_l = labor hourly rate.

Regarding the setup cost for the finish-machining operations, it can be calculated using the equations reported in section 2.2.3. Therefore, the total setup cost, including the setup cost for WAAM and milling can be calculated using Equation 41:

$$C_s^{waam} = C_s^{build} + C_s^{finishing} \quad \text{Equation 41}$$

Where:

C_s^{waam} = total setup cost for WAAM including the WAAM and machining operations
 C_s^{build} = total setup cost for the only WAAM operation;
 $C_s^{finishing}$ = total setup cost for the finis-milling operation.

2.3.5. Non-productive cost

Both non-productive costs for WAAM and finish-milling operations must be accounted. Regarding the finishing operation, the non-productive cost can be calculated using the equations reported in section 2.2.4. For what concerns the WAAM deposition process, the two main cost drivers for non-productive cost are the wire spool and gas bottle changing. During the building of one single part many gas bottles and wire spool could be used, depending on the duration of the operation and on the total amount of required material.

Thanks to experimental measurements taken during the test performed along the research activity presented in this thesis, it can be stated that the spool replacement takes 6 minutes and the gas bottle replacement takes 4 minutes. The non-productive time due to the wire spool changing can be calculated using Equation 42:

$$t_{ctot}^{spool} = \frac{V_{dep} \cdot \rho_w}{m_{spool}} \cdot t_{change}^{spool} \quad \text{Equation 42}$$

Where:

t_{ctot}^{spool} = total non-productive time due to spool changings;
 V_{dep} = total amount of deposited material;
 ρ_w = density of the welding wire;
 m_{spool} = mass of a new welding wire spool;

Equation 43 can be used to calculate the non-productive time due to the replacements of the bottle occurred during the deposition procedure.

$$t_{ctot}^{gas} = \frac{\dot{V}_{gas} \cdot P_{atm} \cdot t_{dep}}{P_b \cdot V_b} \cdot t_{change}^{bottle} \quad \text{Equation 43}$$

Where:

t_{ctot}^{gas} = total non-productive time due to gas bottle changings;
 \dot{V}_{gas} = shielding gas flow rate;
 P_{atm} = atmospheric pressure;
 t_{dep} = total deposition time;
 P_b = pressure of the gas bottle;
 V_b = volume of the gas bottle;
 t_{change}^{bottle} = time required to change one gas bottle.

Adding the two non-productive time related to the WAAM operation, the total non-productive time is obtained (Equation 44), while non-productive time cost can be calculated through Equation 45:

$$t_{np}^{wbuild} = t_{ctot}^{spool} + t_{ctot}^{bottle} \quad \text{Equation 44}$$

Where:

t_{np}^{wbuild} = total non-productive time for WAAM;
 t_{ctot}^{spool} = total non-productive time due to spool replacement;
 t_{ctot}^{bottle} = total non-productive time due to gas bottle replacement;

$$C_{np}^{build} = t_{np}^{build} \cdot (r_m^{waam} + r_l) \quad \text{Equation 45}$$

Where:

$$\begin{aligned} C_{np}^{build} &= \text{total non-productive cost for WAAM;} \\ t_{np}^{build} &= \text{total non-productive time for WAAM;} \\ r_m^{waam} &= \text{hourly rate of the WAAM machine;} \\ r_l &= \text{labor hourly rate.} \end{aligned}$$

Since to obtain the final shape of the part, both WAAM and milling operations must be performed, the overall non-productive cost can be calculated adding the non-productive cost for WAAM and the non-productive cost for finishing. Therefore, through Equation 46 the total non-productive cost can be achieved:

$$C_{nptot}^{waam} = C_{np}^{build} + C_{np}^{finishing} \quad \text{Equation 46}$$

Where:

$$\begin{aligned} C_{nptot}^{waam} &= \text{overall non-productive cost (due to WAAM and finishing);} \\ C_{np}^{build} &= \text{total non-productive cost for WAAM;} \\ C_{np}^{finishing} &= \text{total non-productive cost for finish-milling.} \end{aligned}$$

2.3.6. Overall production cost

Adding all the costs that have been calculated in the previous sections, the overall production cost is achieved (Equation 47).

$$C_{total}^{waam} = C_{mat}^{waam} + C_{manuf}^{waam} + C_{setup}^{waam} + C_{np}^{waam} \quad \text{Equation 47}$$

Where:

$$\begin{aligned} C_{total}^{waam} &= \text{overall cost of the WAAM production process;} \\ C_{mat}^{waam} &= \text{total material cost;} \\ C_{manuf}^{waam} &= \text{total manufacturing cost;} \\ C_{setup}^{waam} &= \text{total setup cost;} \\ C_{np}^{waam} &= \text{total non-productive cost.} \end{aligned}$$

Finally, to obtain the total production time, Equation 48 can be used:

$$t_{total}^{waam} = t_{manuf}^{waam} + t_{setup}^{waam} + t_{np}^{waam} \quad \text{Equation 48}$$

Where:

$$\begin{aligned} t_{total}^{waam} &= \text{overall production time for WAAM;} \\ t_{manuf}^{waam} &= \text{total manufacturing time for WAAM;} \\ t_{setup}^{waam} &= \text{total setup time for WAAM;} \end{aligned}$$

t_{np}^{waam} + total non-productive time for WAAM.

2.4. Comparison with CNC milling and sensitivity analysis

To test the cost calculation framework, the geometry of a dummy stiffened panel has been considered as case study (Figure 61).

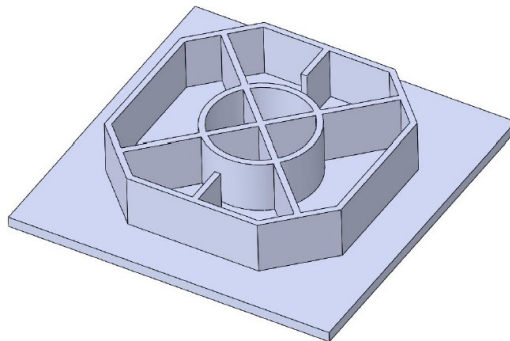


Figure 61 The test case used for the cost model

Figure 62 and Figure 63 report the results of the comparative analysis between WAAM and milling operations, while Table 8 and Table 9 show the manufacturing facts and parameters for WAAM and pure CNC milling respectively.

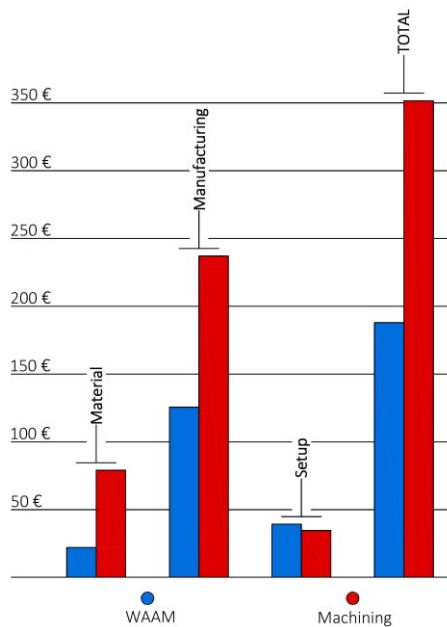


Figure 62 Cost comparison between WAAM and CNC milling

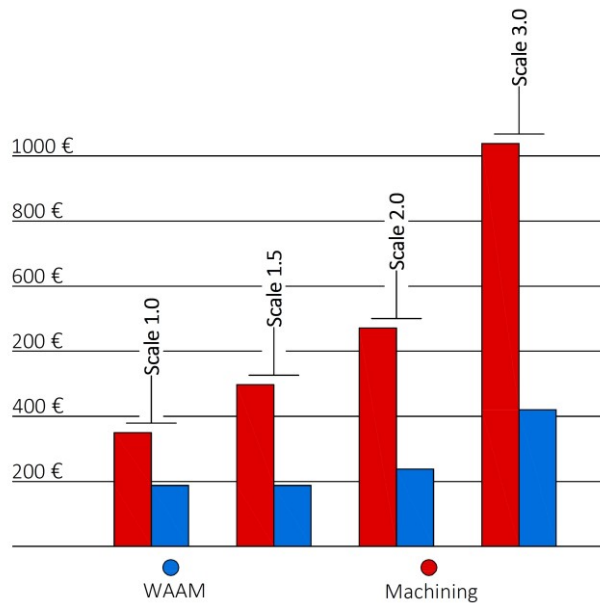


Figure 63 Effect of scale

Table 8 Main WAAM Manufacturing parameters for the case study

Item	Name	Data	Unit
Total Production	Batch Size	1	-
Wire	Wire Material	Carbon Steel	-
	Wire Diameter	0.8	mm
	Mass of wire in a spool	15	kg
Substrate	Substrate Material	Carbon Steel	-
	Substrate Dimensions	250x250x8	mm
Shielding Gas	Shielding gas type	18%CO ₂ – 82%Ar	-
	Shielding gas bottle size	14	l
	Bottle inner pressure	200	bar
Finishing Process Parameters	Taylor Tool life Index (HSS)	0.125	-
	No of tools	2	-
	<i>Top Surface Finishing</i>		
	Radial Depth of Cut	4,90	mm
	Feed	220	mm/min
	<i>Vertical Surface Finishing</i>		
	Axial Depth of Cut	3.2	mm
Feed	220	mm/min	
WAAM Process Parameters	Wire Feed Speed	4.60	m/min
	Voltage	18	V
	Feed	300	mm/min
	Layer height	1.5	mm
	Free end walls extension	3	mm
	Shielding gas flow rate	14	l/min
WAAM Machine	Machine cost	25000	euro

	Machine utilization	80%	-
	Deprecation Period	5	years
	Welding unit energy efficiency	90%	-
	Working hours per year	2080	hours
	Rapid Feed	1000	mm/min
CNC Machine	Machine Cost	150000	euro
	Machine utilization	80%	-
	Deprecation period	5	years
	Working hours per year	2080	hours
	Average power consumption	7.5	kW

Table 9 Main process parameters for CNC machining from solid

Item	Name		Data	Unit
Material	Billet dimensions		185x185x45	mm
Process	Taylor tool life index (HSS)		0.125	-
	<i>Roughing</i>			
	Total volume to be machined		924747	mm ³
	Radial depth of cut		4	mm
	Axial depth of cut		2	mm
	Feed		120	mm/min
	<i>Finishing</i>			
	Finishing top surface	Radial depth of cut	4.90	mm
		Feed	220	mm/min
	Finishing vertical surface	Axial depth of cut	3.7	mm
Feed		250	mm/min	
CNC Machine	Machine Cost		150000	euro
	Machine utilization		80%	-
	Deprecation period		5	years
	Working hours per year		2080	hours
	Average power consumption		7.5	kW

Referring to Figure 63, it is interesting to notice how increasing the dimension of the component, the CNC costs highly increase. This result shows how WAAM technology could be interesting for very large parts. Moreover, the cost increase of the CNC operations could be even bigger when dealing with difficult to cut materials such as titanium or high-grade steel that are widely used in the aerospace and Oil & Gas sectors.

3. 3-axis feature-based CAM software for WAAM

As all metal AM processes, WAAM requires dedicated software to automatically generate the deposition path to speed up the process planning phase. This performs a slicing operation, extracting the 2D geometry of the cross-sections and then, using this data, define a suitable path to deposit them. The algorithms to create the 2D section have been deeply investigated by several authors. Ding et al. [41] proposed to split the cross section in convex polygonal regions according to a divide-and-conquer strategy, depositing the regions with a combined contour and zig-zag approaches, two common strategies in polymer AM. The same authors proposed an alternative strategy [42] based on the medial axis transformation, introduced by Kao and Printz [43], which avoids the formation of empty gaps inside the workpiece sections. Nilsiam et al. [44] modified an existing open source slicer (CORA) dedicated to FDM (Fused-Deposition-Modelling), to make it suitable for WAAM path generation.

All the presented algorithms use a multiple pass strategy to create the 2D sections, i.e. despite the thickness of the component wall, the deposition path consists of several parallel overlapped beads [45]. This may not be convenient in the case of thin walled components that are the ones this thesis is addressed to. Analyzing the existing literature, it can be stated that none of the proposed solutions explores the possibility of automatically creating the deposition toolpath for the component using a single welding pass for each layer. The single pass strategy exploits the possibility of adjusting the layer dimension by tuning the process parameters [13]. This is a convenient alternative for thin walled parts since WAAM allows to deposit wide layers, achieving the section geometry without bead overlapping, hence with a significant decrease of the manufacturing time. Moreover, bead overlapping requires the usage of specific models [46] to determine the overall width of overlapped beads, including further uncertainties in the path generation algorithms. The toolpath generation module presented in this chapter addresses this lack of the state of the art, proposing the base architecture of automated 3 axis CAM software for WAAM deposition without bead overlapping.

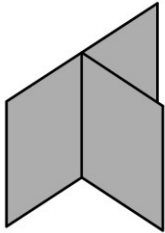
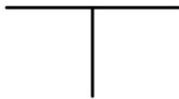
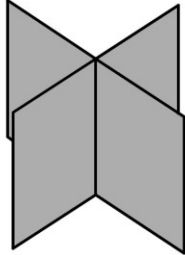
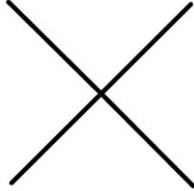
The most critical aspect of the single pass approach is represented by the crossing structures, since an improper deposition strategy could lead to a non-uniform layer thickness. Moreover, different types of crossings require different strategies, as shown by Mehnen et al. [47] and Venturini et al. [23]. The presented toolpath generation framework overcomes this issue by implementing a feature recognition algorithm, an approach successfully implemented

in different technologies, such as injection molding [48] and milling [49]. The internal workflow of the proposed CAM software is the following: the skeleton surface (midsurface) of the workpiece is imported in the CAM software; a feature recognition algorithm identifies the different crossings based on a proposed taxonomy; the deposition path is then generated by using specific strategies for each type of the detected features.

3.1. Proposed toolpath generation framework: general description

Especially in the aerospace field, several components are thin walled to be extremely lightweight. Typical examples are wing rib and stiffeners or other components such as parts for landing gears [50]. To achieve satisfactory structural stiffness, these components shows several stiffeners often intersecting each other and originating “crossings”. Such crossings can have various shapes which can be classified as specified in Table 10.

Table 10 Classification and schematic view of T-Crossing and Direct Crossing features

T Crossing		Direct Crossing	
3D View	Top View	3D View	Top View
			

The crossing features are critical, since they may require internal fillets to reduce stress concentrations, assure a good fatigue strength (Figure 64) and assure accessibility during milling operations, while porosity and flaws in these zones must be avoided for the same reasons.

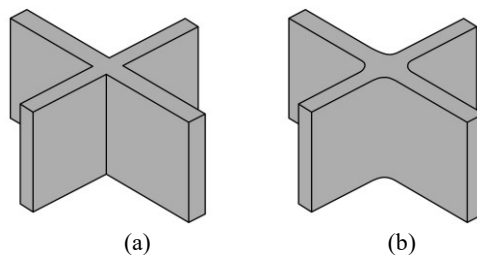


Figure 64 Direct Crossing with no internal fillets (a) and with internal fillets (b)

Hence, suitable deposition strategies for the crossings must be developed to avoid the occurrence of flaws and porosity. During the research activity presented in this thesis, several deposition strategies for crossings and tubulars have been tested and their implementation in the proposed toolpath generation framework will be shown. The presented CAM software is

completely automatic, since the input required to the user is just the selection of the CAD model. Since the software uses a single welding pass strategy (i.e. each layer is manufactured without bead overlapping), the input CAD model is composed just by the skeleton surfaces (i.e. midsurfaces) in an IGES 144 format. Therefore, it is not important to draw the exact final shape of the part including all the details such as the internal fillets of the crossings. In presented CAM software, the wall thickness of the part is assumed as constant and its value is an input the user must provide to the software. Figure 65 compares the full CAD model of a thin walled part and the skeleton surfaces required by proposed CAM software.

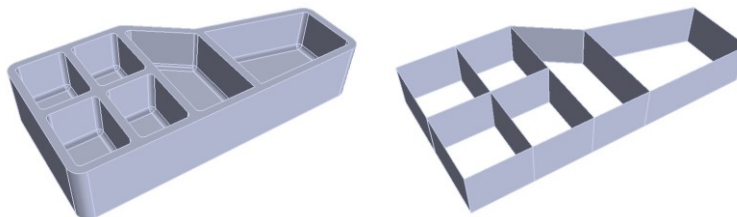


Figure 65 The complete CAD model (left) and the midsurface-only CAD model (right) for a stiffened panel

The proposed CAM software is composed by three modules, as shown by the schematic overview depicted in Figure 66. Every module is described in detail in the following sections.

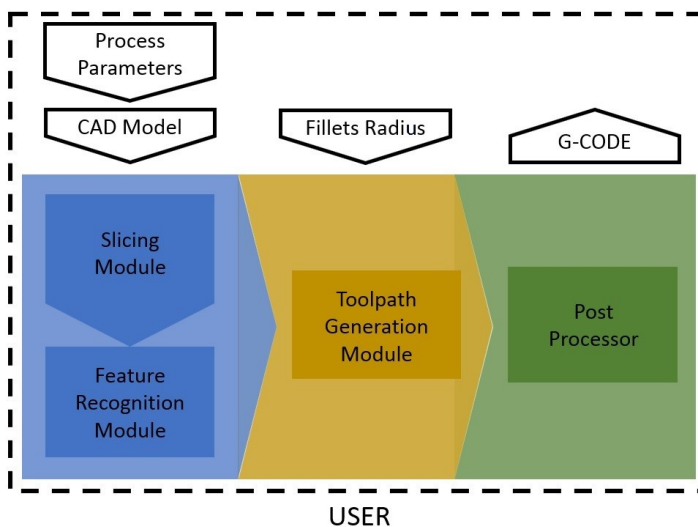


Figure 66 The three modules composing proposed CAM software

The first module is the Feature Recognition one, which takes the CAD model of the final part as input, recognizing and classifying all the different features of the component. The Toolpath Generation module computes the deposition path by performing several operations, such as the generation of additional segments to deposit extra material in the corners of the crossings, ensuring a fair amount of stock allowance to machine the fillets. The radius of such fillets is an input that the user must give to the software (Figure 66). At this stage, the software creates a Cutter Location File (CL File), which contains all the points of the toolpath in the

reference system of the part. Finally, a post processor translates the CL file into a G Code with G01, G02 blocks and WAAM specific M instructions such as torch ignition and shut-off. G04 instructions are also used in the G Code to keep the axes of the WAAM NC machine in an idle state before starting the deposition while the arc is igniting.

The following sections present in detail each module of the CAM software together with the deposition strategies for crossings, tubular shapes and open impellers. The algorithms are described without referring to a specific programming language. Only the fundamental logic concepts and logical operations are presented. This approach enables the implementation and reproduction of the proposed CAM software with different programming tools and languages. However, the toolpath generation module has been implemented in the using the graphical programming language (or G Language) through the software Grasshopper.

3.2. Proposed toolpath generation framework: description of the input

The input format of the workpiece geometry is an IGES 144 file. This because it is a well-known interexchange format that can be read and produced by every CAD software suite. Besides, many literature works dealing with the analysis and processing of such format are available [51], together with algorithms under the Open Source License format. Moreover, since the proposed CAM software is tailored for thin walled components to be manufactured by stacking a single bead over the other, the midsurface, is the only required geometrical input. Therefore, an input CAD model for the proposed CAM software can be obtained by drawing the sketch of the midsurface base profile and extruding every curve of it along the building direction (i.e. usually the Z+ direction). This returns a midsurface-only CAD model with the desired height (Figure 67).

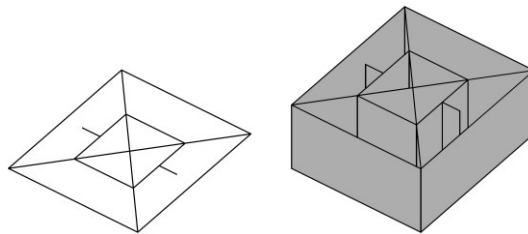


Figure 67 Base curve (left) and midsurface-only CAD model obtained extruding the base curve (right)

It is important to notice, for a good comprehension of the following sections, that an IGES file as the one represented in Figure 67 is composed by several surface entities, as shown in Figure 68.

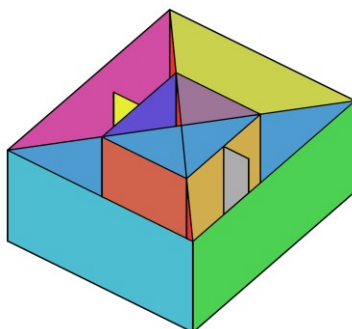


Figure 68 The several surfaces composing the input CAD model

It is important to point out this aspect since, due to this representation of the surfaces, the single entities composing the final CAD geometry are processed individually in the software, for both feature recognition and toolpath generation.

Since the developed CAM software is totally automated, it can also be embodied in an application without a graphic area to view the input part or CAD tools to modify it. For this reason, the input geometry must be modeled assuming that the origin of the CAD software frame of reference will be the same of the deposition path. The WAAM machine work offset will be accordingly adjusted.

In addition to the CAD model, the proposed CAM software requires further values to calculate the deposition toolpath:

- The Effective Wall Width (EWW).

As stated in several pieces of literature dealing with direct energy deposition techniques [3], two different values for the wall thickness can be identified: the Effective Wall Width (EWW) and the Total Wall Width (TWW). EWW is the maximum wall width after the finishing operations, achievable for a given set of welding parameters. TTW is the thickness of the wall just after the deposition, i.e. without any post processing. Figure 69 clarifies the distinction between TWW and EWW.

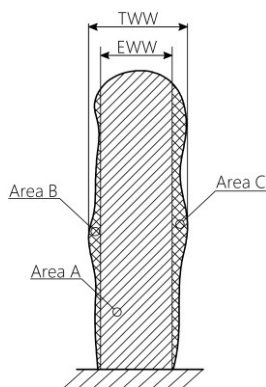


Figure 69 Definitions of Effective Wall Width and Total Wall Width. Adapted from [3].

As earlier mentioned, such values depend on the set of deposition parameters and must be determined by experiments, according to the procedure reported in [52]. It can be noticed that the most desirable condition is to achieve an TWW as close as possible to the EWW to maximize the deposition efficiency DE that is defined as depicted in Equation 49:

$$DE = \frac{AreaA}{AreaA + AreaB + AreaC} \quad \text{Equation 49}$$

- The value of the radius of the internal fillets of the crossings.
For the presented CAM software, it is assumed that all the internal fillets in the part have the same radius.
- The layer height (LH).
This input is used to perform the slicing operation, the starting point to obtain the toolpath from the input surfaces of the CAD model. The layer height depends on the weld bead height, which is related to the welding parameters. It can be determined through experiments in which several single beads and walls are built. The height of the single bead manufactured using a specific and repeatable set of welding parameters can be measured using a laser scanning device or a profilometer [46]. This procedure returns a first attempt value of LH. To achieve a more accurate estimation, a wall with a fixed number of layers can be manufactured using specific condition of interpass temperature. At the end of the manufacturing phase, an average LH value can be obtained by measuring the total wall height and dividing it by the number of deposited layers.
- The number of extra layers to be added (refer to section 2.3.1);
- The amount of the toolpath extension for the free end walls (refer to section 2.3.1).

3.3. Proposed toolpath generation framework: the feature recognition module

This section details the Feature Recognition Module, which is the first part of the workflow of the proposed CAM software. This first module also includes the slicing algorithm to obtain the deposition toolpath from the input surfaces.

After the input geometry has been imported in the CAM environment, it is decomposed in its basic entities as depicted in Figure 70. From a software point of view this means that every surface entity is extracted from the original input file and inserted in a list to be further processed in the next steps.

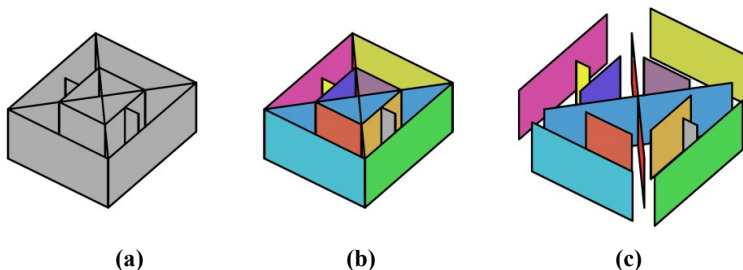


Figure 70 Input midsurface-only CAD model (a) and the several surfaces composing it (b and c)

The subsequent step is the slicing procedure of every single item in the list. To perform such operation a surface-to-surface intersection operation must be carried out. The intersection operation is performed between a plane with the normal oriented according to the building direction, i.e. the z-axis (0.0,0.0,1.0), and with a distance from the base plane equal to the layer height (determined by the user). The result of this step is a list of curves, each derived from a surface in the input IGES file. However, such list, called “First Layer Curve List”, represents the preliminary deposition toolpath for the first layer that will be further processed to obtain an optimized deposition strategy, especially in the zones of the crossings. All the operations of the Feature Recognition Module and Toolpath Calculation will be performed on such list. At the end, when the optimized toolpath has been generated for this list of curves, all the curves in the list itself are repeated in the Z direction a number of times equal to the height of the part divided by the layer height (the result is rounded to the closest higher integer). Then some extra layers (the number is an input) are added to assure the presence of some allowance material for machining.

The further step is the feature recognition procedure itself. In this skeleton representation, the crossing features are identified as points (Figure 71).



Figure 71 In the CAD skeleton representation, each crossing feature is represented with a point located in the intersection of the surfaces composing the feature itself

This stage identifies and classifies the central point of each different feature in the model. The proposed algorithm is based on the specifically developed features taxonomy, depicted in Table 11. First, every curve in the list is reparametrized to ensure that the curve parameter ranges from 0.0 to 1.0. At this stage, every curve of the list is intersected with all the other ones and the resultant points are stored in an array named “Intersection Strategy Array”. Then the end-points of every curve in the list (i.e. the points corresponding to a curve parameter value of 0.0 and 1.0) are extracted and stored into another array named “End-Points Strategy Array”. All the steps described up to this point are schematically outlined in the flowchart of Figure 72.

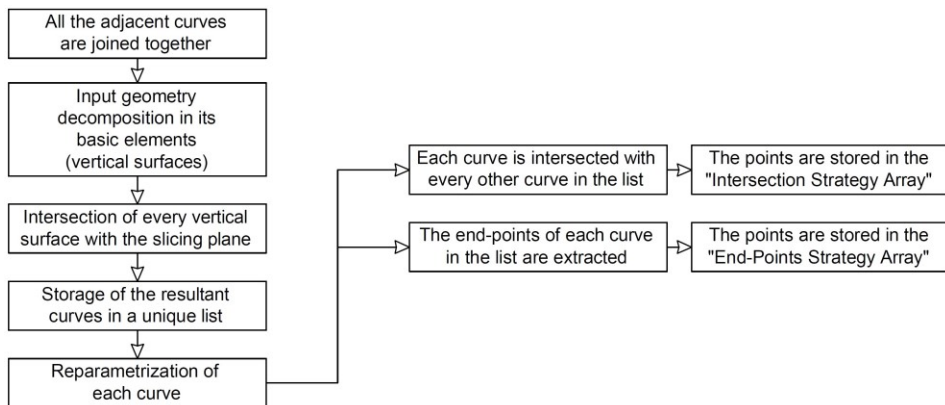
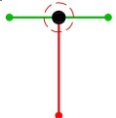
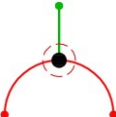
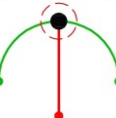

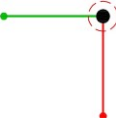
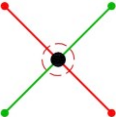
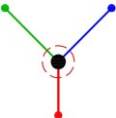
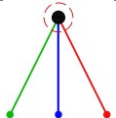
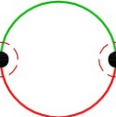
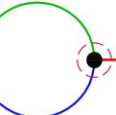


Figure 72: Flowchart explaining the procedure to obtain the “End-Points Strategy Array” and “Intersection Strategy Array”

When the procedure to extract the points terminates, the feature recognition algorithm starts. The base concept is that each crossing or feature is represented in the CAD space by a point. The result of the algorithm is hence an array of points in which every item represents the central point of a different crossing/feature and will be one of the inputs for the further toolpath calculation procedure. The first step to locate the features is to cull the eventual duplicate points in the “Intersection Strategy Array” and in the “End-Points Strategy Array”. The duplicated/triplicated points are identified as the array elements having a distant between each other below a given threshold value. In this paper, the threshold value was set to $1.0e-6$ mm. At the same time the number of occurrences of every deleted duplicated point (i.e. the valence) is stored in another array, respectively one for the “Intersection Strategy Array” array called “Intersection Valence Array” and one for the “End-Points Strategy Array” array called “End-Points Valence Array”. This means that if there are three equal points in the array only the first one is kept and the number “Three” is stored in the valence array. Therefore, the elements of the strategy and valence arrays have a one-to-one relation: the former contains the point coordinates while the latter contains the number of occurrences in the original strategy array.

Table 11 The Intersection Taxonomy developed by the authors on which the Feature Recognition procedure is based

Intersection Topology	“Valence for Intersection”	“Valence for End Points”	Conventional Name of Feature	Entities
	2	1	Straight T-Crossing	2
	2	1	Open T-Crossing	2
	2	1	Closed T-Crossing	2
	0	1	Free End Wall	1
	2	2	Corner Junction	2
	1	0	Direct Crossing	2
	6	3	Open T-Crossing	3
	6	3	Closed T-Crossing	3
	2	2	Continuous Junction	2
	6	3	Odd T-Crossing	3

The first of the further steps is the detection of the points with valence equal to two in the “End Points Array”. Indeed, referring to the taxonomy of Table 11, such points represent two adjacent walls or a simple sharp corner. Therefore, they are not a critical feature since they can be deposited using a continuous toolpath along the curves obtained directly from the slicing procedure. However, to enable the user to check the correct functionality of the software, the implementation presented highlights such points with a small red sphere in the graphic area, as shown in Figure 73.

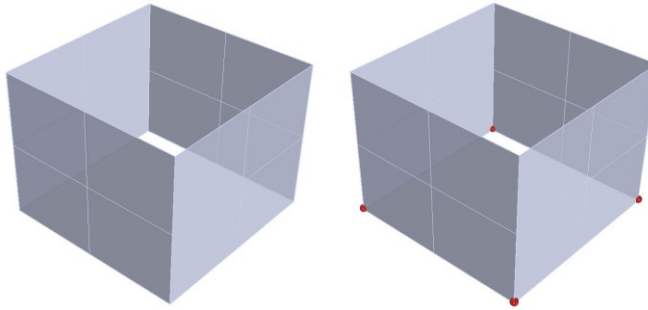


Figure 73 The small red spheres highlight a continuous junction between two adjacent walls

To identify the “Free End Wall” features, it is necessary to compare the two valence arrays, since the points representing such feature appear only once in the “End Points Strategy Array” but do not appear at all in the “Intersection Strategy Array”. Once that such points are detected, they are stored in another array, i.e. the “End-Wall Array”. Despite the “Free End Wall” might not seem a critical feature, it is important to locate them since, as highlighted by previous works [53], a deposition defect is present at both ends of such features, as shown in Figure 74.

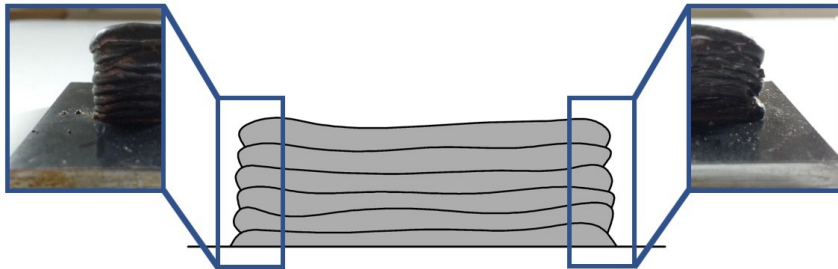


Figure 74 Defects at the ends of a WAAM-manufactured wall

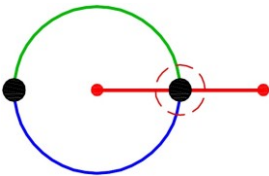
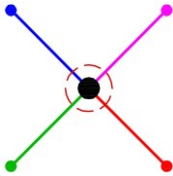
To prevent this issue to affect the quality of the final workpiece, the toolpath must be extended with respect to the wall length, enabling to remove the defective regions during the milling phase.

At this stage, the already detected free end walls, the continuous junctions and all the points appearing only once in the “End Points Strategy Array” are erased from the array itself that will now contain only the points with a valence equal to three; therefore, referring to Table 11, these points represent “Open T-crossing”, “Closed T-Crossing” or “Odd T-Crossing” features. These points are stored in a dedicated array. The detection of the “Direct crossing” features is performed using a similar procedure to the one presented for the free end walls, i.e.

comparing the “End Points Strategy Array” and “Intersection Strategy Array” arrays. That is because a direct crossing appears only once in the “Intersection Strategy Array” but is not present at all in the end points one. For the straight T-Crossing the procedure is slightly different. Indeed, it is necessary to consider the original “End Point Strategy Array” and eliminate from this the already detected points representing the continuous junctions, Open/Closed T-Crossings and Free End Walls. The points that remain in the array represent the straight T-Crossings.

Finally, there is a further case, here referred to as “Odd Direct Crossings”, that must be considered to obtain a comprehensive feature recognition. The “Odd Direct Crossings” are presented in Table 12. Such features would not be identified by the recognition strategy presented so far since the points representing them would be confused with the Continuous Junction. To detect these additional cases, it is necessary to create an array containing the points of the “Intersection Strategy Array” with valence six and an array with the points of the “End-Points Strategy Array” with valence two. Referring to Table 11 and to Table 12, it is possible to detect the points representing the “Odd Direct Crossings” and “Odd T-Crossings” by comparing the two resultant arrays. In Table 12 another case is also reported; this is the “Four Direct Crossings” feature, composed of a respective number of entities (i.e. four vertical surfaces). To detect such feature, it is necessary to look for the points with valence 12 (Direct Crossing) in the “Intersection Strategy Array”.

Table 12 Odd Direct-Crossing and Odd T-Crossing topology

Intersection Topology	Valence For “Intersection Between Curves”	Valence For “End Points”	Conventional Name of the Feature	Entities
	6	2	Odd Direct Crossing	3
	12	4	Four Direct Crossing	4

The outcome of this recognition phase is a series of arrays for each type of feature. These arrays contain the central point of the features themselves. It is hence possible to use a color coding system to highlight the different features in the graphic area of the CAM software to advise the user whether every feature has been detected by the software. The result of this operation is exemplified in Figure 75.

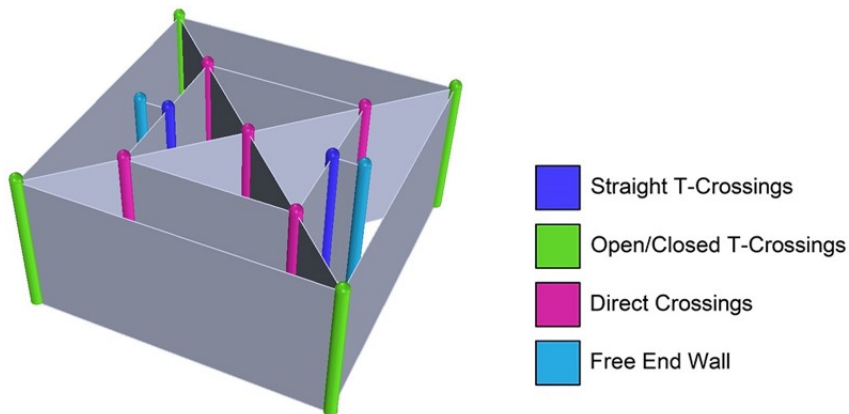


Figure 75 Result of the feature recognition procedure: every different feature is highlighted using a different colour.

To conclude the description of the feature recognition module a further step is needed to address situations such as the one presented in Figure 76, where two separated parts are built on the same substrate.

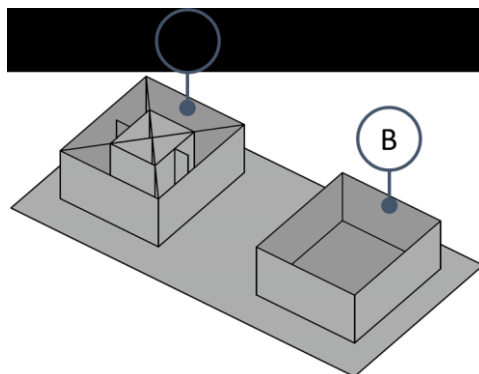
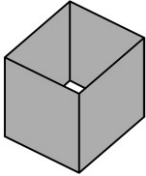
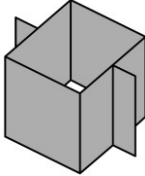
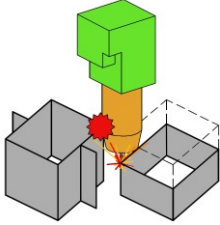
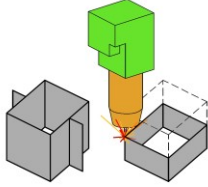


Figure 76 A connected shape (A) and an isolated tubular (B)

Figure 76 highlights that the part A has a complicated geometry which requires features recognition to achieve an optimal toolpath. On the opposite, the part B is a tubular shape without any crossings. It could be hence built by using a helical deposition strategy, i.e. generating a toolpath which is a helix-like curve having a base profile shaped as the tubular cross section and a pitch equal to the layer height. The next section clarifies that the helical strategy is the best suited to create tubular shapes. However, the helical approach can be applied only if no collisions between the different parts present on the substrate occur during the manufacturing procedure. Table 13 clarifies the concept of “isolated tubular”.

Table 13 Topology of isolated tubulars

Case 1	Case 2	Case 3	Case 4
			
The tubular is alone on the building plate: the tubular is “isolated”	The tubular is connected to other geometries: the tubular is “NOT isolated”	During the building of the tubular a collision happens between the torch and an already existing part: the tubular is “NOT isolated”	During the building of the tubular no collisions happen between the torch and an already existing part: the tubular is “isolated”

From a software perspective, to know whether an isolated tubular is present or not in the build plane (i.e. in the input geometry) the Feature Recognition Module of the CAM software acts as explained in the following lines and in Figure 77. The starting point is the “First Layer Curve List” containing all the curves resultant from the slicing procedure. Every curve in the list undergoes a test to understand if it is closed; if a curve is closed, it is stored in an array called “Closed Curve Array” and deleted from the “First Layer Curve List”, otherwise the software goes to the next curve. All the end-points of the curve remained in the “First Layer Curve List” are extracted and stored in a “End-Points Array”.

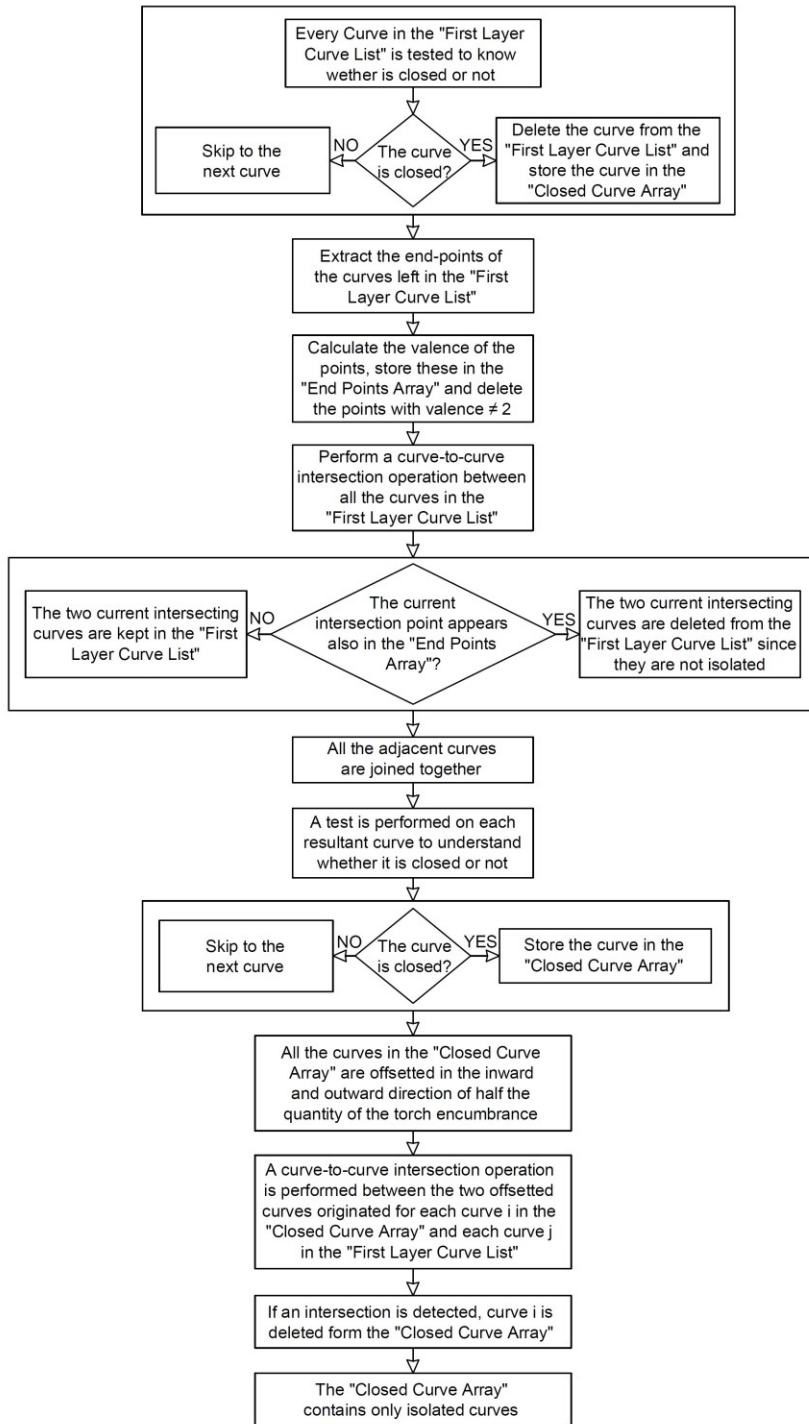


Figure 77 Flowchart of the algorithm developed to detect isolated tubulars

The valence of each point (i.e. how many times the same point appears in the array) is calculated and only the points with valence two (i.e. the points pinpointing the continuous junctions referring to Table 11) are kept in the array. Then, a curve-to-curve intersection operation is performed between each curve remained in the “First Layer Curve List” and all the other ones in the array: each time an intersection point is found it is compared with the points with valence two; if the detected intersection point appears also in the array of the points with valence two, the considered curve and the curve intersecting it are kept because there is a continuous junction between these, otherwise the curve are deleted from the array because it means that they are not isolated. At the end of the curve-to-curve intersection operation all the sets of adjacent curves in the “First Layer Curve List” are joined together. Another test is carried out to detect if there are other closed curves after the joining operation; if the test identifies further closed curves, these are stored in the “Closed Curve Array”. This way all the isolated closed curve (i.e. every base curve of a tubular-shape part) are detected. Now it is important to understand if it is possible to use a helical strategy to build the part. Of course, if such strategy is used, the parts in the building plate are not created all together layer by layer: the tubular parts are built prior or subsequently to the other ones. This is only possible if no collision occurs between the torch and other parts in the building plate, because the separate deposition of the tubular part could lead to collisions between the torch and the already manufactured parts. To detect the presence of possible collisions, a further step is needed: the isolated curve stored in the “Closed Curve Array” are offset in the inward and outward direction of half the quantity of the maximum encumbrance of the torch; then, a reciprocal curve-to-curve intersection operation is performed between the offset curves originated from the curve i in the “Closed Curve Array” and all the other original curves that are present in the same “First Layer Curve List”. If any intersection is detected it means that the tubular related to the curve with index i cannot be built separately from the other parts using an helical strategy, but must be built in layer-wise to avoid collisions. For this reason, it is deleted from the “Closed Curve Array” (Figure 78).

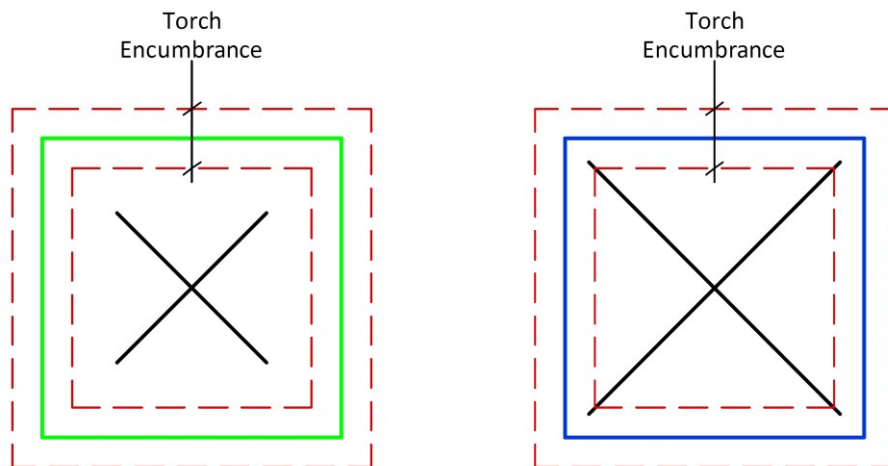


Figure 78 Example of isolated tubular (left, green) and not isolated tubular (right, blue)

3.4. Proposed toolpath generation framework: a deposition strategy for each feature

At this stage of the workflow, the software has generated: i) a preliminary deposition toolpath for the very first layer ii) a series of points subdivided according to the kind of feature they represent iii) a list of isolated curves representing the tubular features that can be built using a helical strategy. The software must now calculate the deposition toolpath specific for every kind of feature. The different deposition strategies implemented in the proposed CAM software are either taken from literature or developed by the author. This section presents and details the deposition strategies available for every different feature together with some experimental results to highlight their effectiveness.

3.4.1. Deposition strategies for direct crossings

Several literature works presented deposition strategies for Direct crossings. For example, Ugla et al [54] and Mehnen et al [55] presented deposition strategies developed and tested specifically for the WAAM process, hence suitable for the implementation in the proposed CAM software. The most relevant deposition strategies for Direct Crossings developed in the aforementioned papers are presented in Figure 79.

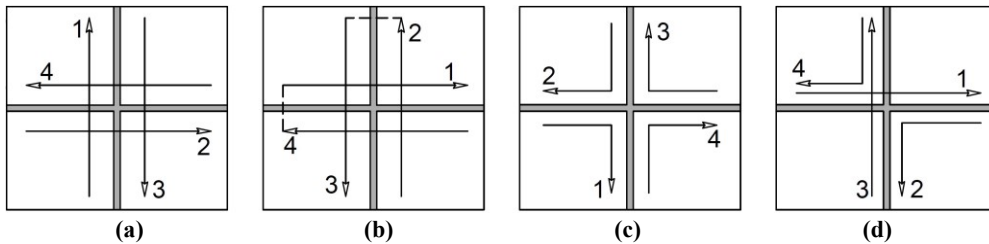


Figure 79 Deposition strategies for Direct Crossings (a) and (c) from [55] (b) and (d) from [54].

Despite their effectiveness, all these strategies require each bead of the direct crossing to be deposited in a specific sense. The implementation of such strategies is hence straightforward only in the case of a single crossing. When dealing with complex workpieces which include many crossing features, using this approach would result in significant complications in the implementation phase. Moreover, the deposition sense constraint could lead to an impossible solution in joining multiple features. Since the goal of the CAM software is to deal with actual components, a deposition strategy for Direct Crossings able to overcome the issues of the literature ones has been developed. The proposed strategy is depicted in Figure 80.

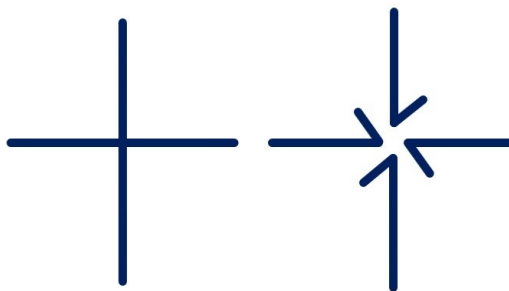


Figure 80 The deposition strategy for Direct Crossings developed by the Authors. Original curves resulting from slicing operation (left) and toolpath for the direct crossing after processing (right)

From a software point of view the toolpath for this deposition strategy can be obtained with the four steps described in Figure 81.

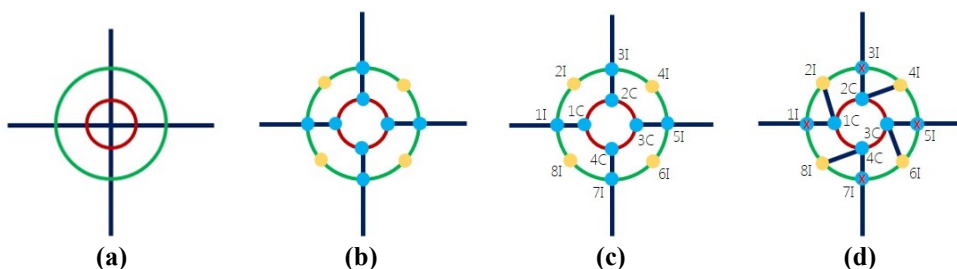


Figure 81 The procedure to calculate the toolpath for the direct crossing implemented in the proposed CAM software

Referring to Figure 81, the deposition toolpath of a direct crossing is performed following the depicted steps:

- Two circumferences centered in the point resulting from the feature recognition step are generated; the inner one is called “Cutting Circle” and it is represented in red in Figure 81 (a); the outer one is called “Influence Circle” and is represented in green;
- The Cutting Circle is tested for intersection with all the curves of the “First Layer Curve List” and only the curves that intersect the circle itself are stored in a dedicated “Direct Crossing Curve Array”. Moreover, the intersection points (cyan marks in Figure 81 (b)) are stored in a dedicated “Cutting Circle Intersections Array”;
- The same operation is performed for the Influence Circle. The intersecting curves are the same that are already stored in the “Direct Crossing Curve Array”; on the opposite, the intersection points are different and are stored in an array called “Influence Circle Intersections Array”;
- Four different arcs are obtained from the Influence Circle by splitting it at the points of the “Influence Circle Intersections Array”, which are stored in the “Quarter Influence Circle Array”. The midpoint of each of the four arcs is then calculated and stored in a new “Influence Circle Midpoints Array” (yellow marks in Figure 81 (b));

- The two curves composing the Direct Crossing are split at the points contained in the “Cutting Circle Intersections Array” and the portions of the curves included in the Cutting Circle are deleted. To detect such curves portions the midpoints of each of the curves obtained after the splitting operations are calculated and then tested for inclusion with respect to the Cutting Circle: if a midpoint is inside the Cutting Circle the correspondent curve portion is deleted (Figure 81 (b));
- The points in the “Cutting Circle Intersections Array” are ordered in a clockwise manner (Figure 81 (c));
- The points in the “Influence Circle Intersections Array” and in the “Influence Circle Midpoints Array” are all stored in a new array called “Influence Circle Toolpath Points Array” and ordered clockwise (Figure 81 (c)); it is important that the first point of the “Influence Circle Toolpath Points Array” and of the “Cutting Circle Intersections Array” lay on the same curve of the Direct Crossing as depicted in Figure 81 (c);
- A line is generated between the first point in the “Cutting Circle Intersections Array” and the second point of the “Influence Circle Toolpath Points Array” (Figure 81 (d)): such line is the first additional toolpath segment to depose the extra material needed for the internal fillet of the Direct Crossing. This procedure is repeated until all the four additional segments have been generated.
- The additional segments are joined to the respective original segments of the Direct Crossing and the “First Layer Curve List” is updated.

It is important to highlight that the proposed strategy does not require any of the crossing beads to be deposited in a specific sense. Two important parameters to achieve a defect free deposition, i.e. with no voids embedded in core of the crossing are the radii of the influence and cutting circles. Figure 82 outlines the theoretical minimum values of such parameters.

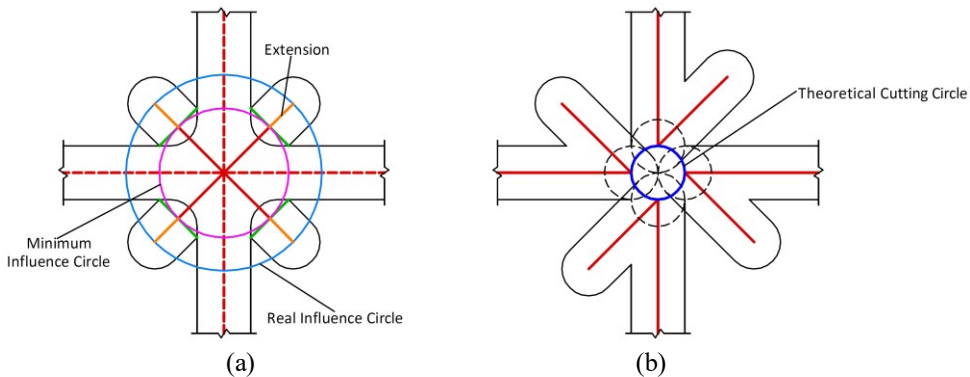


Figure 82: Minimum value of the influence (a) and cutting (b) circle radii.

For what concerns the influence circle radius (Figure 82 (a)): given the skeleton surface of the crossings, the influence circle should be tangent to the four segments (one per each of the crossing branches) perpendicular to the skeleton line and having a length equal to the bead width (green lines in Figure 82 (a)). This results in the minimum influence circle marked by the pink line in Figure 82 (a). However, it is safer to extend the influence circle to locate the

arc start/stop further from the core of the crossing, i.e. in a zone which is removed during the subsequent machining (cyan line in Figure 82 (a)).

Regarding the cutting circle (Figure 82 (b)), its theoretical maximum size is defined as follows: given the four circles (one for each branch of the crossing) with diameter equal to the bead width, centered on the branches and tangent between each other (dashed black lines in Figure 82 (b)), the cutting circle (solid blue line in Figure 82 (b)) should intersect the centers of such four entities. However, to improve the quality of the crossing it is better to decrease such value since an excessively large cutting circle could lead to the formation of a void in the center of the crossing.

Considering the presented discussion, the theoretical values provide must be tested and tuned by performing experiments. In this paper, different combination of influence and cutting circle radii were tested on a sample direct crossing. All the parts manufactured during the present activity have been created using a commercial GMAW machine (AWELCO 250 PULSEMIG), which torch has been fitted on a three-axis milling machine with a dedicated clamp. A unique welding parameter set has been used for all the experiments and it is reported in Table 14.

Table 14 Process parameters used for the experiments

Current [A]	Voltage [V]	Deposition Speed [mm/min]	Wire Feed Speed [m/min]
80	18	300	4.6

The results for different values of such parameters are reported in Figure 83.




Test 1	Test 2	Test 3
		
Influence Circle R: 7.0 mm Cutting Circle R: 2.5 mm	Influence Circle R: 8.0 mm Cutting Circle R: 2.0 mm	Influence Circle R: 10.0 mm Cutting Circle R: 2.0 mm

Figure 83 Some results of the sample direct crossings manufactured to show the importance of the values of the influence and cutting radii

Test 1 was performed using the theoretical radii. It is highlighted that the crossing show both a void in the central zone and a lack of material in the fillet areas. Test 2 and 3 are performed by reducing the cutting circle radius and increasing the influence circle one. The parameters of Test 2 enabled to eliminate the central void but did not resulted in enough

material for the fillets. Test 3 produced the best results, eliminating the void and providing enough machining allowance for the fillets.

3.4.2. T-crossings: deposition strategies with specific deposition directions

For what concerns the deposition strategies for the T-crossing features, since no available solutions were found in literature, two approaches have been pursued during the research activity: the outcome of the first approach are some deposition strategies in which the bead must be deposited in specific directions, while the outcome of the second one is a deposition strategy in which the deposition direction of the beads has no influence. The results of the second approach in terms of simplicity of the deposition toolpath taxonomy and easiness of software implementation are much more promising respect to the ones of the first approach. This because, as already explained in the case of the direct crossings, the implementation of strategies requiring a specific deposition senses of the beads is straightforward only in the case of a single feature. In the case of workpieces which include many crossing features the deposition sense constraint could lead to an impossible solution in joining the multiple features. However, since the implementation and testing of the strategies developed with the first approach achieved very good result in terms of geometrical accuracy of the manufactured parts, these are reported and described in this chapter. Before dealing with the deposition strategies, it is necessary to examine the taxonomy of a T-Crossing through Figure 84.

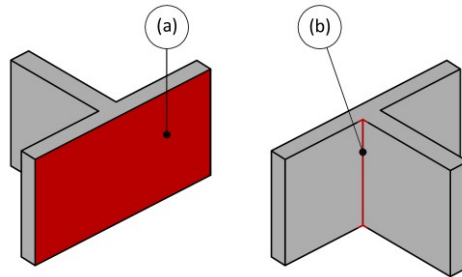


Figure 84 Taxonomy for T-Crossing. (a) back surface, (b) internal corner

Moreover, it is important to remember that the parts manufactured using WAAM must be post-machined to match the required surface finish. Regarding T-Crossings, the most relevant issues for post machining could be the internal corners, since these are not accessible using an end mill (Figure 85). So, creating toolpaths that reshape these zones through the addition of fillets could improve the accessibility of the corners and make the toolpath much more fluent.

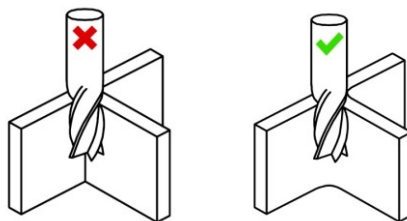


Figure 85 A T-crossing with sharp internal corners cannot be accessed from the top with an end mill (left), while a T-crossing with fillets or extra material in the internal corners can be easily post-machined using a simple end mill (right)

Six different deposition strategies, shown in Figure 86, have been developed and compared. Moreover, many specimens have been built using the developed deposition strategies.

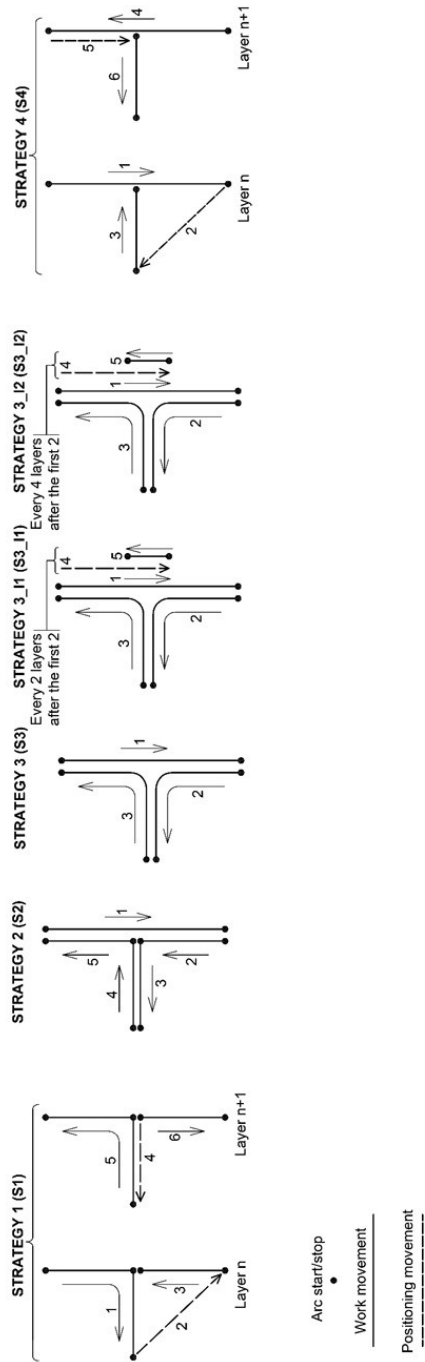


Figure 86 The six developed deposition strategies

All the six strategies have been tested using the same welding parameters. Referring to Figure 86, it is noticeable that all the strategies take into account the compensation of the different conformation of the end and start portions of the weld bead: for every new weld bead, the arc starts in the same points where another bead has ended. Strategies S3, S3_I1 and S3_I2 feature fillets in the toolpath for the internal corners. The value for the radius of the fillet has been chosen looking at the width of the weld bead generated by the used welding parameters in order to have a sufficient amount of overlap in the central zone of the T-Crossing. Given the width of the bead, the value of the radius R can be found graphically (Figure 87).

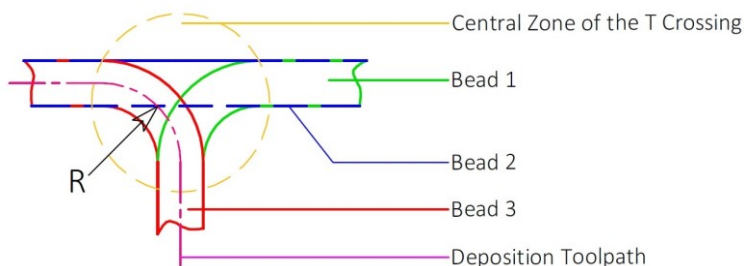


Figure 87 Graphical determination of the radius of the fillet for the toolpath of the S3, S3_I1, S3_I2 strategies

The presence of the fillet in the toolpath is also useful to obtain a smooth and continuous toolpath and to reduce the number of start/stop phases and sharp corners. This will result in a spatter reduction. For each strategy 18 layers (with a layer height of 1.5 mm) have been deposited and two parts have been built. Every two layers a pause of 70 seconds was inserted to allow for cooling of the part and measure the height of the already deposited material. To compare and evaluate the different strategies, five different parameters have been considered:

- The difference D (calculated every two layers) between the height of the central point C and the average heights of the points shown in Figure 88 and named $A1$, $A2$, $B1$, $B2$, $L1$ and $L2$ that are far enough both from the central zone and from the ends of the branches of the T-Crossing.

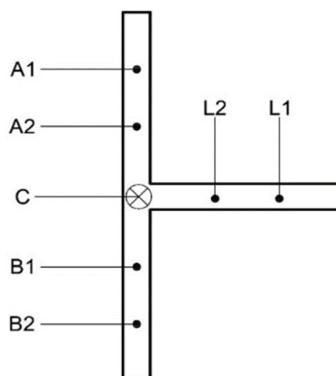


Figure 88 A T-Crossing feature seen from the top. The points were the measurements have been taken during the building procedure are shown.

Also referring to Figure 88, the parameter D can be defined using Equation 50:

$$D = C - \frac{A1 + A2 + B1 + B2 + L1 + L2}{6} \quad \text{Equation 50}$$

- The presence or absence of fillets in the internal corners;
- Flatness of the back surface. To maximize the deposition efficiency, it is important to achieve a back surface as flat as possible. So, an error parameter to evaluate the difference between the real surface and the ideal one is considered. The T-crossing built for the presented research activity have been hosted on a substrate of 150x150 mm that makes those easily and accurately measurable in a Coordinate Measurement Machine (CMM); this will allow for the determination of the flatness of the back surfaces of the manufactured T-Crossings.
- The ratio R between the deposition toolpath length and the total toolpath length (that includes also the repositioning movements). Generally speaking, WAAM is economically interesting especially for large parts, therefore it is important to limit the positioning movements between a bead and the next one, thus reducing the production time and therefore the total manufacturing cost. To evaluate the developed strategies also from this point of view, Equation 51 has been used:

$$R = \frac{\text{active toolpath length}}{\text{total toolpath length}} \quad \text{Equation 51}$$

Therefore, a deposition pattern will be as much time-effective (and so cost-effective) as much the R value will be high.

- The number of start/stop phases. It is important to reduce the number of start/stop phases since these are often cause of spatter and defects.

The deposition strategies have been tested using the Roland Modela MDX40 retrofitted machine presented in section 1.3. At that time a Millermatic 300 welding power source was installed on the machine. The material used to manufacture the specimens is a 0.8 mm diameter AWS ER70S-6 wire. The shielding gas was composed by 82% Ar and 18% CO₂. The substrates were steel plates of 150x150 mm, 12 mm thick made of S245JR steel. The used welding parameters are reported in Table 15.

Table 15 The welding parameters used to test the deposition strategies for the T-Crossings

Parameter	Value
Voltage	19 V
Wire Feed Speed	4.6 m/min
Feed	300 mm/min
Nozzle to work distance	15 mm

During the building process, measurements were taken every two layers during the 70 seconds dwells. The measurements were taken to monitor the relative growth between the

central zone and the zones far from the intersection of the three branches composing the T-Crossing.

After the build procedure was completed, the parts have been cleaned up using a steel brush. First of all, a visual analysis of the specimens revealed that the T-Crossing build with the S3 strategy showed a dramatic deposition failure in the central zone (Figure 89) that inevitably causes an unacceptable drop in the deposition efficiency making S3 strategy not suitable for building T-Crossing features.



Figure 89 The big deposition failure (pointed by the red arrow) in one of the specimens manufactured using the S3 deposition strategy

The visual analysis also confirmed that the central zone of the back surface is one of the most critical ones; indeed, for some strategies, it shows a depression that drastically reduces the deposition efficiency, since will be necessary to machine away much more material to obtain a flat surface (Figure 90 and Figure 91).

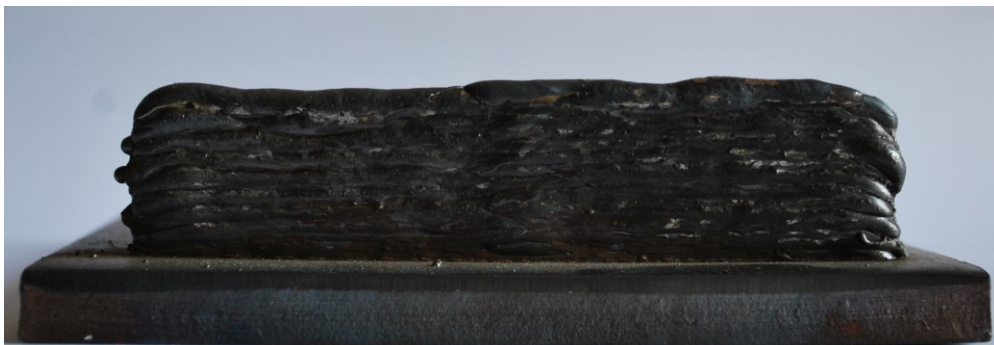


Figure 90 A back surface of a T-Crossing with high flatness

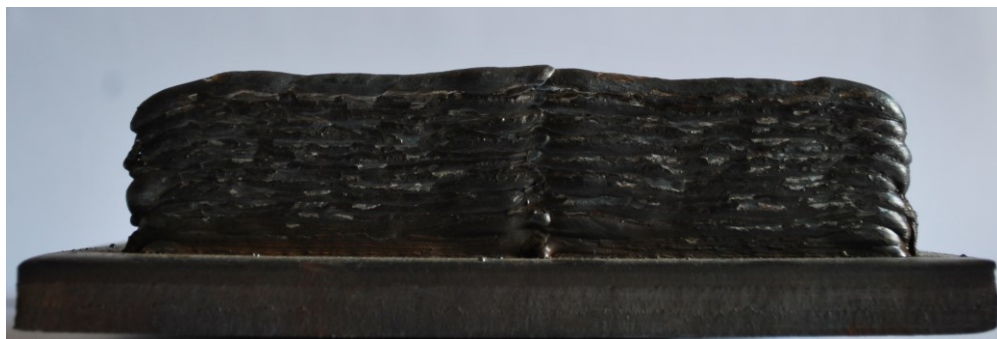


Figure 91 The back surface of a T-Crossing with a small depression in the central zone due to the used deposition strategy

The chart of Figure 92 shows the difference D between the height of the C point and the average height of the zones far from the central point every two layers.

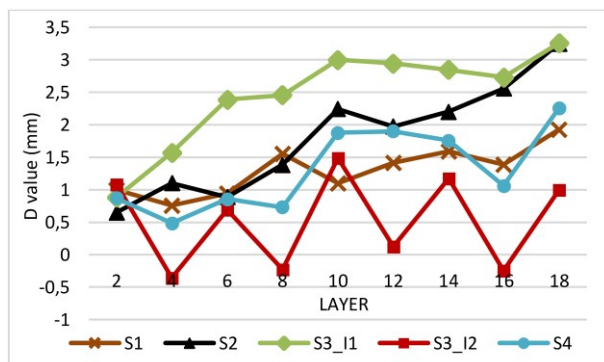


Figure 92 The difference between the height of the C point and the average height of the zones of the T-Crossing far from the central one.

The bar plots shown respectively in Figure 93 and in Figure 94 shows the trends of the best fit line for the data of Figure 92 and the average value of the parameter D across the 18 layers. It is noticeable that strategy S3_I2 achieves the best performance since the low slope of the best fit line reveals that the height of the central point is very close to the height of the other zones in every moment of the building procedure. Moreover, the average value of the D parameter is very small if compared to the other strategies and this means that the height of the central point of the T-Crossing is always very close to the one of the other zones. This aspect is very important for the stability of the deposition process: if the height of the C point would gradually increase too much, the effective distance between the torch and the part would vary leading to severe arc instability.

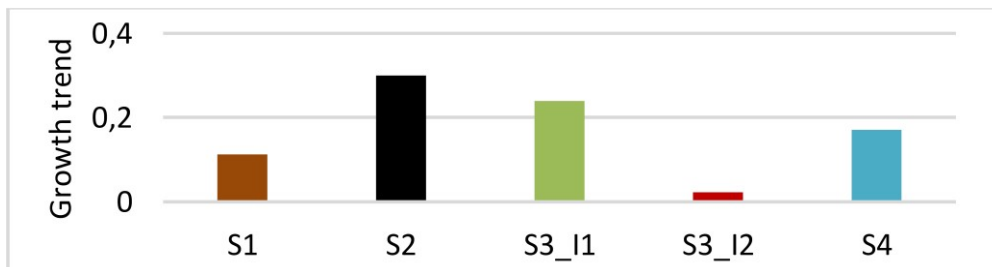


Figure 93 Slope of the best fit line for the data of Figure 92

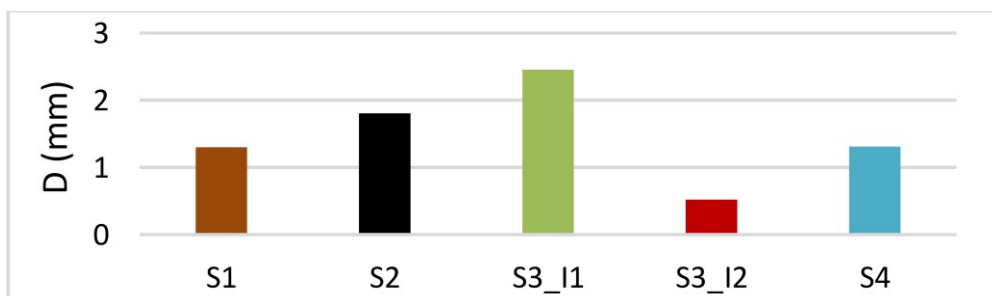


Figure 94 Average value of the D parameter

The back surfaces of the T-Crossings were acquired using a CMM (Mitutoyo Euro-C A776) (Figure 95).



Figure 95 The acquisition of the back surface of one of the manufactured specimens in the CMM machine

As showed by Figure 96, the back surface of each specimen has been acquired for a length of 65 mm including the most critical zone that is the one immediately behind the intersection. The touch probe of the CMM followed eight scanning lines spaced 2 mm one from the other. The acquired points in each line are spaced 0.5 mm.

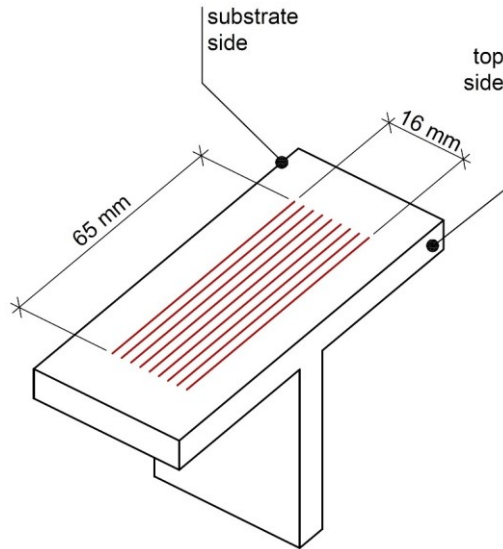


Figure 96 The scanning scheme used to acquire the back surface of the T-Crossings using the CMM machine

The data acquired with the CMM have been processed using the MATLAB software to plot the resultant 3D surface for each of the specimens. An example of the acquired profiles for a specimen manufactured using the S3_I2 strategy is reported in Figure 97.

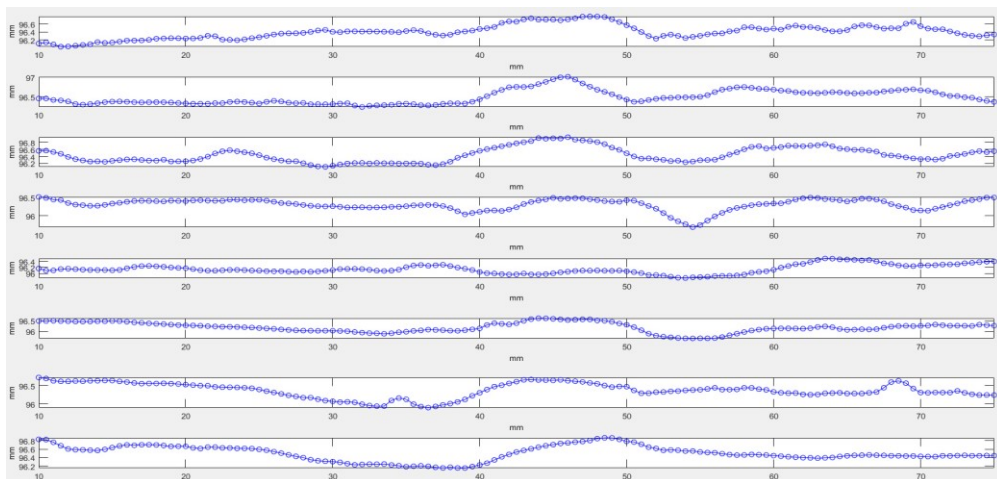


Figure 97 The eight acquired profiles for a specimen manufactured using the S3_I2 strategy

For every different strategy, a best fit plane has been extracted considering only the points far from the central zone (Figure 98).

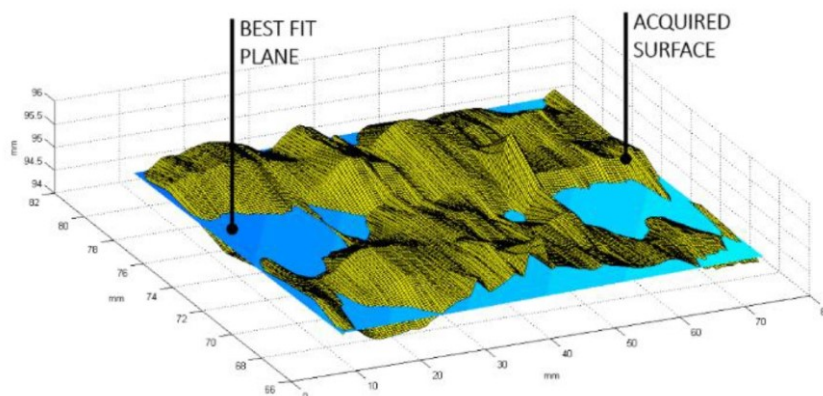


Figure 98 The surface constructed using the points acquired with the CMM machine and the best fit plane for a specimen manufactured using strategy S4

The differences between the obtained best fit planes and the points of the central zone have been calculated. Of course, only the positive results are interesting from a deposition efficiency point of view, since these are related to the total amount of material that must be removed from the back surface (deeper the depression in the central zone bigger the overall volume to be removed from the back surface of the T-Crossing). The norm of the array containing all the positive differences is the parameter used to evaluate the quality of the back surface and it is named “back surface error” and reported in Table 16.

Table 16 Back surface error for the proposed deposition strategies

Strategy	Back Surface Error
S1	1.60
S2	2.12
S3	-
S3_I1	0.74
S3_I2	2.07
S4	1.16

Finally, the number of start/stop phases is reported in Table 17.

Table 17 The number of start/stop phases for each deposition strategy

Strategy	No of start/stop phases
S1	54
S2	45
S3	-
S3_I1	36
S3_I2	32
S4	36

Looking at all the presented data, even if it not achieves the best performance in terms of back surface flatness, the S3_I2 strategy appears to be the best compromise between deposition efficiency, deposition time and process stability. Indeed, strategy S3_I2 achieves the best results in terms of start/stop phases and shows an acceptable R value. A T-Crossing built with the S3_I2 strategy is reported in Figure 99.

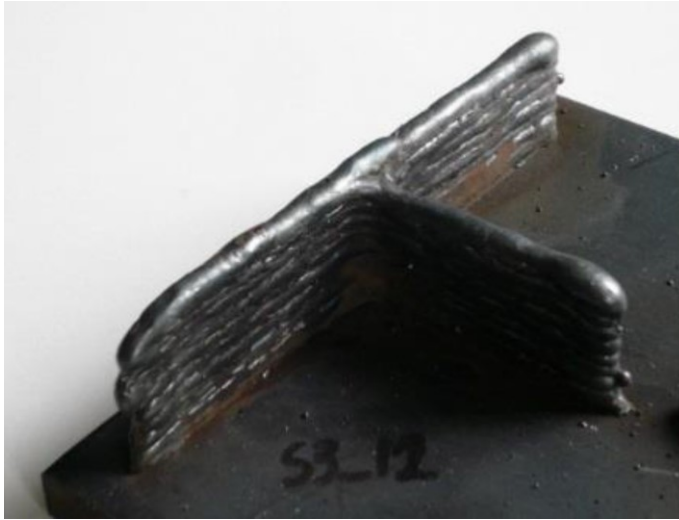


Figure 99 A T-Crossing built using the S3_I2 strategy

3.4.3. T-crossings: deposition strategies without specific deposition senses

Even if the deposition strategies presented in the previous section achieve a very good result in terms of geometrical accuracy, these would require depositing the beads in a specific sense, complicating the software implementation or not resulting in a feasible path. To overcome this issue, another deposition strategy for the T-Crossings has been developed and implemented in the toolpath generation module. Such strategy is very similar to the one developed for the direct crossings and it is depicted in Figure 100.



Figure 100 The new deposition strategy proposed by the Authors for T-Crossings. The original curves from the “First Layer Curve List” (left) and the toolpath optimized for the T Crossing (right)

Since the software procedure to obtain this deposition toolpath is totally similar to the one proposed for the direct crossings, it is possible to refer to section 3.4.1 for details.

3.4.4. Deposition strategy for free end walls

As previously stated in the thesis, it is important to extend the deposition toolpath in the zone of the free end walls to ensure an adequate machining allowance for the finishing operations. This is because arc ignition and extinguishing regions have an irregular geometry and can be affected by lack of fusion defects. Figure 101 shows an example of toolpath extension. The value of the linear extension depends on the welding parameters and can be experimentally determined by measuring the defective zones to be removed depicted in Figure 74.

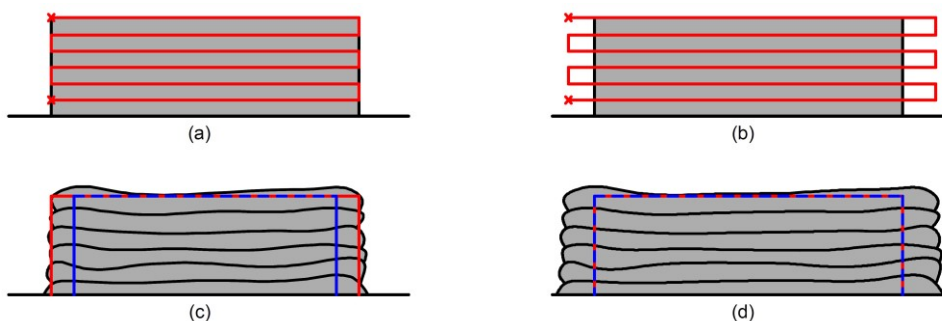


Figure 101 The importance of toolpath extensions for free end walls for a straight wall (a) toolpath with no extensions, (b) toolpath with extensions, (c) expected result (red) and effective result (red) in the no-extensions case, (d) expected result (red) and effective result (blue) in the case of a toolpath with extensions

3.4.5. Deposition strategies for tubulars

The goal of implementing tubular deposition strategies is to prevent the arc ignition and extinguishing defects to affect the flatness of the top surface [55]. Indeed, the region of the layer close to the arc ignition exhibits an excessive thickness with respect to its central part, due to the heat sink effect of the base metal. On the opposite, in the arc extinguishing region, the layer exhibits a reduced thickness due to the arc pressure on the molten pool. Therefore, if a tubular shape is deposited by igniting and extinguishing the arc in the same point for each layer, a deposition defect will be present on the top surface. To overcome these issues, three strategies are proposed: two of them use a layer by layer approach, while the other one uses a helical deposition strategy. Figure 102 depicts these strategies by showing an example of a tubular with circular cross section (i.e. a cylinder).

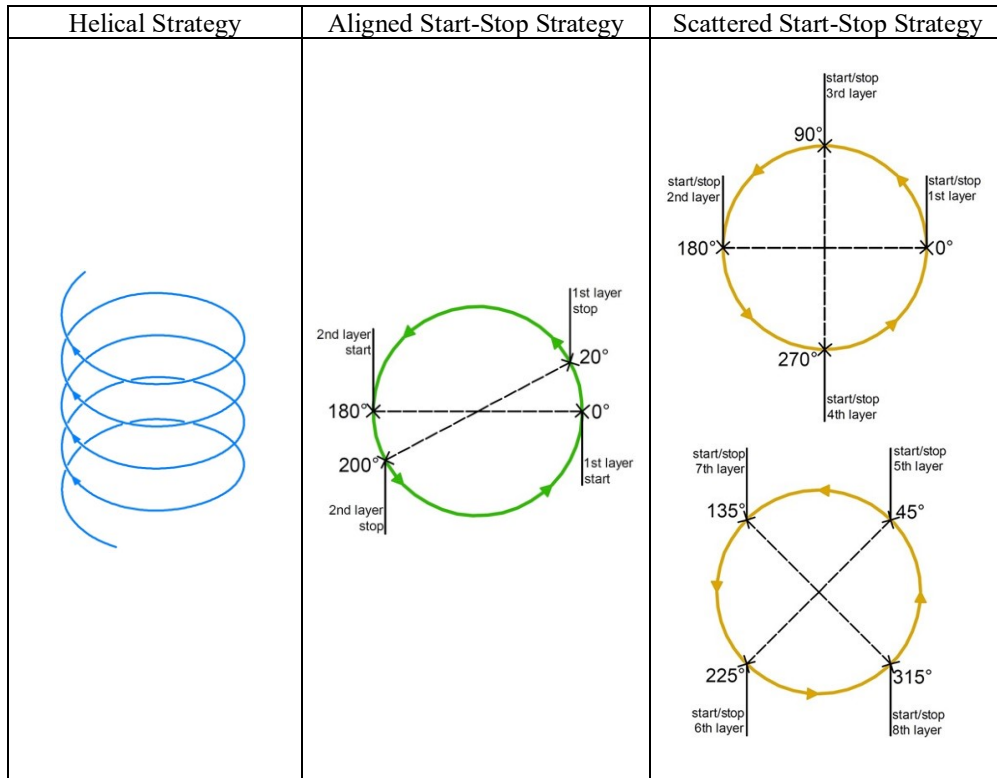


Figure 102 Deposition strategies for tubulars

The helical strategy is basically a continuous deposition pattern, which avoids inter-layer arc ignition and extinguishing. The aligned start-stop strategy aims at compensating for the defect by introducing a self-overlap of the layer in the stop region. This way, the overlapping compensates for the lack of material in the extinguishing region. The overlapping angle depends on the radius of the cylinder and can be calculated referring to Figure 103 and Equation 52.

$$\theta = \frac{O_l}{R}$$

Equation 52

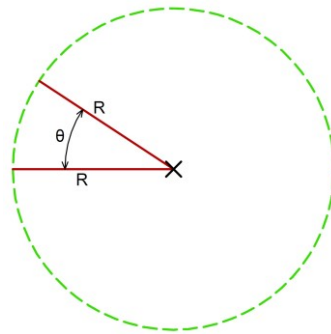


Figure 103 Overlapping angle concept for Aligned Deposition Strategy

Finally, the scattered start-stop strategy distributes the start and stop points along the cross section. This aims at preventing an excessive accumulation of defects in a specific point. The effectiveness of such strategies was compared by manufacturing cylindrical tubulars using the three different approaches. The results were compared in terms of flatness of the top surface of the cylinder, i.e. by measuring its distance from the substrate in different points and analyzing the punctual deviation from the average height value. Figure 104 presents the results of such comparison, while Figure 105. shows the top surfaces of the tubulars manufactured using the three presented deposition strategies.

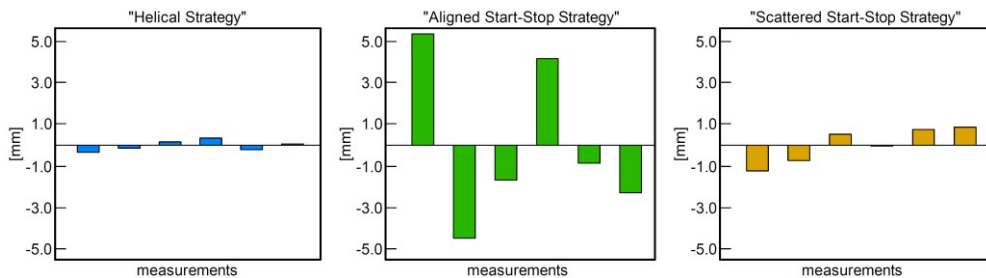


Figure 104 Difference between the mean height and six measurements taken along the cylinder circumference to compare the different deposition strategies



Figure 105 Top surfaces for three different tubulars manufactured with the three presented deposition strategies

It is highlighted that the “Helical Strategy” and the “Scattered Start-Stop Strategy” achieve the best results. Hence, these are the strategies implemented in the CAM software to deposit the tubular shapes. Using the layer by layer strategy (i.e. the “Scattered Start-Stop Strategy”) is mandatory in case of potential collisions when building multiple parts on the same substrate. However, it should be avoided as much as possible since, as shown by Figure 104, it results in a reduced flatness with respect to the helical pattern. Moreover, it leads to many arc ignition phases, an always critical operation in WAAM since the arc could sometimes not ignite, compromising the manufacturing of the part. However, a layer-by-layer approach could be necessary to introduce interlayer idle times to prevent the heat accumulation phenomenon. In this case a helical strategy would not offer any advantage respect to a layer by layer approach. It must be pointed out that, at the current state, the proposed CAM software is not aware of the process thermal issues. The eventual introduction of idle times is up to the user, which can use literature approaches to estimate their value [15].

3.4.6. Deposition strategies for open impellers

The last toolpath calculation sub-module included in the three-axis CAM is addressed to open impellers like the one reported in Figure 106.



Figure 106 Open impeller printable using a 3-axis machine

The geometrical input is, as usual, the midsurface of the component (Figure 107)

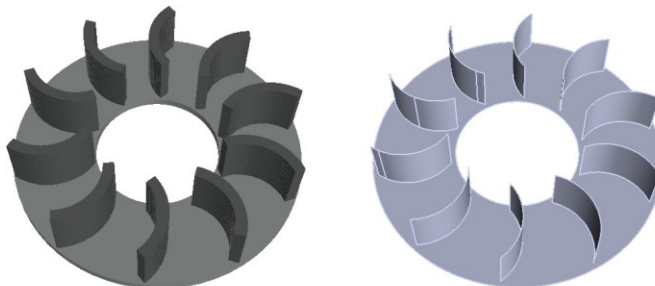


Figure 107 Final CAD (left) and midsurface (right) of an open impeller

It is assumed to build the blades upon an already existing substrate that could be pre-machined to obtain the desired shape and to create features like keyways. It is assumed that the base surface of the input geometry is the top surface of the substrate (Figure 108).

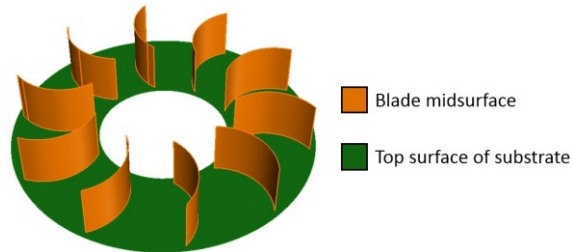


Figure 108 Taxonomy of the input midsurface of the open impeller

The user is asked by the toolpath calculation module to select the blades of the impeller in the order he wants those to be deposited. A possible selection pattern is depicted in Figure 109. The presented selection pattern is also able to mitigate the distortion of the part.

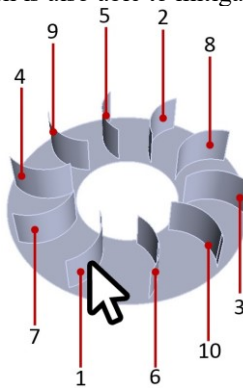


Figure 109 A possible printing sequence for the blades of the impeller

After the selection of the midsurfaces of the blades of the impeller has been carried out by the user, the toolpath calculation algorithm starts and operates as follows:

1. The union bounding box of the midsurfaces of the blades is calculated as shown in Figure 110

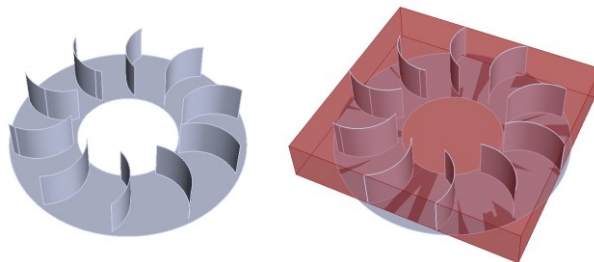


Figure 110 Input geometry (left) and union bounding box of the blades (right)

The union bounding box is defined as the box containing all the blades of the impeller. In Grasshopper it is obtained in form of a BRep. After the union bounding box has been calculated, its height is extracted and used to calculate the number of layers to deposit. Such number is obtained dividing the height of the bounding box by the layer height that is an input from the user; the result is rounded to the closest integer and then an extra layer is added to ensure enough extra material on the top surface of the blades.

2. The barycenter of the base plane of the union bounding box is determined. Then, a series of planes parallel to the plane containing the base surface of the impeller (i.e. the building plane) is generated. The series is composed of N planes, where N is the number of layers to be deposited. The distance between the planes is equal to the layer height.
3. An intersection between the midsurfaces of the blades and the series of parallel planes is performed and the resultant curves are stored in a collection of arrays. The number of arrays NA composing the series is given by

$$NA = N \cdot NB$$

Where:

NA = number of arrays containing the intersection curves;

N = number of layers;

NB = number of blades of the impeller.

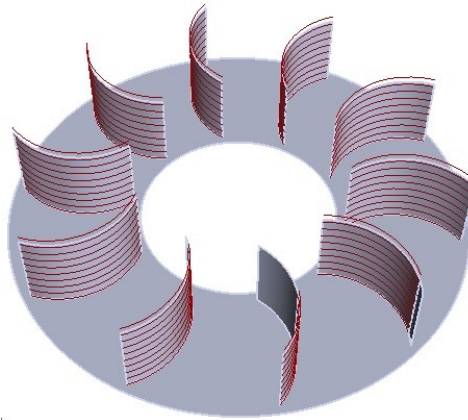


Figure 111 The curves resulting from the intersection procedure

In each array there are all the curves resulting from the intersection between one plane and all the blades of the impeller. The curves are ordered in each array following the selection order selected by the user.

4. The senses of the curves contained in the arrays corresponding to the odd layers are flipped. This because the deposition sense of each layer of a blade coincides with the sense of the curve itself; therefore, it is important to compensate for the difference of shape between the start and end of a bead as when depositing a wall.

Such compensation is obtained starting the bead of a layer upon the end of the bead of the previous layer.

5. The start and end points of each intersection curve are extracted and stored in two different arrays named Start Point Array and End Point Array. The first item in the Start Point Array and the last item in the End Point Array are deleted; then a series of segment is created is created connecting respectively the first point of the End Point Array and the first point of the Start point array, the second point of the End Point Array and the second point of the Start Point Array and so on (Figure 112).

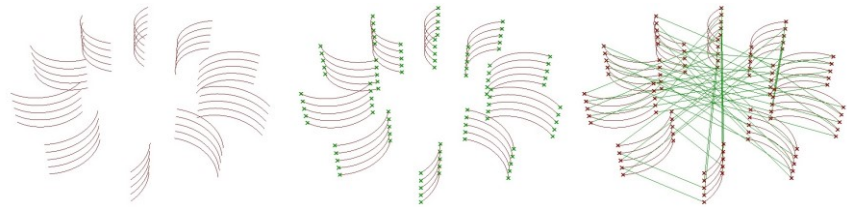


Figure 112 Intersection curves (left), end points of the intersection curves (center) and generation of the rapid movements (right)

6. Finally, the rapid movements and the deposition movements are joined together obtaining a unique polyline that is the final toolpath. The last step before the post processing operation is the generation of a series of equally spaced point on the toolpath that will be the points passed to the numerical control. The distance between a point and the adjacent one is equal to half the resolution of the deposition process. To help the post-processor understanding whether a point is on a repositioning movement or a work movement, the distance between each point and the surfaces of the blades is tested. If the distance is lower than a specified numeric threshold (usually set in the order of 10^{-6}), then the point will be considered laying on the surface of a blade and so a G01 movement will be generated by the post-processor; otherwise the point will be considered laying on a rapid movement and a G00 block will be generated by the post processor.

An image of the final toolpath is depicted in Figure 113, where the repositioning movements are represented in red, and the deposition movements in green. The spheres represent the arc striking points.

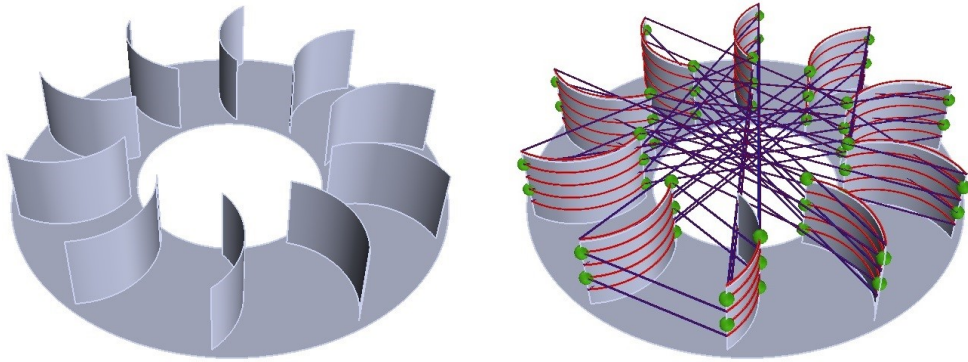


Figure 113 Input midsurface (left) and final toolpath (right) for an open impeller

3.5. Proposed toolpath generation framework: implementation and testing

All the algorithms presented in this chapter have been implemented in a software application using the graphic programming language of Grasshopper that is a plugin of the Rhinoceros CAD software. Grasshopper offers a software development environment, while Rhinoceros is used to manage the input CAD file (that can be produced using any other CAD software and exported in IGES 144 format) and display the toolpath and the outcome of the feature recognition module. Since the implemented solution uses Rhinoceros and Grasshopper, it is strongly dependent on the OpenNurbs standard. The workflow to produce the deposition toolpath for a part is described in the scheme of Figure 114.

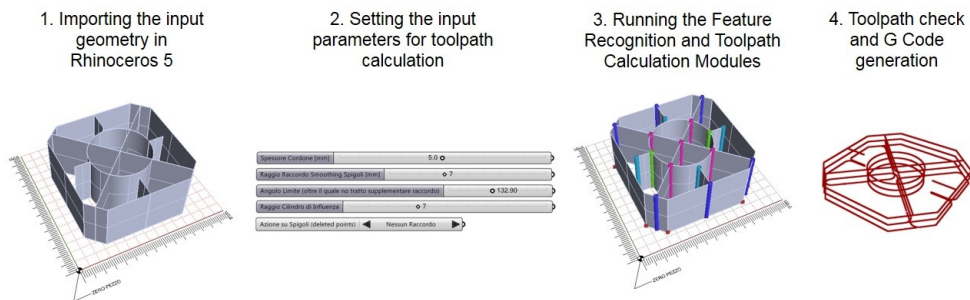


Figure 114 The workflow of the proposed CAM software

The developed CAM software and the feature recognition module were tested on several parts including the features reported in Table 11. Figure 115 presents some examples of results coming out from the feature recognition module.

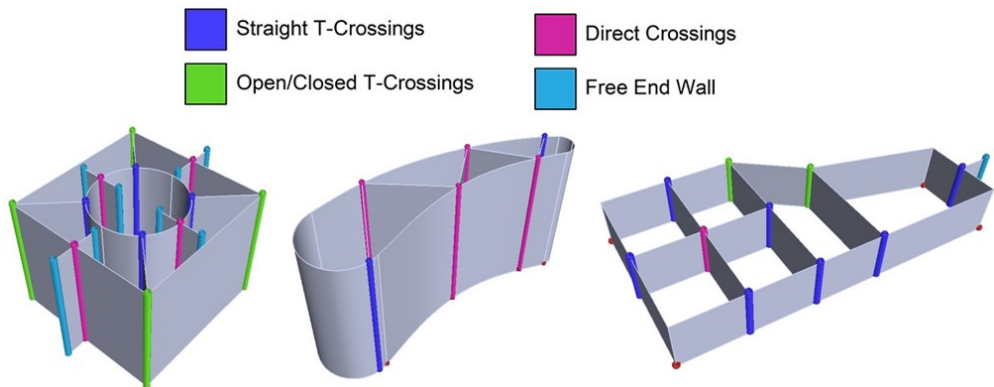


Figure 115 The result of the proposed feature recognition routine on different geometries

The result of these tests highlights that the proposed feature recognition algorithm can recognize all the depicted features. Besides testing the feature recognition algorithm, the proposed CAM software was used to generate the toolpath for the sample component, presented in Figure 116.

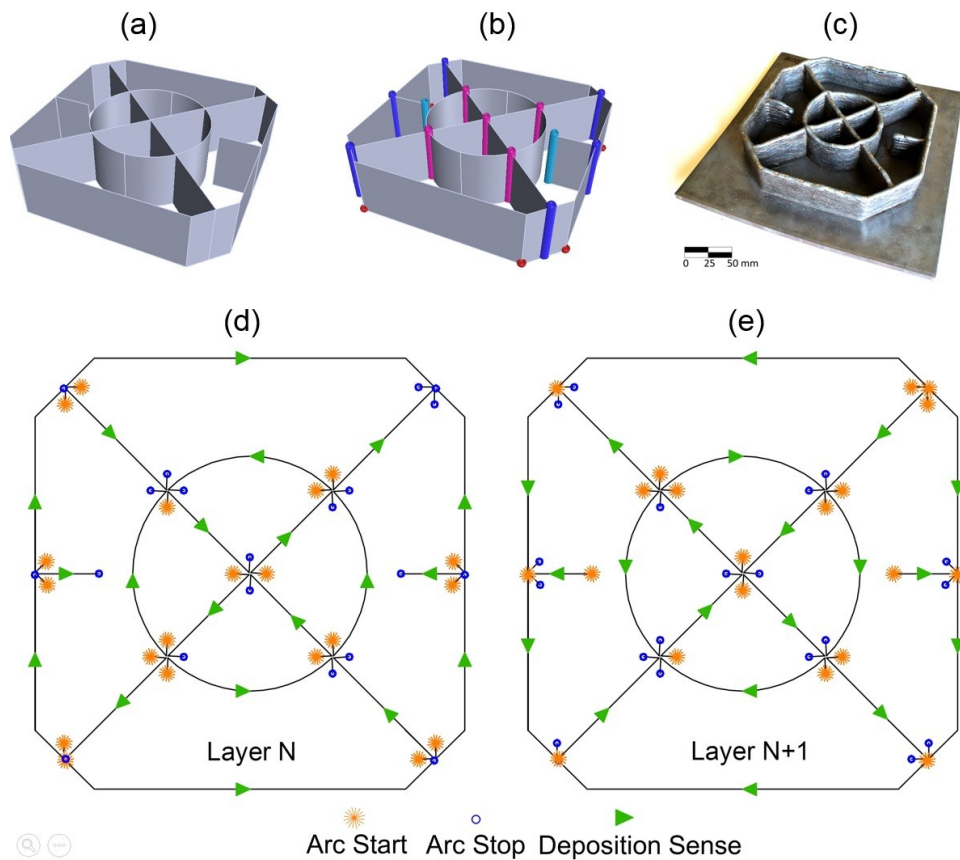


Figure 116 The midsurface-only input CAD file (a); the result of the feature recognition module (b); the manufactured part before the finish machining operations (c); the arc ignitions and stops on a generic N layer (d); the arc ignitions and stops on a generic N+1 layer (e).

Figure 116 (a) shows the midsurface-only CAD model, while Figure 116 (b) shows the outcome of the feature recognition. It is highlighted that the test case part has free end walls, direct crossings and t-crossings, i.e. all the features requiring dedicated deposition path. Figure 116 (d) and Figure 116 show the calculated toolpath; arc start and stop points are highlighted. The test case was actually manufactured using the WAAM machine presented in section 1.3. Figure 116 (c) shows the manufactured test case in the as-welded state, i.e. prior to the finishing operation. It is highlighted that the toolpath generated by the proposed CAM software resulted in the desired shape.

3.6. A proposal for an integrated three axis CAM framework for WAAM

When dealing with WAAM and other additive manufacturing technologies, it is often necessary to print more than one single component or part on a substrate. Since the presented CAM software is based on a modular approach, the deposition toolpath for each single part on the substrate will be calculated using a different module, and each single module outputs a standalone deposition toolpath. For this reason, it will be necessary to join and link together the toolpaths calculated by different modules in order to have a unique deposition toolpath. In this sense, the proposed approach is the one of Figure 117.

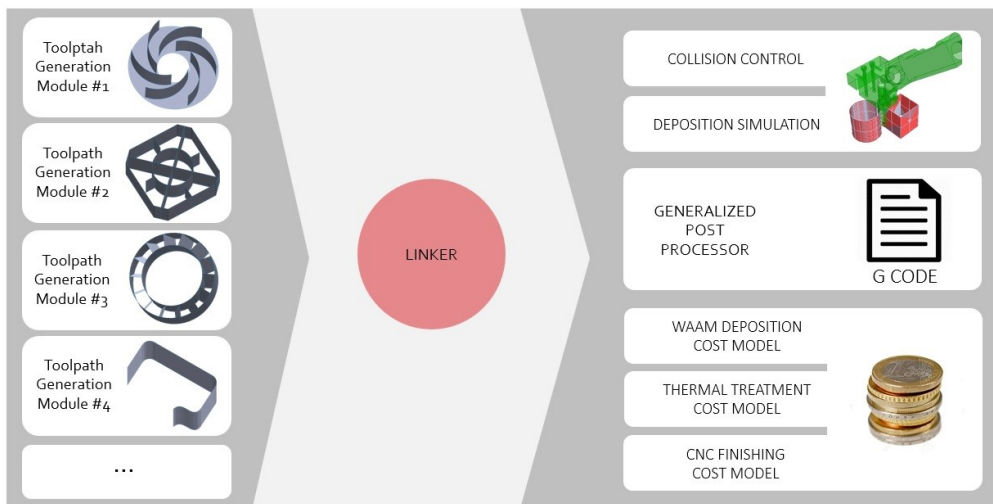


Figure 117 Scheme for the proposed three-axis CAM framework for WAAM

Referring to Figure 117 it is possible to see that the toolpath calculation modules are the starting point: the user examines the parts to be printed, place those on the substrate and decide which toolpath deposition module to use for each different part. After all the deposition toolpaths have been calculated, the linker takes care of re-organizing the overall toolpath (including all the toolpaths generated by the toolpath generation modules). More in details, it generates the final deposition toolpath including in the first layer all the first layers coming from the different deposition toolpaths. If a toolpath coming from a module has a helical strategy it will be left alone and not integrated in the general deposition toolpath. Moreover, the linker generates all the repositioning movements to connect the layers coming from different modules and laying on the same plane. The collision detection module presented in section 3.3 can cooperate with the linker to detect whether different parts can be built on the same platform using a helical deposition strategy or not. After the general deposition toolpath has been generated by the linker combining the toolpaths coming from the different modules, the post processor can be used to generate the G-Code for the numerical control of the used machine. In addition, the final toolpath can be the input for the cost models presented in section 2. Using this configuration for the overall three-axis CAM framework for WAAM, the inputs and outputs of the toolpath generation modules and of the linker are reported in Table 18.

Table 18 Input and outputs of the toolpath generation modules and of the linker module

Macro Section	Inputs	Outputs
Toolpath Generation Modules	Component Midsurface	
	Feed	Polyline representing the deposition toolpath
	Layer Height	
	Nozzle to Work Distance	Equally spaced points laying on the deposition toolpath
	Effective Wall Width	
Linker	Deposition toolpath coming from all the used toolpath calculation modules (both polyline and points)	Overall deposition toolpath obtained re-organizing the toolpaths coming from the modules
		Length of the overall deposition toolpath

4. Design and construction of a 5-axis machine for WAAM operations

In the recent years, many machine tool manufacturers introduced in the market a WAAM based machine. Mutoh presented a very interesting three axis machine [56] (Figure 118). This machine uses water to cool the part during the build procedure, as already suggested in [57].



Figure 118 The 3 axis WAAM based machine from Mutoh

Addilan introduced in the market a three-axis WAAM based machine that is scalable to product parts big up to five meters [58], thus exploiting all the potentialities of the WAAM technology (Figure 119)

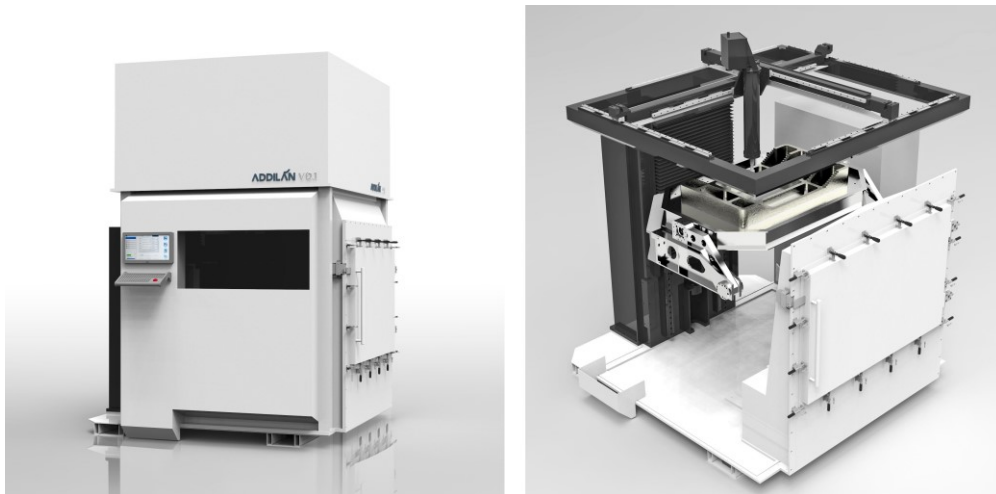


Figure 119 The WAAM based machine from Addilan (from [58])

For what concerns five axis machines, Mazak [59] and Gefertec [60] propose some interesting and promising models, that will be briefly examined in the next lines. The machine from Mazak, named Variaxis J-600 AM, uses a GMAW welder to add material on the substrate. The machine has a XYZBC structure with a roto-tilting table (Figure 120). This machine has also milling capabilities and can therefore be classified as a hybrid machine. Indeed, the structure of the machine seems to derive from the structure of a traditional milling machine.

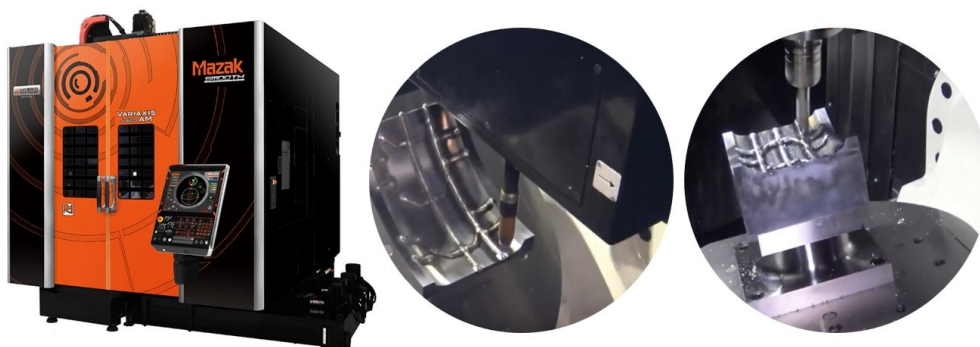


Figure 120 The Variaxis J-600AM WAAM machine from Mazak (left). An additive operation and a milling operation performed on the machine (right)

For the Variaxis J-600 AM, the welding torch is located on one side of the milling spindle; the torch can be retracted during subtractive operations or extended during additive operations. Moreover, a specifically developed cover can be mounted on the spindle during the additive operations, in order to protect it from the welding spatter (Figure 121).

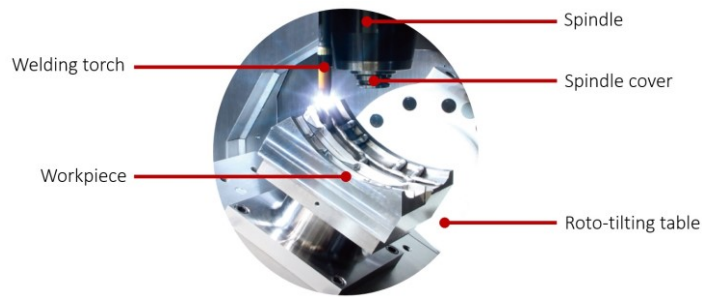



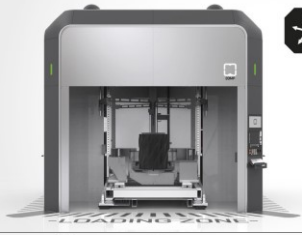


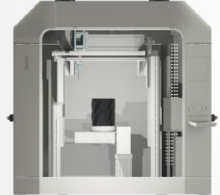

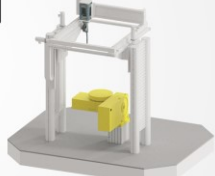


Figure 121 Configuration of spindle and welding torch for the Variaxis J600 AM

Gefertec developed and introduced in the market two big five axis WAAM machines and a three-axis machine. The five-axis ones have an AC roto-tilting table like the ones used in milling machines. These tables are therefore very precise and accurate but also very heavy. The characteristics of the machines developed by Gefertec, taken from their website, are reported in Table 19.

Table 19 The characteristics of the WAAM machines by Gefertec (from [60])

arc 603		  
3-axis capabilities	Production of metallic components up to 3 m with a maximum mass of 3000 kg	
arc 605		  
5-axis capabilities	Production of metallic components up to 0.8 m with a maximum mass of 500 kg	
arc 405		  
5-axis capabilities	Production of metallic components up to 0.06 m with a maximum mass of 200 kg	

Another possible approach to obtain a WAAM machine is the retrofit of an already existing machine tool with a suitable structure. This approach is extensively used in research activities, since it is very flexible and cost-effective. Karunakaran et al. developed the

ArchHLM machine [61] retrofitting an existing milling machine. The resultant machine fits a GMAW welding unit enabling to perform both milling and welding operations (Figure 122).



Figure 122 The machine by Karunakaran et al. (from [61])

Another retrofit example was shown by Cranfield university [8] (Figure 123). They retrofitted a friction stir welding machine equipping it with a welding power source and a rolling system able to perform inter-layer rolling operations [30]. This is done to improve the microstructure of the deposited material.



Figure 123 The machine obtained by Cranfield university through the retrofit of a former friction stir welding machine (from [8])

Finally, 3D Hybrid proposes a head equipped with WAAM technology that can be mounted on any CNC machine, enabling it to perform additive operations (Figure 124). Such head has a standard connection and can be easily mounted on the spindle of a milling machine.

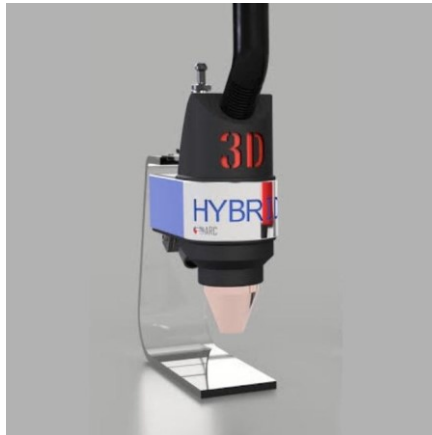


Figure 124 the retrofit head developed by 3D Hybrid (from [62])

Another way to perform three and five axis WAAM operation is using a welding robotic facility like the one reported in Figure 125.



Figure 125 A WAAM robotic welding facility

Robots are very flexible and reconfigurable, even if these are not so accurate when performing milling operations [63]. To perform five axis capabilities a robot can be used with or without a roto-tilting table. In the first case, showed in Figure 126, the robot arm is usually employed to perform the X, Y and Z linear movements, while the roto-tilting table takes care of the rotations.

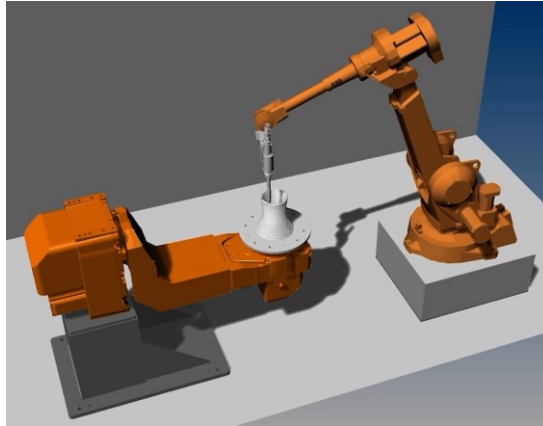


Figure 126 Robotic welding facility with robot arm and roto-tilting table

Stratasys and Siemens successfully applied this configuration in a 3D demonstrator that uses FDM technology to deposit composite materials (Figure 127).



Figure 127 The 3D demonstrator by Stratasys and Siemens (from [64])

However, the robot can also be used to perform a five-axis deposition through the inclination of the welding torch as successfully performed by Kazanas et al. [24]. In this case the material can be deposited up to a certain self-support inclination (Figure 128).

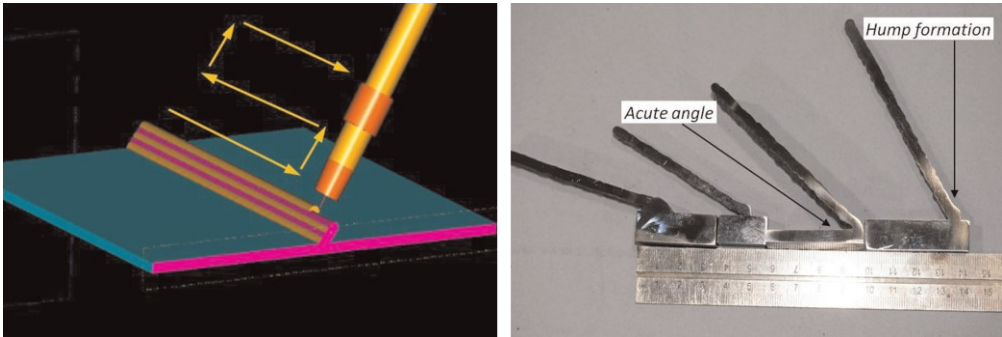


Figure 128 Deposition of inclined walls using a robot. Deposition pattern (left) and various resulting walls (right). From [24].

The overall system is very sensitive to the used welding parameters, but if these are optimally tuned, even the deposition of horizontal walls can be achieved (Figure 129)

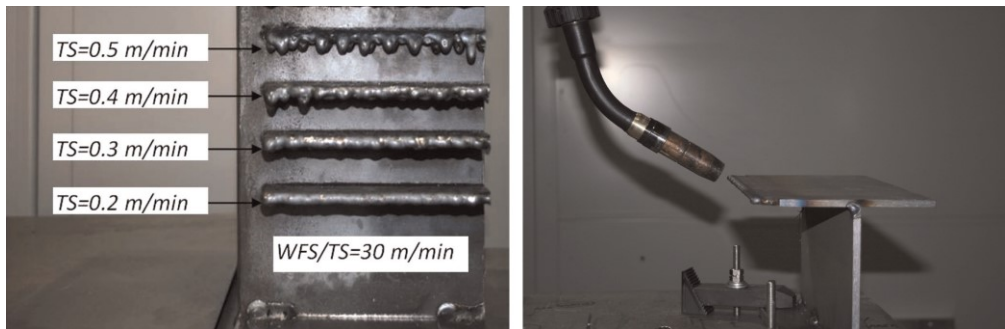


Figure 129 Influence of the welding parameters on the deposition of a horizontal wall (left) and the deposition of a horizontal wall using a robot (right). From [24].

Apart for the application of Kazanas et al., all the WAAM machines show a table-table configuration (Figure 130) in which the part is oriented below the welding torch through a roto-tilting table. In a five-axis operation, this means that both the rotary axes are on the part side. This way, the molten pool is kept always horizontal, resulting in a good process stability and easiness of setup of the process parameters.

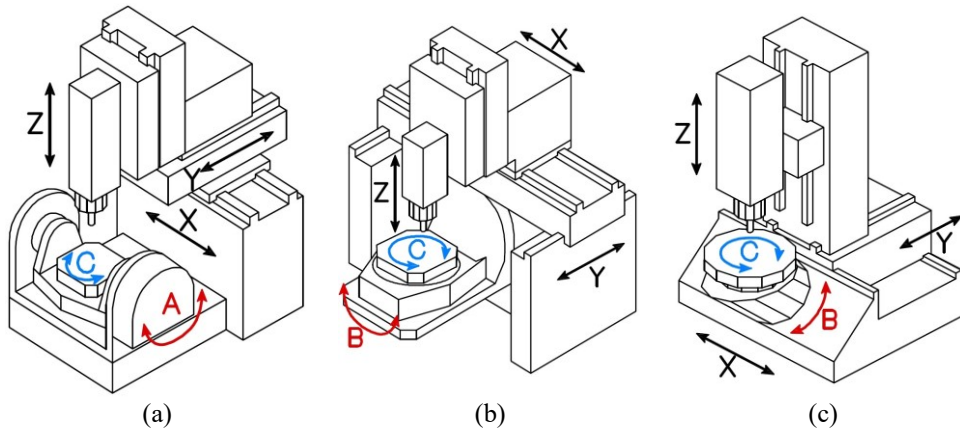


Figure 130 The three possible table-table configurations for a 5-axis machine: (a) XYZAC, (b) XYZBC, (c) XYZBC with B axis at 45 degrees.

During the research activity presented in this thesis, a five-axis machine for WAAM operations has been designed and built. In the following sections the design process and the description of the machines are outlined.

4.1. The choice of the best configuration for the WAAM machine

Looking at the literature research outlined in the previous lines, it is clear that the most reconfigurable and cost-effective solutions for a 5-axis WAAM machine are the retrofit of a former CN milling machine or the purchase of a robot with a roto-tilting table. A third way could be the retrofitting of a three-axis milling machine. In this case both the installation of a welding torch and of a roto-tilting table should be accounted. To keep the overall cost as low as possible also the retrofit of a manual 3-axis milling machine would be interesting. In this case also the motors and the numerical control should be selected, installed and configured. It is also important to highlight that nowadays many low cost or even open-source PC based numerical control software are available. Examples are the Mach3 software [65], or the LinuxCNC [66] one. These are easily to set up and shows a very high re-configurability and accessibility making the idea of creating a new numerical control from scratch very attractive. Of course, such machine would not be as reliable and precise as a commercial one, but it is important to consider that it would be used only for research purposes and therefore it must not assure the reliability that one expects from an industrial-grade machine. Using stepper motors to move the axes, the maximum achievable feed will be low, but it is important to note that the deposition speed is usually quite low for WAAM if compared to traditional milling process or even high-speed machining processes. Indeed, in the test carried out in the presented research activities the deposition feed was very rarely over 300 mm/min.

The use of a 6-dof robot arm without the roto tilting table has not been considered, since no advanced GMAW power source (such as CMT by Fronius) would have been available, and because a configuration with a roto-tilting table appeared as the most reconfigurable one. The expected characteristics of the WAAM machine developed for this research activity are listed below:

- Low cost (less than 5k euro)

The target cost of 5k euro included both the structure of the machine and the cost of the welding power source.

- High hardware and software accessibility and re-configurability
Since a retrofit must be carried out, it is necessary to create an interface between the numerical control of the machine and the retrofit control unit. For this reason, the used numerical control should be as much reconfigurable as possible. Moreover, it would be interesting to be able to implement in the numerical control new macros or new M instructions to control all the ancillary equipment brought by the retrofit and the welding power source itself.
- Max part volume of 150 x 150 x 150 mm
- Possibility of performing both milling and additive operations
Hybrid operations are out of the scope of this thesis for what concern the toolpath calculation. However, it would be interesting if the machine could perform milling operations in the future.
- Easiness of control (i.e. kinematic structure as simple as possible).
Since to obtain the values of the machine axes a specifically developed post processor is needed, it would be interesting to have a kinematic structure of the machine as much simple as possible in order to not invest too much time on the development of the post processor (that is out of the scope of this thesis) and concentrate the efforts in the development of the algorithm for the toolpath generation.

First of all, a comparison between all the possible alternatives has been carried out in order to choose the best solution between robot and retrofit of a milling machine. The result of the comparison is reported in Table 20. The design and building of a WAAM machine from scratch has been explored too. A preliminary design has also been developed (Figure 131); however, this solution was too expensive and time consuming and was abandoned.

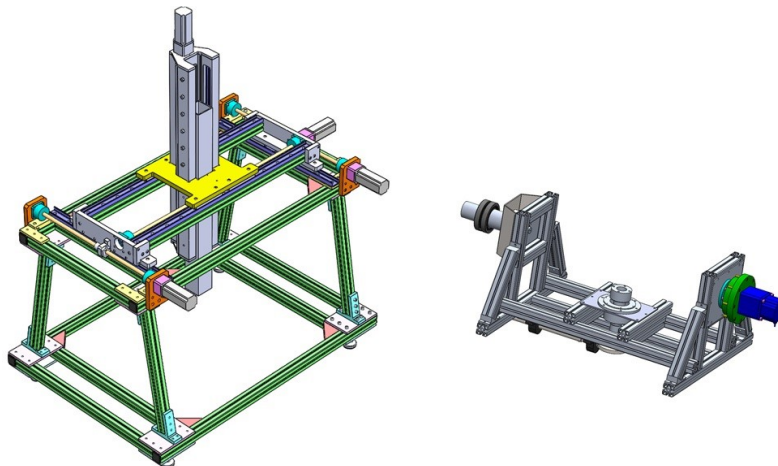


Figure 131 Preliminary design of a machine (left) and of a rotary table (right) for WAAM operations

The purchase of a robot or the retrofit of an already existing machine seemed to be much more cost and time-effective.

Table 20 Comparison between the possible configuration for a WAAM facility capable of five-axis operations

Robot and table		Retrofit of a 5-axis CNC milling machine		Retrofit of a 3-axis manual milling machine	
Cost	0	Cost	-1	Cost	+1
Easiness of control	-1	Easiness of control	+1	Easiness of control	+1
NC reconfigurabilty	-1	NC reconfigurabilty	0	NC reconfigurabilty	+1
180x180x180 mm part	+1	180x180x180 mm part	+1	180x180x180 mm part	+1
Reliability	+1	Reliability	+1	Reliability	-1
TOTAL SCORE	0		2		3

From the comparison emerged that the retrofit of a manual 3-axis milling machine and the construction of a numerical control from scratch could be the best solution to obtain a WAAM machine in a very short time and at a low cost. Therefore, the first step was to select the milling machine to start from. The BF20 Vario 3-axis manual milling machine produced by OPTIMUM was chosen as base machine for the retrofit. A picture of the BF 20 Vario machine is reported in Figure 132, while its characteristics (taken from the user manual) are listed in

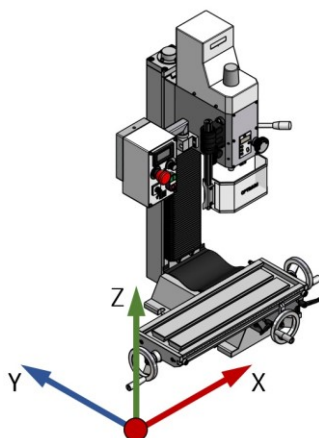
Table 21. The reference system of the machine is showed in Figure 133.



Figure 132 The BF20 Vario 3-axis manual milling machine used as basis for the 5-axis machine retrofit project

Table 21 Technical data of the BF20 Vario 3-axis manual milling machine

Parameter	Value/description
Spindle engine	230 V/ 50 Hz / 850 W
Drilling capacity	ϕ max 16 mm
Milling capacity of end-mill cutter	ϕ max 20 mm
Spindle interface	MT2
Table length	500 mm
Table Width	180 mm
T-slot size / distance	12 mm / 63 mm
X Axis travel	280 mm
Y Axis travel	175 mm
Z Axis travel	280 mm
Total height	935 mm
Total width	745 mm
Total depth	565 mm
Total Weight	103 kg

**Figure 133 Configuration of the reference system in the BF20 Vario machine**

4.2. The mechanical design

To obtain a fully working five-axis WAAM machine three main mechanical modifications must be carried out on the milling machine. These are listed below and will be explained in detail in the next subsections:

- Design and installation of the motors and transmission system for the X, Y and Z axis;
- Design and construction of the roto-tilting table;
- Design and installation of a torch support;

The first step of the mechanical design phase was the creation of a detailed 3D CAD model of the whole machine in order to facilitate the further steps of the design phase such as the collision check for the roto-tilting table. Some images of the resultant CAD model are reported in Figure 134 and in Figure 135.

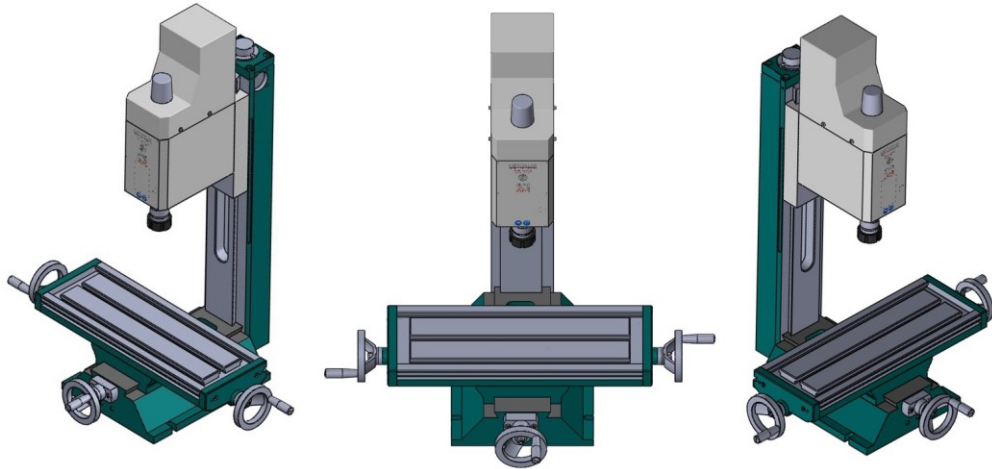


Figure 134 Views of the 3D CAD model

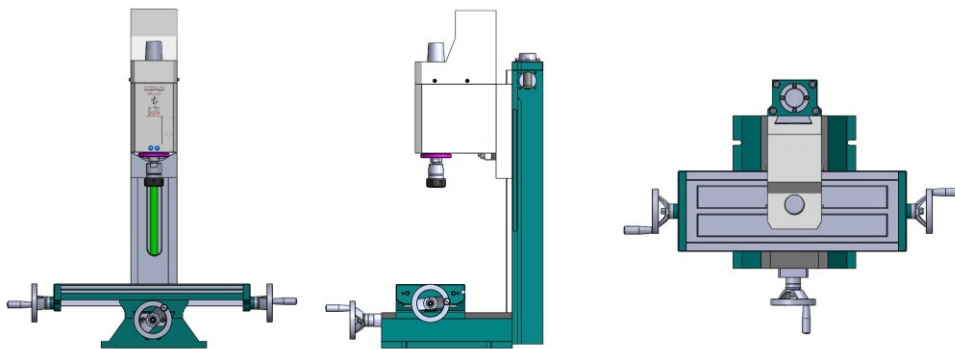


Figure 135 Front, side and top view of the 3D CAD model of the BF20 Vario machine

To make the 3D CAD model, the machine has been completely disassembled (Figure 136). The disassembly of the machine helped in individuating all the possible locations to attach the retrofitting stuff.

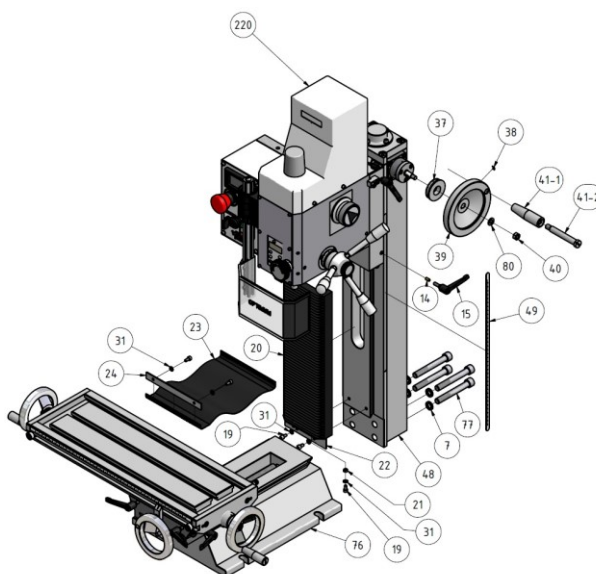


Figure 136 An exploded view from the manual of the BF20 Vario milling machine

4.2.1. Design and installation of the support and transmission system for motors

In order to keep the overall encumbrance of the machine as much compact as possible, it has been decided to keep the axes of the motor parallel to the ones of the screws of the X, Y and Z axes and to transmit the rotary motion from the motor to the screw using a toothed belt. such configuration is reported in Figure 137.



Figure 137 General configuration of the motor and screw (green element) for a linear axis of the machine. The yellow element in the picture is the toothed belt

For what concerns the motors, stepper motors have been selected, since they are much easier to be controlled respect to servo motor; this because no closed loop on position must be implemented and so it is not necessary to install position sensor on the machine (Figure 138).

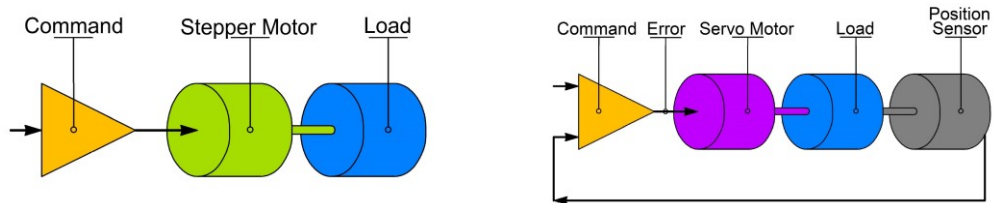


Figure 138 Control scheme for stepper motors (left) and servo motors (right)

Regarding the torque requirement for each axis, a high-grade CNC retrofit kit offered by OPTIMUM has been examined [67]. Such retrofit kit assures a torque of 2.75 Nm on each linear axis. Since in this kit a ball screw for each axis is included too, while in the BF20 Vario used for the WAAM activity lead screws are installed, the torque requirement for each axis has been set as depicted in Table 22. However, in the future the pulley installed on the screw can be changed with a bigger one, if more torque is necessary.

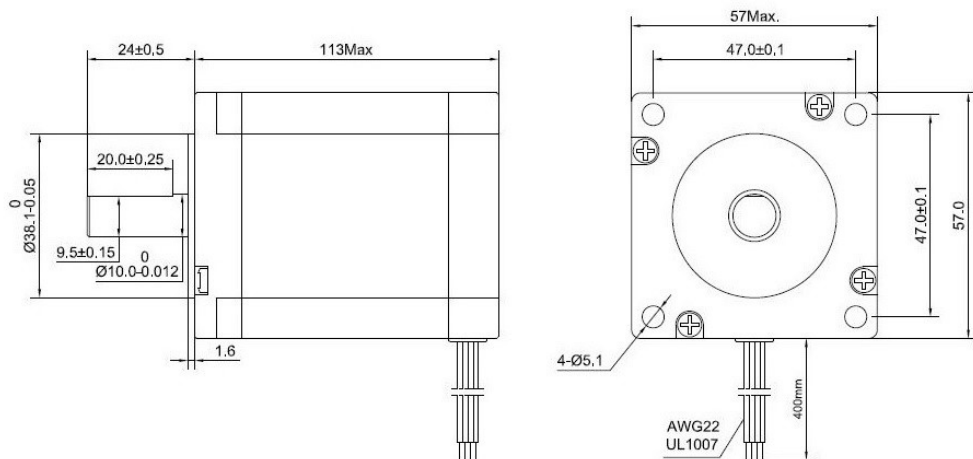
Table 22 Torque target for each linear axis

Axis	X	Y	Z
Torque	3.75 Nm	3.75 Nm	5.0 Nm

Then the stepper motors have been selected. The same kind of motor have been selected for all the linear axes. The technical data of such motor is reported in Table 23, while its dimensions are showed in Figure 139.

Table 23 Technical data for the stepper motor of the linear axes

Parameter	Value/Description
Step angle	1.8°
Positional accuracy	±5%
Number of Phases	2
Max temperature rise	80 °C
Inertia of the rotor	800 g·cm ²
Dielectric strength	500 V AC
Insulation resistance	100 MOhm (500 V DC)
Operating environment temperature	-10 °C / 50 °C
Insulation class	B
Weight	1.6 kg
Holding torque (both phases on)	3 Nm
Rated Current/Phase	4.2 A DC
Phase resistance (±10%)	0.9 Ohm
Phase inductance (±20%, 1kHz)	3.8 mH

**Figure 139 The dimensions of the motor selected for the linear axes**

To better understand some of the data of Table 23, it is important to refer also to Figure 140, that shows the relationship between the torque and the rotational speed of the motor.

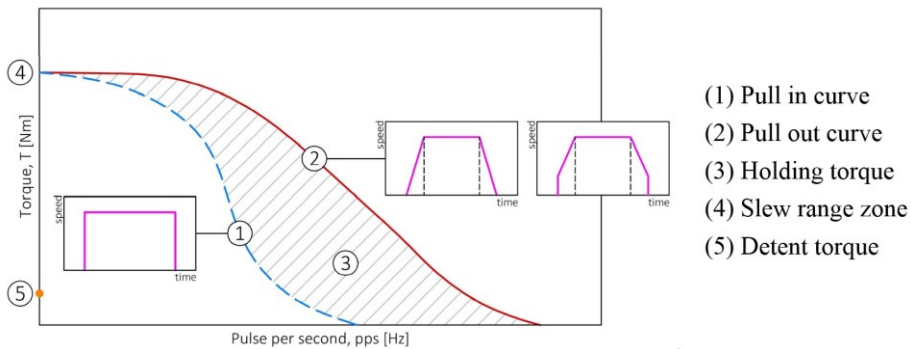


Figure 140 Generic Pull-in and Pull-out curves for a stepper motor

Referring to Figure 140, the Pull-out curve represents the maximum torque that the motor can provide at each rotational speed. If the operation point of the motor (represented by a value of rotational speed and one value of required torque) will stay below the Pull-out curve, the motor won't "lose" any step. The shape of the Pull-out curve depends on the motor and on the driver used to supply the current to the motor itself. The holding torque is the maximum torque that the motor can provide when it is not rotating and the maximum allowed current is supplied to all its phases.

Looking at Figure 140, it is noticeable that the maximum current that can be supplied to the motor is 4.2 A per phase, therefore a driver with a maximum current of 5.0 A like the one reported in Figure 141 can be used to control the motor.



Figure 141 The HY-DIV268N-5A driver used to control the motors of the linear axes

Since no Pull-out curve was available for the chosen motor-driver combination, it has been decided to use the holding torque of 3.0 Nm reported in the datasheet of the motor as reference. Keeping this value as reference the number of teeth for the pulley to be mounted on the motor and of the pulley to be mounted on the screw have been selected for each linear axis, also keeping in mind the required torque values of Table 22. The results are reported in Table 24.

Table 24 Belt and pulley configuration for the linear axis

X Axis	No. teeth motor pulley	16	Motor Torque	Torque on Axis
	No. teeth screw pulley	20		
	Wheelbase	120 mm		
	Belt length \ Teeth No.	330 mm/66		
	Belt width	16 mm		
Y Axis	No. teeth motor pulley	16	Motor Torque	Torque on Axis
	No. teeth screw pulley	20		
	Wheelbase	107.5 mm		
	Belt length \ Teeth No.	305 mm/61		
	Belt width	16 mm		
Z Axis	No. teeth motor pulley	15	Motor Torque	Torque on Axis
	No. teeth screw pulley	25		
	Wheelbase	90 mm		
	Belt length \ Teeth No.	280 mm/56		
	Belt width	16 mm		

For each axis the wheelbase has been chosen as short as possible to keep the assembly as much compact as possible. To calculate all the data regarding the length of the belt and the wheelbase an application has been implemented in Grasshopper (Figure 142) including all the needed math.

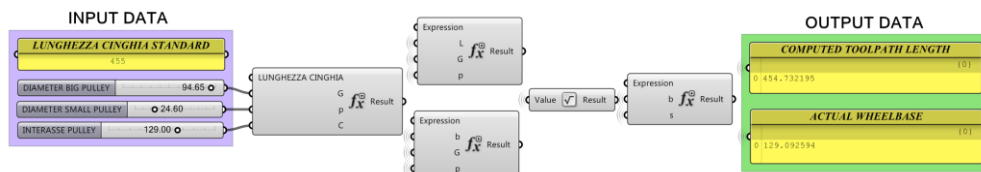


Figure 142 Overview of the application implemented in Grasshopper to calculate the data for the belt transmission

To install the motors the original hand wheels have been removed from the machine and a pulley has been mounted on the screw of each linear axis as shown in Figure 143.

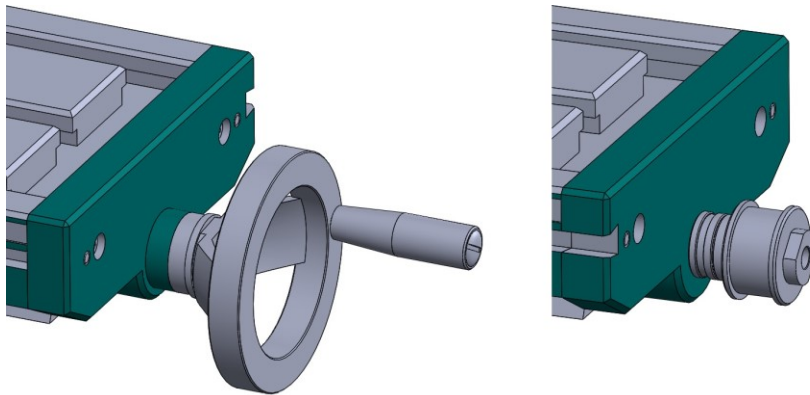


Figure 143 The configuration of the X-axis screw before (left) and after (right) the removal of the hand wheel and the installation of the pulley

The motors have been mounted on an aluminum support obtained milling a plate that can be attached to the machine frame. The shape of such aluminum support is different for each axis drive, but the general concept is the same, as one can see from Figure 144, Figure 145 and Figure 146.

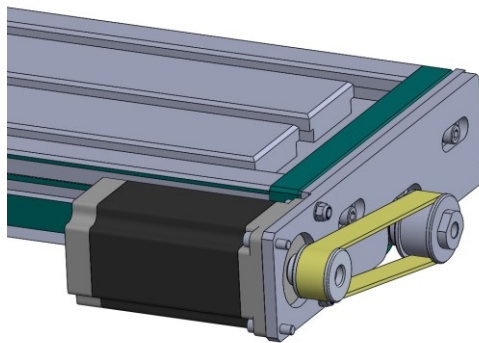


Figure 144 Configuration of the motor for the X-Axis

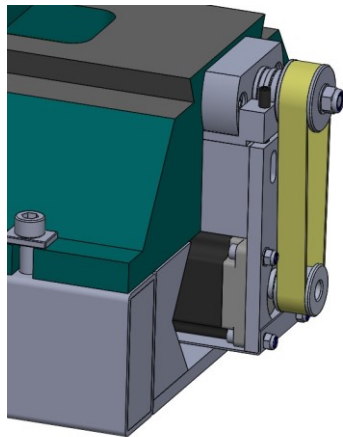


Figure 145 Configuration of the motor for the Y-Axis

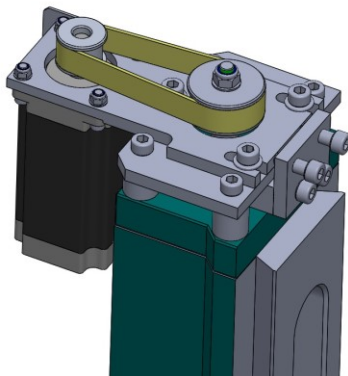


Figure 146 Configuration of the motor for the Z-Axis

Regarding the configuration of the Y axis, since the motor will rest below the machine, a special metal frame to lift the whole machine and make room for the motor has been created (Figure 147).

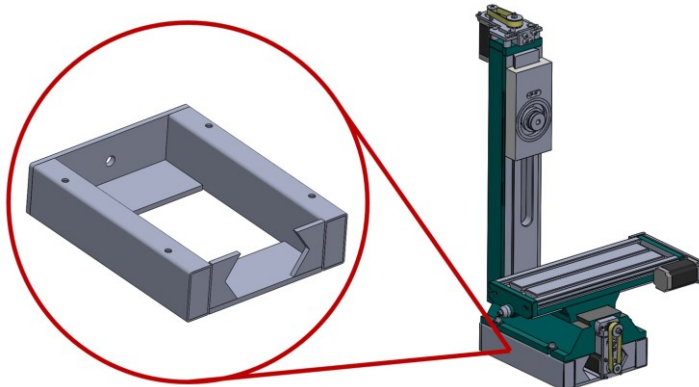


Figure 147 The metal frame built to lift the machine to create room for the motor of the Y axis

For all the three axes, the position of the aluminum support of the motor can be adjusted in order to stretch the toothed belt. Referring to Figure 148 (where the Z axis configuration is shown as example) the procedure for tensioning the belt starts unscrewing the screws A; then the screws B are screwed until the desired tension in the belt has been achieved. Finally, the screws A are tightened again to hold the motor support in its right position.

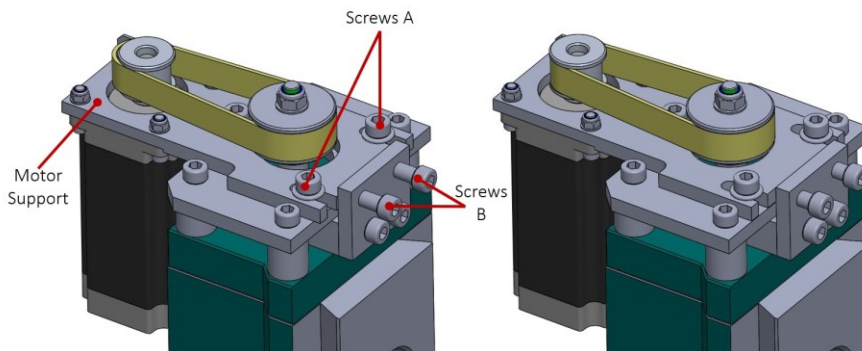


Figure 148 The configuration of the tensioning system for the Z axis. On the left the system is in the non-tensioned configuration, while on the right the right belt has the right tension

Figure 149 and Figure 150 respectively show the configuration of the X and Y axis regarding the system to stretch the belt. The configuration is a little bit different respect to the one of the Z axis, but the principle of operation is exactly the same. In Figure 149 and Figure 150 the same nomenclature of Figure 148 for the screws is used to make everything clearer.

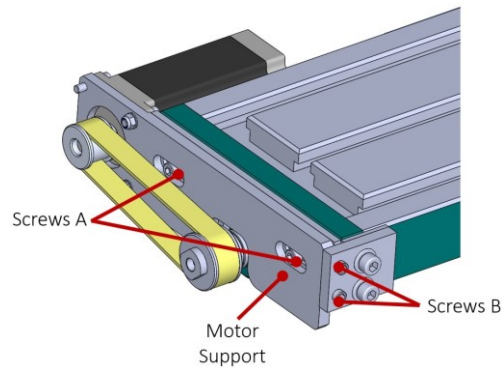


Figure 149 The system to stretch the belt for the X-axis

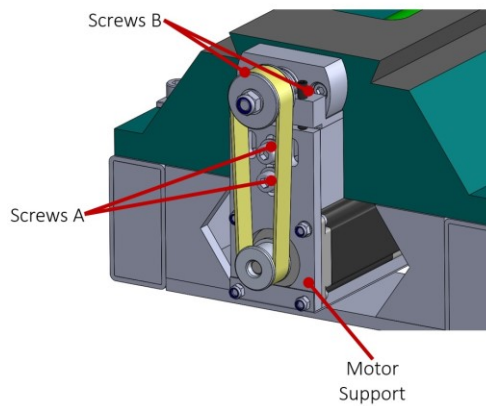


Figure 150 The system to stretch the belt for the Y axis

To cover the pulleys and the spindle and thus to protect the operator that will use the machine a carter has been mounted on each linear axis. The carters are made laser-cutting and bending an aluminum sheet.

Each motor has a dedicated cooling fan that cools down the motor itself during its functioning.

4.2.2. Design and construction of the roto-tilting table

Once the design of the drives for the linear axes has been completed, the roto-tilting table must be designed. The first step is the selection of the configuration between AC and BC (refer to Figure 130). To make this choice the available workspace on the BF20 Vario still in the 3-axis configuration can be analyzed (Figure 151).

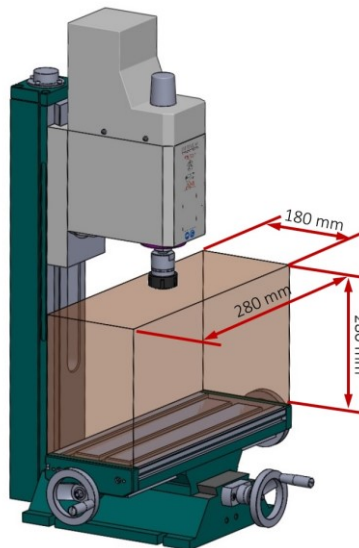


Figure 151 The workspace of the BF20 Vario still in the 3-axis configuration

Referring to Figure 151, it is noticeable that there is a lot of space in the X direction, therefore an AC configuration for the table would seem the best one. However, when the table would tilt, and the Y carriage is near its maximum travel (in the Y-direction), the table would collide with the Z axis column (Figure 152).

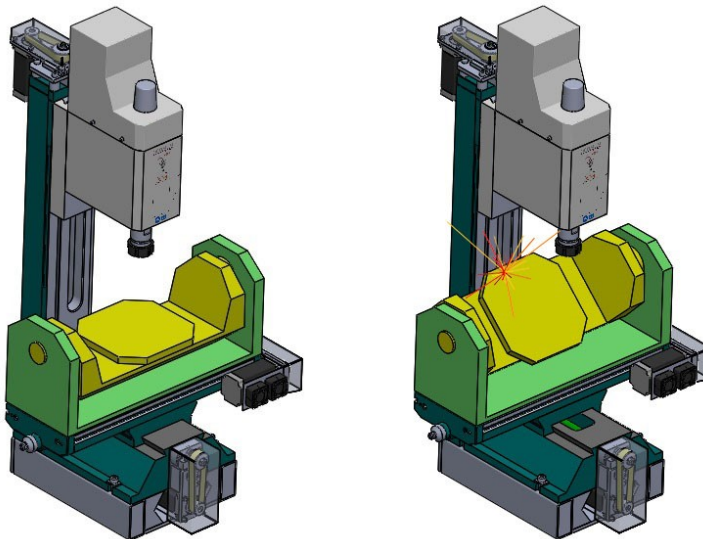


Figure 152 Mounting an AC table on the machine (left) would result in possible collision between the column of the Z axis and the table itself (right)

Therefore, a BC configuration like the one reported in Figure 153 has been chosen. Looking at Figure 153, it is possible to notice that no collision will occur during the tilting of the table in such configuration.

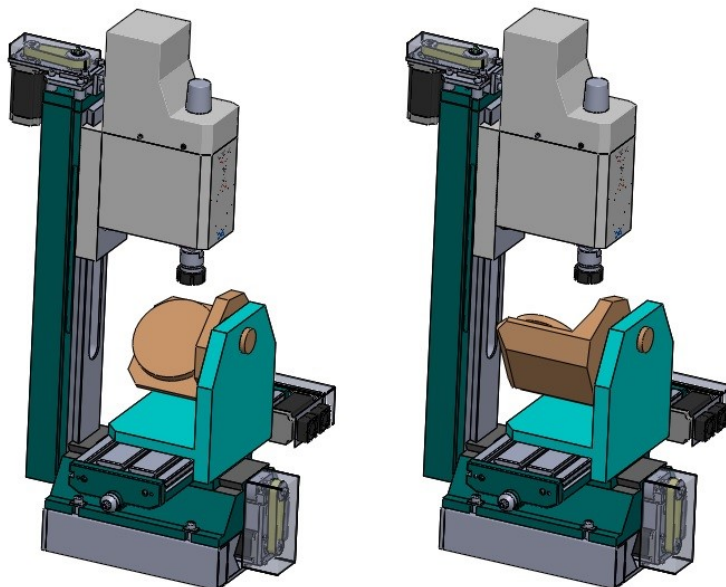


Figure 153 BC table configuration

Of course, the total encumbrance of the table will not be longer than the X table (Figure 154), otherwise the travel of the Y axis will be shortened to avoid collisions with the Z axis column.

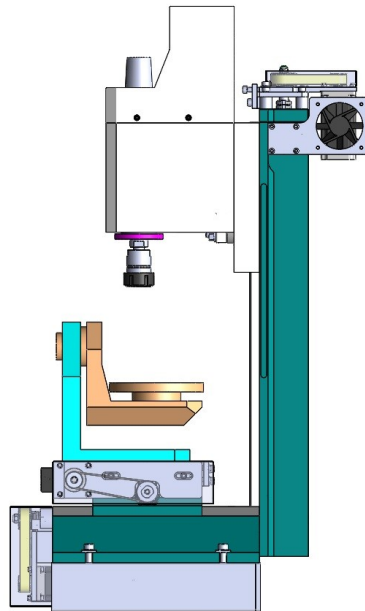


Figure 154 Side view of the BF20 Vario machine. The encumbrance of the BC table is inside the X axis carriage

Since an off the shelf roto-tilting table like the one shown in [68] would be too big for the selected machine frame and too much expensive, it has been decided to design an innovative roto-tilting table especially oriented to the WAAM technology. The target requirements of the roto-tilting table are listed below:

- Working volume of 150 x 150 x 150 mm (Figure 155)

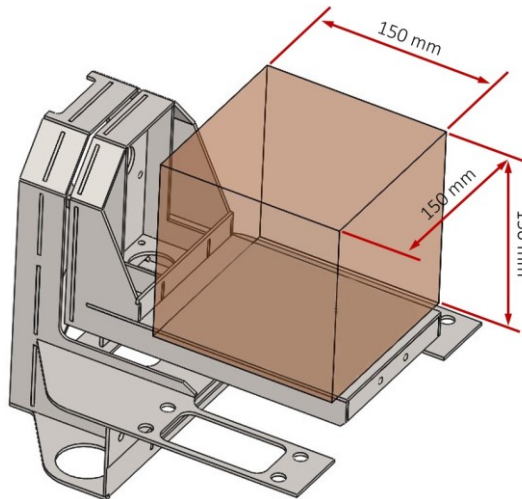


Figure 155 Working space of the roto-tilting table

- Maximum deflection of 0.7 mm under a load of 10 kg in the horizontal position and in the $B = 90^\circ$ position (Figure 156)

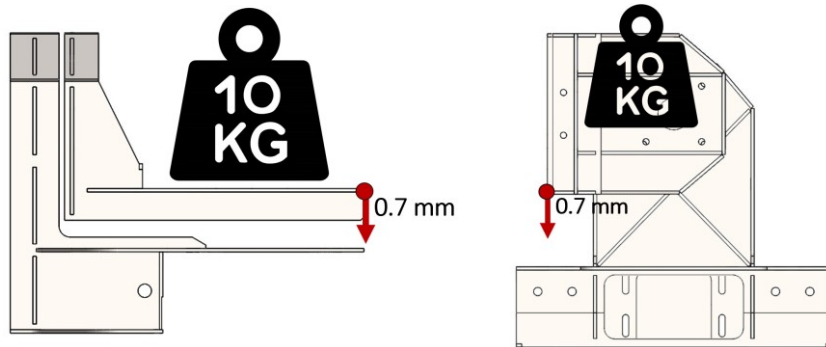


Figure 156 Maximum deflection in the horizontal position (left) and in the $B = 90^\circ$ position (right)

The choice of the value of 10 kg is not casual. Looking at the preliminary economical comparison between WAAM and CNC milling showed in section 1 and referring to Figure 18, it can be stated that, for a given working volume, it is economically convenient to manufacture a WAAM component if it has a volume equal to 18% of the total working volume. Supposing to manufacture steel parts, an object with a volume of $150 \times 150 \times 150$ mm, i.e. 0.003375 m^3 , weights 26.325 kg (considering a density of 7800 kg/m^3 for steel). Therefore the 18% of 26.325 kg is about 5 kg. This value has then been doubled to extend the manufacturing capability of the machine.

- Lightweight and WAAM oriented design
In WAAM operation there are no forces between the torch and the part, while for what concerns the finish-milling operations the cutting forces are much lower respect to the ones in roughing operations (Figure 157). Therefore, it is not necessary to have bulky components even in a hybrid WAAM machine.

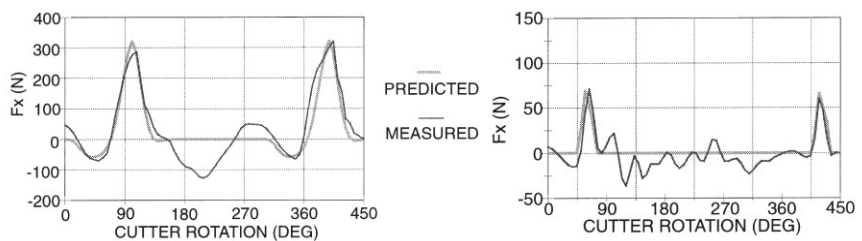


Figure 157 Cutting forces for a 5-axis roughing (left) and finishing (right) operation. (from [69])

Looking for an innovative and lightweight design for the roto-tilting table, it has been decided to build it using steel sheet metal parts obtained through laser cutting. The parts composing the table fits each one in the other using one of the joints reported in Figure 158.

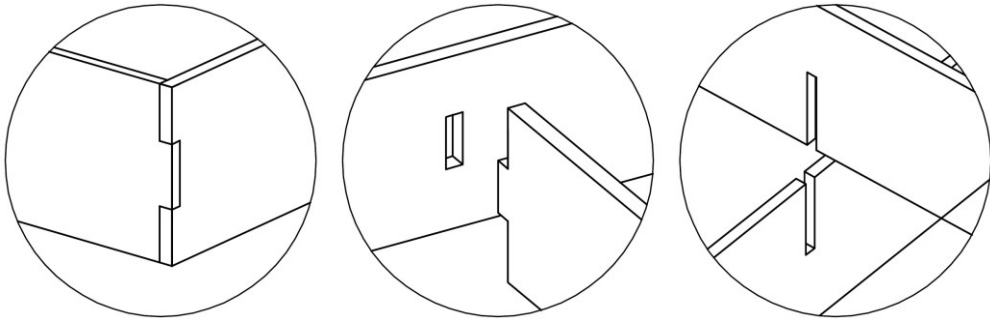


Figure 158 Joints for sheet metal parts. (left) finger joint, (center) slot and tab joint, (right) half lap joint (adapted from [70])

Then the parts composing the table will be welded together to obtain a solid structure. The same kind of stepper motor selected for the linear axes has been chosen to drive the B and C axes. Looking for the most compact configuration for both the B and C axis, it has been decided to mount the motors in the configuration reported in Figure 159.

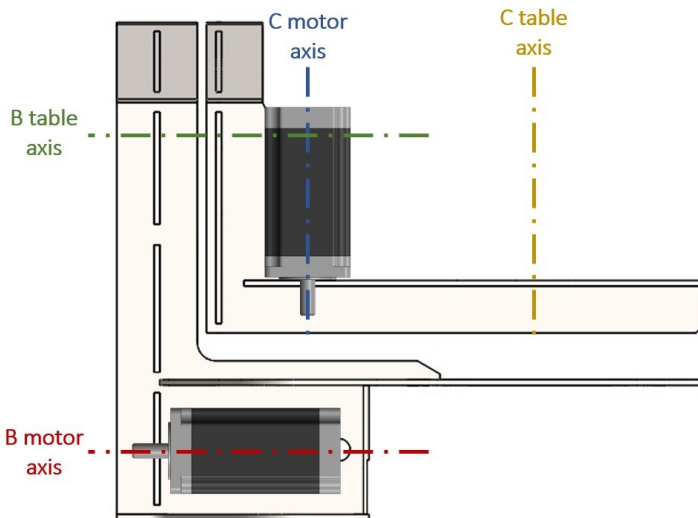


Figure 159 Configuration of the motors for the C and b axis

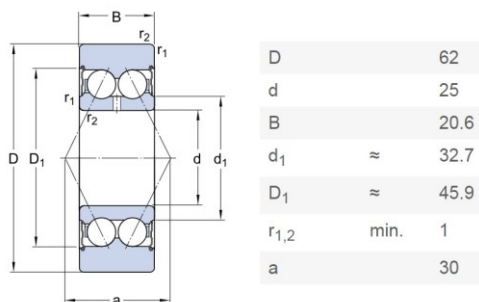
Using the configuration reported in Figure 159 the B-axis table will stay as much low as possible thus not reducing the Z-axis travel of the machine. To transmit the rotation from the motors to the B and C table, toothed belts have been used. This allowed the introduction of a multiplication ratio between the axle of the motor and the rotary tables. Considering the inertial loads (the only one present in a WAAM operation), the torque requirements for the B and C axis have been calculated and the belt drives have been designed. The Grasshopper application showed in Figure 142 and used also in the design of the linear drives has been used. The resultant configurations respectively for the B and C axis are reported in Table 25

Table 25 Belt drive configuration for the B and C axes

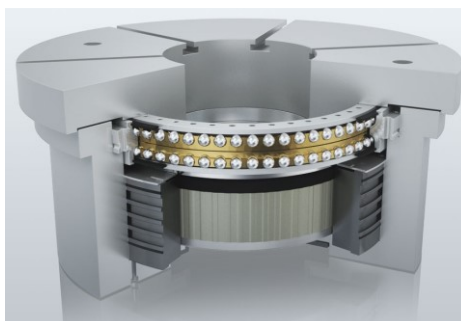
B Axis	No. teeth motor pulley	16	Motor Torque	Torque on Axis
	No. teeth table pulley	60		
	Wheelbase	178 mm		
	Belt length \ Teeth No.	550 mm/110		
	Belt width	16 mm		
C Axis	No. teeth motor pulley	16	Motor Torque	Torque on Axis
	No. teeth screw pulley	20		
	Wheelbase	129 mm		
	Belt length \ Teeth No.	445 mm/91		
	Belt width	16 mm		

At this point a preliminary design of the roto-tilting table has been carried out and then optimized using finite element analyses.

The bearing for both the axis must afford radial and axial loads, therefore the bearing of Figure 160 has been selected for both the rotary axis.

**Figure 160 Technical data of the bearings of the B and C axes (from [70])**

The kind of bearing reported in Figure 160 is widely used in the rotary tables for machine tool as shown in Figure 161.

**Figure 161 Cutaway of a commercial direct drive rotary table for machine tools (from [71])**

The roto-tilting table is attached to the X axis table of the machine through eight bolted connections that exploit the T-slots of the X table itself (Figure 162).

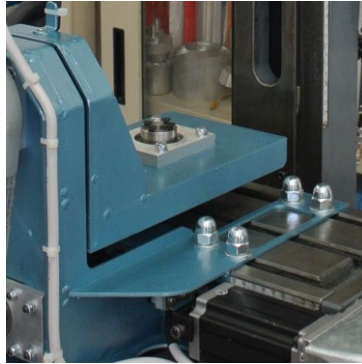


Figure 162 Close view of the bolts holding the frame of the roto-tilting table

To study and improve the performance of the roto-tilting table two kinds of finite element analysis have been carried out. For all this activity the Optisruct solver [72] has been used. All the pre-processing activities have been carried out using the software Hypermesh by Altair [73].

The first kind of analysis that has been performed is a static analysis in the horizontal configuration ($B = 0^\circ$) and in the $B=90^\circ$ configuration. A mass of 10 kg is placed at 75 mm above the plane of the B table in both cases and all is subjected to the gravitational acceleration. The parts composing the table have been modeled using shell elements because of the ratio between their thickness and their overall size. The welded joints have been modeled joining the interface nodes of the adjacent components. The X table is considered as a rigid body and the frame of the roto-tilting table is rigidly attached to it through some rigid connections modelling the bolts.

So, the first step was to obtain the defeatured midsurface of the roto-tilting table. Later, the geometry has been meshed and all the boundary conditions have been applied (Figure 163)

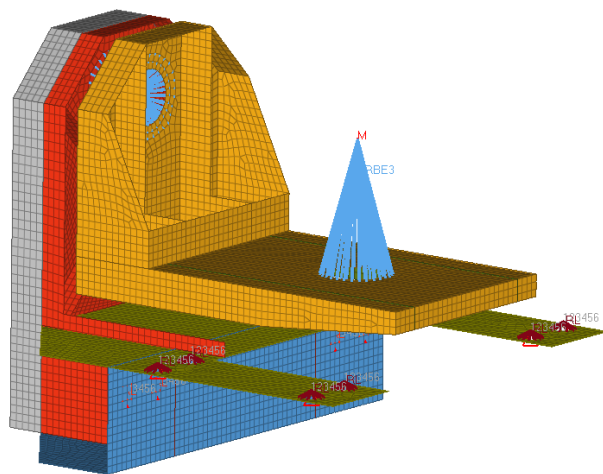


Figure 163 The finite element model

To satisfy the desired requirement in terms of maximum deflection at the end of the B table both in the case $B=0^\circ$ and $B=90^\circ$, several thicknesses have been tested (2, 3 and 4 mm). However, the FEM simulations revealed that increasing the thickness was not enough (or even counterproductive), therefore several reinforcement configurations have been designed and tested through FEM simulations (Figure 164 and Figure 165).

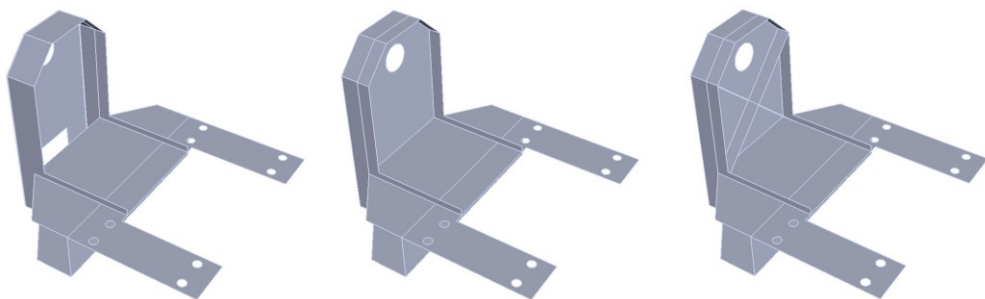


Figure 164 The evolution of the reinforcements for the frame of the table

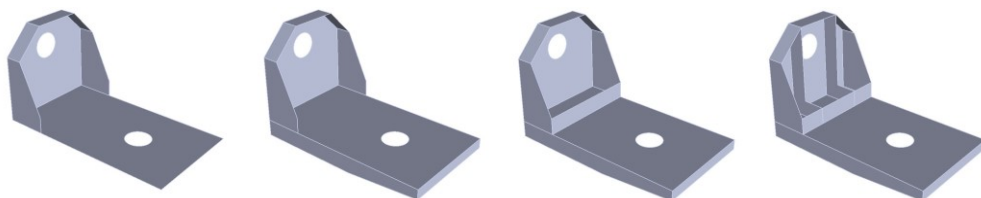


Figure 165 The evolution of the reinforcements for the tilting table

At the end of this iterative process the configuration that achieved the best performance was the one with 3 mm thickness and the reinforcement configuration reported in Figure 166.

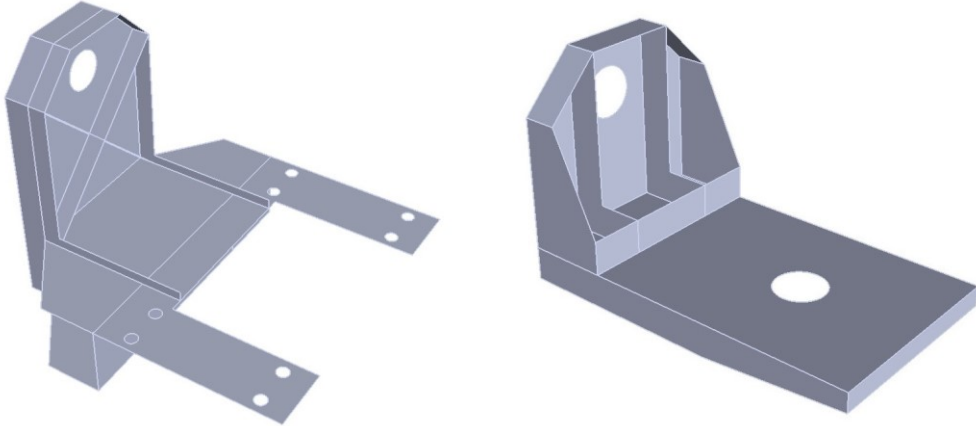


Figure 166 The configuration for the frame (left) and for the tilting table (right) that achieved the best performance in terms of total deflection

The results of the static finite element analysis for this configuration are reported in Figure 167 and Figure 168.

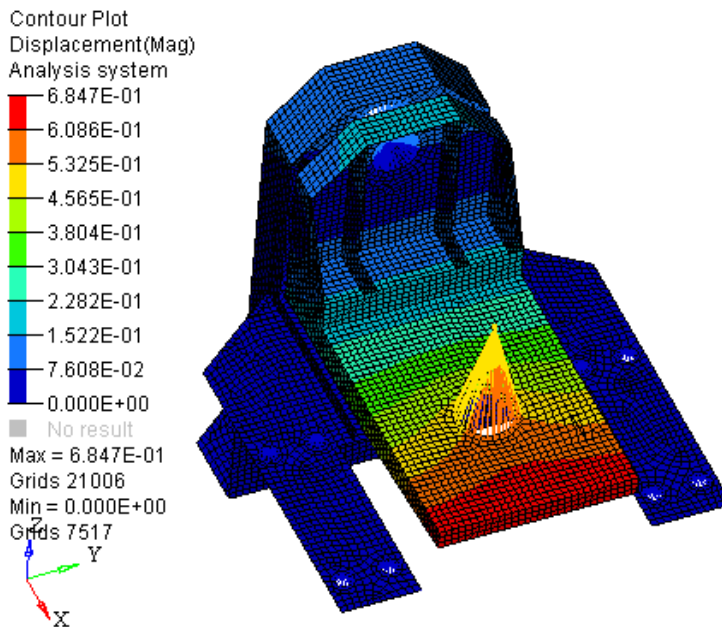


Figure 167 Contour plot resulting from the static analysis of the roto-tilting table in the $B = 0^\circ$ configuration

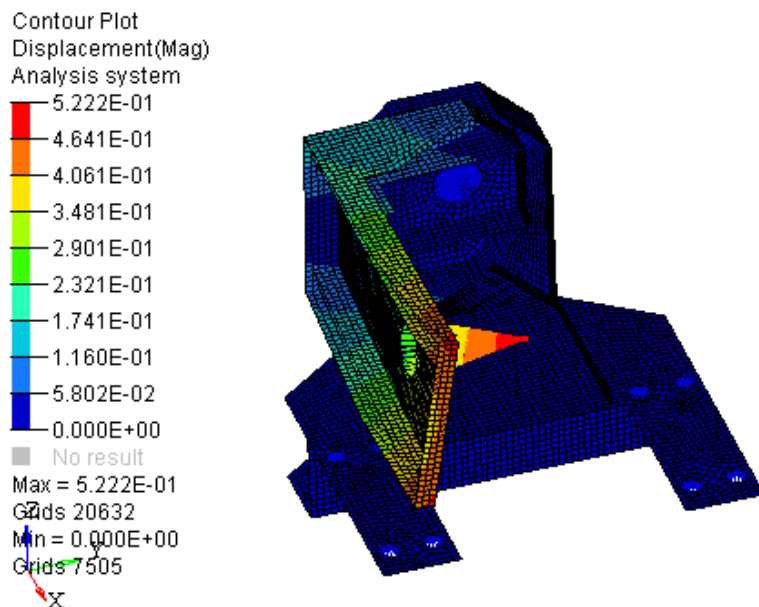


Figure 168 Contour plot resulting from the static analysis of the roto-tilting table in the $B = 90^\circ$ configuration

Finally, a free-size analysis has been performed on the configuration reported in Figure 166 to optimize the weight of each single part of the roto-tilting table. The input thickness for the analysis was 3 mm, and the load configuration was the same one of the static analysis for the $B=0$ position. The result of such analysis is shown in Figure 169. The shape of some components of the roto-tilting shape has been modified accordingly and the final configuration is reported in Figure 170.

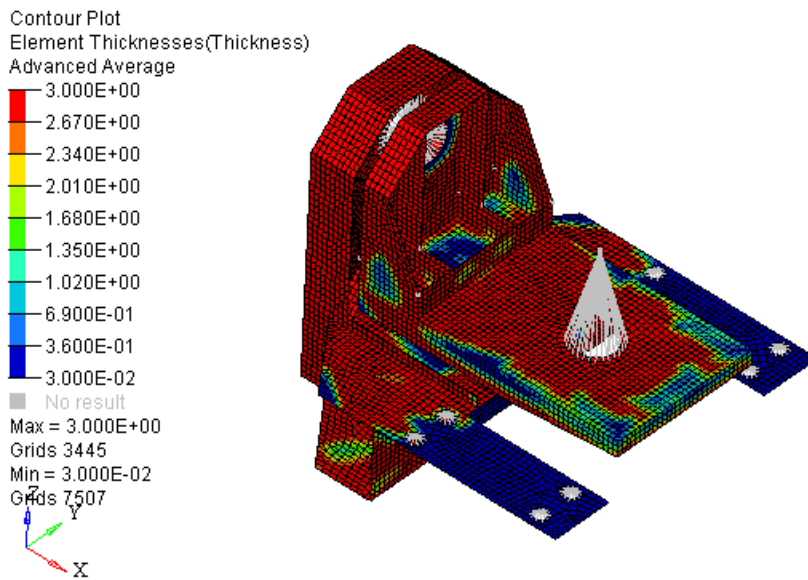


Figure 169 Contour plot resulting from the free-size analysis

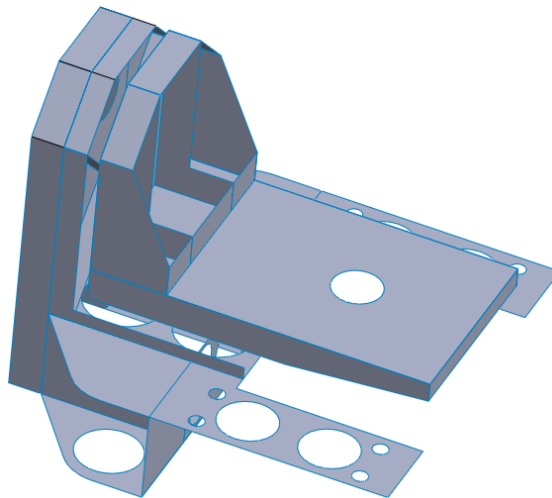


Figure 170 The roto-tilting table (only the midsurface is shown) after the modifications carried out looking at the results of the free-size analysis

At this point the detailed design of the table has been carried out as shown by Figure 171.

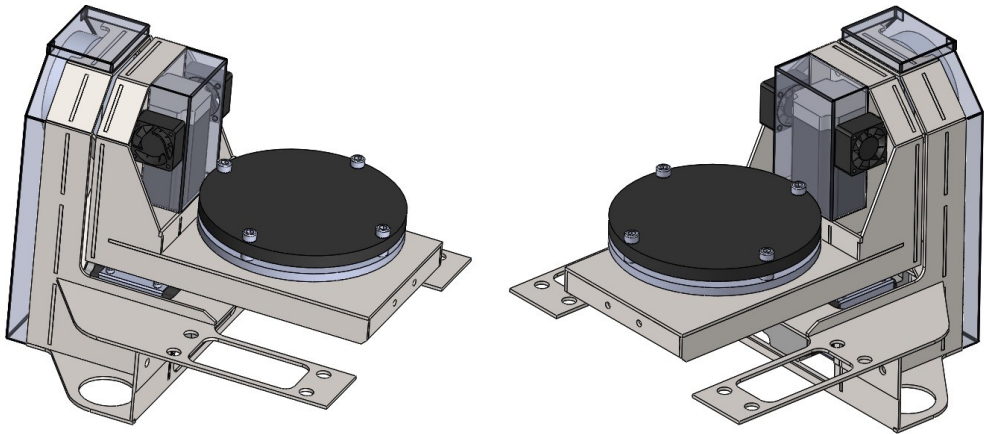


Figure 171 The complete 3D model of the roto-tilting table

The 2D drawings of the sheet metal parts have been created and every part has been manufactured using laser cutting.

The supports for the bearings have been milled from an aluminum block (Figure 172, Figure 173), while the shaft of the B table has been created turning a steel bar.



Figure 172 Milling of one of the bearing supports

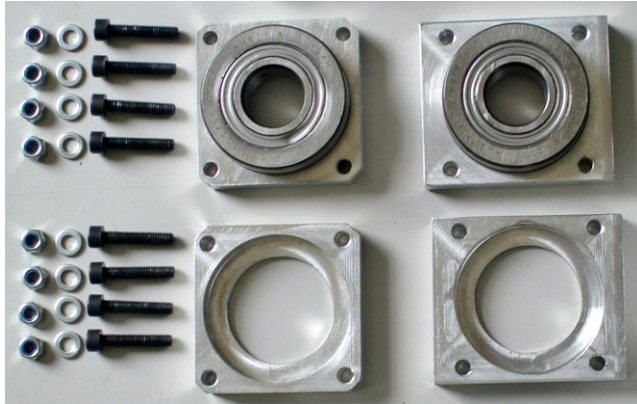


Figure 173 The bearing supports of the B and C drives. The bearings are shown inserted in the supports.

The C table has been obtained milling a 10 mm thick steel plate (Figure 174)



Figure 174 Milling of the C axis table (left) and final result (center and right)

Once every component has been manufactured, the sheet metal parts have been assembled together to test the connections (Figure 175) and then welded (Figure 176)

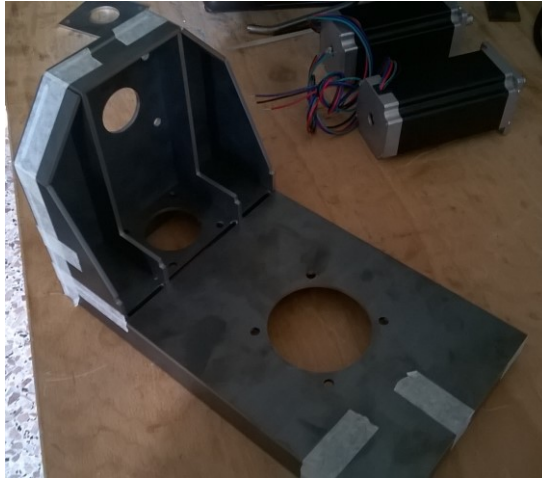


Figure 175 The B table assembled before the welding operations

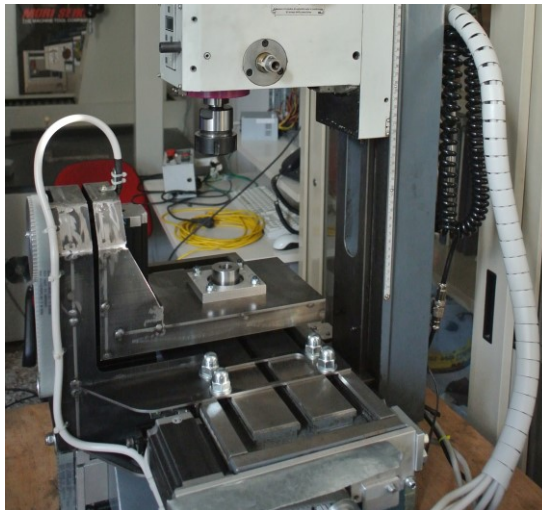


Figure 176 The complete roto-tilting table after the welding operations mounted on the machine for testing purposes

Finally, the table has been painted (Figure 177) and installed on the machine (Figure 178).

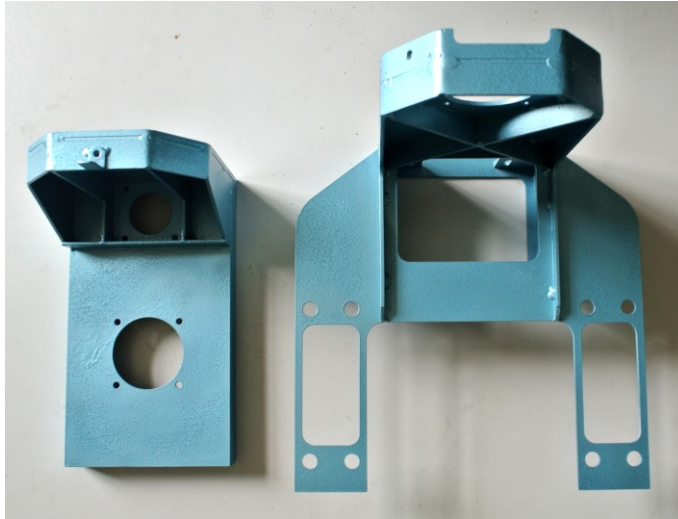


Figure 177 The table and the frame of the roto-tilting table

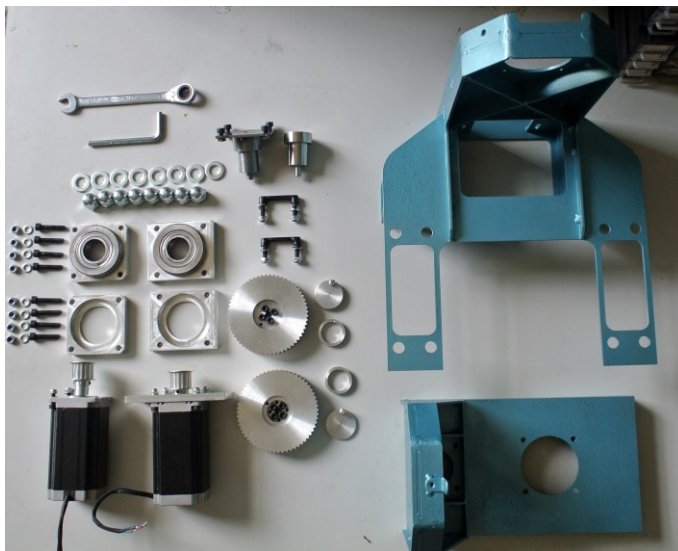


Figure 178 All the components of the roto-tilting table

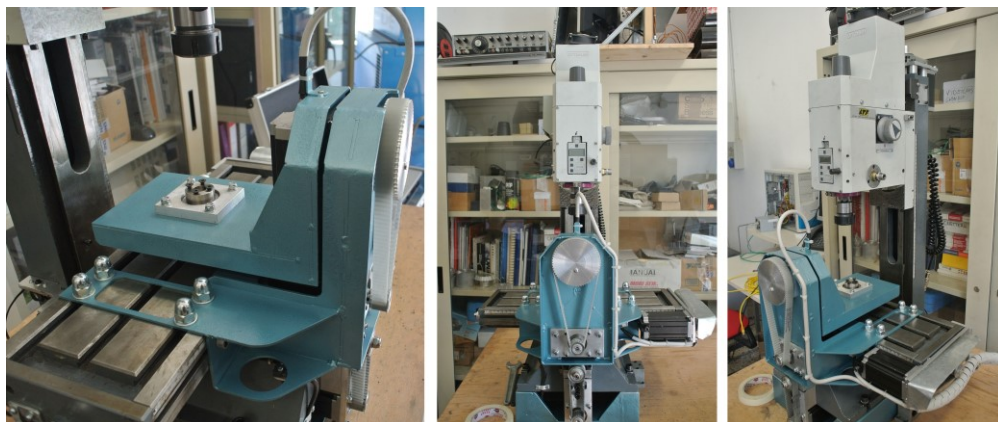


Figure 179 The roto-tilting table mounted on the machine

An important detail of a roto-tilting table for WAAM operations is the connection between the ground cable of the welding machine and the rotary table. In the case of the presented activity, the solution is depicted in Figure 180.

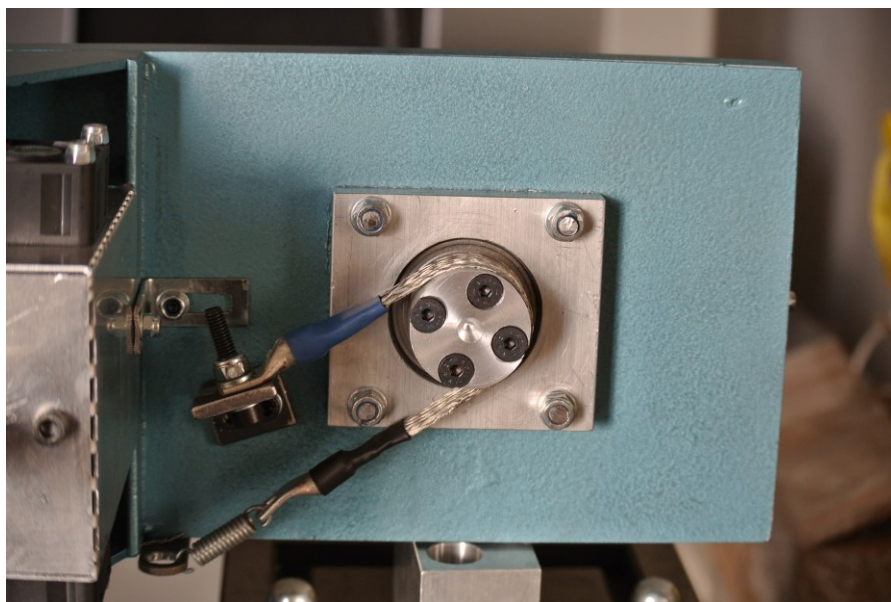


Figure 180 The solution adopted to connect the ground cable of the welding unit to the rotary table

The substrates used for the production of components can be obtained through laser cutting from a metal sheet of the desired material and can be attached to the table of the machine thanks to four threaded holes. Four spacers are inserted between the substrate and the table to let the air flow in the interspace and to limit the heat flow from the substrate to the table of the machine (Figure 181).

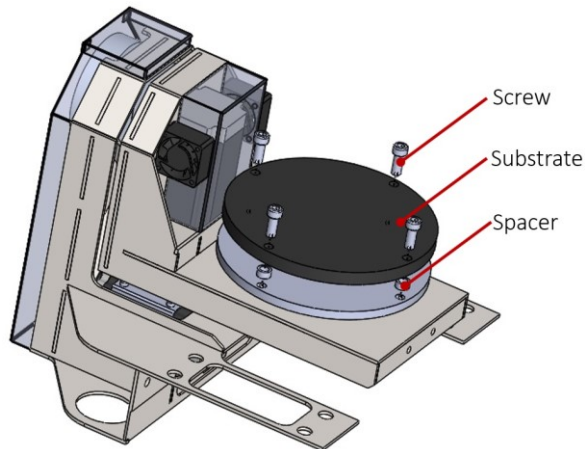


Figure 181 Exploded view of the system to attach the substrate to the rotary table

Cooling fans have been installed around the motors of both the B and C axis and also below the B table to cool down the belt that is directly in contact with the C axis shaft.

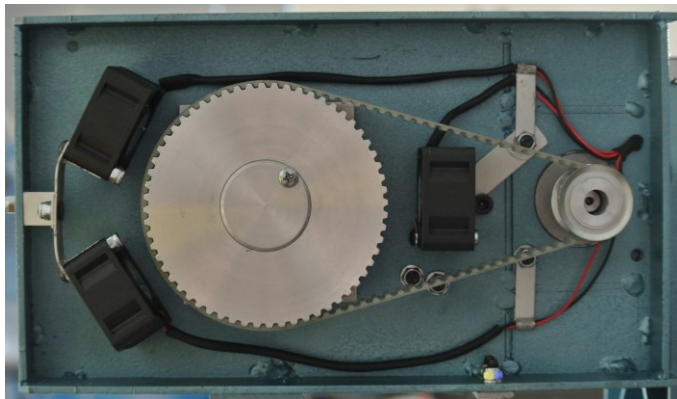


Figure 182 The disposition of the cooling fans for the belt of the C axis

4.2.3. The welding unit and the design and construction of the torch support

A Prestomig 200MP welding unit by SAF-FRO (Figure 183) has been selected for the 5-axis WAAM machine presented in this chapter.



Figure 183 The Prestomig 200 MP by SAF-FRO

The Prestomig 200 MP is a professional synergic welding unit and is equipped with a manual torch (Figure 184).



Figure 184 The WMT2 manual torch

Regarding the interface between the numerical control and the welding machine, the idea is to set the welding parameters manually through the LCD display (Figure 185) and knobs on the welding machine; then the numerical control will send an on/off signal to the welding machine using a simple relay.

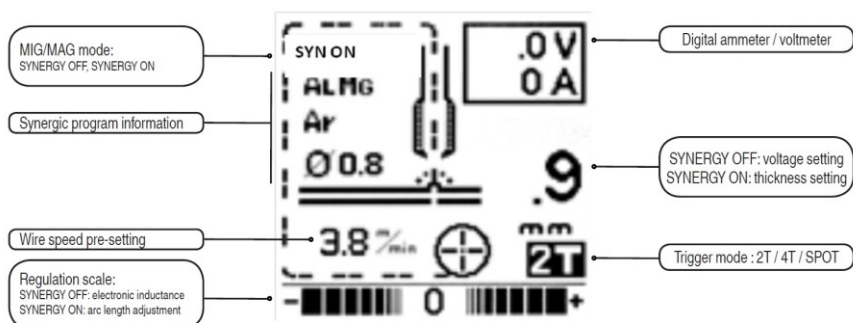


Figure 185 The LCD screen of the welding unit with an explanation of the adjustable parameters

Moreover, it was necessary to design and build a support to attach the torch to the head of the machine. It was decided to leave the original spindle unit on the machine to be able, in the future, to perform also milling operations. Therefore, the welding torch has been attached on the left of the spindle box. To assure no interference between the spindle and the torch, the torch itself has been mounted on a pre-assembled linear drive moved by a stepper motor. This motor is the sixth one that the numerical control of the machine will have to control. With this arrangement, the welding torch can be retracted when performing milling operations (Figure 186). Even if the torch is mounted on the left, the X axis travel is long enough to let both the torch and the axis of the spindle covering the required length of 150 mm. The torch has been disassembled to be mounted on the support. Moreover, an extension tube has been attached to the original torch tube to obtain the desired length. The linear drive is covered by an aluminum carter to avoid welding spatter intrusion and for safety reasons (Figure 186). While disassembling the torch, the cables of the manual switch have been individuated and connected to an output of the numerical control (refer to next section for details)

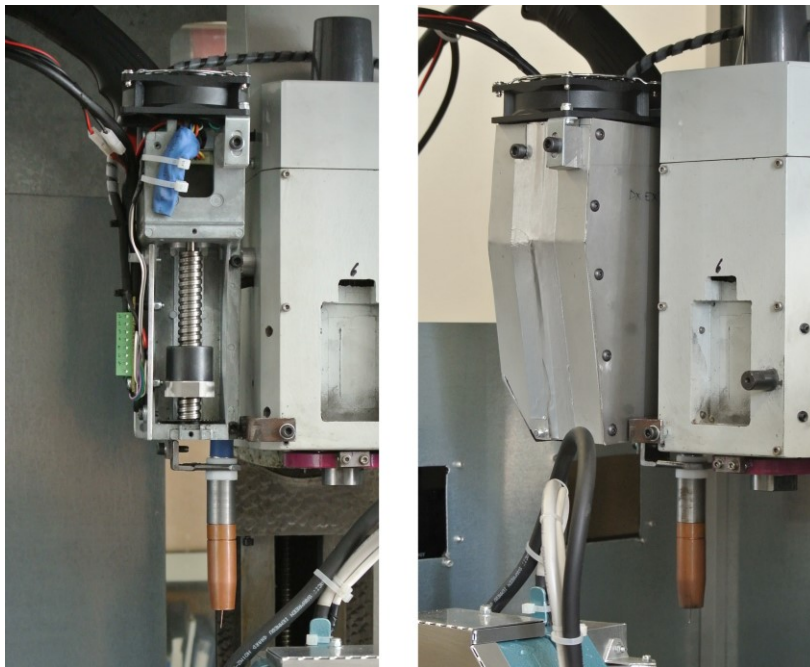


Figure 186 The support for the torch

4.3. The implementation of the numerical control

The numerical control of the presented five-axis WAAM machine has the following characteristics that will be explained in this section:

- Simultaneous control of six axis (Table 26) moved by stepper motors;

Table 26 Axes nomenclature and description

Axis Name	Notes/Description
X	Linear
Y	Linear
Z	Linear
B	Rotary
C	Rotary
A	Linear (torch axis)

- On/off output for the torch;
- On/off input for a signal from a photoresistor;
- The numerical control is PC-based. This means that, from a hardware point of view, the processing unit of the numerical control is a common pc with a specific software installed in;
- The numerical control is low-cost;
- Input for the emergency stop button;
- Input for the limit switches.

For the sake of simplicity and for the low-cost software and hardware solutions available in the market, a PC-based configuration has been chosen. Therefore, the numerical control is composed of the following hardware (Figure 187):

- **PC**
The PC is the processing unit of the numerical control. A special software installed on it is able to read the g-code and send output signals to a breakout board through a parallel or USB interface;
- **Breakout board**
This is an integrated circuit board that receives the signals from the computer (elaborated by the numerical control software installed in the computer itself) and send those to the drivers;
- **Drivers**
The drivers power the phases of the motors depending on the signals coming from the breakout board. The output of the drivers is connected to the motors, while these receive in input the signals from the breakout board and power from a power supply. Controlled-current and controlled-voltage driver exist. The drivers used in the presented application are controlled-current type; this means that these take care of keeping constant the selected value of current in the phases of the motor;
- **Power supply**
The power supply provide power to the drivers and, so, to the motors.

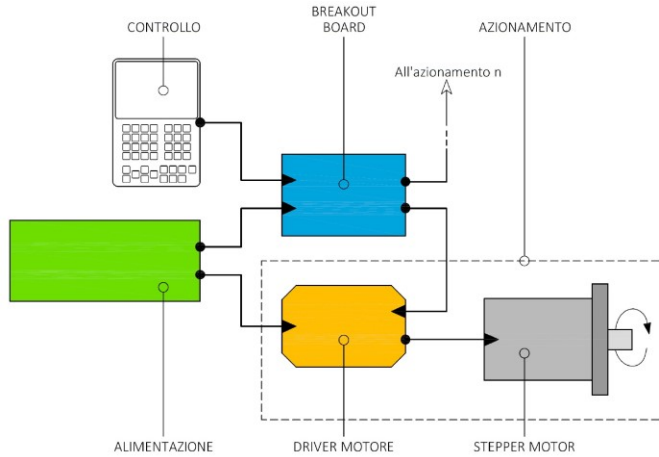


Figure 187 Layout of the numerical control (only one driver and one motor are shown)

The software installed in the PC of the numerical control is MACH3 from Newfangled Solutions [65]. It is a very powerful and low-cost CNC software able to control many axes. The interface of the Mach3 software is customizable. A specific graphic user interface has been developed for the present application (Figure 188) including all the needed features.

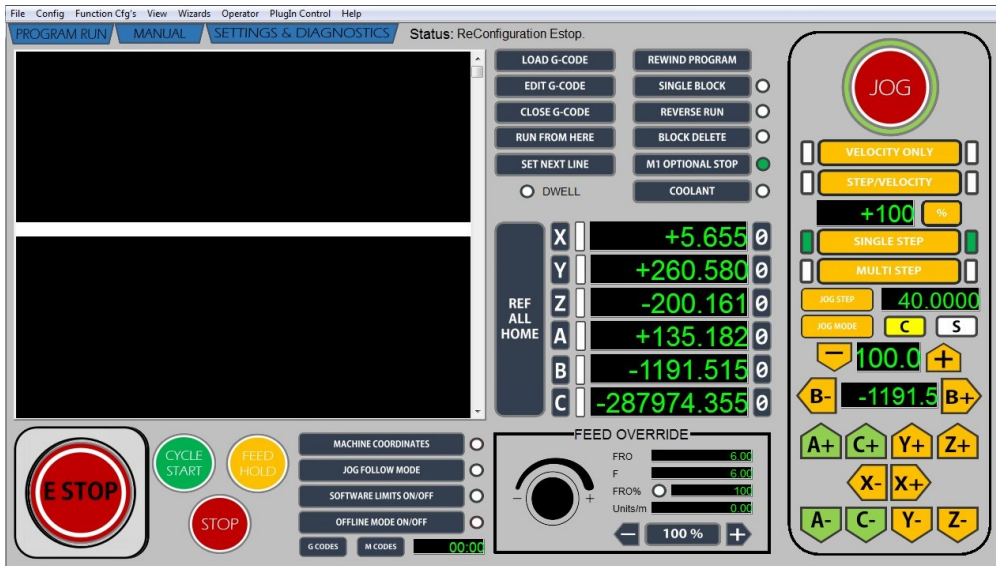


Figure 188 The custom graphic user interface of the Mach3 software

The Mach3 software offers also a series of tool to set up the machine, such as the definition of the speed profiles for the drives (Figure 189), or the steps per millimeter/degree calculator

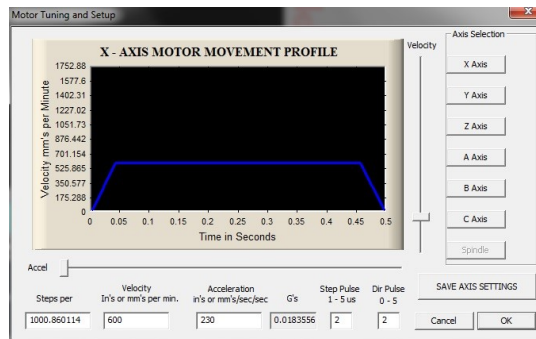


Figure 189 Mach3 motor setting window

The breakout board selected for the machine has a USB interface and is named DDSM6V5.0 (Figure 190).



Figure 190 The USB breakout board used for the project

This breakout board can control up to six axes and has several dedicated input and output (Figure 191).

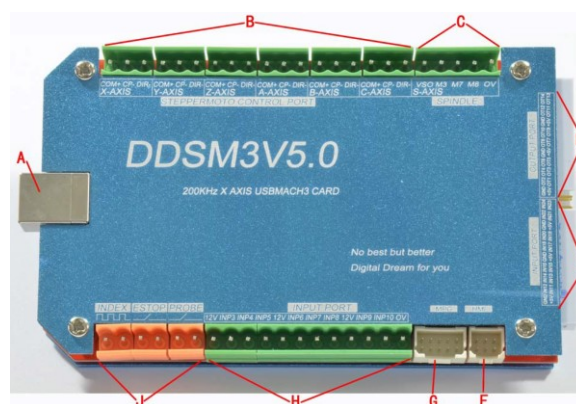


Figure 191 Image showing the input and output ports of the DDSM6V5.0 board

Referring to Figure 191, the M8 output can be used to turn on and off the torch. The other input and output are self-explanatory.

The DIV268M-5A are the drivers used in the numerical control. These are connected to each motor output of the breakout board as depicted in Figure 192.

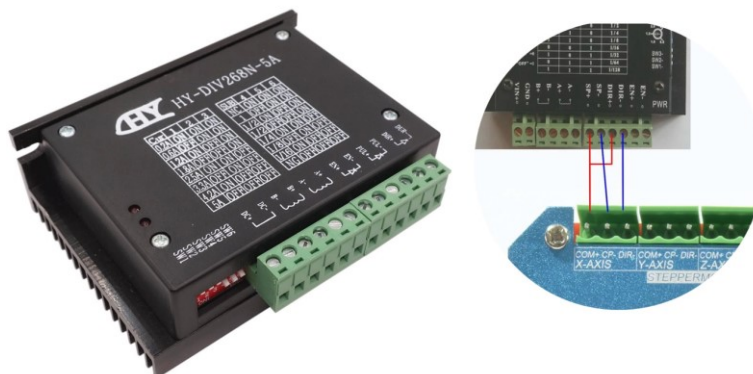


Figure 192 The driver used for the numerical control and the wiring diagram to connect it to the breakout board

An important function that has been implemented in the presented numerical control, is the capability of moving the axes of the machine only when the electric welding arc has ignited. This because if the machine axes are moved and the welding unit is turned on at the same time, the real point where the deposition begins will be different from the programmed one. This because the welding wire takes a while to reach the substrate or the previous layer. To let the numerical control understand if the arc has ignited or not a photoresistor has been used. The photoresistor is an electronic component able to change its resistance depending on the amount of light investing it. Since the welding arc emits light with a very high energy, the consequent change of the resistance of the photoresistor will be very high and easily detectable. In the present application, the resistance of the photoresistor is monitored by an Arduino UNO that is programmed to turn on or off a relay when such resistance is below a certain threshold value. The state change of the relay can be read by one of the input pins of the breakout board. On the Mach3 side, a special macro has been developed. It is invoked with a custom M instruction. Such instruction must be written in the G-code every time that the torch must be turned on. When called, the macro turns on the welding machine and “waits” for the consensus from the photoresistor circuit before moving the axes. When the state of the photoresistor circuit is on, it means that the arc has ignited, therefore the axes can start moving. The photoresistor is installed on the head of the machine and points toward the tip of the torch. It is placed inside an aluminum case that has the function of shielding the photoresistor from changes in the environmental light caused not by the welding arc ignition (Figure 193).

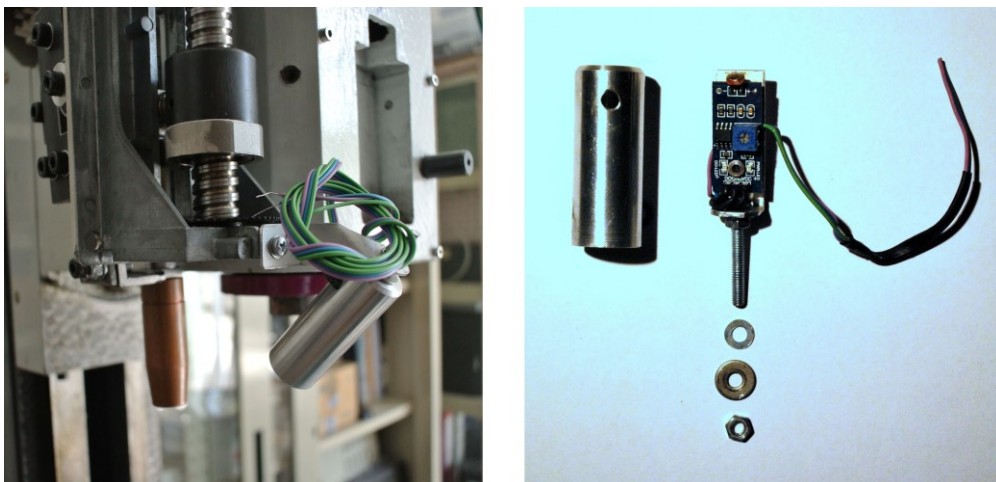


Figure 193 The photoresistor assembly mounted on the machine (left) and the photoresistor circuit and its housing (right)

To conclude, Figure 194 shows the electrical cabinet of the numerical control.

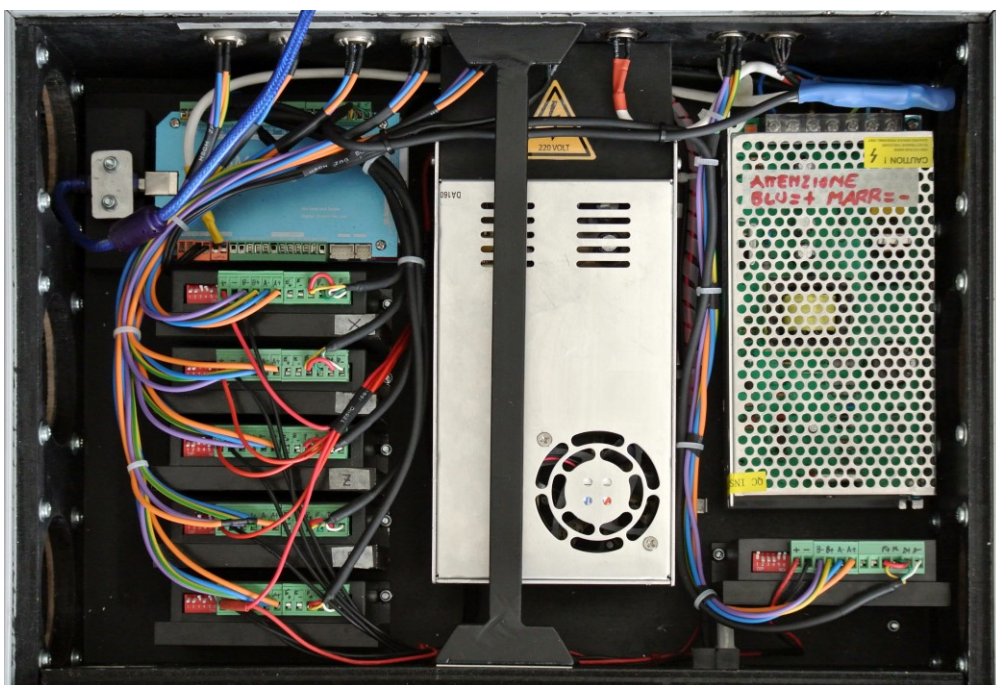


Figure 194 The electrical cabinet of the numerical control

4.4. Machine testing

After the mechanical design and construction of the machine and the development of the numerical control have been concluded, all the components have been assembled and the machine was widely tested.

First of all, many measurements were carried out (Figure 195) on the machine, mainly to check three important aspects:

- Parallelism between the X axis carriage and the B table in the B=0 position;
- Mutual orthogonality of the B and C axes;
- Intersection between the C axis and B axis.

Both these three aspects are very important, since the CAM and especially the post-processor must exactly know the geometrical parameters of the machine. The development of a post-processor is out of the scope of this thesis and the used post-processor assumes that the B and C axes are mutually intersecting and orthogonal. Fortunately, the results from all the above three measurements sessions were positive and it was possible to step to the further actions of the testing phase without any mechanical adjustments to the machine.



Figure 195 A measurement taken on the machine

The next step has been the setting and calibration of the rotary axis (Figure 196). This has been done thanks to the “set steps per unit” wizard of the Mach3 software.



Figure 196 A picture taken during the determination of the steps/degree ratio for the C axis

Finally, many part programs have been launched “in air” and then real welding tests have been performed (Figure 197).

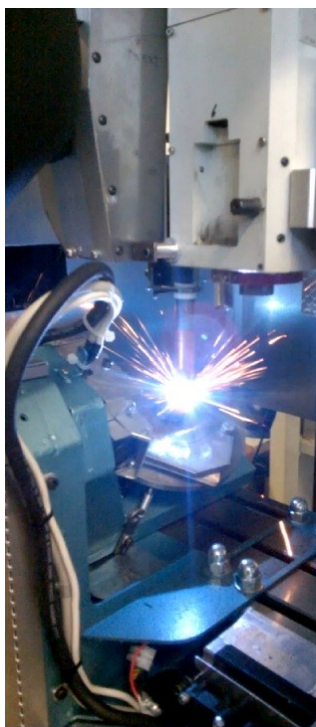


Figure 197 The five-axis WAAM machine during a deposition test

A detailed checklist with all the sequences of operation to warm up and use the machine has been produced to easily use the machine. The checklist must be followed every time that the machine is turned on to be sure to achieve a successful deposition operation and avoid damages to the machine itself. Two pictures of the ultimated five axis machine are reported in Figure 198.



Figure 198 Two pictures of the 5-axis WAAM machine

5. A vertical 5-axis CAM software for WAAM

The interesting application of the five-axis deposition for WAAM presented in section 1.3 must be empowered by a valuable CAM software solution to be effective. In literature many works are available regarding 5-axis toolpath generation for direct energy additive manufacturing technologies and both feature-based and non-feature-based solutions have been adopted. Some of those generate a toolpath for indexed operations. This means that the five-axis of the machine are not used simultaneously: the rotary axes are used to orient the part and then the linear axis do the deposition job to build a feature of the part. When the feature is concluded the rotary axes move the part to build the next feature (Figure 199).

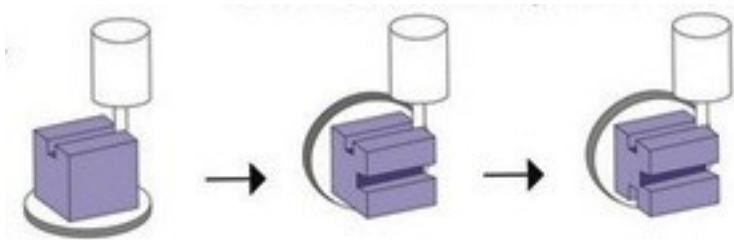


Figure 199 An example of indexed five-axis operation

Other algorithms can generate a toolpath in which all the five axes are moved simultaneously resulting in a continuous five-axis deposition.

Both STL files and parametric CAD data are taken as input by the algorithms presented in literature. In the first case, a slicing approach for toolpath generation is generally used, while in the second case the parametric data of the surfaces included in the file can be extracted and used to calculate the toolpath (Figure 200). However, the slicing approach can be used also in the case a parametric CAD file is taken as input, if needed. Indeed, there are many algorithms in literature that can be used to calculate the intersection between a BRep and another BRep, or between a BRep and an infinite plane.

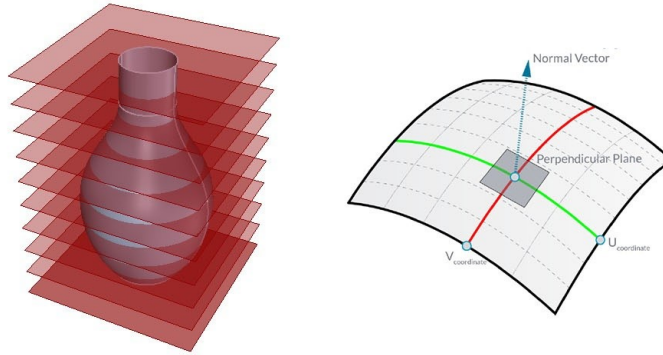


Figure 200 Slicing approach (left) and surface isocurve extraction (right)

Kamioka et al. [57] proposed a general approach to manufacture elbow pipes using a four-axis WAAM machine and varying the deposition parameters (especially the deposition feed) to compensate the variable distances between the consecutive section calculated by the algorithm. Varying the deposition speed results in different dimensions of the bead and therefore a variable height can be achieved. This approach requires a good characterization of the welding power unit, since it is necessary to exactly know how a difference in the deposition speed affects the height of the bead. Moreover, the welding process could not be stable for certain deposition speed that therefore must be avoided during the deposition procedure (Figure 201).

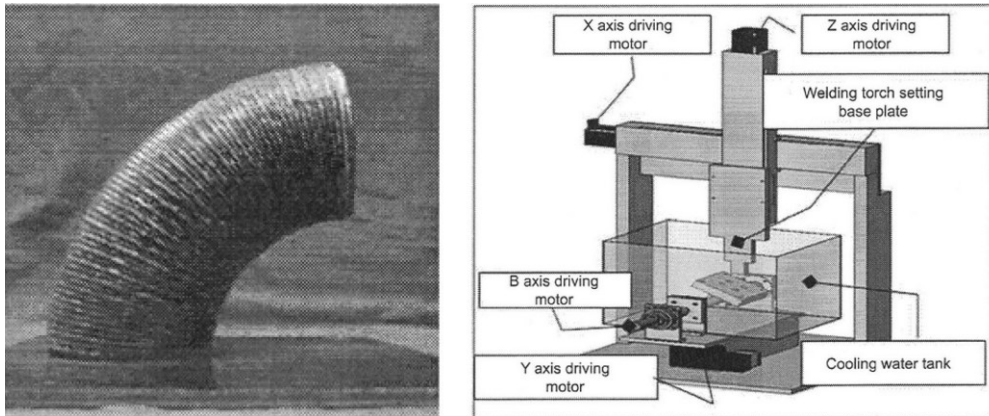


Figure 201 The elbow pipe (left) and the machine used to produce it (right) (from [57])

Xiangping et al. [74] showed an algorithm to generate the toolpath for freeform shapes, especially dedicated to ducts. The toolpath is obtained through a segmentation of the input geometry and a consequent slicing of each of the obtained sections. The segmentation is carried out looking at the local curvature of the input geometry: low curvature will result in a long segment, while high curvature will result in multiple short segments (Figure 202)

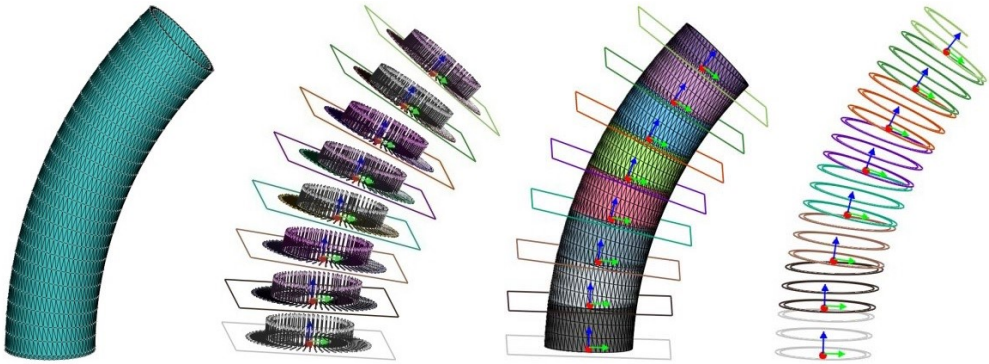


Figure 202 An example of application of the algorithm by Xiangping to a curved tube. From left to right: input mesh, normal and tangent vectors, segmented mesh, output slices (from [74])

Dwivedi et al. [75] used the so called “morphological skeleton” of the geometry as a basis for the toolpath calculation. Indeed, after the skeleton curve has been obtained, the toolpath can be obtained slicing the input geometry with planes that are orthogonal to the skeleton curve itself (Figure 203).

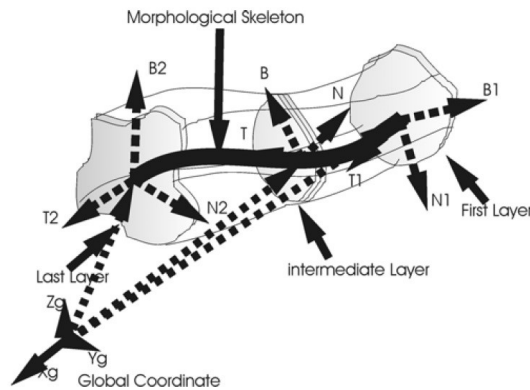


Figure 203 Global coordinate and Frenet frame for skeleton (from [75])

In the work by Ding et al. [76] a multipurpose algorithm has been developed. Such algorithm takes an STL file as input and it can carry out a segmentation and defeaturing of the part. The defeaturing phase aims at eliminating or modifying the features of the input geometry that cannot be created using the selected additive technology. Indeed, especially holes and small features are not easy to be manufactured using a DED AM technology or cannot be created at all. Therefore, it is useless to generate the toolpath for these features, since the deposition process won't be able to manufacture those because of its resolution. Such features must be eliminated from the toolpath and will be created after the deposition process using traditional subtractive technologies (Figure 204).

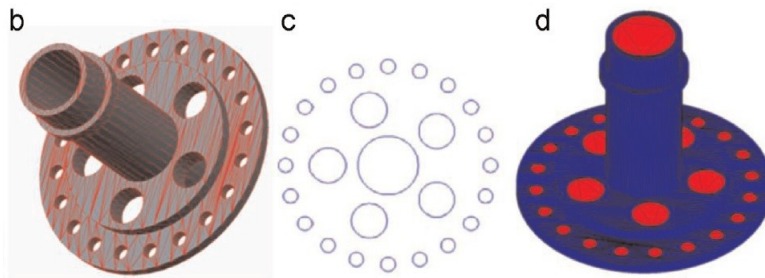


Figure 204 Defeaturing of an STL geometry: (b) original STL geometry, (c) detected holes, (d) simplified model without holes (from [76])

The algorithm presented by Ding et al. is able to carry out a segmentation of the input geometry depending on its taxonomy and then to perform a slicing operation on each of the segments (Figure 205). The outcome of this method is a deposition toolpath for indexed operations.

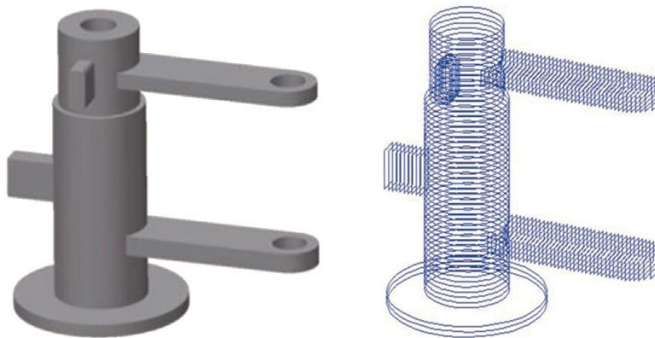


Figure 205 Input STL model (left) and resulting deposition toolpath (right) (from [76])

Kapil et al. [25] et al presented a tool to calculate the disposition toolpath for open impellers and many other complicate components using both a planar slicing method and a non-planar slicing method.

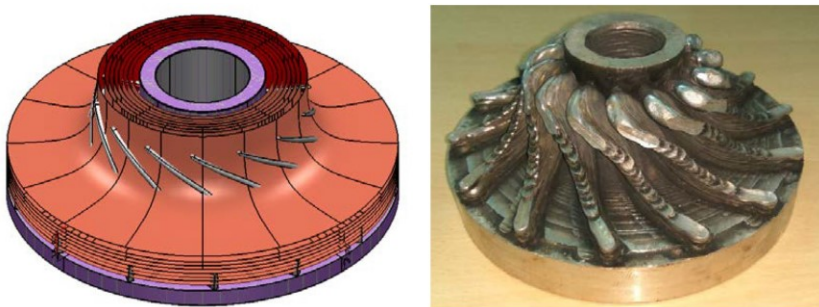


Figure 206 Non-planar slicing procedure for an open impeller (left) and WAAM manufactured impeller (right) (from [25])

Finally, Carter et al. [77] implemented a method to obtain a deposition toolpath for multi-axis AM technologies reversing a traditional milling toolpath (Figure 207).

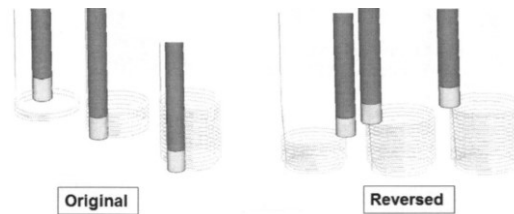


Figure 207 Original milling toolpath (left) and the additive toolpath obtained reversing the milling toolpath (right) (from [77])

Regarding commercial software solutions available in the market, many big companies propose multipurpose CAM software for direct energy deposition technologies. Some years ago, Siemens introduced in the market its NX Hybrid Additive Manufacturing CAM software for direct energy deposition technologies [78]. This has a feature-based approach and requires many inputs from the user that must select the surfaces and zones of the part for which the deposition toolpath must be calculated (Figure 208).

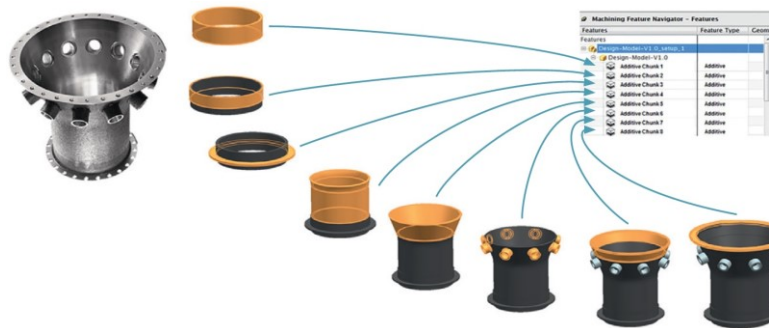


Figure 208 The steps to generate the toolpath for a complicate part (source: Siemens)

It is a powerful software that also includes the kinematic simulation of the deposition process. The simulation of the machine movements and of the growing part are mandatory features for a reliable 5 axis CAM software. Indeed, it is fundamental to virtually test the calculated deposition toolpath before testing it in the real machine to understand whether collision would occur thus avoiding potentially fatal damages to the machine itself. Another advantage of this software is the integration with the traditional five axis CAM software for milling operations. This aspect makes the CAM software from Siemens very suitable for the programming of hybrid machines, since it is possible to switch between additive and subtractive toolpath calculation during the toolpath setup.

Autodesk introduced multi-axis additive capabilities in its PowerMill CAM software [79] that is also used to calculate the toolpath in the WAAMPeller project [80] (Figure 209).

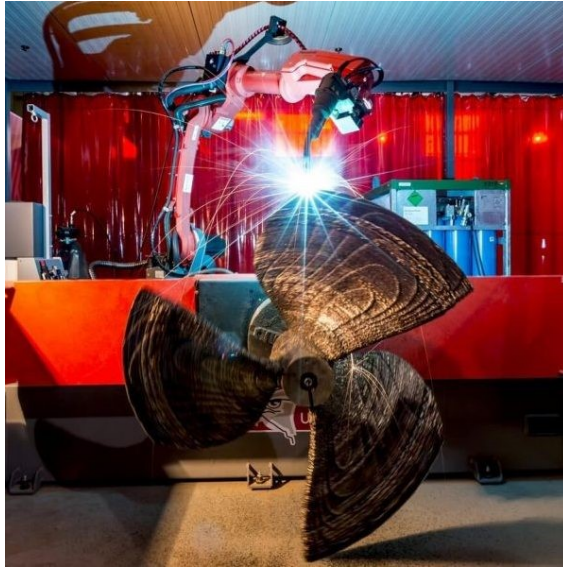


Figure 209 The production of a WAAMPeller (a marine propeller) (from [80])

Finally, Dp Technology developed an additive module to be integrated in its ESPRIT CAM software [81] (Figure 210)

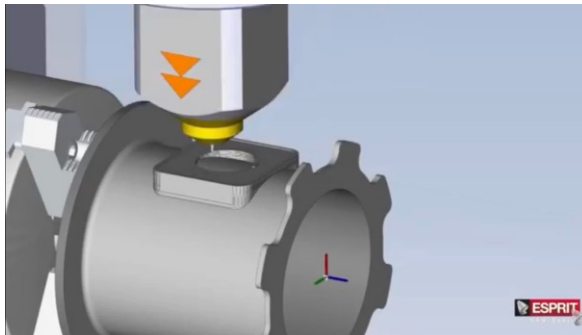


Figure 210 An image of the additive toolpath simulation module integrated in the ESPRIT CAM software (from [81])

Both the products from Dp Technology and Autodesk feature additive and milling capabilities and can simulate the deposition process.

In the present thesis a five-axis toolpath generation framework for freeform geometries is presented. The presented software, implemented using Grasshopper, is especially addressed to thin walled components and has a modular approach. This means that the developed tool is composed by several sub-modules each one dedicated to a different geometrical shape. There is a module for open impellers, another for twisted blades and two for freeform ducts (Figure 211).

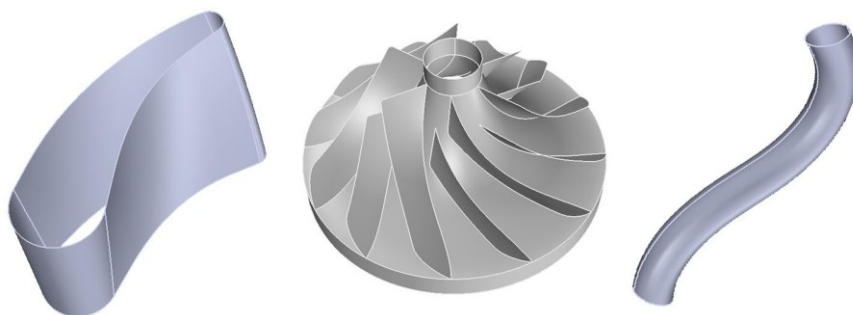


Figure 211 The three geometrical shapes the developed modules of the presented five-axis CAM software are addressed to. From left to right: twisted blade, open impeller and freeform duct

In the future the addition of new toolpath calculation modules will be possible. Moreover the 3-axis toolpath calculation modules and the 5-axis ones can be integrated in a unique overall framework that can be used to perform the calculation of pure three-axis, five-axis continuous and five axis indexed deposition toolpaths. More details are reported in the next sections. Each module presents a novel method and algorithm for the calculation of the deposition toolpath of the feature is addressed to.

As for the 3-axis CAM framework, the input geometry is the midsurface of the part, since all the algorithms are dedicated to thin-walled components (Figure 212).

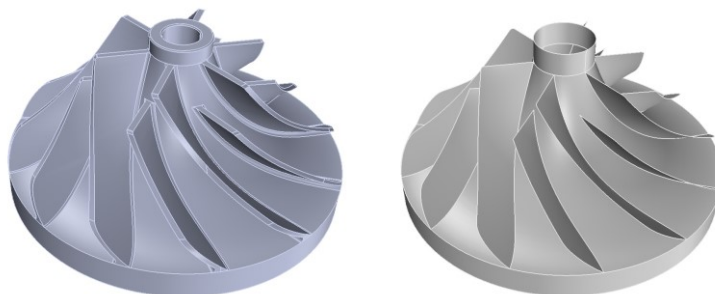


Figure 212 CAD model of the final part (left) and the midsurface CAD model that is the input for the presented CAM software (right)

5.1. Toolpath calculation module for open impellers

Open impellers like the one showed in Figure 213 are very suitable to be produced using five axis WAAM operations.

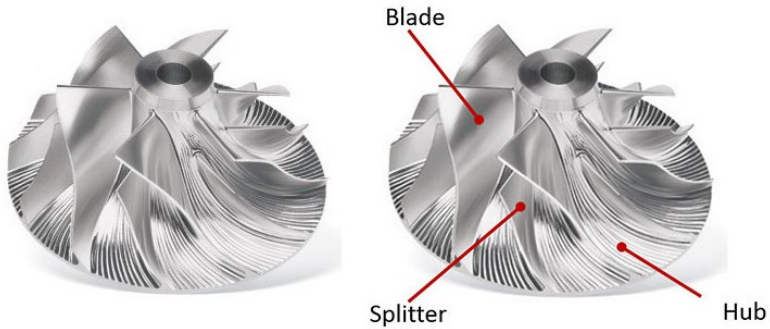


Figure 213 Open impeller (left) and impeller taxonomy (right)

Moreover, these are an interesting case study for hybrid manufacturing. Indeed, an impeller like the one showed in Figure 213 can be manufactured using one of the following three approach:

- 1) Machining from stock (Figure 214). In this case the impeller is obtained through five axis milling operations, starting from a solid stock obtained turning a bar.



Figure 214 Machining of an open impeller from stock

- 2) Using additive manufacturing and milling (Figure 215). Both the hub and the blades of the impeller can be manufactured using an additive manufacturing technology (powder bed or direct energy deposition), and then milled using a traditional 5-axis machine.



Figure 215 Impeller manufactured using WAAM technology (left) and its post finishing operation (right) (source: Gefertec)

- 3) Using a hybrid manufacturing approach. In this case the hub of the impeller is obtained turning a bar and the blades are added on the hub itself using a direct energy deposition additive manufacturing technology (Figure 216).

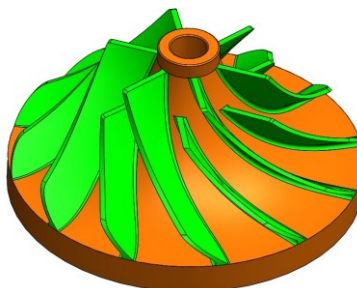


Figure 216 A cost-effective way to produce an impeller is to obtain the hub (orange part in the picture) using traditional subtractive technologies, and to add the blades (green) using a direct energy deposition additive manufacturing technology

This approach is very interesting in terms of time saving. This because the hub has a simple shape and therefore can be obtained in a very fast way using traditional techniques like turning. Regarding the blades they can be added using additive manufacturing that can achieve a near-net-shape geometry. This additive process is usually faster than the rough milling operation, especially for hard materials.

This hybrid approach is used also for closed impellers by Sulzer [82] that achieves great time savings in the manufacturing time respect to other traditional production technologies used for closed impellers (Figure 217, Figure 218)



Figure 217 Hybrid building procedure for a shrouded impeller (from [82])

Production time for different manufacturing processes (days)

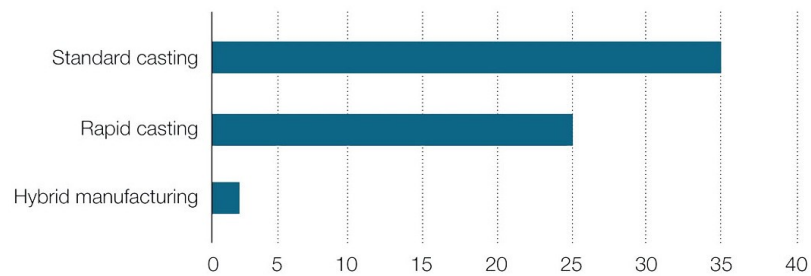


Figure 218 Time savings achieved using the hybrid production approach for a closed impeller (from [82])

The presented toolpath calculation module for open impellers takes care of calculating the deposition toolpath only for the blades of the impeller. Indeed, it is assumed that the hub is manufactured through a traditional subtractive technology like turning. If it is necessary to manufacture also the hub using AM technologies, it is possible to use one of the 3-axis strategies for tubulars presented in section 3.4.5 or a specific 3-axis deposition strategy developed for bulky impeller hubs and here presented. Such strategy creates a deposition toolpath to manufacture a solid impeller hub. The user must select the surfaces composing the hub. Then a BRep to Plane intersection between such surfaces and a series of equally spaced planes is performed. The distance between the planes is equal to the layer height (Figure 219).

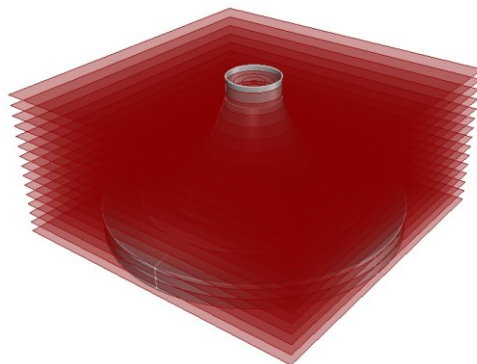


Figure 219 The input geometry of the impeller hub is intersected with a series of parallel and equally spaced planes

The result of such intersection procedure is a series of curves representing the intersection between the surfaces composing the hub and the intersection planes (Figure 220).

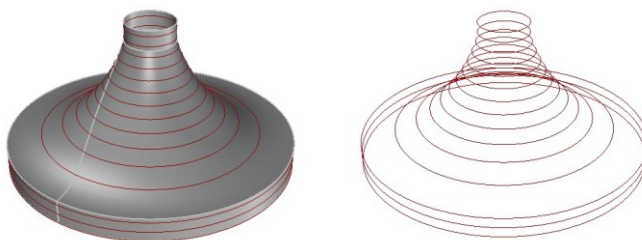


Figure 220 The result of the intersection procedure is a series of curves

Each curve is offset towards the inward direction until the minimum achievable dimension (Figure 221).

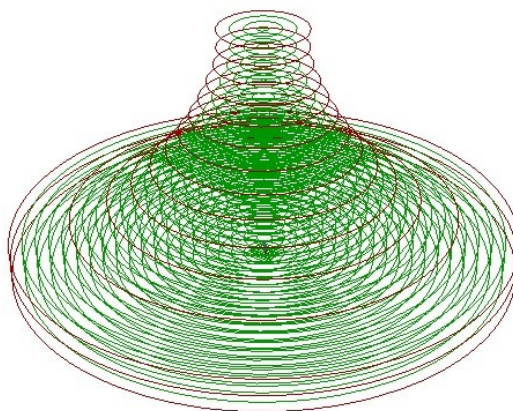


Figure 221 The green curves are the result of the offset procedure

The offset distance OD is given by Equation 53, where w is the width of the deposited weld beads that is an input, together with the layer height for the toolpath calculation module. The value 0.738 is taken from Ding et al [46] who researched about the optimal overlapping distance for adjacent welding beads.

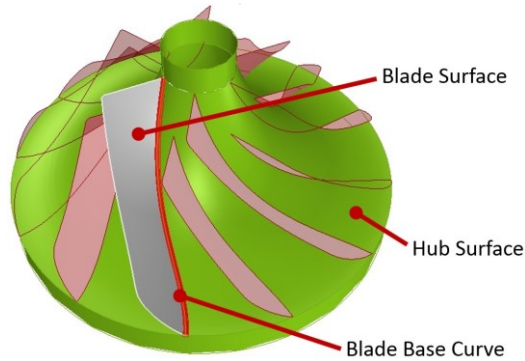
$$OD = 0.738 \cdot w$$

Equation 53

This way, the deposition toolpath to obtain a fully dense impeller hub is achieved. Regarding the generation of the deposition toolpath for the blades and the splitters, the procedure is as follows:

- 1) The user selects from the graphical interface the blades and the splitters in the order he wants those to be built.
For the sake of clearness, in the next lines both blades and splitters will be referred as “blades”. Moreover, the described operations are carried out for each of the blades selected by the user.

- 2) The base curve of each blade is extracted by the algorithm thanks to an intersection between the hub and the blade itself.



- 3) A series of planes orthogonal to the base curve is created. The distance between the planes will be the overall resolution of the toolpath and can be set half the resolution of the deposition process. Then an intersection between each plane and the surface of the blade is performed obtaining the result of Figure 222.

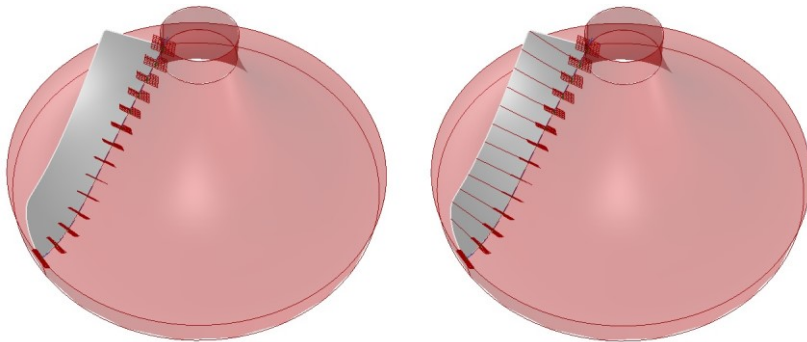


Figure 222 The planes orthogonal to the base curve of the blade (left) and the curves resulting from the intersection between such planes and the blade (right)

- 4) On each curve resulting from the intersection of the previous step, equally spaced points are generated and stored in a separated array (named Intersection Point Array 1, 2, ... n). Each array is ordered in a manner that the first point is the point closest to the hub and the last the one on the top of the blade. After this operation the first point of each of the arrays is picketed up and inserted in a new array (called Toolpath Curve Array 1, 2, ... n) that will contain all the points composing the deposition toolpath for the first layer of the blade. The same operation is repeated for the points in the second position of the Intersection Point Arrays and so on. The result of this operations is a series of arrays containing each one the points composing the deposition toolpath for the nth layer (of course the size of each array could be different).

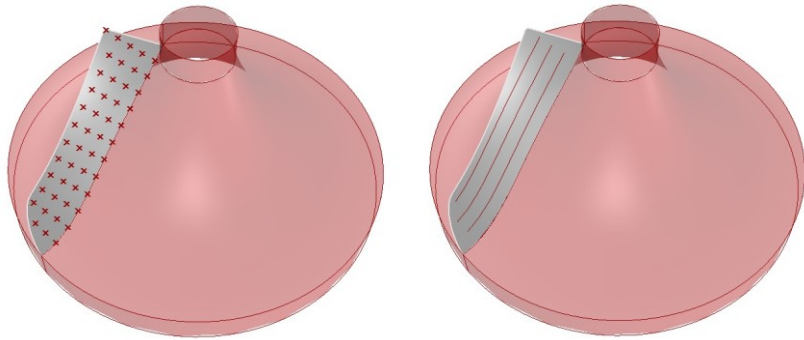


Figure 223 The generated points compose the deposition toolpath for one of the blades of the impeller

- 5) A polyline curve is created with the points contained in each of the Toolpath Curve Arrays. Later the curves are extended a little bit at both the extremes to be sure to cover all the surface of the blade (Figure 224). On each of the resulting curves a series of equally spaced points is generated; the distance between the points is equal to half the process resolution. Only the points laying on the surface of the blade are kept. All the points from one curve are loaded in a separated array named Toolpath Points Array 1,2, ... n. these points are the points constituting the deposition toolpath (Figure 225).

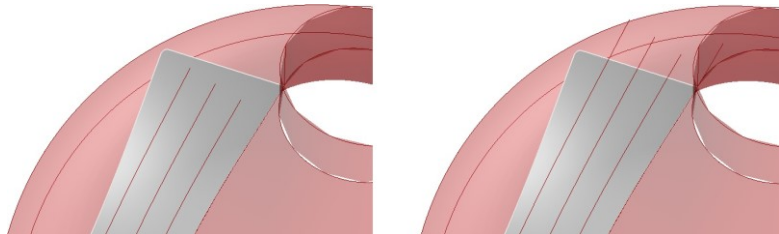


Figure 224 The curve obtained at step (5) before (left) and after the extension (right)

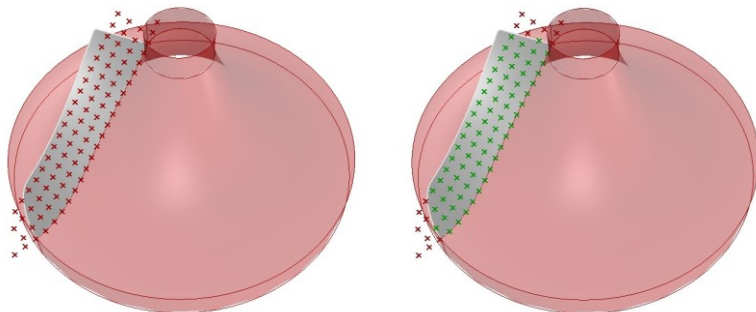


Figure 225 The points obtained on the extended curves (left) and the points valid for the deposition toolpath (green points in the right picture)

- 6) For what concerns the determination of the torch axis (TA), it is obtained as the vector tangent to the surface of the blade evaluated for each of the points contained in the Toolpath Points Arrays (Figure 226). The programmed point (i.e.) the controlled point of the torch will lay on the torch axis at a distance equal to the nozzle to work distance from the origin of the torch axis itself.

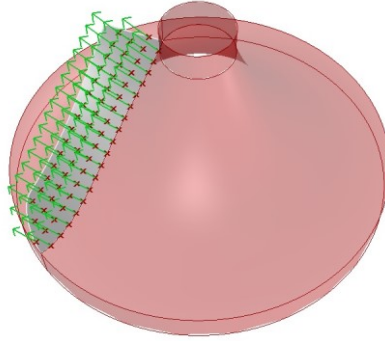


Figure 226 The final points composing the deposition toolpath (red crosses) and the torch axes (green vectors)

5.2. Toolpath calculation module for twisted hollow blades

The toolpath calculation module presented in this section is addressed to twisted hollow blades like the one reported in Figure 227.



Figure 227 A twisted blade

Aerospace components such as blisks usually feature that kind of blade geometry. The blisks are usually manufactured milling a solid block with a 5-axis milling machine (Figure 228).



Figure 228 Machining of a blisk (from [83])

However, this is a very time-consuming process, and could be interesting to use an approach similar to the one showed for the open impeller in section 5.1. So, the idea is to manufacture the hub using traditional subtractive technologies and the blades using a direct energy deposition technique. DMG mori shows an example of this manufacturing process; they use the Laser Powder Deposition AM technology to additively manufacture the blades of a blisk (Figure 229).

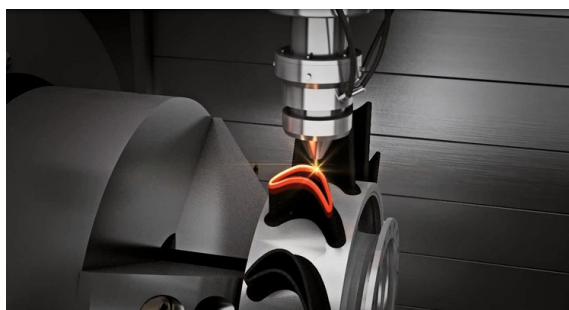


Figure 229 Blisk hybrid manufacturing (source: DMG Mori)

A turbine rotor can also be manufactured mechanically assembling a disk and a series of blades as shown in Figure 230.



Figure 230 The two ways to obtain a turbine rotor: hub and blades assembly (left) and blisk (right) (from [83])

In the left case of Figure 230, the blade can be manufactured using DED technologies such as WAAM. The material is deposited upon an already existing root as depicted by Figure 231 and suggested also by [74].

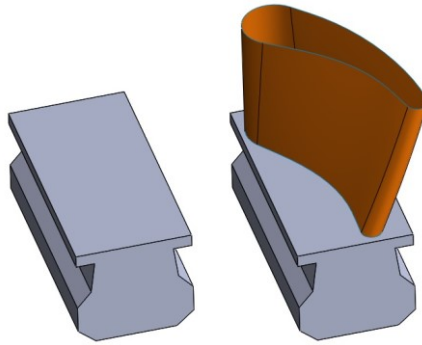


Figure 231 The root-shaped substrate (left) and the final component (right). The blade (orange part) is manufactured using WAAM

In this section a method to calculate the deposition toolpath for twisted blades is presented. The starting point is the midsurface of the blade. The algorithm is composed by the following steps:

- 1) The bounding box of the input geometry is calculated, and its height is extracted (Figure 232). The resultant value is the total height of the blade.

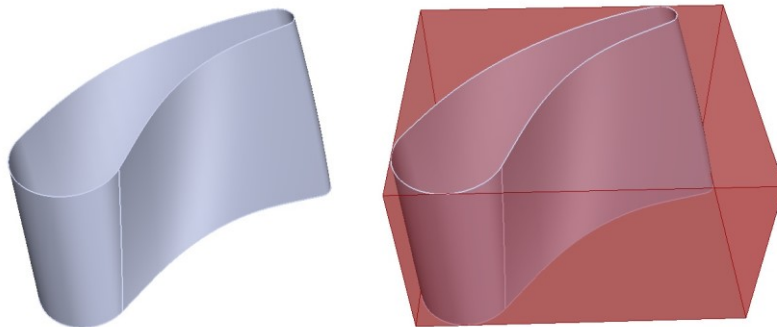


Figure 232 The input midsurface (left) and its bounding box (right)

- 2) The number N of layers to be deposited is calculated dividing the total height obtained at step (1) by the layer height.
- 3) A series of N equally spaced planes parallel to the base substrate with a step equal to the layer height is generated and an intersection between these planes and the input geometry is performed Figure 233.

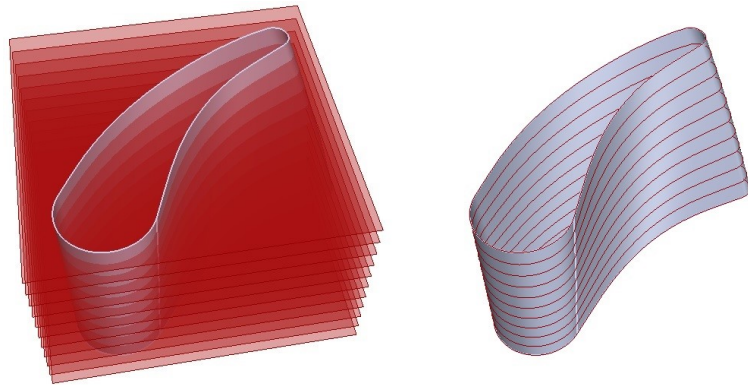


Figure 233 The slicing procedure (left) and its result (right)

- 4) On each one of the curves obtained at step (3) a series of equally spaced points is generated. The distance between the points is set to be equal to half the resolution of the used DED process that is an input the user must provide to the toolpath calculation module. A series of N arrays is created. Each one of the arrays in the series contains all the equally spaced generated points for one layer. These points compose the deposition toolpath (Figure 234).

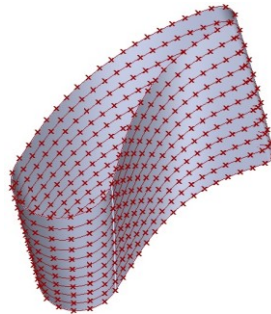


Figure 234 The points composing the deposition toolpath

- 5) To be sure that the start and end of each layer are not aligned, the arrays generated at step (4) are sorted in a manner the starting deposition point is in a random position of the original curve. To achieve this result, a random number between 0 and the size of the arrays is generated for each one of the arrays. Then, for each one of the arrays containing the toolpath points, the element with the index corresponding to the random points is set as the first one and the array is re-assembled again (Figure 235).

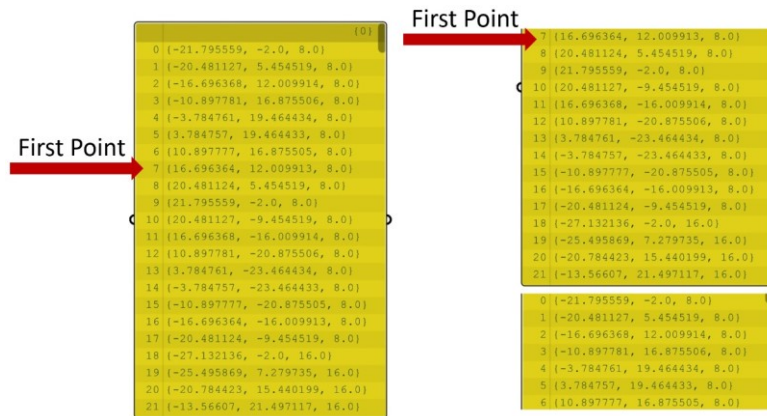


Figure 235 Original array (left) and re-assembled array (right)

- 6) The normal vector to the input midsurface is evaluated at each of the points contained in the arrays of step (5). For each layer an array containing all the normal vectors is created. Then a check on the normal vectors is performed to understand whether these point in the inward or outward direction. In the first case all the vectors are reversed. To understand if the vectors point in the outward or inward directions, an inside/outside BRep test is carried out.
- 7) For each point of the toolpath a plane is constructed using the point itself as origin, the normal to the surface as X axis and the vertical as Y axis (Figure 236).

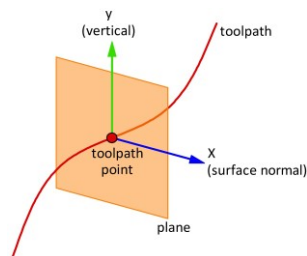


Figure 236 Definition of reference frame for every toolpath point

- 8) The torch axis for each point of the toolpath is calculated as the vector laying on the plane generated at step (7) and inclined respect to the normal (the Y axis of the plane generated at step (7)) of a cross angle Ω (Figure 237).

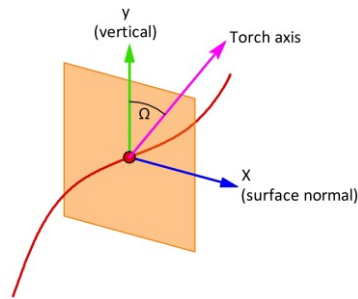


Figure 237 Definition of cross angle Ω and torch axis

The value of the cross angle is an input the user must provide to the toolpath calculation module

Figure 238 shows an image of the resulting toolpath with the torch axes. The layer height is exaggerated for the sake of clearness. The programmed point (i.e.) the controlled point of the torch will lay on the torch axis at a distance equal to the nozzle to work distance from the origin of the torch axis itself.

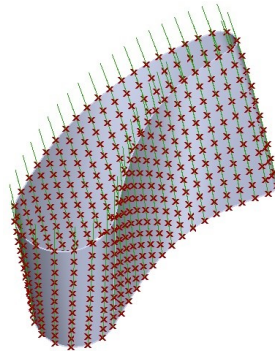


Figure 238 The points composing the deposition toolpath for a twisted blade (red crosses) and their torch axes (green vectors)

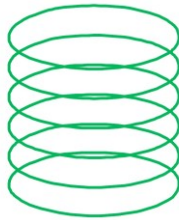
5.3. Toolpath calculation modules for freeform ducts

The presented 5-axis CAM framework features two module for the calculation of the deposition toolpath for freeform ducts like the one reported in Figure 239.

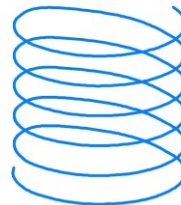


Figure 239 An example of freeform duct

The first module uses a slicing approach to generate the toolpath, while the second one outputs an helicoidal toolpath (Figure 240).



(a)



(b)

Figure 240 (a) Layer by layer toolpath, (b) Helical toolpath

Both kinds of toolpath have advantages and disadvantages that will be examined in the following lines. Basically, a helical deposition pattern results in a continuous deposition toolpath in which no start/stop of the arc are included, thus avoiding the related defects. However, using the helical strategies no internal features can be manufactured. For example, component like the one reported in Figure 241 cannot be manufactured.

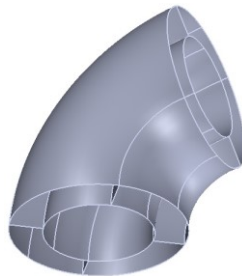


Figure 241 Elbow pipe with internal stiffeners

On the opposite, the slicing approach results in a layer by layer toolpath that allows for the generation also of internal features. The disadvantage is that the arc is shut off and started at least one time per layer, and this could result in the occurrence of defects.

Freeform ducts are very suitable to be manufactured using five axis deposition, and many examples are available both from the literature (as explained in the state of the art of this chapter) and from industrial applications like the one reported in Figure 242 and implemented by BEAM [84].

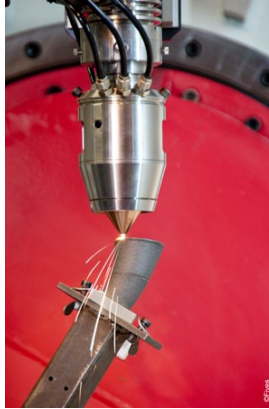


Figure 242 A freeform duct produced in a five-axis machine by Beam (from [84])

The geometrical input for both the modules is the midsurface of the component to be manufactured. For the module based on the slicing approach, the midsurface can be composed by an arbitrary composition of surface entities, while for the other one, the geometry of the duct must be composed of one unique surface entities or two symmetric halves (Figure 243). This is due to the functioning of the algorithms used to calculate the toolpath.

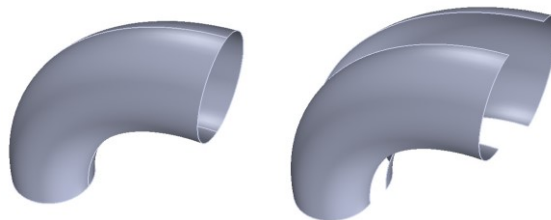


Figure 243 The midsurface of an elbow pipe composed by two halves

For what concerns the module based on the slicing approach, the user must provide to the software the input geometry, the layer height and must select the base curve of the duct (Figure 246). The steps performed by the software to obtain the toolpath from the input midsurface are the following:

- 1) The surface entities composing the input CAD model, are joined together to obtain a unique BRep entity.
- 2) All the edges of the BRep obtained at step (1) are extracted from the BRep itself. The extracted edges are classified in two different categories: “Naked” and “Interior”. The first ones are the free edges (as shown in Figure 244), while the others are the edges at the interfaces between the surface entities composing the input CAD model.

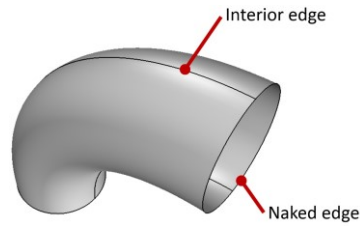


Figure 244 Taxonomy of the edges in a BRep

- 3) The adjacent naked edges (that lay on the free edges of the input midsurface) are joined together to obtain two closed curves: one for the bottom of the duct and the other for the top. To help the user understanding that the edge recognition has been successful, the interior edges and the naked edges are highlighted in the graphic area in blue and red respectively (Figure 245).

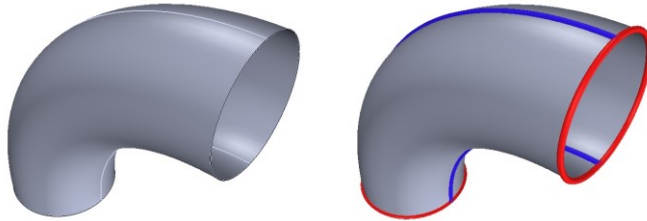


Figure 245 An elbow pipe before and after the edge recognition procedure. The red edges are the naked ones, while the blue the interior ones

The user is asked to select the base curve generated by the junction of the naked edges of at the base of the duct (Figure 246). This curve is an input for the next steps.

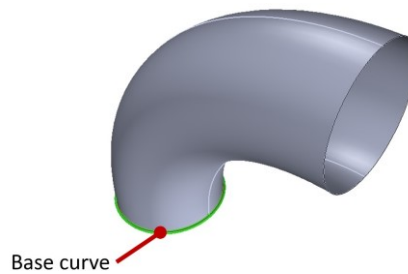


Figure 246 The base curve of a freeform duct is the curve that lays on the building platform

- 4) A loop composed of the following steps starts and calculates the deposition toolpath:
- i. The centroid of the area delimited by the base curve selected by the user is determined and named C1. Referring to Figure 247, the

coordinates of the centroid c of an area A can be defined using through Equation 54 to Equation 57.

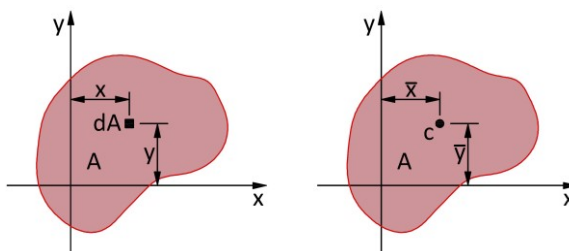


Figure 247 Centroid c of an area A

$$Q_x = \int_A y dA \quad \text{Equation 54}$$

$$Q_y = \int_A x dA \quad \text{Equation 55}$$

$$\bar{x} = \frac{Q_y}{A} \quad \text{Equation 56}$$

$$\bar{y} = \frac{Q_x}{A} \quad \text{Equation 57}$$

- ii. The equation of the plane on which the base curve lays is determined (Figure 248). To perform this step, it is enough to use the general equation of a plane containing three given points. The input points for the equation calculation can be three non-aligned arbitrary points taken on the base curve.

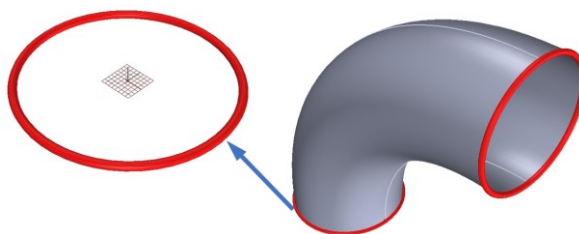


Figure 248 Close view of the base curve of the duct with the plane laying on it

- iii. The plane is offset in the direction pointed by the normal to the plane determined at step (ii). If the origin of the plane resulting from the offset is outside the BRep constructed using the input geometry closed by two planar caps, the process is interrupted, since it means all the input geometry has been already processed. If the origin of the plane is inside the control volume, the process goes on (Figure 249).

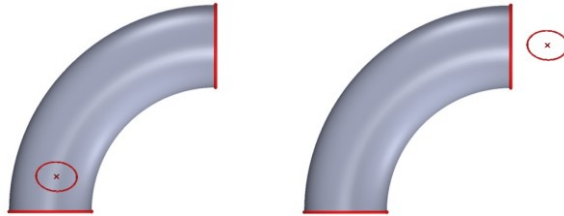


Figure 249 If the point is inside the BRep (left) the process goes on, otherwise (right) the process is stopped

- iv. An intersection between the plane resulting from the offset and the input midsurface of the duct is performed and the resulting curves (if more than one) are joined together to obtain a unique curve.
- v. A re-orientation of the plane used for the intersection is performed in order to account for the curvature of the input geometry. Referring to Figure 250, the centroid of the surface included in the intersection curve determined at step (iv) is calculated and named C2. Taking in mind also the step (i), a vector $(C2 - C1)$ is determined. This vector can be considered as the normal of the re-oriented intersection plane that is now totally defined (it is enough to have a normal vector and its application point to define a plane).

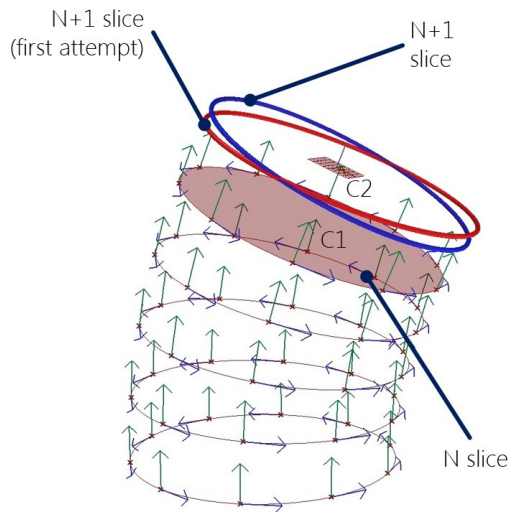


Figure 250 The re-orientation of the first-attempt slice

- vi. An intersection between the input geometry and the re-oriented plane is calculated and the resulting curves are joined together to obtain a unique curve.
- vii. On the curve defined at step (vi) a series of equally spaced points is determined. The distance between such points is half the resolution of the used deposition process. These points are the deposition toolpath points. The determined intersection curve is evaluated at each one of the equally spaced points and its tangent and normal vector are determined. The cross product between the tangent and normal vector of the curve is evaluated for each point and its result gives the torch axis (Figure 251). The programmed point (i.e. the controlled point of the torch) will lay on the torch axis at a distance equal to the nozzle to work distance from the origin of the torch axis itself.

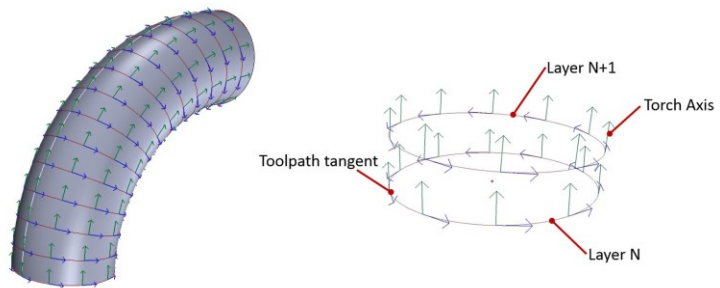


Figure 251 Final toolpath for an elbow pipe (left) and definition of the elements composing the layers (right)

- viii. The loop starts again from step (i) until the exit condition described at step (iii) is achieved.

In the case of component with a high curvature, the distance between two consecutive slices determined using this algorithm can be very variable. If the local distance between two consecutive layers do not overcome a defined threshold, it is possible to solve the problem using the approach proposed in [57]. The maximum allowable local distance depends on the process parameters and on the range of bead height achievable with the used welding apparatus and five axis machine and must be determined experimentally following the approach used by [85]. If the local distance between two consecutive layers overcomes the specified threshold an additional toolpath segment must be added between the two slices in all the zones when the local distance overcomes the defined threshold.

Figure 252 and Figure 253 show two examples of deposition toolpath calculated with the slicing approach.

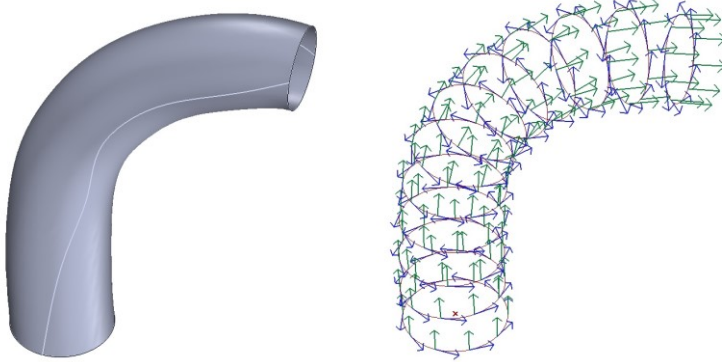


Figure 252 input geometry (left) and calculated toolpath (right) for a freeform duct with variable diameter

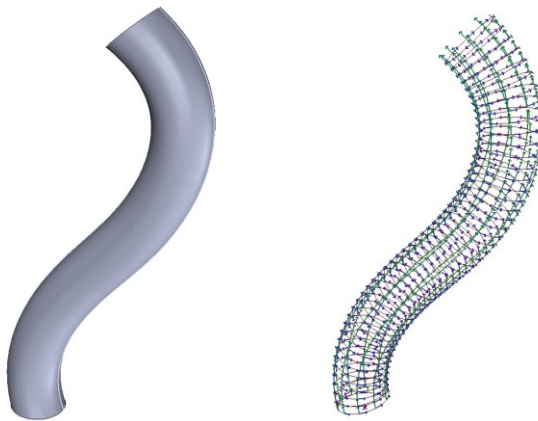


Figure 253 Input geometry (left) and resulting deposition toolpath (right) for a freeform duct with constant diameter

Using the slicing approach allows also creating ducts with internal features like the one depicted in Figure 254.

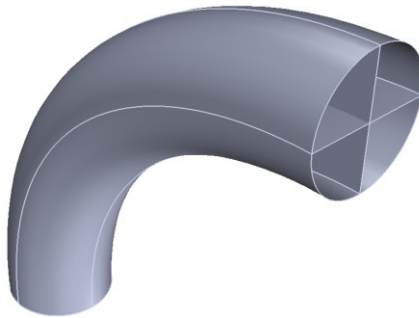


Figure 254 Elbow pipe with internal stiffeners

In this case the curves resulting from each new intersection (Figure 255 (a)) must be classified following two categories: external boundary (Figure 255 (b)) and internal curves (Figure 255 (c)).

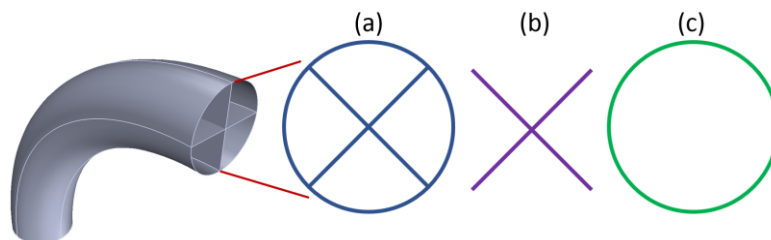


Figure 255 Intersection taxonomy for an elbow pipe with internal stiffeners. (a) Intersection curves, (b) Internal curves, (c) External Boundary

The external boundary will be used as input for the centroid calculation and the determination of the intersection planes. However, all the curves resulting from an intersection procedure, compose a planar layer. In fact, the toolpath resulting from the slicing-based module, is an indexed toolpath. This means that the rotary axes are used to orient the machine in a way that the current (re-oriented) intersection plane is parallel to the XY plane of the machine reference system, and then the layer is deposited using the linear axes. Therefore, the deposition of each layer, carried out after the orientation of the geometry, is a three-axis operation. For this reason, all the feature recognition algorithms and toolpath deposition strategies developed for stiffened panels and presented in section 3 can be used for each of the calculated slices (Figure 256).

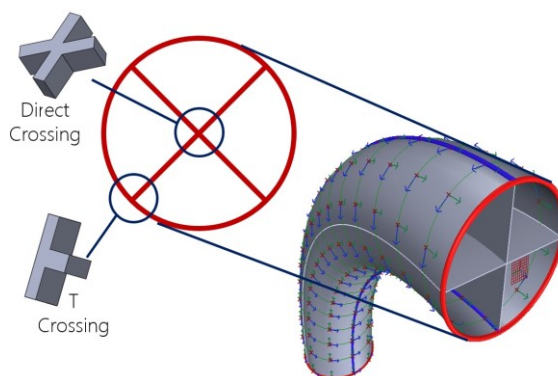


Figure 256 Conceptual application of the 3-axis feature recognition module to a slice from an elbow pipe with internal stiffeners

Regarding the other toolpath calculation module for freeform ducts, it is able to calculate an helicoidal deposition pattern. Many algorithms are available to calculate a helix on a freeform surface with the desired pitch exploiting the parametric data of the input CAD geometry (Figure 257)

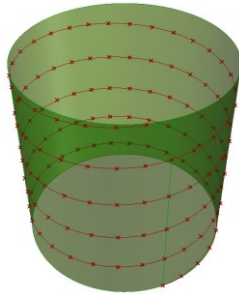


Figure 257 Helical deposition toolpath for a cylinder

However, these algorithms are addressed to CAD model composed by a unique surface entity that is a condition often unavailable. Indeed, several times a surface model of a freeform duct is composed by two symmetric halves (Figure 243), therefore there could be no continuity between the parametric curves of a halve and the parametric curves of the other halve. For this reason, it is necessary to find a workaround to achieve the continuity between the two surfaces. This can be achieved performing a resurfacing operation, or through the “knit surface” algorithms offered by high-level CAM software. These operations of surface joining must be performed manually by the user. Therefore, looking for a high automation of the toolpath calculation procedure, a new approach dedicated to freeform ducts is presented in which the user is only asked to import the input geometry in the Rhinoceros 5 CAD software and then to select the base curve of the duct (as for the slicing-based toolpath calculation module). Then the following steps are performed by the algorithm to calculate the deposition toolpath:

- 1) The surface entities composing the input CAD model, are joined together to obtain a unique BRep entity.
- 2) All the edges of the BRep obtained at step (1) are extracted from the BRep itself. The extracted edges are classified in two different categories: “Naked” and “Interior”. The first ones are the free edges, while the others are the edges at the interfaces between the surface entities composing the input CAD model (Figure 258).

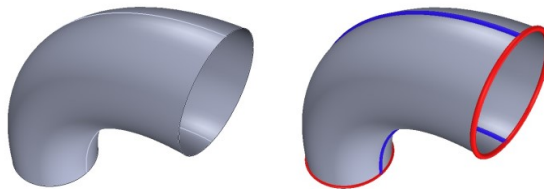


Figure 258 The input midsurface (left) and (right) highlight of the naked edges (red) and interior edges (blue)

- 3) The adjacent naked edges (that lay on the free edges of the input midsurface) are joined together to obtain two closed curves: one for the bottom of the duct and the other for the top. To help the user understanding that the edge recognition has been successful, the interior edges and the naked edges are highlighted in the graphic area in blue and red respectively (Figure 258). The

user is asked to select the base curve generated by the junction of the naked edges of at the base of the duct. This curve is an input for the next steps.

- 4) A series of equally spaced points is generated in the base curve (Figure 259). The distance between the points of the series is set equal to half the resolution of the used deposition process. The points in the series are sorted along the base curve they lay on in a clockwise (or counterclockwise manner).

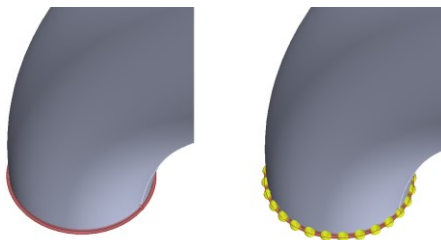


Figure 259 The base curve highlighted in red (left) and the equally spaced points generated on the base curve (right, yellow dots)

- 5) For each one of the two surfaces composing the duct and for each of the point of the series, the u and v isocurve passing from each of the points of step (4) are extracted. Only the longitudinal isocurves are kept (Figure 260). Now the algorithm checks for the presence of duplicated curves. Indeed, if one of the points generated at step (4) lays on the junction line between the two adjacent surfaces, it will generate a curve on one of the surfaces and another in the other one and this is not acceptable for the next steps. Therefore, if there are two duplicated longitudinal isocurves, only one is kept and the other one is deleted. The direction of the curves is checked and if it does not point from the bottom to the top of the duct, it is reversed. All the curves are then re-parametrized to have the parameter ranging from 0.0 to 1.0.

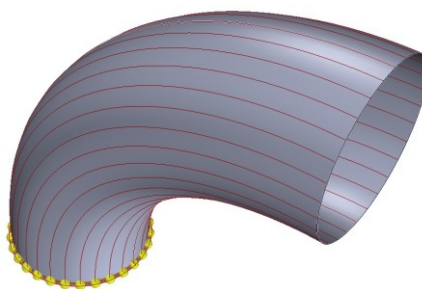


Figure 260 The longitudinal isocurves

- 6) The idea is now to create the helical deposition pattern “walking” along and across the longitudinal isocurves using their parameters. To do this several points must be created with a certain distance between them on the longitudinal isocurves. Such points compose the deposition toolpath. The torch axis is obtained as the local tangent vector to the isocurve evaluated at

the various point of the toolpath. Firstly, the average length AL of the longitudinal isocurves is calculated using Equation 58.

$$AL = \sum_i^n \frac{L_i}{n} \quad \text{Equation 58}$$

Where:

L_i = Length of the i -th longitudinal isocurve;
 n = total number of isocurves;

Then, the total increment PTI for the curve parameter to obtain a complete turn of the helix is calculated using Equation 59:

$$PTI = \frac{LH}{AL} \quad \text{Equation 59}$$

Where:

LH = layer height (input from user);
 AL = average length of the longitudinal isocurves;

Finally, the increment of the parameter for each curve PCI to obtain a complete turn is obtained using Equation 60:

$$PCI = \frac{PTI}{n} \quad \text{Equation 60}$$

Where:

PTI = total increment of the parameter for a turn of the helix;
 n = number of longitudinal isocurves.

Then, a loop executing the following steps is performed:

- i. The i -th curve in the list of the longitudinal isocurves is considered
- ii. The total increment of parameter for the considered curve is calculated using Equation 61:

$$PCI_i = k \cdot PCI \quad \text{Equation 61}$$

Where:

PCI_i = total current increment of the parameter for the i -th curve;
 k = number of the current iteration of the loop;
 PCI = increment of the parameter for each curve.

Then a check is performed on the value of PCI_i : if it is more then 1.0, it means that all the deposition toolpath has already been calculated and so the calculation loop is concluded.

- iii. A point is generated on the curve at the parameter value calculated at step (ii).
- iv. The torch axis is calculated as the tangent vector to the current parametric curve evaluated at the parameter value determined at step (ii).
- v. The (i+1)-th curve is considered and all the operations from (ii) to (iv) are repeated while the exit condition described at step (ii) is not achieved.

Figure 261 and Figure 262 show two examples of deposition toolpaths generated with the presented method.

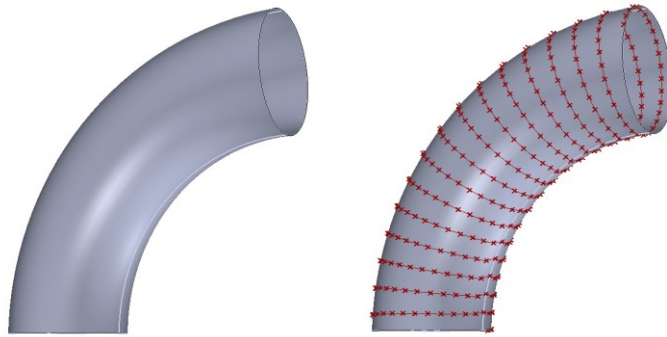


Figure 261 Input geometry (left) and resulting helical deposition toolpath (right) for an elbow pipe

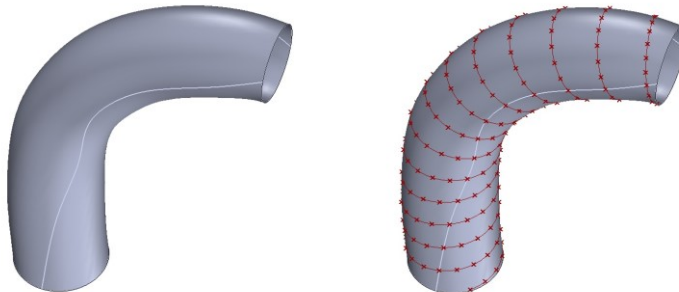


Figure 262 Input geometry (left) and resulting helical deposition toolpath (right) for a freeform duct with variable diameter (the layer height is exaggerated for the sake of clarity).

5.4. A machine simulation module for five axis operations

In order to virtually test the calculated deposition toolpath two simulation modules have been developed. These have been developed using traditional techniques taken from literature and are here shown for the sake of clarity and completeness. The first module is able to simulate the movements of the torch respect to the workpiece while the second one shows the movements of all the components of the machine. The two modules have been both

implemented in Grasshopper. Both the modules use the “keyframe” animation technique to display the movement of the parts [86]. As shown by Figure 263, the keyframe animation technique is based on the idea of creating a series of photograms and show them one after the other (exactly like in the projection of a film) in order to “animate” the machine.

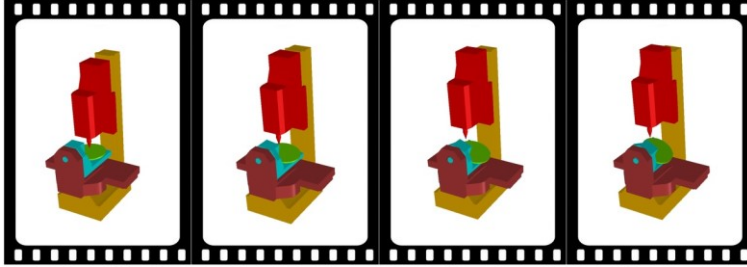


Figure 263 The conceptual idea of the keyframe animation

The first step of the creation of a simulation module is the realization of a simplified CAD model of the machine as shown by Figure 264. The simplified model will have only six parts: B axis, C axis, X axis, Y axis, Z axis and frame.

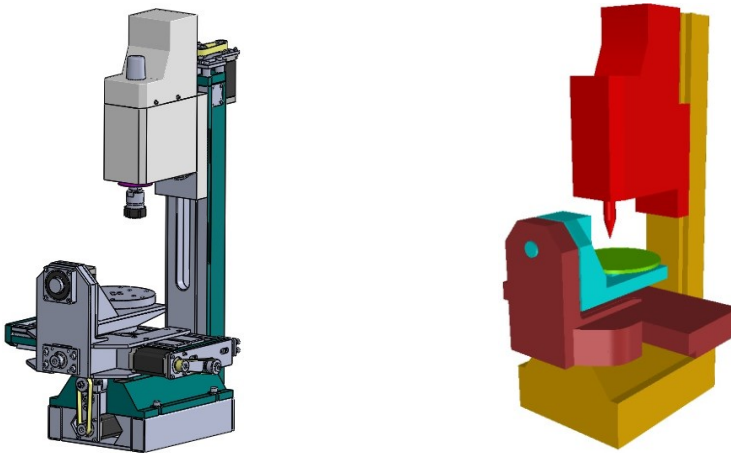


Figure 264 Original (left) and simplified (right) CAD model of the five-axis machine presented in this thesis

Then, the dependences between the parts composing the machine are individuated. For example, in the five-axis machine presented in this thesis, the dependencies between the several part composing the machine itself are presented in Table 27.

Table 27 Axes dependencies in the five-axis machine

Axis	... is carried by
B	X, Y
C	B, X, Y
X	Y
Y	-
Z	-

Once the dependences have been determined it is possible to assemble the roto-translation matrix for each part composing the simplified model, like in the example of Figure 265.

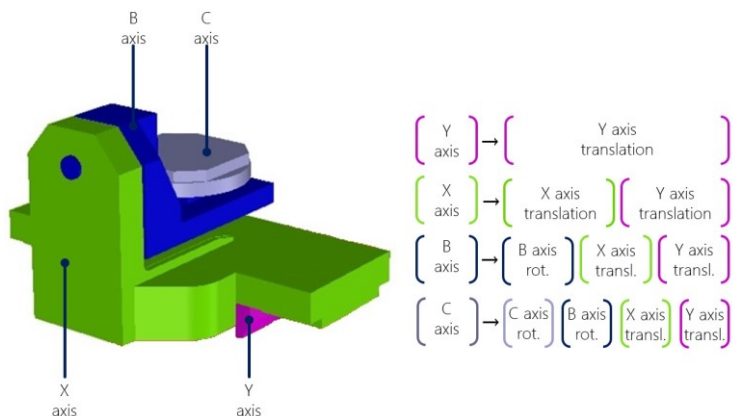


Figure 265 Composition of the roto-translation matrix for the components of the simplified model

Each roto-translation matrix is a 4x4 matrix that contains information both on the rotation and on the translation. The information for the rotation comes from the components of the torch axis associated to the toolpath points, while the translation is calculated looking at the linear coordinates of the toolpath point itself. To “animate” the machine it is necessary to perform a loop that reads all the points of the toolpath, calculates the translation and rotation and applies these to the components of the machine. In order to achieve a good result, it is important that the points are quite close one to the other, otherwise the movement of the machine will not be smooth.

To simulate the deposited material, it has been decided to generate a mesh sphere for each of the points of the deposition toolpath (of course only for those laying on a deposition movement) (Figure 266). Therefore, once a point is considered in the simulation loop the mesh sphere is generated and, in the case of the complete machine simulation, linked to the C table in order to be moved with this in the next step of the simulation.

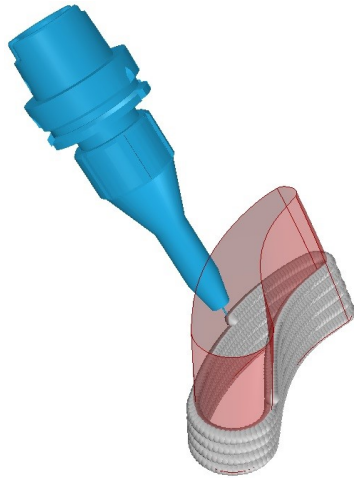


Figure 266 Simulation of the deposition of a hollow twisted blade

6. A monitoring system for WAAM deposition operations

6.1. The need for a process monitoring system for WAAM operations

The welding technology used in the research work presented in this thesis is GMAW welding. GMAW welding is prone to several defects that can occur during the manufacturing process. Also according to [40], these defects can be classified as reported in Table 28. Figure 267 shows a visual explanation of the defects listed in Table 28.

Table 28 Classification of WAAM defects

Defect	Possible Causes
Porosity	Insufficient gas flow rate
	Low gas purity
	Wrong deposition parameters
	Excessive travel speed
	Impurities in the welding wire
Lack/excess of deposited material	Excessive welding current
	Excessive travel speed
	Incorrect torch inclination
	Chemical composition of the welding wire
	Insufficient or excessive wire feed
Humping	Excessive travel speed

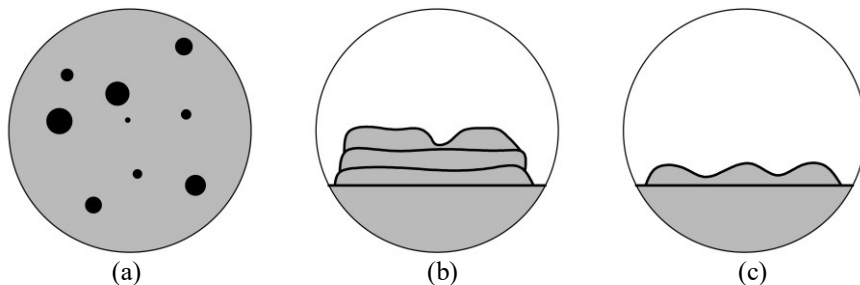


Figure 267 Visual explanation of WAAM defects. (a) Porosity, (b) Lack of material, (c) Humping

The cause of these defects can be both casual and non-casual. Therefore, the second ones can be avoided setting the right welding parameters and optimizing the deposition process, while the first ones cannot be foreseen and depend on many aspects that cannot be easily controlled. These casual-defect can compromise the part building, since a lack or excessive accumulation of material in a layer will propagate along the whole part causing the failure of the building process or even a collision between the part and the torch (Figure 268).

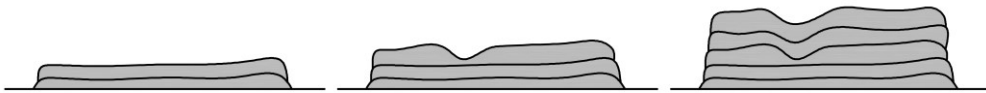


Figure 268 WAAM defect caused by local lack of deposited material and its propagation

Looking at Figure 268, it is noticeable that the defect occurs in the third layer, but all the successive layers are affected too and the whole part is compromised. The same thing would happen in the case of an excess of material as depicted in Figure 269.

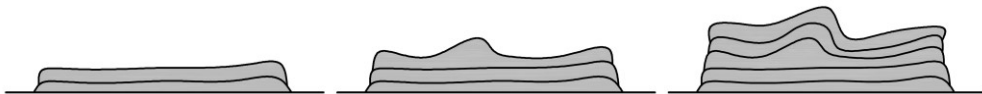


Figure 269 WAAM defect caused by local excess of deposited material and its propagation

The casual defects can be caused by several aspect that cannot be foreseen analytically. Moreover, even the non-casual defect can occur casually. In fact, especially humps and excessive material accumulation, can occur due to non-correct deposition speed. It is straightforward that the programmed deposition speed is hard to be respected in the case of five axis operations (especially if non-high-speed numerical controls are used) or in the case of sharp corners. In the first case, movements that involve all the five axes of the machine with high angular variations can cause a slowdown of all the axes and a consequent reduction of the effective tangential deposition speed. In the second case, i.e. in the case of a sharp corner, the machine axes have to slow down until they stop for a while to avoid a deviation from the deposition pattern while changing direction completely; this causes an accumulation of material that is accentuated by the fact that the in branch and the out branch of the sharp corner are very close causing the bead to overlap for a certain portion of the toolpath (Figure 270)

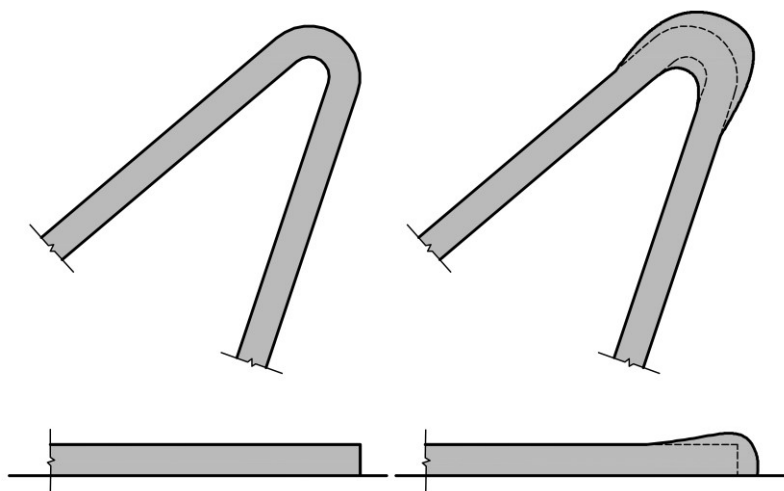


Figure 270 Desired shape of a sharp corner (left, top and side view) and real obtained shape (right, top and side view)

For all the above reasons, a process monitoring system is very useful, especially if it can monitor the geometry of the welding bead during its deposition. Then, if the outcome of this process-monitoring system can be interfaced with a numerical control able to perform corrections on the parameters of the process, a closed loop system could be obtained. This would allow letting the WAAM machine almost unattended. Indeed, the final objective (that is beyond the scope of this thesis) is to create an adaptive numerical control able to perform corrections on the deposition process depending on the inputs coming from the monitoring system. To be able to do this, the first step is developing and testing the monitoring system itself. For this reason, in this thesis a process-monitoring system based on a stereovision 3D scanner is presented and its performance and novelty are discussed.

6.2. Process monitoring systems for AM: state of the art and proposed approach

Nowadays many commercial AM machines have the hardware to perform controls on the process. In particular, the most common performed monitoring include 2D deposition layer geometry control and temperature profile in powder bed techniques [87], control of temperature and size of the molten pool in direct energy deposition metal technologies [88] [89]. Systems to control the geometry of the deposited bead in direct energy deposition technologies have been developed too [90]. The cost of the hardware needed to perform such monitoring is very high. The high cost could be not a problem if the system is installed in a laser-based machine which price is already very high. However, the cost of a high-level and high-performance monitoring system could represent a big percentage of a WAAM machine. This because WAAM machine, except for the ones obtained from high-performance five axis milling machining centers, have usually a very low cost, respect to laser-based ones or even to pure milling centers.

According to Everton et al. [91], the in-situ measurements modules available from AM machine manufacturers and measurements specialists can be classified as reported in Table 29.

Table 29 In-situ measurement modules for AM technologies (from [91])

AM process	Machine Manufacturer	Module name	Failure mode Monitored	Parameter altered	Equipment
EBM	Arcam	LayerQam™	Porosity	N/A	Camera
PBF	B6 Sigma Inc (specialist)	PrintRite3D® INSPECT™	Unknown	N/A	Thermocouple and high-speed camera
		Concept Laser	QM Melt Pool	Melt Pool Monitoring	Laser Power
	EOS	N/A	Unknown	N/A	Camera
DED	DEMCON	LCC 100	Melt pool monitoring	Laser Power	Camera
	DMD 3D Technology	DMD-Closed Loop feedback system	Melt pool monitoring and build height	Laser Power	Dual color pyrometer and three high-speed CCD cameras
	Laser Depth	LD-600	Depth Measurement	Laser Power	Inline coherent imaging
	Promotec	PD 2000	Melt pool monitoring	N/A	CMOS-camera
		PM 7000	Melt pool monitoring	N/A	1D photo detector
	Stratronics	ThermaViz system	Melt pool temperature	Laser Power	Two-wavelength imaging pyrometers

In the case of direct energy deposition techniques, such as WAAM, LWD or EBAM, many controls can be performed. Before analyzing these systems, it is important to remember that, usually, the direct energy deposition techniques, are performed using multi-axis machines or anthropomorphic manipulators. This aspect makes the monitoring procedure of the molten pool or of the deposited material more complex; this because, during the building procedure, some moving parts of the machine or of the robot can cover the zone where the material is being deposited. Therefore, the hardware used to control the process must be designed considering also this aspect. In fact, the monitoring hardware is usually linked to the deposition head to have always a good visibility of the deposition zone.

Three monitoring systems have been found in literature especially developed for WAAM or arc welding technology and these will be briefly presented in this paragraph before examining the proposed monitoring system. The first work, by Xiong et al. [90], is composed by two mutually orthogonally oriented CCD cameras; a narrow-band filter is mounted on the optic of each camera. The two cameras directly see the welding process (Figure 271).

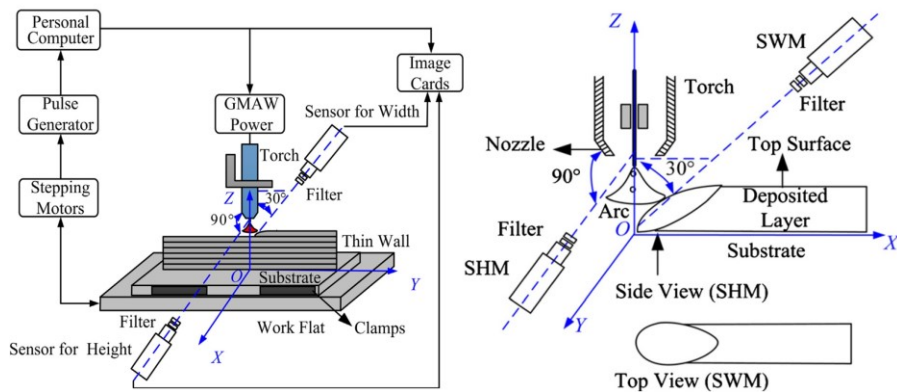


Figure 271 The monitoring system developed by Xiong (from [90])

The role of the narrow-band filter is to cut all the wavelengths except for the principal ones of the fused metal. Of course, cutting all the wavelengths except the ones coming from the molten pool is mandatory to obtain a clean signal from the molten pool itself. The aperture of the camera optics is set at the lowest value in order to “simplify” the acquired image and to make simpler the further processing of the image itself. The software developed to process the acquired images (one from both the cameras) uses special designed filters to detect the boundaries of the deposited bead. At this point, thanks to the calibration of the cameras, the software detects where the correspondent pixels are in both the two images from the cameras and reconstructs the geometry of the bead. In particular, through the Hough filtering procedure, the software can easily reconstruct the shape of the cross section of the bead. The computational time of this method can be speeded up avoiding analyzing all the complete pictures but looking only into a Region of Interest (ROI) of the acquired images. Probably the most relevant advantage of this system is the use of passive system to acquire data from the welding procedure. Anyway, this system is not able to follow a freeform movement of the torch and therefore is not suitable to be installed in general purpose WAAM machine.

Another work from literature is the one from Doumanidis [92]. It is based on a laser and camera triangulation system. A laser blade is used to scan the deposited welding bead. This system is especially suitable to monitor traditional welding operation in which a straight bead is deposited to join two parts. The system can monitor only monodirectional straight weld beads. For this reason, it is not adaptable to WAAM since it would not be able to follow all the possible movements of the torch. However, the use of laser and camera triangulation system is very attractive also for WAAM since in literature many robust and well-known algorithms to process the images exist. The hardware and schematic of such system is reported in Figure 272.

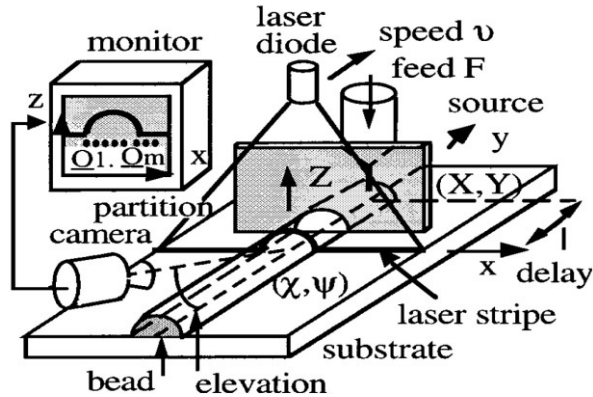


Figure 272 Schematic of the monitoring system from Doumanidis [92]

The laser used in the activity from Doumanidis is diode-based and has a power of 20 mW and a wavelength of 680 nm. Referring to Figure 272, the delay between the torch and the laser stripe is 25.4 mm. To allow the camera to capture the laser stripe and not getting over-exposed by the arc light, a shield is placed between the torch and the laser itself. This shield protects the camera lens from the arc. The camera has a CCD sensor and has a narrow-band filter in front of the lens centered on the laser wavelength. It is important to notice that because of the delay between the laser stripe and the molten pool, an occurring defect cannot be immediately detected. Of course, this delay cannot be eliminated, otherwise there would be optical interference between the light coming from the molten pool and the laser stripe itself. An important aspect to consider when using a laser-camera system to perform the acquisition of a welding bead is that common red lasers cannot be used because the spectrum of the light coming from the molten pool may have fundamentals wavelength in the red band and this would make the processing software not able to distinguish between the laser stripe and the hot zone of the bead.

The last system that will be analyzed in this literature review is the one proposed by Saeed et al. [93]. This system, which basic configuration is reported in Figure 273, is essentially composed by a He-Neon laser and a high-speed and high-resolution camera.

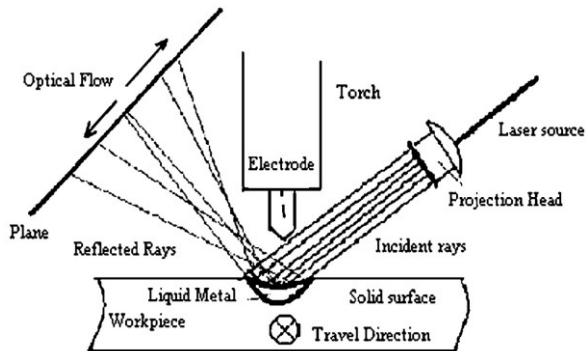


Figure 273 Schematic of the acquisition system from Saeed [93]

The Saeed's system uses the properties of an incident light ray (projected by a laser source) on a specular surface to reconstruct the shape of the welding pool. At this point, it is important to notice that according to [94], the welding pool is a specular surface. This property can be used to determine the shape of the molten pool itself even when it is still in a fluid state. The fundamental hypothesis of this study is that the molten pool has nearly the same shape when it still fluid and when it has already solidified. Taking into account this assumption, the shape of the molten pool is reconstructed using the surface reflection laws [95]. The system is able to reconstruct the analytical surface fitting the shape of the molten pool (Figure 274).

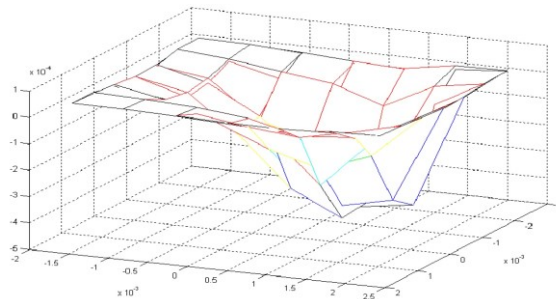


Figure 274 The surface fitting the shape of the molten pool reconstructed by the software (from [93])

Since a high-speed camera is used, many pictures can be collected in the unit time and the equation of the surface determined thanks to an acquisition can be compared to the equation of the surface estimated from the next acquisition allowing the superposition of successive estimations and resulting in an increase of the accuracy of the overall system.

Regarding a possible application of this system to the WAAM technology, one of the main problems is that most of the analytical laws used to determine the shape of the molten pool are derived from laser-based welding technique and therefore these cannot be directly adapted to WAAM. Moreover, the used laser source and the high-speed camera are very expensive pieces of hardware and this is not in the philosophy of the system developed in the present activity. Finally, this system is not always able to properly acquire the shape of a molten pool if the deposition speed exceeds a certain limit due to the excessive fast changing of the reflected laser rays.

Looking also at the outcome of the literature research, it can be stated that from a process point of view the most important controls to perform during the deposition process to avoid the aforementioned failures are:

- Temperature control of the molten pool or of the portion of already deposited material;
- Control of the geometrical dimensions of the bead (width and height).

The first control has not been considered in this activity, since a thermomechanical simulation-driven toolpath generation has been pursued. In fact, it is assumed that the programmed toolpath used to build the part has already been optimized from a thermal point of view, and so no failure should occur due to thermal accumulation. It is also important to say that heat accumulation in the part can be fully foreseen using finite element models like the one proposed in [96]. For this reason, the procedure chosen in this activity is to generate a

toolpath and then to optimize it through the simulation of the toolpath itself and the introduction of dwells in the manufacturing process using, for example, the algorithm proposed in [15]. Anyway, in general, also a thermal control would be useful to assure that the actual temperature of the part is close to the simulated one.

Regarding the control of the dimensions of the bead, the two relevant dimensions of the cross section of a welding bead are the height and the width, as reported in Figure 275.

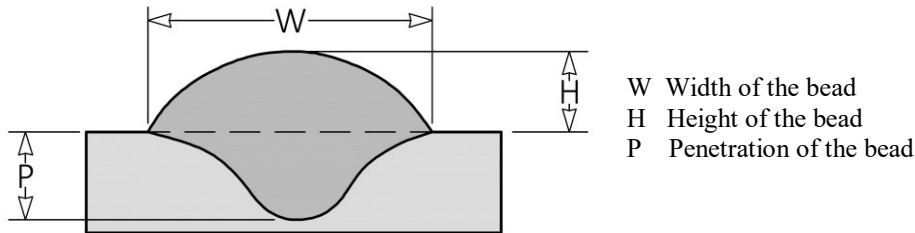


Figure 275 Main geometrical parameters of a weld bead

In the present thesis a system to monitor the W and H dimensions of the bead is presented and analyzed. The first important characteristic of the presented system is that it has specifically been designed for WAAM, i.e. for a direct energy deposition process that uses arc welding as power source. In fact, this system exploits the hardware and characteristics of welding and of the welding arc. The output of the system is given almost in real time and is composed by the width and height of the welding bead, together with the point cloud representing the bead being deposited. Moreover, since WAAM operations are usually performed on multiaxis machines or robots, the system has been designed to be mounted on both these devices. This means that the system is able to detect width and height not only of straight welding bead like the system presented in [92], but also of beads with a freeform shape or, in general, non-monodirectional beads.

Another important aspect that has been considered is the overall cost of the system. Since WAAM is especially convenient from an economical point of view, and the WAAM-based machines are usually lightweight and cheap respect to laser-based machines of the same size, it was important to keep the total cost of the device as low as possible to make it interesting and convenient to be mounted on a WAAM machine. This objective has been achieved, since the total cost is in the order of hundreds of euro. This aspect, together with the real time operation, makes the system very attractive and suitable for the introduction in a closed loop performed by the numerical control, able to make corrections to the parameters during the deposition process itself. For what concerns the target resolution of the system it has been decided to obtain a 0.5 mm accuracy. This because it is one order of magnitude lower than the accuracy of the WAAM process implemented in the machines developed in the present activity, that is of about 1.0 mm.

6.3. Introduction to the developed system: input, output and general architecture

After the analysis of the state of the art, it is clear that there are many monitoring systems both for traditional arc welding techniques and for additive manufacturing processes in general. Anyway, none of the analyzed systems can be adapted directly to the WAAM

technology or even can be purchased at a low price. For this reason, a new acquiring and monitoring system especially designed for WAAM has been developed. In this paragraph, the general architecture of the developed monitoring system is presented. The objectives of the presented system are:

- Low cost of hardware and software (in the order of hundreds of euro);
- Capability to follow the movements of a multi-axis machine or robot (i.e. the system must be able to acquire beads of any shapes and not only mono-directional beads);
- The system must use non-contact acquisition devices;
- The output of the system must be in real time or quasi-real time (in fact, the future objective is to create a closed loop inside the numerical control);
- The system must have an accuracy of 0.5 mm;
- The final output of the system must be the height and the width of the welding bead.

Keeping in mind the objective of the low cost of the hardware and looking at the activities found in the state of the art, especially the one from Doumanidis, a configuration based on an active scanning system has been chosen. A stereo vision configuration has been selected. Thus, the proposed system is essentially composed by two cameras and a pattern projector. A schematic of the acquisition system is reported in Figure 276.

In front of the lens of each of the two cameras there is an optical band filter to allow the cameras to correctly acquire the scene; the reason of the presence of such filters and the selection process of each piece of hardware is described in the next paragraphs.

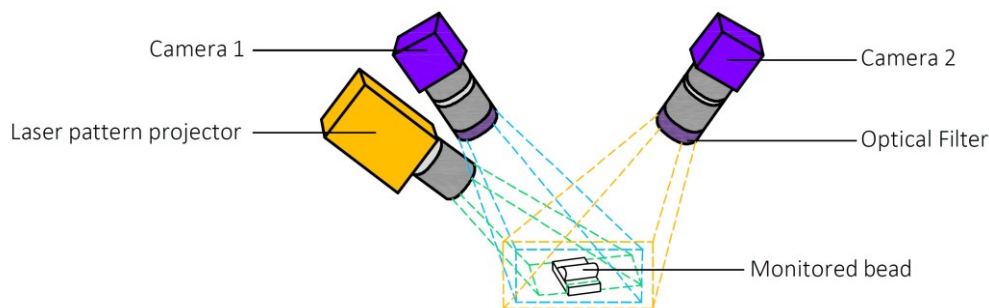


Figure 276 Scheme of the proposed acquisition/monitoring system

Both two cameras take a picture of the scene simultaneously, while the pattern projector projects a specific pattern on the weld bead. The acquired images are then sent to a computer that takes care of the triangulation process and the very first output is a point cloud representing the portion of the weld bead acquired by the cameras plus a certain part of the surrounding scene. Then, the point cloud is further processed to extract the parameters of the weld bead, i.e. the width and the height of the weld bead itself.

6.4. Preliminary design of the system

Since an active vision scanning configuration has been chosen to create the monitoring system, two important aspects must be considered: the first one is the selection between mono and stereo configuration, while the second one is the selection of the kind of pattern to be projected on the weld bead using a laser source. In order to select between the mono and stereo configurations, these have been compared both from a hardware and a software point of view, as depicted in Table 30.

Table 30 Software and hardware comparison between mono and stereo active 3D scanning systems

Configuration	Hardware constraints	Comments
Stereo Configuration (2 cams + pattern)	No camera-camera mutual movements are allowed	Cameras reciprocal position required by the software. The position of the pattern projection is not required
	High-precision system calibration required	
	Field of view overlap between the field of view of the cameras and of the pattern projector	
	The pattern must be acquired by both the cams with no disturbs	
Mono Configuration (1 cam + pattern)	No camera/pattern projector movements are allowed	The position between the camera and the projector must be well known by the software. Moreover, the projected pattern must hit the part in any configuration and this could be a problem for patterns like stripes or dot grids
	The projected pattern must be well known	

After the comparison, the stereo configuration has been selected, since even if it is a little bit slower from a computational point of view, is robust in many scenarios. Moreover, since common consumer-level CMOS cameras will be used, the difference of cost between the mono and stereo configuration is affordable and can be considered a little price to pay for an improved robustness. In addition, the main problem of the mono configuration is represented by the projected pattern; in fact, it must be extremely well known and perfectly calibrated. In literature there would be many patterns that could be used for a mono camera system [97], but all of these are strongly coupled with the application they have been developed for and no pattern has been developed for the application considered in the present thesis.

The second aspect to consider is the selection of a proper pattern to be projected on the part. Regarding this aspect, the use of a speckle pattern (Figure 277) has been considered.



Figure 277 An image of a typical speckle pattern (from [98])

A speckle pattern has no specific direction (as a laser blade has) and thus can be projected on the part from any position on the machine. This is very important since the use of laser stripes or blades (as in Doumanidis) can lead to a failure of the parameter extraction when the deposition direction changes (Figure 278). Moreover, a speckle pattern introduces features that can be strongly correlated across the two images taken by the cameras.

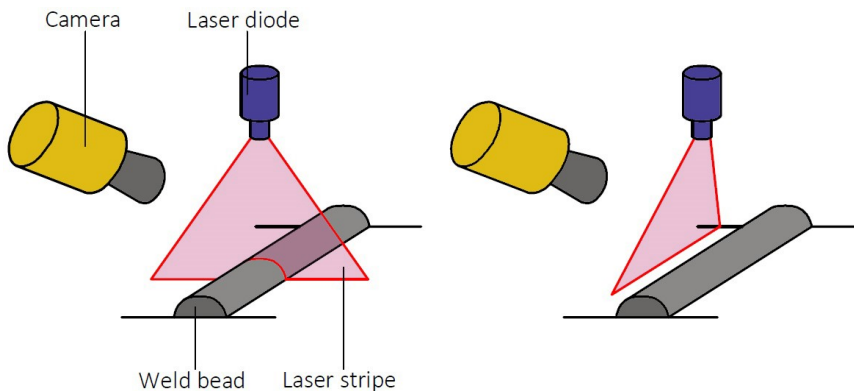


Figure 278 The problem of a mono vision system: the pattern must follow the weld bead (left), otherwise no useful data can be triangulated (right)

The unique requirement to be satisfied is that the speckle pattern must be always projected near the deposition torch, allowing the system to reconstruct the geometry of the just deposited material. Moreover, the speckle diffraction is a well-known technique and obtaining a speckle pattern is relatively easy. In literature a few 3D scanners implementing a speckle pattern have been found; the systems proposed by Schaffer [98] and Jeong [99] show how this technique achieves very attractive performances and a high acquisition speed.

Since the system will operate during the welding procedure, it is important to be able to acquire images of the scene that are not affected by the very intense light coming from the arc. In fact, if simple optics without any filter will be used, all the images will be overexposed and therefore not usable for the triangulation. A shield could be used, like in the activity of Domanidis, but it should be oriented depending on the direction of movement of the torch requiring a very complicate hardware and a sophisticate control software. It is straightforward that an optical filter is the best tool to obtain correct images. Surely, the most effective and cheapest solution is to use a narrow-band filtering glass placed in front of the optics of the two cameras. Such filtering glasses are easily available and very cheap, since these are used in the safety masks and goggles for manual welding (Figure 279).



Figure 279 A couple of welding glass filters

6.5. Welding spectrum analysis, optical filter and projected pattern selection

As stated in the previous paragraph, one of the main problems is the acquisition of correct images that are not influenced by the light coming from the welding arc, since one of the most important characteristics of the proposed system is the ability to extract the parameters of the bead also in zones that are very close to the torch. The arc has a high energy and emits light with a wide spectrum. Different materials lead to different emission spectra and the shapes of the spectra are not so influenced by the welding parameters or by the plasma temperature in the arc.

The use of shielding gas is mandatory for all the GMAW techniques to prevent oxidation of the deposited metal. The shielding gas can be a pure inert gas, such as Ar or He, or a mixture of gases where a certain percentage is composed by an active gas such as CO₂ that is used to improve the metal transfer. The addition of such active gas has also the effect of increasing the arc light emission. For all the activities of this thesis, the low carbon steel filler material ER70S-6 has been used together with a STARGON C18 shielding gas (82 % Ar + 18 % CO₂), so the spectrum emitted by the arc using the cited material and shield gas is the reference one in the present thesis. Furthermore, in order to limit the overall cost of the image acquisition hardware (i.e. of the two cameras), it has been decided to use cameras that work only in the visible range. Thus, the only interesting band of the welding spectrum is the visible one (Figure 280).

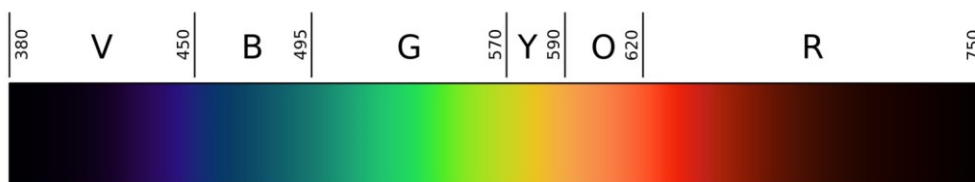


Figure 280 Visible wavelengths

Looking at Figure 281, representing a spectrum for steel welded at 180 A, it can be stated that the region of minimum relative emission is between 600 and 700 nm, so the red light does not have many important components in the radiation from the welding pool or from the arc.

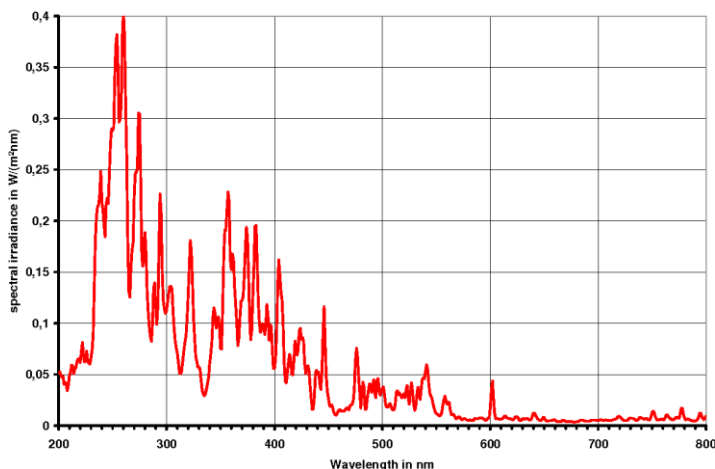


Figure 281 Emission spectrum for steel welded using MAG at a welding current of 180 A (from [100])

In Figure 282 the correlation between the welding current with the complete emission is shown. The chart shows that a linear trend exists: higher the welding current, higher the integral value of the spectrum emission.



Figure 282 Correlation between welding current and total emission (from [100])

As studied in [100], there are two local minima in the spectra: the first one is at 505-515 nm, and the second one is at 530-540 nm. The second minimum in the visible band of the analyzed spectrum is in correspondence with the green wavelength. The radiation at 180 A of MIG process with pure Ar shielding gas is 5 W/m², while with the same parameters but active shielding gas the emission is at least the double. Both for MIG and MAG operations, the major optical disturb comes from the emissions of the welding arc, while the other sources of emission (i.e. the emission from the molten pool and from the liquid metal droplets) can be considered as less disturbing. The welding spectrum has a minimal value between 500 nm and

550 nm. In this band there is only one disturbing peak at 525-528 nm, but it has a lower value respect to the other peaks in the spectrum. Thus, for what concerns the selection of the wavelength of the light emitted by the pattern projector, the best wavelength for such light should be between 500 and 550 nm, i.e. in the green range. In this way, the pattern projector will work in a band where the disturb from the arc is the lowest one.

Overcoming the emission from the arc and from the welding pool over the whole spectrum would require a very high energy and this would result in a dangerous pattern projector that could damage the eyes of the operator during the tests of the monitoring systems. To overcome this issue a laser source that emits light only at a precise wavelength has been chosen. The light projected by the laser source will hit the scene and, when reflected, will be recorded by the two cameras. For this reason, a filter is needed that allows only the specific used wavelength to reach the sensors of the cameras, otherwise their sensors will get overexposed. So, for what has been previously stated, such filter must be transparent between 500 and 550 nm and as much dark as possible respect to all the other wavelengths. This filter would cut all the disturbing wavelength coming from the welding zone and would allow only the wavelength of the laser light from the pattern projector to reach the sensor. It is important that the intensity of the laser used in the pattern projector overcomes the intensity of the disturbing peak detected in the band 500-550 nm in the welding spectrum, otherwise the image would not be usable for the 3D reconstruction of the weld bead. In other words, the cameras must distinguish the projected green laser light in the acquired images. In the market several narrow-band and very precise filters exists that are used in laser scanning applications. Such filters are able to cut all the wavelengths except for the desired one. These are very precise (Figure 283), but also very delicate and expensive and so not suitable for the prototype object of this chapter.

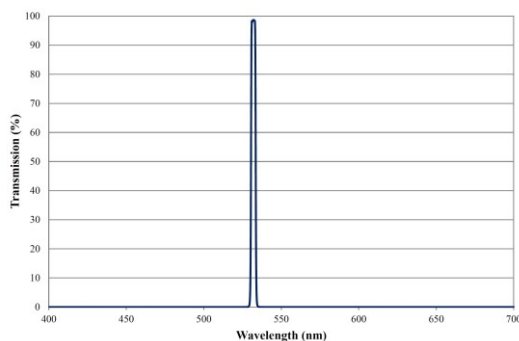


Figure 283 An example of spectrum for a 532 nm OD 6 laser-line bandpass filter, 2.0 nm bandwidth (from [101])

Trying to keep the cost of the system as low as possible, the adiactinic glass filters used for protective masks and goggles in manual welding have been considered because of their very low cost. These glasses can be considered narrow-band filters, are easily to be found and very cheap. However, obtaining precise information on the filtered and unfiltered wavelengths is quite difficult. Therefore, some tests have been carried out with different commercial shielding glasses to evaluate their transmittance in the visible field. Such tests have been carried out using the following hardware:

- EPL Camera, FullHD 24bit RGB, MA1080CSP-48 CMOS;

- Full-Range RGB led 10W diode (Figure 284);

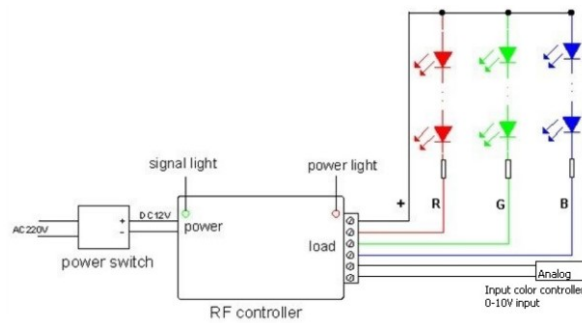


Figure 284 Electrical scheme of the full range RGB led apparatus used in the tests

- Wooden box (Figure 285). The box has a small hole on one face; the opposite face has some hinges and can be opened to install pieces of hardware inside the box itself. The structure of such box is the same of a pinhole camera.



Figure 285 A wooden box that can be used for the tests of the welding glasses

First of all, a DIN5 welding glass filter has been tested. The schematics of the arrangement used for these tests is depicted in Figure 286.

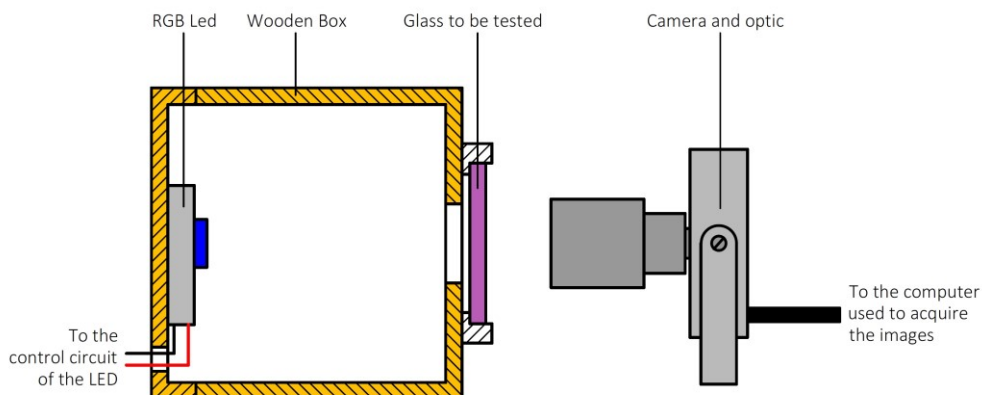


Figure 286 The experimental setup used to test the welding filtering glasses

The full range led is installed inside the box, attached to one of the walls; on the opposite wall there is a small hole to let the light of the led going outside the box. The welding glass filter to be tested is placed in front of the hole, while the camera is placed in front of the glass filter. To evaluate the spectrum of the filter, two photos are taken while the RGB led is on: the first one is without the filter and the second one is with the filter placed on the hole of the box. The two photos are used to compare the pixel intensity for each RGB channel. To make this comparison, only a region of interest of 300 x 200 pixel has been considered; this ROI is placed in the central zone of the picture (Figure 287), where the light emission is uniform and there are no border effects.

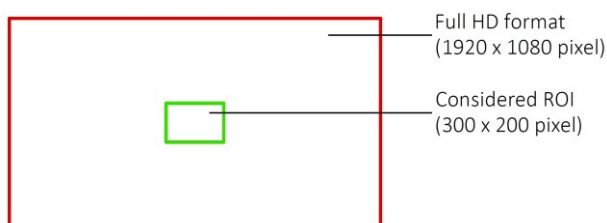


Figure 287 ROI considered for the investigation of the transmittance property of the welding glass

A loss ratio for each RGB value has been obtained comparing the pixel intensity of the picture without filter with the one with the filter. To do this the Matlab software have been used. Going more in details, to convert the RGB value to the correspondent wavelength, the Dan Bruton's approximated tables have been used. A chart for the Dan Bruton's approximation is reported in Figure 288.

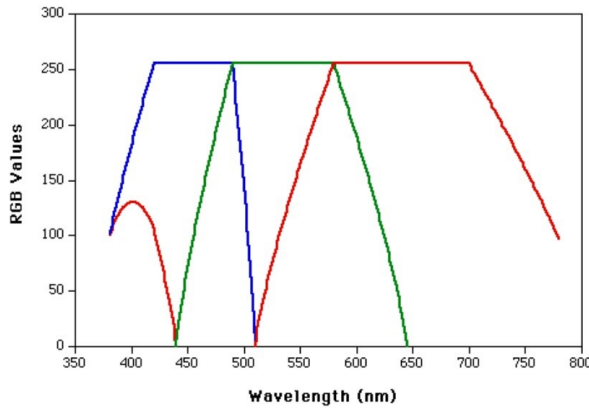


Figure 288 Chart for the Dan Bruton’s approximation to obtain the wavelength from the RGB value of each pixel

The result of such analysis is the qualitative spectrum of the tested filter. It has a gaussian shape (Figure 289) centred at 525 nm.

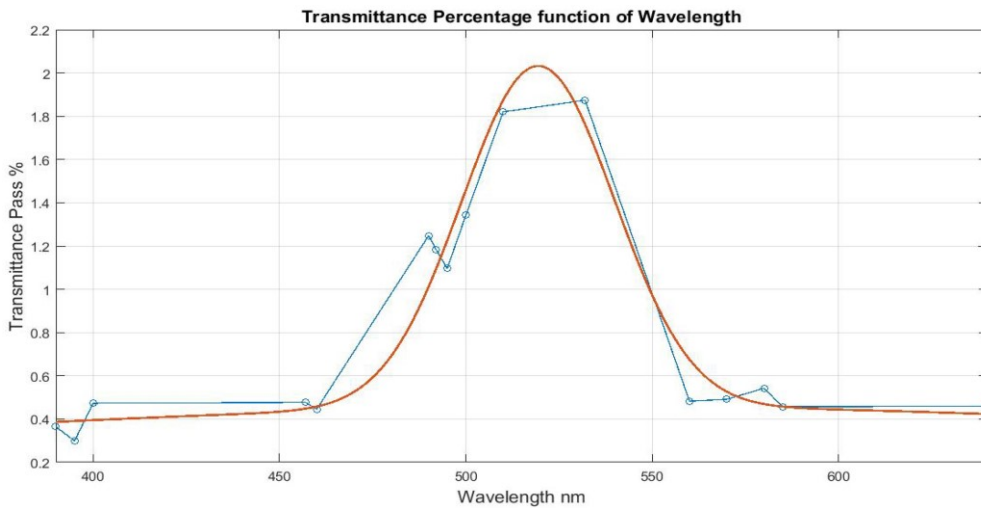


Figure 289 Spectrum of the DIN5 welding glass filter

Comparing the obtained spectrum with the one of a commercial narrow band filter (Figure 283), the dispersion is higher, but it can be stated that for the specific application and the required performance, such glass filter will be the optimal solution.

Since the peak of the spectrum of Figure 289 is at 525 nm, the green light appears to be the most powerful that can pass through the glass (this can be also confirmed with a simple real welding test: the scene will appear in the green light looking at it through the DIN5 glass filter). For this reason, the pattern projector will use a laser diode with that green wavelength. The glass filters available in the market have several degrees ruled by the DIN regulation. The choice of the DIN degree depends on the welding current used during the acquisition, anyway the shape of the spectrum of the filters is the same regardless of the DIN grade.

For what concerns the pattern projected on the scene, as stated in the previous paragraphs, the speckle one seems to be the best (Figure 290). The speckle effect is caused by an interference phenomenon brought by a constructive and destructive interference between light waves scattered from a rough surface or a diffuser.

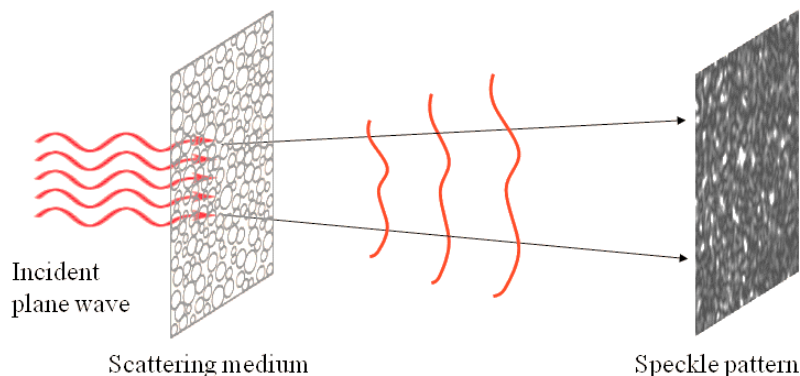


Figure 290 Originating a laser speckle pattern using a scattering medium (from [102])

Each point composing the speckle is completely uncorrelated with all the others, therefore the speckle pattern can be considered as randomly distributed [103].

In literature the studies about diffusers [104] show that any sort of material that is crossable by coherent light can produce a speckle effect.

Since to obtain the speckle, totally coherent light is needed, a laser diode (Figure 291) has been chosen to generate this light.

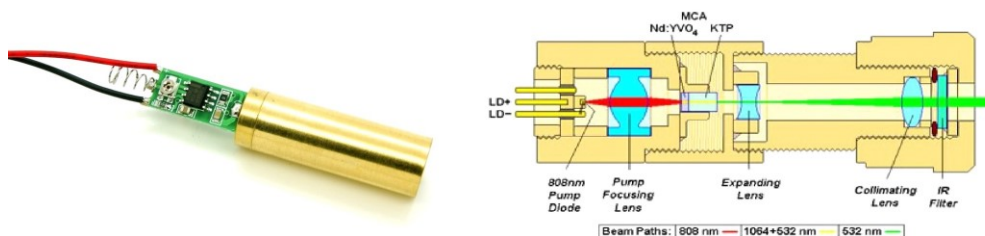


Figure 291 A green light laser diode (left) and its cross section (right)

The laser diode is powered by a 12v power source and controlled by a TTL based circuit.

6.6. Configuration of the cameras

In a stereovision 3D scanning system (Figure 292), the optics mounted on the cameras and the spatial configuration of the cameras influence the performance and acquisition capabilities of the scanning system itself.

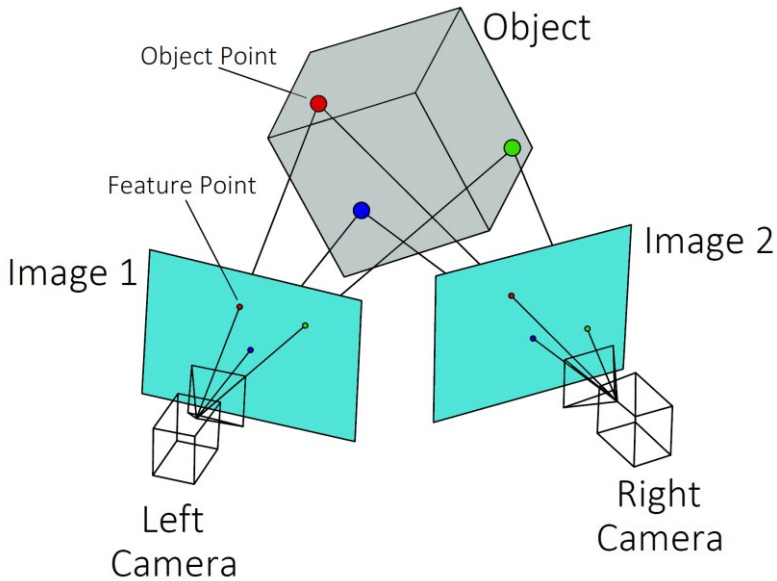


Figure 292 Scheme of a stereovision 3D scanning system

Going deeper in detail, referring to Figure 293, the spatial resolution of the acquisition system depends on the focal length of the optics, on the distance between the cameras and on the distance between the acquired point and the camera itself.

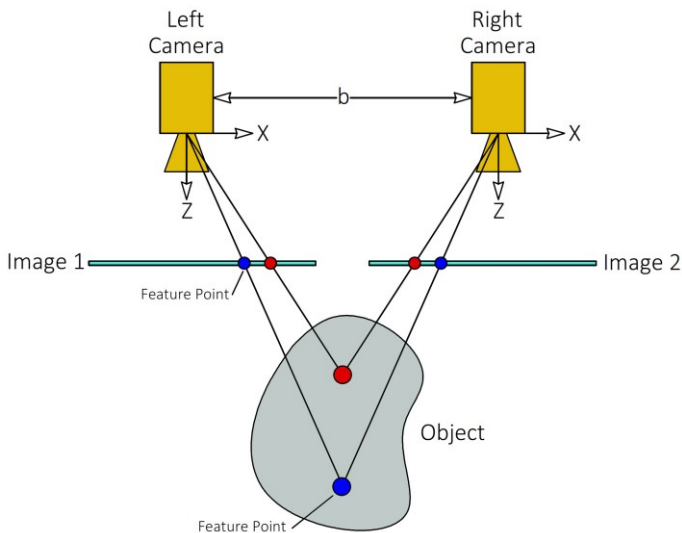


Figure 293 Parameters of a 3D stereovision scanning system

To evaluate the Z and X/Y spatial resolutions, Equation 62 and Equation 63 can be used in the case of a symmetrical 3D stereo-vision scanner, like the one presented in this chapter.

$$\Delta Z = \frac{z^2}{f \cdot b} \cdot \Delta_{px} \quad \text{Equation 62}$$

$$\Delta X = \Delta Y = \frac{z}{f} \cdot \Delta_{px} \quad \text{Equation 63}$$

Where:

ΔZ = spatial resolution of the scanner in the Z direction;

ΔX = spatial resolution of the scanner in the X direction;

ΔY = spatial resolution of the scanner in the Y direction;

f = focal length of the camera;

Δ_{px} = pixel size of the camera sensor;

b = distance between the two cameras of the stereovision scanning system;

z = distance between the camera sensor and the acquired point.

From Equation 63 it can be seen that the X/Y resolution depends on the pixel size Δ_{px} of the camera (Figure 294), on the focal length f (Figure 295) of the used optics and on the distance z between the camera sensor and the acquired target.

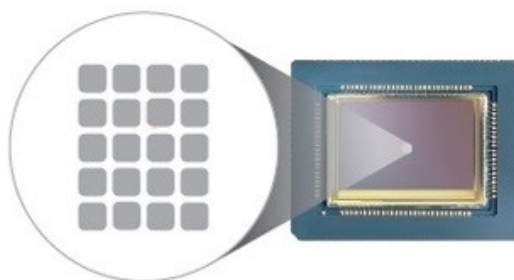


Figure 294 Schematic representation of the pixel size of a camera sensor

Instead, the Z resolution depends on the distance b between the two cameras too and it is quadratic with the distance z between the sensor and the target.

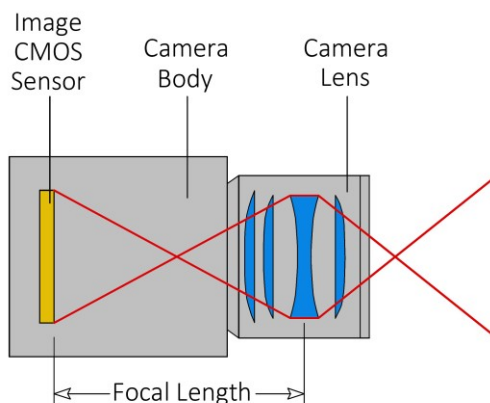


Figure 295 Visual explanation of the focal length of a camera lens

Looking at the resolution requirement of the proposed scanning/monitoring system (that was 0.5 mm) and keeping in mind the equations Equation 62 and Equation 63, the used camera lenses should have at least a focal length of 4 mm, while pixel size of the sensors of the camera should be no more than 6 μm .

The choice of the optimal focal length for the application, is a compromise between an improved resolution of the system and field of view of the cameras. In fact, if the focal length is very long, the spatial resolution will be very low, but the zone seen by both the cameras will be very small. The same thing is valid for the distances between the cameras. To obtain a good compromise between the dimensions of the zone seen by both the two cameras and the resolution of the system, a distance between the cameras of 100 to 150 mm should be pursued for the presented scanning system. The characteristics of the cameras used in the developed monitoring system are reported in Table 31, while the characteristics of the optics mounted on the cameras are reported in Table 32.

Table 31 Characteristics of the used CMOS USB camera

Characteristic	Value
Sensor type	CMOS OV2710
Resolution	1920 x 1080 (Full HD)
Output format	JPEG
Sensor Dimensions	5.856 x 3.276 mm
Exposition Mode	Auto or Manual
White balance Mode	Auto or Manual
Power requirements	5v DC, 150 mA
Working temp.	-20 to +70 °C
Dimensions of case	38 x 38 x 10 mm
Type of Case	Metal case
Fps at 1080 p output	30 fps
Hardware interface	USB 2.0



Table 32 Characteristics of the used zoom lenses

Characteristic	Value
Lens type	Zoom lens
Lens Mount	M12
Focal length range	2.8 to 12 mm
Focusing type	Manual
Image format	1/2.5"
Aperture/iris	Fixed, f/1.4
MOD	15 mm
Zoom type	manual



For what concerns the optical filters, two round DIN5 grade filters have been attached to the optics of the cameras. To attach such filters on the optics these have been glued on a soft plastic tube that has been press-fitted on the optics (Figure 296)

**Figure 296 Top view and side view of the filters for the lenses**

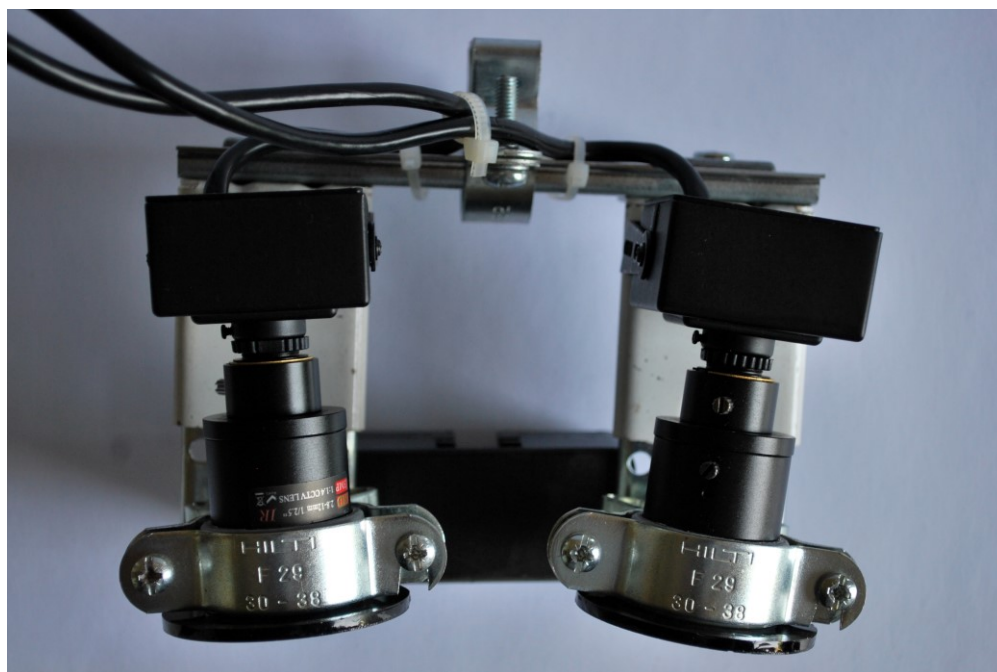
The expected characteristics of the designed monitoring system are reported in Table 33. These data have been obtained considering all the parameters specified in the previous lines and an average distance between the cameras and the scene of 200 mm.

Table 33 Expected characteristics of the monitoring system

Characteristic	Description/Value
X/Y Resolution	0.06 mm
Z Resolution	0.13 mm
MOD	200 mm
sfps (single frames per second)	25
cfps (coupled frames per second)	10
Dimension of a single frame	6 Mb

In order to be used for 3D scanning purposes, the two cameras must be mounted on a solid support able to keep the orientation of the cameras and the distance between those fixed. Besides, such support must be mountable on a WAAM machine. The machine selected to test the presented acquisition system is the retrofitted Roland Modela MDX40 presented in section 1.3. This because at the time of the development of the monitoring system the five-axis machine (presented in section 4) was still in the design stage. Moreover, the front of the Roland Modela MDX 40 offers a good accessibility and enough space to easily attach the monitoring system.

The developed fixture allows mounting of different lenses on the cameras and adjusting the distance between the cameras and their orientation. The weight of such fixture system is only 135 grams; therefore, it is easily attachable also on a small robot or small cartesian machine. The camera fixture is depicted Figure 297, Figure 298, Figure 299, Figure 300 and Figure 301.

**Figure 297 Top view of the support for the cameras with the cameras mounted on**

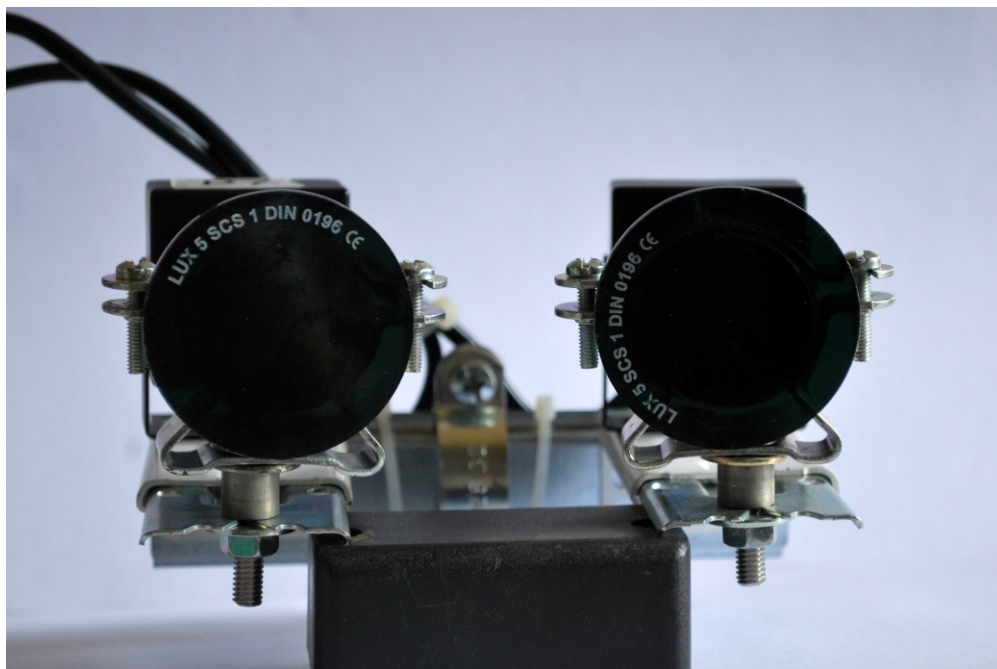


Figure 298 Front view of the camera assembly

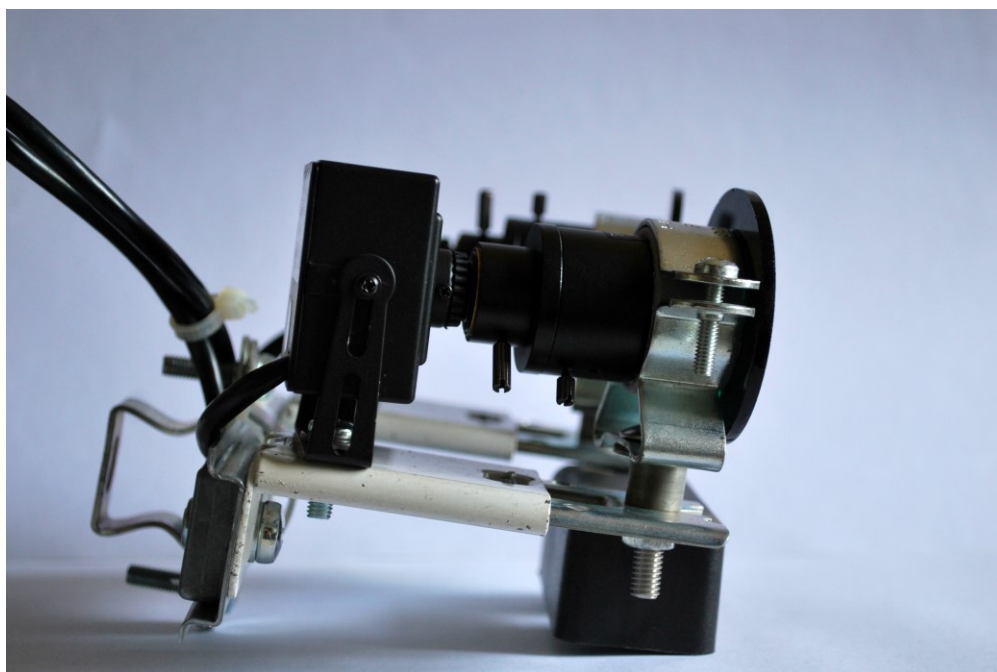


Figure 299 Side view of the camera assembly

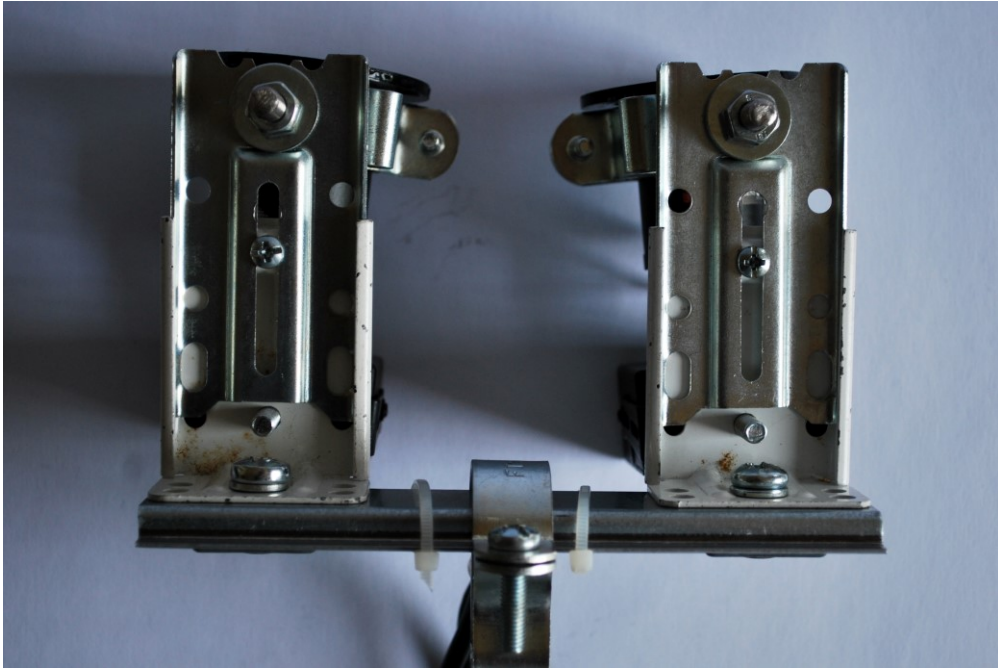


Figure 300 Bottom view of the camera assembly

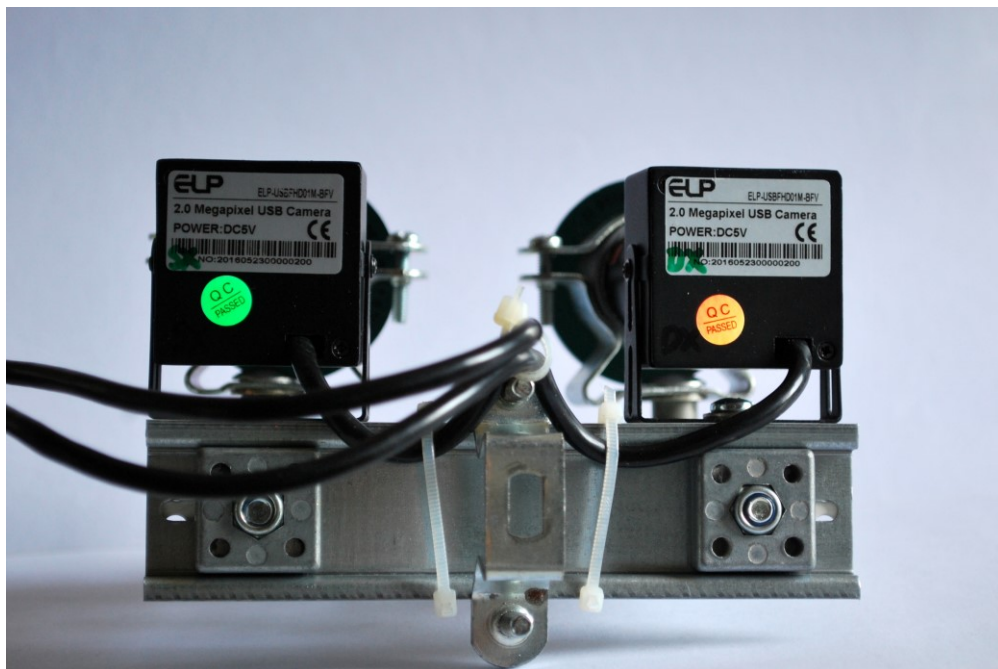


Figure 301 Back view of the camera assembly

The cameras are attached to the support through a screw; besides, to keep their orientation fixed, the lenses are hold by a standard connection element like the one reported in Figure 302. Figure 303 shows a detailed view of the system adopted to keep the camera orientation fixed.



Figure 302 A standard connection element used to create the support for the cameras



Figure 303 Fixturing of the camera lens

The camera assembly (i.e. the fixture with the cameras mounted on it) is attached to the Roland Modela MDX40 machine using a solid metal rod.

To use the monitoring system, a calibration of the cameras is needed to let the acquisition software knowing all the information on the configuration of the cameras themselves [105]. The calibration has been performed using the Camera Calibration Toolbox present in the MATLAB software and following the steps explained in [106].

To perform the calibration procedure a reference chessboard has been printed using a high-resolution printer (2800 dpi). The side of a single square of the chessboard is 7.8 mm. Such chessboard, printed on normal white paper, has then been attached to a face of a granite prism to assure a good planarity. The cameras, mounted on the support, have been placed on a plane in front of the granite prism (Figure 304).



Figure 304 The two cameras mounted on the support and placed in front of the prism for the calibration procedure

The steps present in the Matlab Camera Calibration Toolbox have been followed and several couple of pictures (a picture from each camera for each of the couples) of the prism have been taken in order to be further processed by the software algorithm. This first part of the calibration procedure aims at adjusting the reciprocal position of the cameras, i.e. the extrinsic parameters of the scanning system. Thanks to this first calibration step, the coupled field of view of the cameras is optimized and the cameras reciprocal position adjusted (Figure 305).

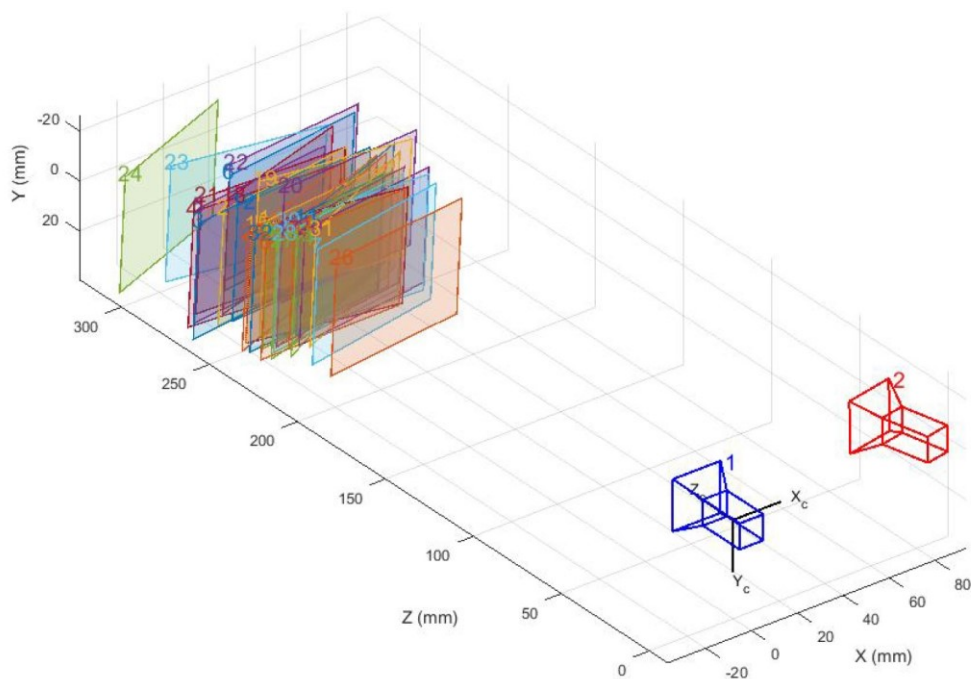


Figure 305 One of the results of the calibration procedure

Then another set of calibration steps is performed to determine the so called intrinsic parameters of the stereovision system. To carry out this calibration procedure 213 couples of photos of the chessboard has been taken in which each couple is composed by a picture from the first camera and a picture from the second camera. After the processing of the pictures by the Camera Calibration Toolbox, the mean reprojection error was about 0.09 pixel.

6.7. The pattern projector

To add feature that can be easily recognized and triangulated by the software a speckle pattern is projected on the scene. The configuration and reciprocal position of the cameras and the speckle pattern projector is reported in Figure 276. Since the triangulation is performed across the two pictures taken by the two cameras, it is not important that the processing software exactly knows where the pattern projector is, it is used only to add features in the pictures.

The lens to obtain the speckle pattern (i.e. the diffuser) has been manufactured using a PET, EN 13206 D-Class plastic film. The choice of this specific plastic material is due to its optical properties. To obtain the desired roughness on the lens, it has been decided to impress the PET sheet with a sheet of sandpaper. The PET sheet is placed on a rigid metal plate, the sandpaper is placed on the PET sheet and, finally, a heavy brick is placed over the sandpaper. Everything is placed in an oven at 70 °C for about 70 minutes. This configuration has been set up using a trial and error approach. With the same approach the grain of the sandpaper has been chosen and set to 600. The result is reported in Figure 306.



Figure 306 The PET sheet used to manufacture the lens for the speckle before (left) and after it has been impressed with a P600 sheet of sandpaper (right)

Finally, the manufactured plastic lens has been cut in the shape of a disk and glued on a C-mount flange to be mounted in front of the laser diode (Figure 307).

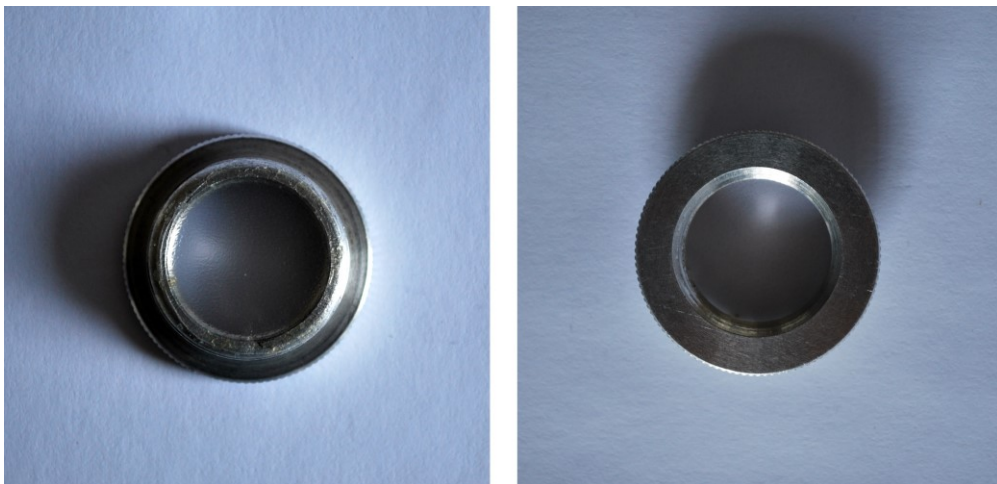


Figure 307 Bottom (left) and top view (right) of the plastic speckle lens attached on the C-Mount flange

Figure 308 shows the resulting speckle pattern. The relative distance between the manufactured speckle lens and the laser diode has been manually adjusted until the best result has been achieved.

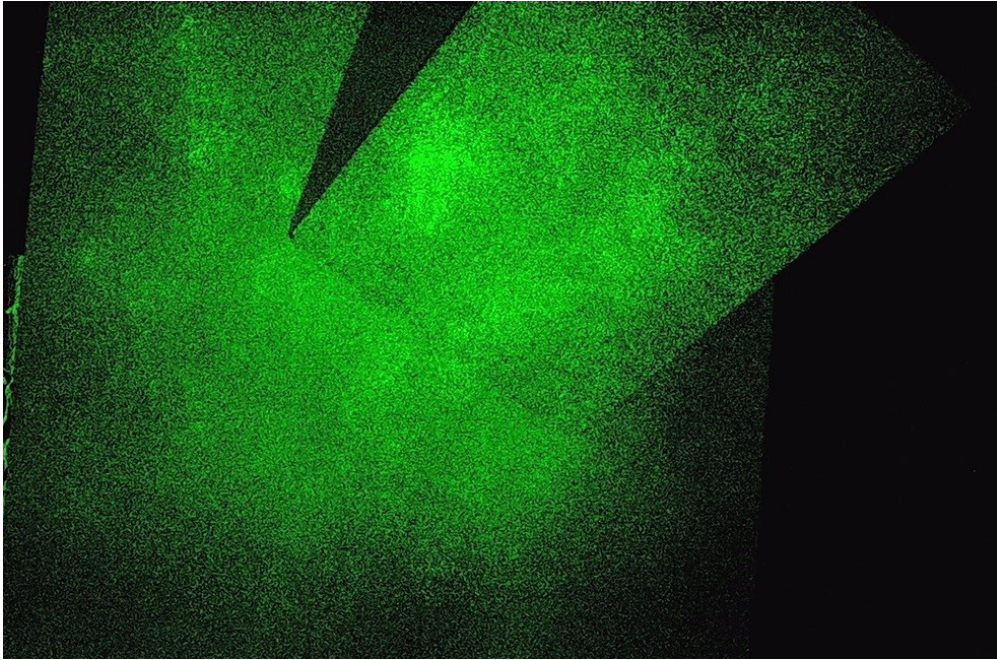


Figure 308 The speckle pattern obtained with the selected laser diode and the manufactured plastic lens

Finally, an enclosure for the laser diode, its controlling circuit and the speckle lens has been found. Therefore, the pattern projector is composed by the following hardware:

- Diode-based 532 nm green laser with power of 50 mW;
- TTL controlled laser driver;
- Speckle plastic lens;
- Protective enclosure;

To test the goodness of the speckle pattern a test has been carried as suggested by [107]. Several images of the speckle pattern projected on a white planar surface have been acquired using a full-hd camera. Then, the acquired images have been further processed using a software routine. First, the image undergoes an intensity normalization, then a region of interest of 200 x 300 pixels is extracted from the centre of the image. At this point, a 2D autocorrelation of the ROI is performed and the result is compared with an artificial reference test case. In fact, the resultant autocorrelation is compared with a random 200 x 300 matrix generated using MatLab. If the resultant value is near or smaller than the reference one, it means that the obtained speckle is randomly distributed and therefore acceptable for the developed application. The reference parameter is 1.4×10^{-4} , while the one resulting from the elaboration of the image of the real speckle is 1.9×10^{-4} . Therefore, the obtained speckle can be considered randomly distributed and suitable for the application.

Pictures of the hardware of the pattern projector are reported in Figure 309, Figure 310 and Figure 311.



Figure 309 Front view (left) and side view (right) of the pattern projector assembly

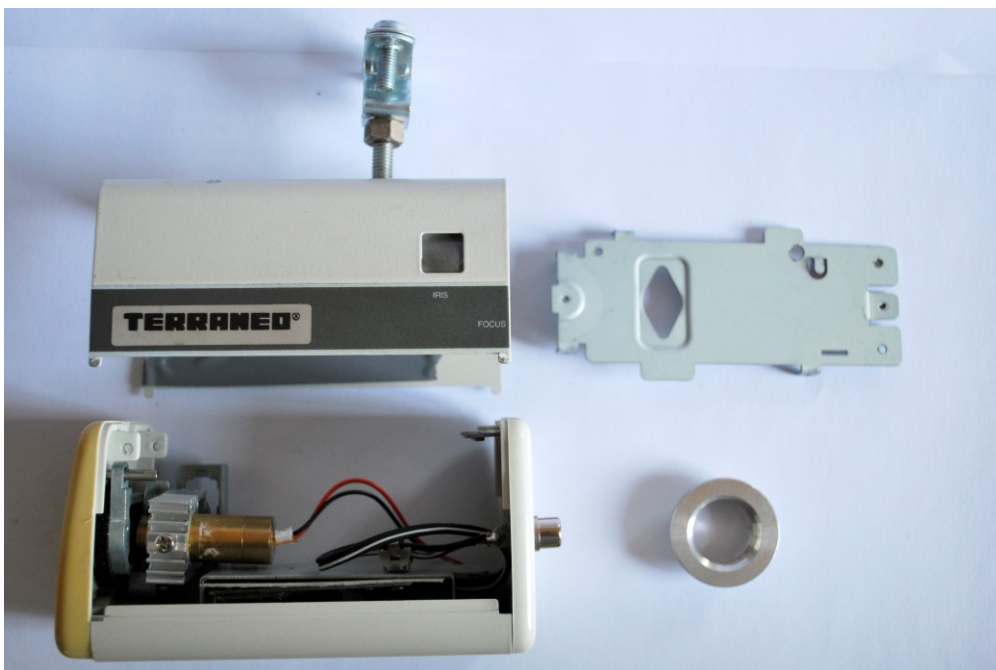


Figure 310 The pattern projector disassembled

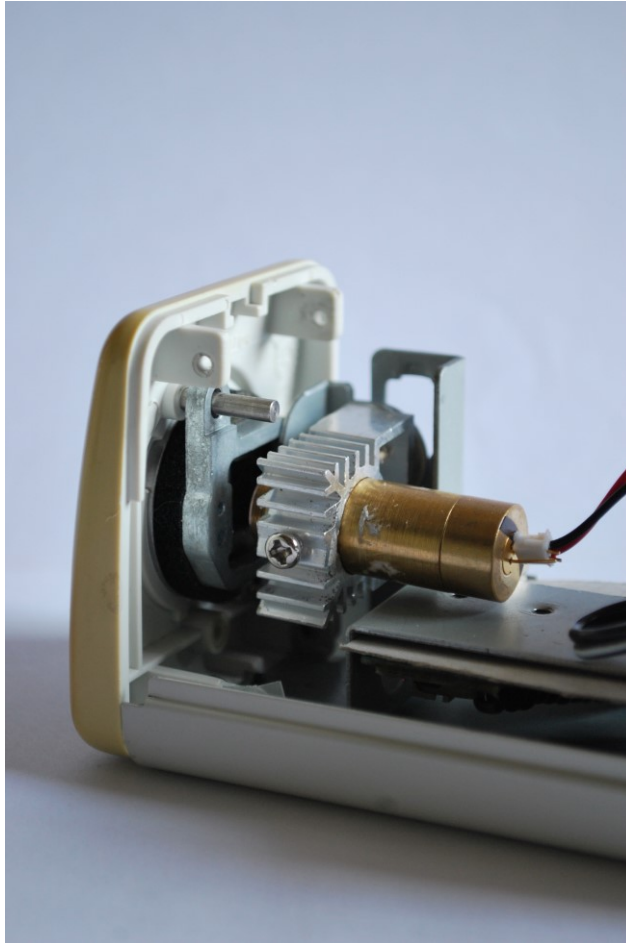


Figure 311 A close view of the laser diode inside the case of the pattern projector

Such hardware allows for some adjustments; in particular the distance between the laser and the lens can be adjusted and also the inclination between the laser and the lens. Both these parameters influence the quality of the laser speckle. For this reason, before testing the hardware, autocorrelation test of the obtained speckle must be performed to be sure no variations have occurred inside the protective case.

6.8. The structure of the software

The main functions of the software are:

- Acquisition of the two images (one for both the two cameras);
- Reconstruction of a point cloud of the scene;
- Post processing of the point cloud to extract the width and height of the weld bead.

Since for all these three main functions and for the calibration of the cameras, the MATLAB software offers many toolboxes, it has been selected as the programming environment for the presented activity. The developed software follows the main steps listed below to obtain the geometrical characteristics of the weld bead from the two acquired images:

- Image acquisition (the software developed in Matlab takes also care of controlling the cameras and acquiring the images);
- Correction of the images to eliminate the deformations brought by the lens distortion;
- Extraction of the green channel from the images and equalization of the resulting images;
- Filtering of the images;
- Extraction of features from the two images and clustering;
- Features matching and bad correspondences screening;
- Coupled features triangulation and second screening;
- Registration and de-noising of the point cloud;
- Statistical analysis of the point cloud and extraction of the geometrical parameters of the weld bead.

The points are extracted from the images thanks to robust matching elements, taking advantage of the speckle characteristics. The speckle texture is characterized by the presence of so called “blob zones” (Figure 312).

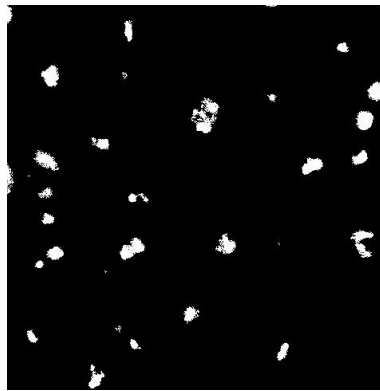


Figure 312 Blobs in a speckle pattern

The properties of a blob (Figure 313) are easy to be extracted from an image and matched between a picture from the first camera and the other from the second camera.

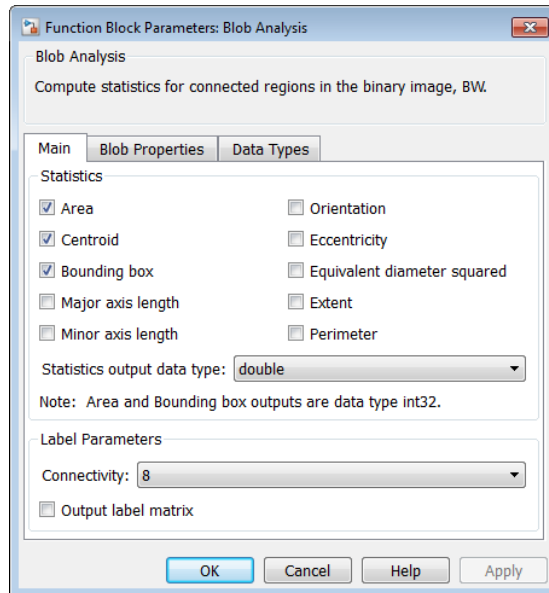


Figure 313 The Matlab form showing some of the properties that can be extracted from the blobs of the speckle pattern in the acquired image

This because the binarization of an image containing a speckle pattern produces a resultant image containing a series of points with a precise and low variance (Figure 314).

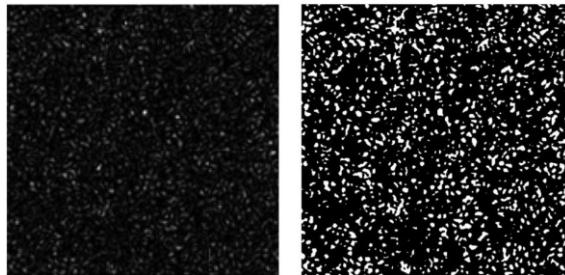


Figure 314 Acquired speckle pattern before (left) and after (right) binarization (from [108])

The grouping and clustering of such points is carried out considering groups of points with a high spatial and neighborhood correlation using the statistical clustering analysis offered by the MATLAB software. This appears to be the best feature recognition procedure, since when a set of points is statistically correlated also the epipolar characteristics are similar. Therefore, the successive point screening using the epipolar constraint is facilitated. Figure 315 reports the flowchart for the feature extraction algorithm, while Figure 316 shows the flowchart for the feature matching and bad correspondence screening for a single cluster.

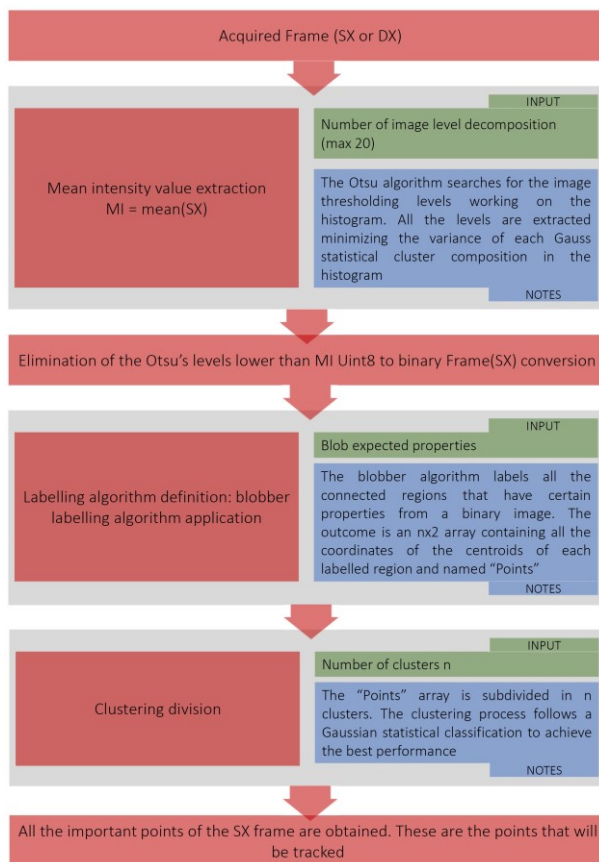


Figure 315 Feature extraction algorithm flowchart

Referring to Figure 316, the Kanade Lucas Tomasi (KLT) algorithm is a feature tracker and matching algorithm [109]. Going deeper in detail, given the two coordinates of a point (pixel) in a first image I_1 , the goal of such algorithm is to find the correspondent point coordinates in a second coupled image I_2 ; the algorithm has also to consider that the two images, taken by two different cameras, can be translated of a planar vector v . The KLT algorithm works on a window which sides are ω_x and ω_y .

The system works searching the minimal value for the residual formulation of the problem. To decrease the computational time, it is recommended to perform a pyramid decomposition of the images carried out using the methods reported in [110].

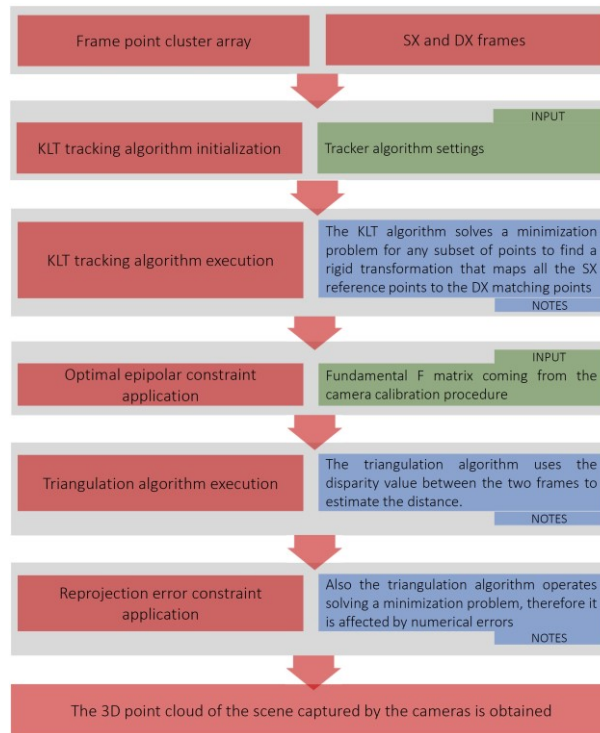


Figure 316 Features matching for a single cluster algorithm flowchart

So, the most important parameters and aspects in the KLT algorithm are:

- Searching window size;
- Number of pyramid decomposition;
- Number of iterations;
- Quality of the reference matching points.

Once the point cloud of the scene has been acquired, this must be analyzed and processed to extract the information regarding the welding bead being deposited. The flowchart explaining the operations performed on the obtained point cloud is reported in Figure 317.

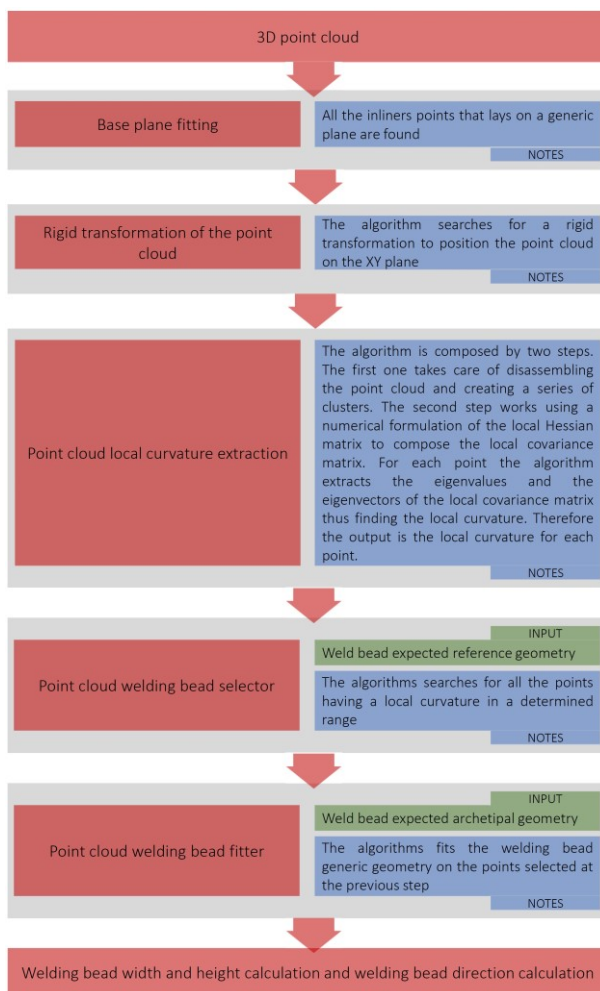


Figure 317 Parameters extraction algorithm flowchart

To eliminate all the points that do not represent part of the welding bead, the software uses the information of the local curvature of the point cloud: all the points which local curvature is in a specific range are on the weld bead. It is important to notice that the Gaussian curvature, which describes the local curvature of a surface, is invariant to rigid transformations and depends only on the local surface morphology; for this reason, the curvature values of the points won't be affected when re-orienting the point cloud respect to a known reference system in order to facilitate the processing of the point cloud itself. For a generic parametric surface, the Gaussian curvature can be calculated using the analytical formulation of the surface itself. Anyway, in the case of a point cloud, a finite numerical formulation must be used, because it is not possible to easily find an analytical formulation of the surface.

In the case of an analytical surface formulation [111], expressed by Equation 64, the Gaussian curvature K is given by Equation 65:

$$\sigma(x, y) = (x, y, f(x, y)) \quad \text{Equation 64}$$

$$K = k_1 \cdot k_2 \quad \text{Equation 65}$$

$$k_i = i - \text{th eigenvalue of } Q = [F_1^{-1}F_2]$$

Where Q is the Hessian Matrix, F_1 and F_2 are the principal matrices. Using a finite difference formulation of the first and second order derivatives, a numerical form of the Gaussian curvature can be obtained through Equation 66:

$$f(x + \Delta x) = f(x) + \sum_{n=1}^{\infty} \frac{\partial^n f \cdot (\Delta x)^n}{\partial x^n \cdot n!} \quad \text{Equation 66}$$

The eigenvalues of the Hessian matrix Q can be extracted using the SVD decomposition and the local curvature radius can be obtained as the reciprocal of the local curvature value. To improve the speed and facilitate the steps of such procedure, a neighborhood tree mapping of the point cloud can be carried out. This way, for each point, a certain number of neighbor points are selected and used to calculate the approximate Hessian matrix and, then, the local curvature on the current point.

The next step is the weld bead model fitting, this is important to exactly locate the bead in the obtained point cloud first and then extract the parameters of the weld bead itself. To obtain this result, an algorithm derived from the RANSAC method [112] has been implemented in the software. In this step, the shape representing the welding bead is searched in the section of point cloud which points have a curvature value in a specific range. This step is mandatory to let the software understand the welding direction, i.e. the longitudinal direction of the bead which section encumbrance is the desired output of the presented system. To carry out these operations, a curve model for the cross section of the weld bead must be specified. The simplest curve model is a parabola [13], but in this activity a Gaussian curve has been selected to obtain the best fitting results, especially near the root of the weld bead. Keeping in mind that the trajectory of the torch is a polyline made of straight segments, complex point clouds, originated from the acquisition of complex geometries, can be decomposed to facilitate the processing procedure and to speed it up. Considering the bead as a succession of rectilinear segments makes sense, since the output of the post processor for three axis operation is a polyline made of straight segments. Keeping in mind also this last aspect, the following steps can be applied to locate the bead and the welding direction in the point cloud:

- Given the set of points which curvature value is in the acceptable range, a set of N couple points can be extracted from the point cloud itself;
- For each set, from 1 to N and for each couple of points A and B contained in the set, a vector (A-B) connecting the point A to the point B is calculated;
- The point cloud undergoes a rigid transformation to orient the original Y axis like the (A-B) vector;
- All the points of the transformed point cloud are projected on the XZ plane;
- A certain number of points around the point A, n_A , and the same number of points around point B, n_B , are extracted obtaining the subset of points $S = \{n_A, n_B\}$;
- A fitting of the Gaussian curve model on the XZ plane using the S subset of points is carried out;

- The best fit is evaluated using the RANSAC algorithm (the Matlab software is used in this case);

After the Gaussian curve has been fitted on the point cloud, the welding direction has been detected, since it is represented by the (A-B) vector, while the height and width of the bead can be easily extracted.

6.9. Testing of the monitoring system and setting of the software parameters

6.9.1. Artificial tests

First, a series of test outside the welding machine has been carried out to understand whether the output of the system was correct or not. The objective of these tests was to evaluate the accuracy of the system. The acquisition target was a surface with good planarity. The granite prism with the attached chessboard was used in these tests. During the tests the pattern projector was turned off and the optical filters were not installed, therefore the feature used by the software for the triangulation were only the one present in the real scene, there was no help from the pattern projector. Ten scanning procedures were carried out at an average distance from the target of 350 mm. An example of the resultant acquisition and triangulated points are reported in Figure 318.

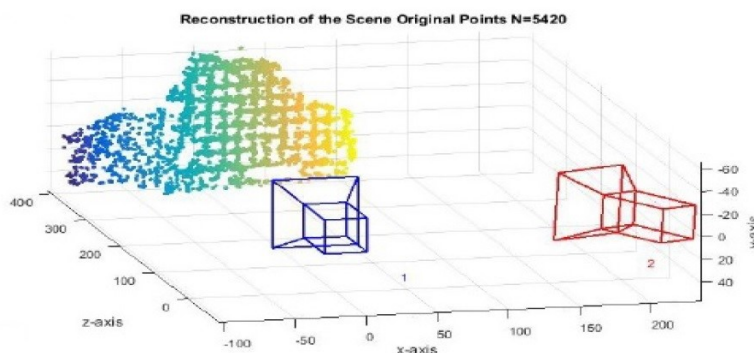


Figure 318 Point cloud resulting from the acquisition of a planar surface

The deviance of the points acquired in these tests was $\sigma = 0.01$ mm, while the mean residual deviance from a reference perfect plane was 0.084 mm (with a maximum deviance value of 0.2 mm).

The second set of tests was carried out acquiring the granite plane of a Mitutoyo Euro-C A776 Coordinate Measurement Machine and the 45-degree plane of the granite prism used in the previously described test and for the camera calibration procedure. In this session of tests, the pattern projector was turned on during the acquisition. A sample image with marks that highlight the triangulated point is reported in Figure 319.

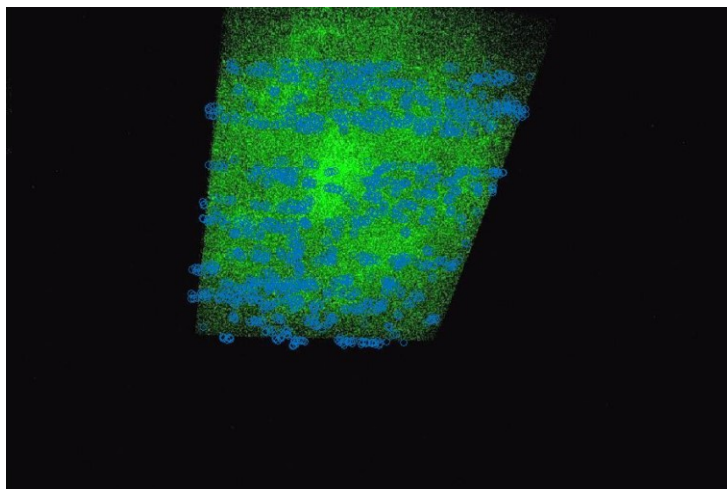


Figure 319 Sample image acquired by one of the two cameras. The green speckle pattern is visible. The blue marks are the points used by the software for the triangulation

In terms of accuracy the results of the acquisition of the planar surface were the same of the previous test. For what concerns the acquisition of the inclined surface the mean deviation from a reference plane still remains under the 0.5 mm, that is the accuracy required by the specification. The resultant acquisition of the inclined plane is shown in Figure 320.

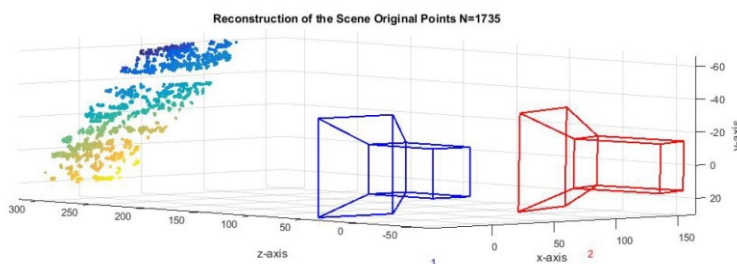


Figure 320 Point cloud resultant from the acquisition of the inclined surface with the pattern projector on and the optical filters mounted on the lenses of the cameras

This simple set of tests was carried out to obtain the best performance of the scanner in an undisturbed environment and with a simple target geometry: the results of these tests would have been the milestone for the test carried out in a real welding environment.

The last artificial set of tests was carried out using an RGB 5050 SMD LED to simulate the light emitted by the welding arc. Using a specific driver for the LED, it is possible to modulate the emitted power in order to simulate the welding arc. These tests aimed at determining all the parameters to be set in the software and to test the acquisition performance of the monitoring system in a near-to-real scenario. Two different kind of tests were executed: in the first one, the planar surface of the previously used granite prism was scanned, while in the second one two planes at different Z coordinates were acquired (Figure 321).

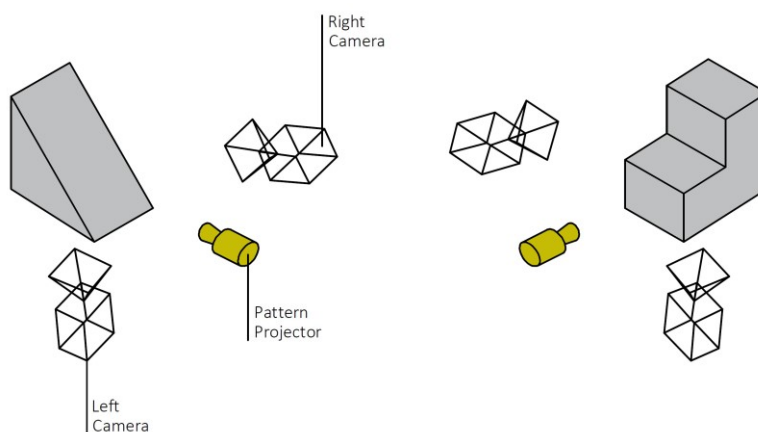


Figure 321 Inclined surface (left) and two-levels step (right) acquisition scheme

This way, both the performance in a near-to-real scenario and the Z resolution of the system were evaluated. Figure 322 shows an example of acquired image with the LED turned on.

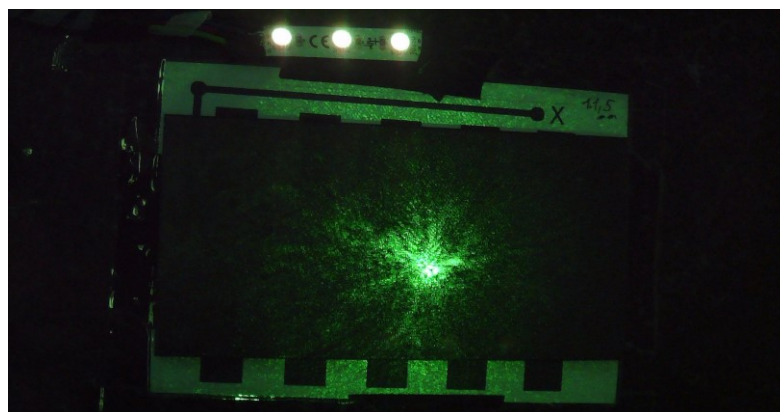


Figure 322 Acquisition test in near-to-real conditions. A led simulates the light emitted from the welding arc

Regarding the results, the planar surface was acquired with the same performance of the previous test; also for the planar surfaces at different height the acquisition performance was the same of the single planar surface. To make the software able to correctly acquire the scene, several manual adjustments have been carried out during these tests to reach the optimal performance. The set of parameters that gave the best results is reported below:

- Epipolar constraint confidence: 96%;
- Reprojection error confidence: 96%;
- No of clustering groups: 4;
- KTL window dimensions: 31 x 13 pixels;
- No of pyramid image decompositions: 4;

- No of image gaussian decomposition: 20;
- Fixed exposure value for the cameras.

6.9.2. Tests in a real welding scenario

To test the scanning system in a real welding scenario, it has been attached to the three axis Roland Modela MDX40 machine. The arrangement of the cameras and of the pattern projector have already been described in the previous chapter, but the overall configuration is reported here again in Figure 323 for the sake of clarity. The support with the two cameras is mounted on a transversal metal bar, while the pattern projector is attached directly to the torch carriage through a metal support.

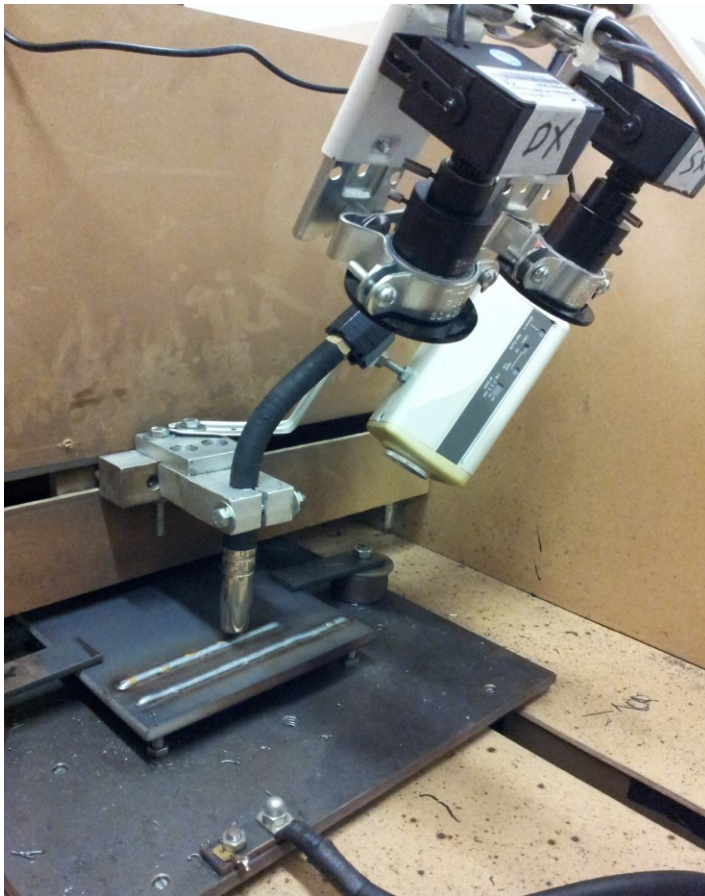


Figure 323 The monitoring system installed in the Roland Modela MDX40 machine

The ambient conditions are listed below:

- GMAW DC welding machine (AWELCO 250 PULSEMIG);
- Mean welding amperage from 40 to 60 A;

- Diameter of the welding wire: 0.8 mm;
- The smoke originating from the welding is not removed;
- Pattern projector placed 150 mm far from the torch tip and directly attached to the torch clamp.

Three different shapes have been acquired during these tests (Figure 324), all on a planar surface:

- Linear bead;
- L shaped bead;
- Circular sector bead.



Figure 324 One of the specimens produced for the testing of the monitoring system

The setting parameters for the first real cases were estimated using the settings from the artificial tests. It is important to notice that the acquired scene is very dynamic, therefore the convergence parameters of the KLT algorithm cannot be evaluated without a real test; so, the settings of such parameters may be adjusted every time the welding current changes or, in general, when a change in a parameter of the acquired scene occurs. However, the parameters used for the real tests described in this paragraph are the same determined in the artificial test described in section 6.9.1.

At the moment there are no triggering devices for the software procedure, therefore it is necessary to start the welding procedure using the numerical control of the machine and, at the same time, manually press the start button on the software interface of the acquisition system.

Figure 325 and Figure 326 report respectively a couple of images acquired by the two cameras and the correspondent result of the filtering algorithm on the acquired images.

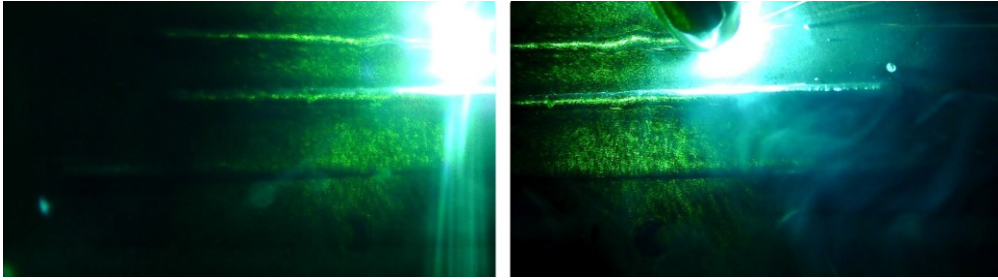


Figure 325 Two image acquired during one of the real welding tests. The image on the left is from the left camera, the one on the right is from the right one

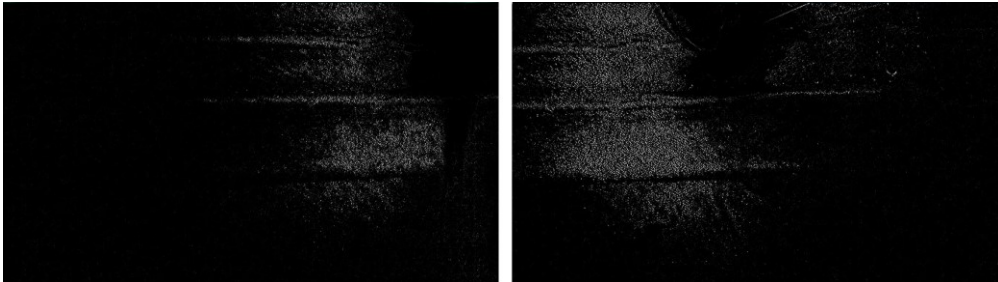


Figure 326 The images of Figure 325 after the filtering procedure has been carried out

Moreover, Figure 327 and Figure 328 show a comparison between a real image and the correspondent reconstructed point cloud in the case of a linear and of a curved bead.

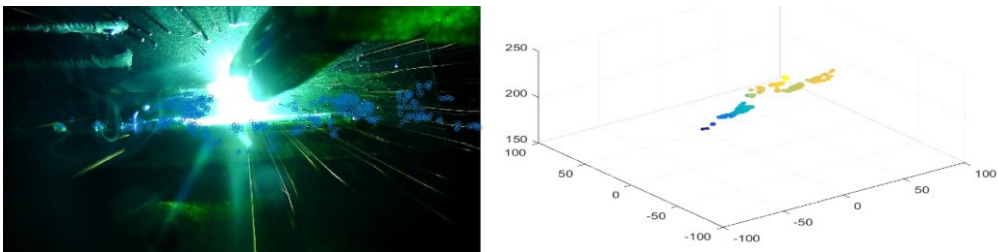


Figure 327 One of the acquired images (left) and the reconstructed point cloud (right) for the deposition of a linear bead. The blue marks on the real image are the triangulated points

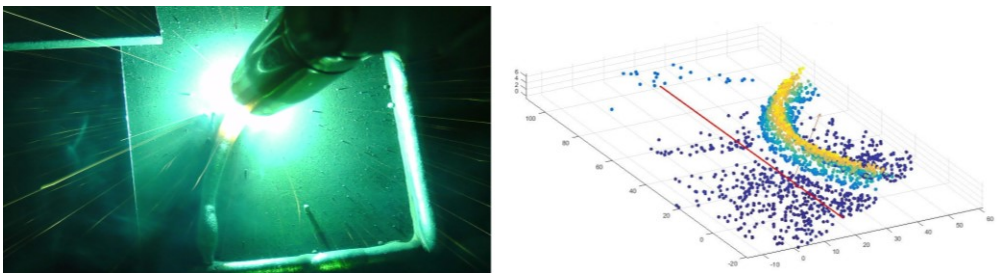


Figure 328 One of the acquired images (left) and the reconstructed point cloud (right) for the deposition of a curved bead

The analysis of the results of the acquisition of the linear bead shows that the system is able to acquire a complete point cloud also in a real welding environment. Anyway, increasing the welding current leads to an excessive light emission that sometimes make the cameras not able to acquire the scene in the correct way. To solve this problem, a possible solution could be varying the exposure value of the cameras depending on the value of the welding current itself. Moreover, a wider set of optical filters should be evaluated to tailor the right filter for the current value of welding current. However, increasing the welding current above a certain limit would require the use of a much more powerful laser source, and this could be a problem in terms of healthy issues and would require the development of adequate safety devices and procedures. Anyway, nowadays the trend in WAAM is going towards very low current GMAW variants that have a mean current value lower than the one used to carry out the presented tests (Figure 329).

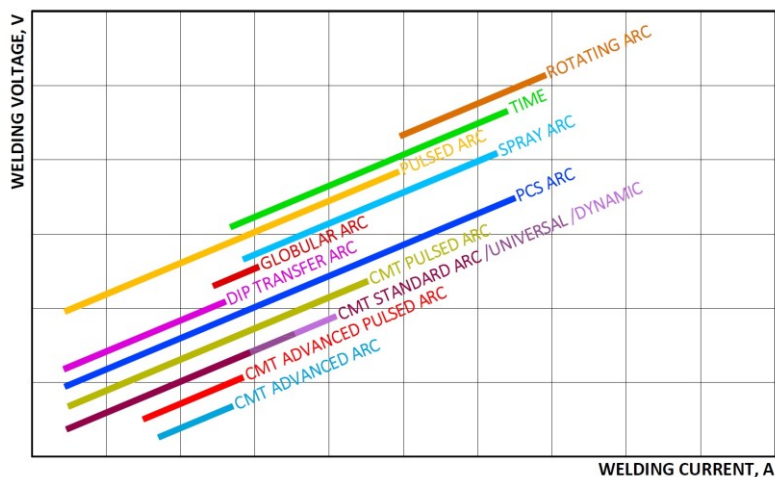


Figure 329 Current and voltage values for different MIG welding technique (adapted from [113])

The analysis of the processing speed of the software revealed that using a region of interest instead of the whole acquired image increases a lot the computational speed. The calculation time for each triangulated point is 0.1 ms, so the resultant point cloud is extracted in a very short time.

The average density of points in the hot zone of the welding bead is 8 points per square millimeter, while the average density of triangulated points far from the hot zone is 15 points per square millimeter. Inside the welding plasma zone, no point is acquired (Figure 330).

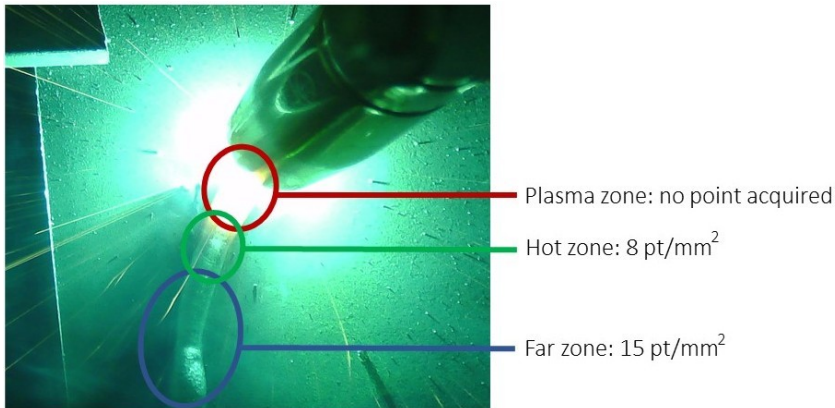


Figure 330 Different acquisition densities for the different zones of a weld bead

For what concerns the second step of the software procedure, i.e. the weld bead parameters extraction, it required a little bit of manual optimization to find the best set of parameters starting from the first attempt one. All the optimized parameters are reported in Table 34.

Table 34 The parameters for the triangulation and the weld bad parameters extractor

Kanade-Lucas-Tomasi Triangulation		Welding Bead Parameters Extractor	
Parameter	Value/Description	Parameter	Value
Image size	1080p	Radius cut-off	17 mm
Pyramid Decomposition	4 levels	Number of trials	1000
Block size window	13x33 pixel	Max Height	10 mm
Bidirectional Error	1 pixel	Max Width	20 mm
Parallel Cluster	4 clusters	Inliners threshold	0.25 mm

An example of extraction of weld bead shape and fundamental parameters for a linear bead is reported in Figure 331. In this case the system detected a width of 5.645 mm and a height of 3.063 mm for the weld bead. Referring to Figure 331 the blue curve representing the best fitted Gaussian curve is noticeable.

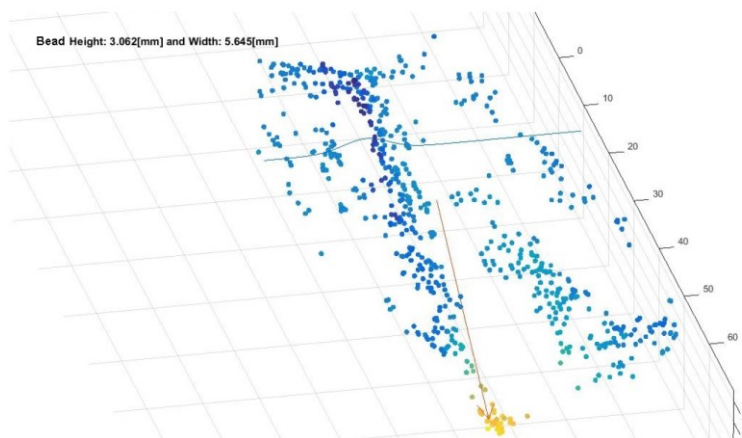


Figure 331 The point cloud for a linear bead and the best fitted gaussian curve. The system detected a width of 5.645 mm and a height of 3.063 for the weld bead

For what concerns the acquisition of more complex shapes such as circular beads or L shaped beads, the point of view of the monitoring system become a fundamental parameter. The best condition would be to mount the monitoring system directly on the welding head, i.e. the monitoring system should move with the torch; for this reason, the best condition would be to mount the monitoring system directly on the end effector of a robot. This way, the visibility would always be the best one for the monitoring system. Figure 332 shows a possible solution in this sense.

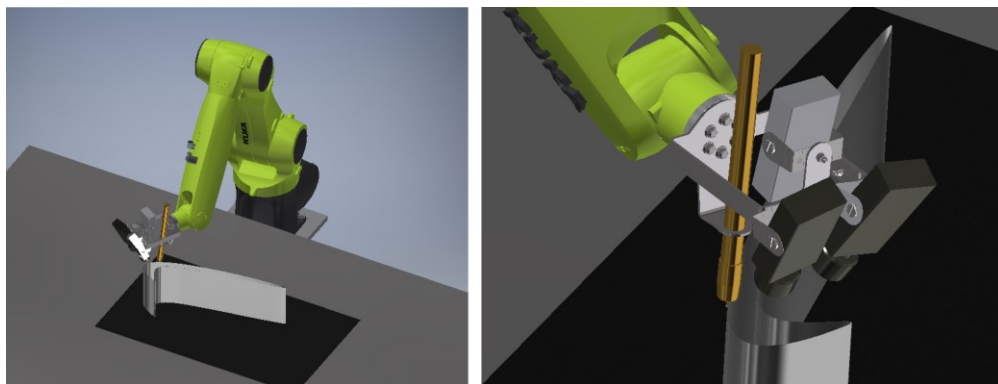


Figure 332 A possible configuration in which the monitoring system is mounted on a welding robot

In the Roland Modela MDX40 machine the visibility is not always optimal for the monitoring system, due to the configuration of the machine itself; anyway, in general, a machine with a cartesian structure will not offer the best visibility conditions if the monitoring system is rigidly attached to a part of the machine. To obtain a good visibility in all the possible machine configurations, also the position and orientation of the monitoring system should be controllable by the numerical control.

Regarding the extraction of the parameters of the weld bead, in the case of beads with a shape more complex than the rectilinear one the subdivision of the acquired point cloud in smaller sections is mandatory, otherwise the parameters extraction fails in most cases (Figure 333)

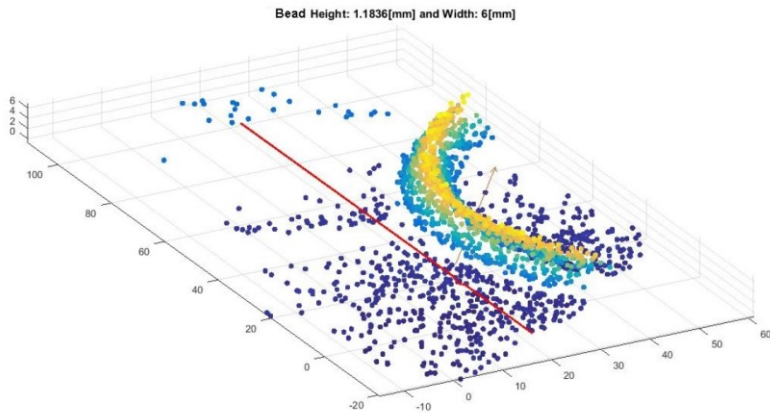


Figure 333 Failure of the parameter extractor software

Such subdivision of the point cloud is carried out automatically by the software and seems not to slow down the overall computational speed: a point is processed in 0.9 ms and the parameters extraction succeeds (Figure 334).

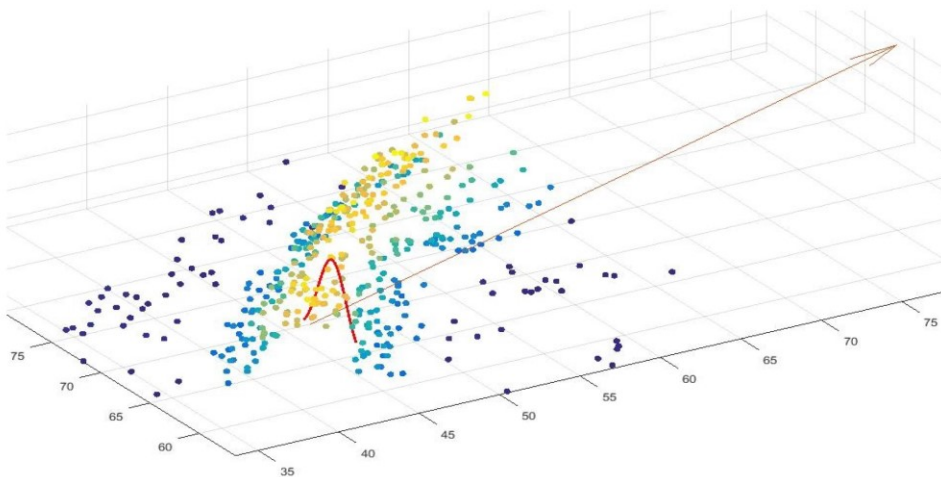


Figure 334 After the segmentation of the point cloud, the software can correctly extract the geometrical parameters of the weld bead

To validate the performance of the parameter extraction procedure, the beads deposited during this test were measured using a Vernier caliper and the result of the comparison between

the dimensions extracted by the software and the dimension acquired on the real specimen are reported in Table 35.

Table 35 Comparison between the width and height of the deposited beads obtained using a manual caliper and the values extracted with the presented monitoring system

Bead type	Measured Height (manual caliper) (average value)	Measured Width (manual caliper) (average value)	Extracted Height (software)	Extracted Width (software)
Linear bead	2.975 mm	5.23 mm	3.06 mm	5.64 mm
Curved bead	2.525 mm	5.6 mm	2.71 mm	5.85 mm
L shape bead	2.535 mm	5.025 mm	2.6 mm	5.22 mm

Referring to Table 35, it is noticeable that all the differences between the real value and the one extracted by the monitoring system are below 0.5 mm that was the accuracy target value for the proposed monitoring system.

7. Conclusions and final remarks

This thesis deals with the development of a CAM system for the calculation of deposition toolpaths for the WAAM additive manufacturing technology. This process is very promising and nowadays it is being studied by many Research Centers and Universities. The focus on this technology is due the possibility of building parts large up to meters with a high deposition rate. Especially in the aerospace and oil & gas sectors, this is very attractive, since it would be possible to build large parts without the problems related to the supply chain of the stocks and savings large amounts of material. In fact, the volume of the deposited material is very close to the final one, especially if compared to the case of subtractive manufacturing, where the starting stock is a solid billet. Moreover, it is worth remembering that in the cited sectors the BTF ratios are usually very high, since the components often feature thin walls; for this reason, introducing the WAAM technology would lead to a large amount of material and cost savings.

However, the spread of the WAAM process in the industry world is still limited due to many factors. Among the main ones there are the high residual stress and distortions induced by the process itself in the final part, the lack of automatic software for the toolpath programming of complex parts and the lack of specific manufacturing guidelines and procedures. Moreover, since WAAM is a Direct Energy Deposition technology, it offers the possibility of building parts without the needing for supports, using a five-axis machine. Especially for five-axis applications, just a few software tools for the toolpath calculation are available in the market or even in the research world.

For these reasons, the present thesis proposes two CAM modules for toolpath calculation dedicated to WAAM and both addressed to thin walled components, i.e. parts which walls can be built stacking just one welding bead over the other. The first module can be used to program three-axis toolpaths. In three-axis thin walled components, one of the main issues is related to the crossings, where two or more walls intersect each other. The proposed software tool includes some algorithms for the calculation of the toolpath in such critical zones thus making the overall calculation procedure as automatic as possible. Moreover, software tools such as anti-collision control and other ancillary calculation modules for tubulars have been implemented to obtain a complete software usable in real industrial applications.

The second CAM module is a vertical software tool dedicated to five-axis toolpath calculation; it is composed by several sub-modules each one dedicated to a specific geometric

shape (impellers, twisted hollow blades and freeform ducts). Both the three axes module and the five axis one, are almost automatic and request a very limited input from the user that has to set the process parameters such as layer height, layer width and to select some geometric elements the calculation algorithms start from. To test the toolpaths and the deposition strategies implemented in the three axis CAM module, several deposition tests have been carried out to understand which the best ones were and set the best parameters for each selected strategy. This synergy between experimental activity and software development has been fundamental to achieve a reliable product that seems to be one of the few automatic CAM tool for WAAM available in literature.

For what concerns the five axis CAM module, also a kinematic simulation tool has been implemented and presented. This is fundamental to test the calculated toolpath before launching it in the real machine to avoid possible damages due to collisions between the part and the machine or between two parts of the machine itself. Five-axis simulation modules for direct energy deposition technologies are rarely visible in literature even if they are fundamental for the toolpath programming of complex five axis operations. Both a simulation application in workpiece coordinates and another one showing the complete machine are presented and discussed.

To test the five axis deposition toolpaths and to understand the difficulties and characteristics of the WAAM five axis deposition, a five-axis machine with roto-tilting table has been developed. An innovative design for the roto-tilting table based on laser cutting of sheet metal has been presented. This design is especially dedicated to WAAM since it is lightweight and differs from some machines available in the market that are based on bulky five-axis machining centers. In fact, even if WAAM manufactured parts need some additional milling operations to match the desired surface quality, these are just finishing operations in which the milling forces are usually low; therefore, also a lighter machine structure could withstand this kind of forces.

Finally, two additional chapters are included in the thesis: one dedicated to a cost model for WAAM and the other one dedicated to a process-monitoring system. The presented cost model can be a valid tool to help in the selection of the production process for a specific part. The interesting aspect of the presented implementation is that the cost model is toolpath based, i.e. the main input for the cost calculation is the toolpath for the deposition of the part. Moreover, also the finish-milling cost is included to have the real cost of the final part; this is calculated with a surface-based approach, since the cost of finish milling operations is related to the total surface to be machined rather than to the volume. Since the cost model is toolpath based, it can be integrated with the CAM software modules obtaining a seamless tool that can output both the deposition toolpath and the final cost of the part. Further work is needed in this field to include other cost drivers such as the failures that can occur in the first manufacturing attempts of a components that could fail due to severe deformations of other WAAM-related defects. However, the presented cost model can be a valid automatic tool to obtain an early accurate estimation of the final cost of a WAAM manufactured part.

For what concerns the monitoring system, it is a real time 3D scanning laser-based acquisition system that is able to acquire the geometry of the deposited material while the WAAM machine is working. It has been tested in three axis operations and the results are very promising. The output of this system is a point cloud representing the acquired portion of deposited bead. An interesting future development for this system is the integration with the numerical control of the WAAM machine, thus obtaining a system able to control the process in real time and even automatically correct occurring defects such as lack of material or waviness.

In conclusion, the core of this thesis is the innovative automatic CAM software, but it also presents some ancillary systems such as the cost model and the monitoring system trying to propose some solutions that can overcome the limits of the WAAM technology. The experimental activity supported by the designed and built five axis WAAM machine completes and strengthens the proposed solutions.

Bibliography

- [1] F. Martina and S. W. Williams, "Wire + arc additive vs. traditional machining from solid: a cost comparison," 2015.
- [2] D. Ding, Z. Pan, D. Cuiuri, and H. Li, "Wire-feed additive manufacturing of metal components: technologies, developments and future interests," *Int. J. Adv. Manuf. Technol.*, vol. 81, no. 1–4, pp. 465–481, 2015.
- [3] S. Jhavar, N. K. Jain, and C. P. Paul, "Development of micro-plasma transferred arc (μ -PTA) wire deposition process for additive layer manufacturing applications," *J. Mater. Process. Tech.*, vol. 214, no. 5, pp. 1102–1110, 2014.
- [4] B. A. Szost *et al.*, "A comparative study of additive manufacturing techniques: Residual stress and microstructural analysis of CLAD and WAAM printed Ti–6Al–4V components," *JMADE*, 2015.
- [5] R. Singh, "Welding and Joining Processes," in *Applied Welding Engineering (Second Edition)*, 2016, pp. 163–195.
- [6] Y. M. Zhang, Y. Chen, P. Li, and A. T. Male, "Weld deposition-based rapid prototyping: A preliminary study," *J. Mater. Process. Technol.*, vol. 135, no. 2–3 SPEC., pp. 347–357, 2003.
- [7] A. Yaedu, P. Da Silva, and A. D'Oliveira, "Influence of dilution on microstructure and mechanical properties of a cobalt-based alloy deposited by Plasma Transferred Arc welding," *Proc. Internatinal ...*, no. April 2015, pp. 1–8, 2002.
- [8] S. W. Williams, F. Martina, A. C. Addison, J. Ding, G. Pardal, and P. Colegrove, "Wire + Arc Additive Manufacturing," vol. 32, no. February 2015, pp. 641–647, 2016.
- [9] C. Scott, "Cranfield University May Have Just Created the Biggest Metal 3D Printed Part Ever," 2016. [Online]. Available: <https://3dprint.com/152111/cranfield-university-metal-3d-part/>. [Accessed: 18-Nov-2018].
- [10] H. Lockett, J. Ding, S. Williams, and F. Martina, "Design for wire + Arc additive manufacture: Design rules and build orientation selection," *J. Eng. Des.*, vol. 28, no. 7–9, pp. 568–598, 2017.
- [11] Y. Zhai, "Early cost estimation for additive manufacture," Cranfield University, 2012.
- [12] F. Li, S. Chen, J. Shi, H. Tian, and Y. Zhao, "Evaluation and Optimization of a Hybrid Manufacturing Process Combining Wire Arc Additive Manufacturing with Milling for the Fabrication of Stiffened Panels," *Appl. Sci.*, vol. 7, no. 12, p. 1233, 2017.
- [13] J. Xiong, G. Zhang, H. Gao, and L. Wu, "Modeling of bead section profile and overlapping beads with experimental validation for robotic GMAW-based rapid manufacturing," *Robot. Comput. Integr. Manuf.*, vol. 29, no. 2, pp. 417–423, 2013.
- [14] J. Xiong, Z. Yin, and W. Zhang, "Forming appearance control of arc striking and

- extinguishing area in multi-layer single-pass GMAW-based additive manufacturing,” *Int. J. Adv. Manuf. Technol.*, no. June, 2018.
- [15] F. Montevecchi, G. Venturini, N. Grossi, A. Scippa, and G. Campatelli, “Idle time selection for wire-arc additive manufacturing: A finite element- based technique,” *Addit. Manuf.*, vol. 21, no. January, pp. 479–486, 2018.
- [16] P. M. S. Almeida, “Process control and development in wire and arc additive manufacturing,” Cranfield University, 2012.
- [17] H. Geng, J. Li, J. Xiong, and X. Lin, “Optimisation of interpass temperature and heat input for wire and arc additive manufacturing 5A06 aluminium alloy,” *Sci. Technol. Weld. Join.*, vol. 0, no. 0, pp. 1–12, 2016.
- [18] A. H. Nickel, D. M. Barnett, and F. B. Prinz, “Thermal stresses and deposition patterns in layered manufacturing,” *Mater. Sci. Eng. A*, vol. 317, no. 1–2, pp. 59–64, 2001.
- [19] P. Taylor *et al.*, “Beneficial effects of low - frequency pulsed MIG welding on grain refinement of weld metal and improvement of solidification crack susceptibility of aluminium alloys : Study of low - frequency pulsed MIG welding Beneficial effects of low-frequency pulsed,” *Weld. Int.*, no. February 2015, pp. 37–41.
- [20] A. S. Azar, “A heat source model for cold metal transfer (CMT) welding,” *J. Therm. Anal. Calorim.*, vol. 122, no. 2, pp. 741–746, 2015.
- [21] K. F. Ayarkwa, S. Williams, and J. Ding, “Investigation of pulse advance cold metal transfer on aluminium wire arc additive manufacturing,” *Int. J. Rapid Manuf.*, vol. 5, no. 1, pp. 44–57, 2015.
- [22] P. Gerhard, K. Ferdinand, and C. Harald, “Manufacturing of turbine blades by shape giving CMT Welding,” *Met. Addit. Manuf. Conf.*, no. November 2014, p. 10, 2014.
- [23] G. Venturini, F. Montevecchi, A. Scippa, and G. Campatelli, “Optimization of WAAM Deposition Patterns for T-crossing Features,” in *Procedia CIRP*, 2016, vol. 55, pp. 95–100.
- [24] P. Kazanas, P. Deherkar, P. Almeida, H. Lockett, and S. Williams, “Fabrication of geometrical features using wire and arc additive manufacture,” *Proc. Inst. Mech. Eng. Part B J. Eng. Manuf.*, vol. 226, no. 6, pp. 1042–1051, 2012.
- [25] S. Kapil *et al.*, “5-Axis Slicing Methods for Additive Manufacturing Process,” *Annu. Int. Solid Free. Fabr. Symp.*, pp. 1186–1896, 2017.
- [26] R. Brooks, “Diecast tooling developer expanding R&D, production,” 2016. [Online]. Available: <https://www.foundrymag.com/materials/diecast-tooling-developer-expanding-rd-production>. [Accessed: 18-Nov-2018].
- [27] M. Saunders, “Lightweight lattices liberate new product performance,” 2017. [Online]. Available: <https://www.altairnlighten.com/opinion/lightweight-lattices-liberate-new-product-performance/>. [Accessed: 18-Nov-2018].
- [28] J. M. Wilson, C. Piya, Y. C. Shin, F. Zhao, and K. Ramani, “Remanufacturing of turbine blades by laser direct deposition with its energy and environmental impact analysis,” *J. Clean. Prod.*, vol. 80, pp. 170–178, 2014.
- [29] J. Guo, “Feature based cost and carbon emission modelling for wire and arc additive manufacturing,” Cranfield University, 2012.
- [30] A. R. McAndrew *et al.*, “Interpass rolling of Ti-6Al-4V wire + arc additively manufactured features for microstructural refinement,” *Addit. Manuf.*, vol. 21, no. February, pp. 340–349, 2018.
- [31] J. Y. Jung, “Manufacturing cost estimation for machined parts based on manufacturing features,” *J. Intell. Manuf.*, vol. 13, no. 4, pp. 227–238, 2002.
- [32] A. Fiorentino, “Cost drivers-based method for machining and assembly cost

- estimations in mould manufacturing,” *Int. J. Adv. Manuf. Technol.*, vol. 70, no. 5–8, pp. 1437–1444, 2014.
- [33] G. Boothroyd, P. Dewhurst, and W. A. Knight, *Product design for manufacturing and assembly*, 3rd ed. CRC Press, 2010.
- [34] G. Boothroyd and C. Reynolds, “Approximate cost estimates for typical turned parts,” *J. Manuf. Syst.*, vol. 8, no. 3, pp. 185–193, 1989.
- [35] E. G. Klocke F, “Dry Cutting,” in *CIRP Annals*, 1997, vol. 46, no. 2, pp. 519–526.
- [36] P. Zhang, *Advanced industrial control technology*. William Andrew Publishing, 2010.
- [37] P. Dewhurst and G. Boothroyd, “Early cost estimating in product design,” *J. Manuf. Syst.*, vol. 7, no. 3, pp. 183–191, 1988.
- [38] K.-H. Chang, *Product Manufacturing and Cost Estimating using CAD/CAE*. Academic Press, 2013.
- [39] “Huisman successfully load tests world’s first 3d printed offshore crane hook,” 2018. [Online]. Available: https://www.huismanequipment.com/en/media_centre/press_releases/news_item/110/Huisman-successfully-load-tests-world-s-first-3d-printed-offshore-crane-hook. [Accessed: 18-Nov-2018].
- [40] A. Busachi, J. Erkoyuncu, P. Colegrove, F. Martina, and J. Ding, “Designing a WAAM based manufacturing system for defence applications,” *Procedia CIRP*, vol. 37, no. 2013, pp. 48–53, 2015.
- [41] D. Ding, Z. Pan, D. Cuiuri, and H. Li, “A tool-path generation strategy for wire and arc additive manufacturing,” *Int. J. Adv. Manuf. Technol.*, vol. 73, no. 1–4, pp. 173–183, 2014.
- [42] D. Ding, Z. Pan, D. Cuiuri, H. Li, and N. Larkin, “Adaptive path planning for wire-feed additive manufacturing using medial axis transformation,” *J. Clean. Prod.*, vol. 133, pp. 942–952, 2016.
- [43] J.-H. Kao and F. B. Prinz, “Optimal motion planning for deposition in layered manufacturing,” *Proc. DETC ’98*, pp. 1–10, 1998.
- [44] Y. Nilsiam, P. Sanders, and J. M. Pearce, “Slicer and process improvements for open-source GMAW-based metal 3-D printing,” *Addit. Manuf.*, vol. 18, pp. 110–120, 2017.
- [45] Y. Cao, S. Zhu, X. Liang, and W. Wang, “Overlapping model of beads and curve fitting of bead section for rapid manufacturing by robotic MAG welding process,” *Robot. Comput. Integr. Manuf.*, vol. 27, no. 3, pp. 641–645, 2011.
- [46] D. Ding, Z. Pan, D. Cuiuri, and H. Li, “A multi-bead overlapping model for robotic wire and arc additive manufacturing (WAAM),” *Robot. Comput. Integr. Manuf.*, vol. 31, pp. 101–110, 2015.
- [47] J. Mehnen, J. Ding, H. Lockett, and P. Kazanas, “Design study for wire and arc additive manufacture,” *Int. J. Prod. Dev.*, vol. 19, no. 1/2/3, p. 2, 2014.
- [48] H. L. Lockett and M. D. Guenov, “Graph-based feature recognition for injection moulding based on a mid-surface approach,” *CAD Comput. Aided Des.*, vol. 37, no. 2, pp. 251–262, 2005.
- [49] S. Subrahmanyam and M. Wozny, “An overview of automatic feature recognition techniques for computer-aided process planning,” *Comput. Ind.*, vol. 26, no. 1, pp. 1–21, 1995.
- [50] A. Addison, J. Ding, F. Martina, H. Lockett, S. Williams, and X. Zhang, “Manufacture of Complex Titanium Parts using Wire+Arc Additive Manufacture,” *Titan. Eur. 2015 Conf.*, p. 14, 2015.
- [51] E. A. Nasr and A. K. Kamrani, *Computer based design and manufacturing*. Springer

- US, 2007.
- [52] A. Adebayo, "Characterisation of integrated WAAM and machining processes," Cranfield University, 2013.
- [53] J. Xiong, Z. Yin, and W. Zhang, "Forming appearance control of arc striking and extinguishing area in multi-layer single-pass GMAW-based additive manufacturing," *Int. J. Adv. Manuf. Technol.*, vol. 87, no. 1, pp. 579–586, 2016.
- [54] A. A. Uгла and O. Yilmaz, "Deposition-Path Generation of SS308 Components Manufactured by TIG Welding-Based Shaped Metal Deposition Process," *Arab. J. Sci. Eng.*, vol. 42, no. 11, pp. 4701–4711, 2017.
- [55] J. Mehnen, J. Ding, H. Lockett, and P. Kazanas, "Design study for wire and arc additive manufacture," *Int. J. Prod. Dev.*, vol. 19, no. 1/2/3, p. 2, 2014.
- [56] E. Krassenstein, "Mutoh Industries Unveils New Metal Arc Welding 3D Printer, the Value Arc MA5000-S1," 2015. [Online]. Available: <https://3dprint.com/84633/mutoh-industries-value-arc-3d/>. [Accessed: 18-Nov-2018].
- [57] T. Kamioka, T. Abe, S. Ishikawa, and H. Sasahara, "Fabrication of Elbow Pipe by Direct Metal Lamination Using Arc Discharge While Maintaining the Molten Pool in a Horizontal Position," *Int. J. Autom. Technol.*, vol. 4, no. 5, pp. 422–431, 2010.
- [58] "Our machines are based on WAAM technology and are designed to offer a competitive alternative to manufacturers of high added value components." [Online]. Available: <https://www.addilan.com/en/addilan-machine/>. [Accessed: 18-Nov-2018].
- [59] "New VARIAXIS j-600AM Grows the Mazak Additive Series," 2017. [Online]. Available: <https://www.mazakusa.com/news-events/news-releases/new-variaxis-j-600am-grows-the-mazak-additive-series/>. [Accessed: 18-Nov-2017].
- [60] "3D metal printers for industrial production." [Online]. Available: <https://www.gefertec.de/en/3dmp-machines-en/>. [Accessed: 18-Nov-2018].
- [61] K. P. Karunakaran, S. Suryakumar, V. Pushpa, and S. Akula, "Low cost integration of additive and subtractive processes for hybrid layered manufacturing," *Robot. Comput. Integr. Manuf.*, vol. 26, no. 5, pp. 490–499, 2010.
- [62] "Metal 3D Printing Tools for ANY CNC." [Online]. Available: <http://www.3dhybridsolutions.com/>. [Accessed: 18-Nov-2018].
- [63] Y. Bandari, J. Ding, F. Martina, and S. Williams, "Additive Manufacture of Large Structures: Robotic or CNC Systems?," *26th Int. Solid Free. Fabr. Symp. Austin, Texas*, vol. 1, no. November 2015, pp. 17–25, 2015.
- [64] "The factory of the future is here." [Online]. Available: <https://www.stratasys.com/demonstrators>. [Accessed: 18-Nov-2018].
- [65] "Mach 3." [Online]. Available: <https://www.machsupport.com/shop/mach3/>. [Accessed: 18-Nov-2018].
- [66] "LinuxCNC." [Online]. Available: <http://linuxcnc.org/>. [Accessed: 18-Nov-2018].
- [67] "CNC Kit - BF20L - Complete." [Online]. Available: <https://www.redfoxmachinery.com.au/product/cnc-kit-bf20-complete/>. [Accessed: 18-Nov-2018].
- [68] "CNC Rotary Table Series." [Online]. Available: <https://www.nikken-kosakusho.co.jp/en/product/?category=2>. [Accessed: 18-Nov-2018].
- [69] C. E. Becze, P. Clayton, L. Chen, T. I. El-Wardany, and M. A. Elbestawi, "High-speed five-axis milling of hardened tool steel," *Int. J. Mach. Tools Manuf.*, vol. 40, no. 6, pp. 869–885, 2000.
- [70] K. M. Noonan, "A Unique Design for a Desktop Milling Machine," California State University, 2012.

- [71] “Highest performance rotary axis.” [Online]. Available: http://m.schaeffler.com/content.mobile.products/en/products/zkldf/zkldf_info.html. [Accessed: 18-Nov-2018].
- [72] W. han Choi, J. moon Kim, and G. J. Park, “Comparison study of some commercial structural optimization software systems,” *Struct. Multidiscip. Optim.*, vol. 54, no. 3, pp. 685–699, 2016.
- [73] G. Gopal, L. Suresh Kumar, K. Vijaya Bahskar Reddy, M. Uma Maheshwara Rao, and G. Srinivasulu, “Analysis of Piston, Connecting rod and Crank shaft assembly,” *Mater. Today Proc.*, vol. 4, no. 8, pp. 7810–7819, 2017.
- [74] W. Xiangping, Z. Haiou, W. Guilan, and W. Lingpeng, “Adaptive slicing for multi-axis hybrid plasma deposition and milling,” *Proc. 2014 Annu. Int. Solid Free. Fabr. Symp.*, pp. 1277–1287, 2014.
- [75] R. Dwivedi and R. Kovacevic, “Process planning for multi-directional laser-based direct metal deposition,” *Proc. Inst. Mech. Eng. Part C J. Mech. Eng. Sci.*, vol. 219, no. 7, pp. 695–707, 2005.
- [76] D. Ding, Z. Pan, D. Cuiuri, H. Li, N. Larkin, and S. Van Duin, “Automatic multi-direction slicing algorithms for wire based additive manufacturing,” *Robot. Comput. Integr. Manuf.*, vol. 37, pp. 130–150, 2016.
- [77] D. Carter and K. Yamazaki, “Architecture & implementation of CAMAM for the design of direct laser deposition operations,” pp. 83–96, 2016.
- [78] A. Saar, “New end-to-end additive manufacturing solutions to revolutionize product development,” 2016. [Online]. Available: <https://community.plm.automation.siemens.com/t5/News-NX-Manufacturing/New-end-to-end-additive-manufacturing-solutions-to-revolutionize/ba-p/370615>. [Accessed: 18-Nov-2018].
- [79] C. Perry, “Autodesk Launches PowerMill 2019 CAM with NEW Additive and Simpler 5-axis.” [Online]. Available: <http://www.manufacturinglounge.com/autodesk-launches-powermill-2019-cam-new-additive-simpler-5-axis/>. [Accessed: 18-Nov-2018].
- [80] S. Saunders, “After Successful Testing and Verification, 3D Printed WAAMPeller is Introduced to the Public,” 2017. [Online]. Available: <https://3dprint.com/195791/3d-printed-waampeller-verified/>. [Accessed: 18-Nov-2017].
- [81] “ESPRIT ADDITIVE for Direct Energy Deposition.” [Online]. Available: <https://www.espritadditive.com/ded-systems>. [Accessed: 18-Nov-2018].
- [82] “Hybrid manufacturing for closed impellers,” 2018. [Online]. Available: <https://www.sulzer.com/en/shared/about-us/2018/04/11/10/19/hybrid-manufacturing-for-closed-impellers>. [Accessed: 18-Nov-2018].
- [83] “IDN TAKE: TECH SCAN: A BRIEF REVIEW OF BLISK TECHNOLOGY,” 2016. [Online]. Available: <http://www.indiandefensenews.in/2016/07/idn-take-tech-scan-brief-review-of.html>. [Accessed: 19-Nov-2018].
- [84] “Fives and BeAM sign a partnership on additive manufacturing equipment: complementary expertise for a booming industry,” 2015. [Online]. Available: <https://www.fivesgroup.com/news-press/news/fives-and-beam-sign-a-partnership-on-additive-manufacturing-equipment-complementary-expertise-for-a-booming-industry.html>. [Accessed: 19-Nov-2018].
- [85] S. Suryakumar, K. P. Karunakaran, A. Bernard, U. Chandrasekhar, N. Raghavender, and D. Sharma, “Weld bead modeling and process optimization in Hybrid Layered Manufacturing,” *CAD Comput. Aided Des.*, vol. 43, no. 4, pp. 331–344, 2011.

- [86] R. Stuart Ferguson, *Practical Algorithms for 3D Computer Graphics*, 2nd ed. CRC Press, 2014.
- [87] M. Islam, T. Purtonen, H. Piili, A. Salminen, and O. Nyrhilä, “Temperature profile and imaging analysis of laser additive manufacturing of stainless steel,” *Phys. Procedia*, vol. 41, pp. 835–842, 2013.
- [88] L. Song, V. Bagavath-Singh, B. Dutta, and J. Mazumder, “Control of melt pool temperature and deposition height during direct metal deposition process,” *Int. J. Adv. Manuf. Technol.*, vol. 58, no. 1–4, pp. 247–256, 2012.
- [89] J. Mazumder, D. Dutta, N. Kikuchi, and A. Ghosh, “Closed loop direct metal deposition: Art to Part,” *Opt. Lasers Eng.*, vol. 34, no. 4–6, pp. 397–414, 2000.
- [90] J. Xiong and G. Zhang, “Online measurement of bead geometry in GMAW-based additive manufacturing using passive vision,” *Meas. Sci. Technol.*, vol. 24, no. 11, 2013.
- [91] S. K. Everton, M. Hirsch, P. I. Stavroulakis, R. K. Leach, and A. T. Clare, “Review of in-situ process monitoring and in-situ metrology for metal additive manufacturing,” *Mater. Des.*, vol. 95, pp. 431–445, 2016.
- [92] C. Doumanidis and E. Skordeli, “Distributed-Parameter Modeling for Geometry Control of Manufacturing Processes With Material Deposition,” *J. Dyn. Syst. Meas. Control*, vol. 122, pp. 71–77, 2000.
- [93] G. Saeed, M. Lou, and Y. M. Zhang, “Computation of 3D weld pool surface from the slope field and point tracking of laser beams,” *Meas. Sci. Technol.*, vol. 15, no. 2, pp. 389–403, 2004.
- [94] R. Kovacevic and Y. M. Zhang, “Sensing free surface of arc weld pool using specular reflection: Principle and analysis,” *Proc. Inst. Mech. Eng. Part B J. Eng. Manuf.*, vol. 210, no. 6, pp. 553–564, 1996.
- [95] G. Saeed and Y. M. Zhang, “Mathematical formulation and simulation of specular reflection based measurement system for gas tungsten arc weld pool surface,” *Meas. Sci. Technol.*, vol. 14, no. 9, pp. 1671–1682, 2003.
- [96] F. Montevecchi, G. Venturini, A. Scippa, and G. Campatelli, “Finite Element Modelling of Wire-arc-additive-manufacturing Process,” *Procedia CIRP*, vol. 55, pp. 109–114, 2016.
- [97] J. Salvi, J. Pagès, and J. Batlle, “Pattern codification strategies in structured light systems,” *Pattern Recognit.*, vol. 37, no. 4, pp. 827–849, 2004.
- [98] D. Briers *et al.*, “Laser speckle contrast imaging: theoretical and practical limitations,” *J. Biomed. Opt.*, vol. 18, pp. 0066018-1-0066018-9, 2013.
- [99] J. C. Jeong *et al.*, “High-Quality stereo depth map generation using infrared pattern projection,” *ETRI J.*, vol. 35, no. 6, pp. 1011–1020, 2013.
- [100] D. Schwass, M. Wittlich, M. Schmitz, and H. Siekmann, “Emission of UV radiation during arc welding,” 2011.
- [101] “532nm High Performance Laser Line Filter 12.5mm Dia.” [Online]. Available: <https://www.edmundoptics.com/p/532nm-high-performance-laser-line-filter-12.5mm-dia/7575/>. [Accessed: 19-Nov-2018].
- [102] R. V Vinu, “Shaping and Analysis of Laser Speckle for Imaging Applications,” Indian Institute of Space Science and Technology, 2016.
- [103] J. W. Goodman, “Statistical Properties of Laser Speckle Patterns,” in *Laser Speckle and Related Phenomena*, J. C. Dainty, Ed. Berlin, Heidelberg: Springer Berlin Heidelberg, 1975, pp. 9–75.
- [104] N. Chang, “Speckle in a thick diffuser,” University of Rochester, 2009.

- [105] J. Suriansky and M. Cmarada, "Analysis of Methods for Camera Calibration in 3D Scanning Systems," *Ann. DAAAM 2012 Proc. 23rd Int. DAAAM Symp.*, vol. 23, no. 1, pp. 365–368, 2012.
- [106] "Stereo Camera Calibrator App." [Online]. Available: <https://www.mathworks.com/help/vision/ug/stereo-camera-calibrator-app.html>. [Accessed: 19-Nov-2018].
- [107] T. Hua, H. Xie, S. Wang, Z. Hu, P. Chen, and Q. Zhang, "Evaluation of the quality of a speckle pattern in the digital image correlation method by mean subset fluctuation," *Opt. Laser Technol.*, vol. 43, no. 1, pp. 9–13, 2011.
- [108] M. N. Guzmán, G. Hernán Sendra, H. J. Rabal, and M. Trivi, "Island analysis of low-activity dynamic speckles," *Appl. Opt.*, vol. 53, no. 1, p. 14, 2014.
- [109] R. J. Mstafa and K. M. Elleithy, "A video steganography algorithm based on Kanade-Lucas-Tomasi tracking algorithm and error correcting codes," *Multimed. Tools Appl.*, vol. 75, no. 17, pp. 10311–10333, 2016.
- [110] "Track points in video using Kanade-Lucas-Tomasi (KLT) algorithm." [Online]. Available: <https://www.mathworks.com/help/vision/ref/vision.pointtracker-system-object.html>. [Accessed: 19-Nov-2018].
- [111] A. N. Pressley, *Elementary Differential Geometry*, 2nd ed. Springer-Verlag London, 2010.
- [112] M. a Fischler and R. C. Bolles, "Random Sample Consensus: A Paradigm for Model Fitting with Applications to Image Analysis and Automated Cartography," *Commun. ACM*, vol. 24, no. 6, pp. 381–395, 1981.
- [113] Fronius, "Cold metal transfer." 2012.